THE OHIO STATE UNIVERSITY

In situ Laser Activation of Electrochemical Kinetics At Carbon Electrodes

Richard L. McCreery
Department of Chemistry

Air Force Office of Scientific Research
Bolling Air Force Base, D.C. 20332-0001

Grant No. AFOSR-91-0213
Final Report

May 1994

DISCLAIMER NOTICE

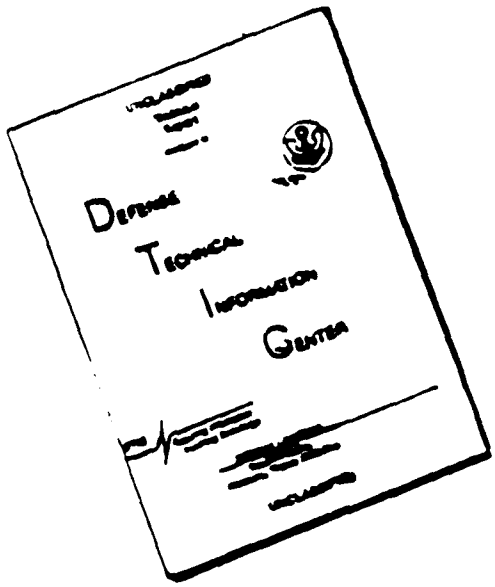

THIS DOCUMENT IS BEST QUALITY AVAILABLE. THE COPY FURNISHED TO DTIC CONTAINED A SIGNIFICANT NUMBER OF PAGES WHICH DO NOT REPRODUCE LEGIBLY.

THE OHIO STATE UNIVERSITY

In situ Laser Activation of Electrochemical Kinetics At Carbon Electrodes

Richard L. McCreery
Department of Chemistry

Air Force Office of Scientific Research
Bolling Air Force Base, D.C. 20332-0001

Grant No. AFOSR-91-0213
Final Report
RF Project No. 768992/724639

May 1994

SECURITY CLASSIFICATION OF THIS PAGE

REPORT DOCUMENTATION PAGE

Form Approved OMB No. 0704-0188

1a. REPORT SECURITY CLASSIFICATION	1b. RESTRICTIVE MARKINGS
2a. SECURITY CLASSIFICATION AUTHORITY	3. DISTRIBUTION/AVAILABILITY OF REPORT: Approved for public release; distribution unlimited.
2b. DECLASSIFICATION/DOWNGRADING SCHEDULE	
4. PERFORMING ORGANIZATION REPORT NUMBER(S): RF 768992/724639	5. MONITORING ORGANIZATION REPORT NUMBER(S): AFOSR-TR- 94 0389
6a. NAME OF PERFORMING ORGANIZATION: Ohio State University Research Foundation; 6b. OFFICE SYMBOL (If applicable): OSURF	7a. NAME OF MONITORING ORGANIZATION: AFOSR/NL
6c. ADDRESS (City, State, and ZIP Code): 1960 Kenny Rd. Columbus OH 43210	7b. ADDRESS (City, State, and ZIP Code): 110 Duncan Ave, Suite B115 Bolling AFB, DC 20332-0001
8a. NAME OF FUNDING/SPONSORING ORGANIZATION: Air Force Ofc Scientific Rsch; 8b. OFFICE SYMBOL (If applicable): AFOSR	9. PROCUREMENT INSTRUMENT IDENTIFICATION NUMBER: AFOSR-91-0213
8c. ADDRESS (City, State, and ZIP Code): Bolling Air Force Base D.C. 20332-0001	10. SOURCE OF FUNDING NUMBERS: PROGRAM ELEMENT NO. 61102F; PROJECT NO. 2303; TASK NO. A1; WORK UNIT ACCESSION NO.

11. TITLE (Include Security Classification)

In situ Laser Activation of Electrochemical Kinetics at Carbon Electrodes

12. PERSONAL AUTHOR(S)

Richard L. McCreery

13a. TYPE OF REPORT	13b. TIME COVERED	14. DATE OF REPORT (Year, Month, Day)	15. PAGE COUNT
Final	FROM 3-1-91 TO 2-28-94	May 31, 1994	103

16. SUPPLEMENTARY NOTATION

17. COSATI CODES			18. SUBJECT TERMS (Continue on reverse if necessary and identify by block number)
FIELD	GROUP	SUB-GROUP	

19. ABSTRACT (Continue on reverse if necessary and identify by block number)

20. DISTRIBUTION/AVAILABILITY OF ABSTRACT ☐ UNCLASSIFIED/UNLIMITED ☐ SAME AS RPT. ☐ DTIC USERS	21. ABSTRACT SECURITY CLASSIFICATION
22a. NAME OF RESPONSIBLE INDIVIDUAL: Richard L. McCreery / MAJ Thomas Frisbie	22b. TELEPHONE (Include Area Code): 614-292-2021 / 202-767-5021 — 22c. OFFICE SYMBOL: NC

DD Form 1473, JUN 86 — Previous editions are obsolete. — SECURITY CLASSIFICATION OF THIS PAGE

Overview:

The overall objective of the project is to identify the structural factors which control electrochemical reactivity at carbon electrode surfaces. The approach combines structural probes such as Raman spectroscopy, XPS, and scanning tunneling microscopy (STM) with measures of reactivity, including electron transfer rate constants (k^o) and adsorption. Laser activation by short but intense laser pulses was used to modify electrode surfaces and enhance reactivity. Work to date has revealed two important conclusions. First, the electronic properties of carbon can differ substantially from that of metals, with major effects on both kinetics and adsorption. Second, the importance of carbon structure to kinetics depends strongly on the redox system in question. These conclusions are described in the following progress report with the citations in brackets referring to the publication list which follows the text.

1. Structural examination of reactive carbon surfaces

Raman spectroscopy is a useful probe for carbon structure, since the phonons observed at ca. 1360 and 1582 cm^{-1} are sensitive to both microcrystallite size and interplanar spacing. We showed previously that the 1360 cm^{-1} band intensity correlates with electron transfer reactivity due to the dependence of both phenomena on disorder. During the current grant period, the Raman probe was enhanced by electrodeposition of Ag particles in situ [1,2] to yield a 10-100 fold increase in intensity. In addition, the surface selectivity of Raman was improved since the SERS enhancement distance (ca. 20 Å) is shorter than the normal Raman sampling depth (ca. 200 Å). After demonstrating the improved surface selectivity on several types of carbon, we used the SERS probe to reveal that several different sp^2 carbon electrode materials (pyrolytic graphite, highly ordered pyrolytic graphite (HOPG), glassy carbon) yield the same surface after electrochemical oxidation (Figure 1). This expands and confirms earlier conclusions based on the less surface selective normal Raman probe [2].

The surface selectivity of STM is unquestioned, and we have used it to characterize laser and pretreatment effects on HOPG and GC. STM of HOPG reveals significant surface damage by a 45 MW/cm^2 laser pulse, the same threshold observed for activation of electrode kinetics [3,4]. The damage mechanism involves rapid nonisotropic thermal expansion of the graphite lattice, creating strain and rupture. The degree of lattice damage was correlated with increases in electrode kinetics and adsorption.

For the case of glassy carbon (GC), one starts with a less ordered and more isotropic material than HOPG, and laser effects are different. SEM, STM, and measurements of anthraquinone 2,6 disulfonate (AQDS) adsorption revealed that 25 MW/cm^2 laser pulses had little effect on GC structure or microscopic surface area [5,6,7]. In fact, procedures which significantly increased electron transfer rates to several redox systems had negligible structural effects observable by these probes. These observations rule out roughness changes, microstructural changes, or surface oxidation as the origin of laser or heat treatment activation of $Fe(CN)_6^{3/-4}$, dopamine, or ascorbic acid electron transfer. At high power densities (>40 MW/cm^2), the GC surface melts, leading to obvious morphological changes which are consistent with predictions of local temperature [5,7].

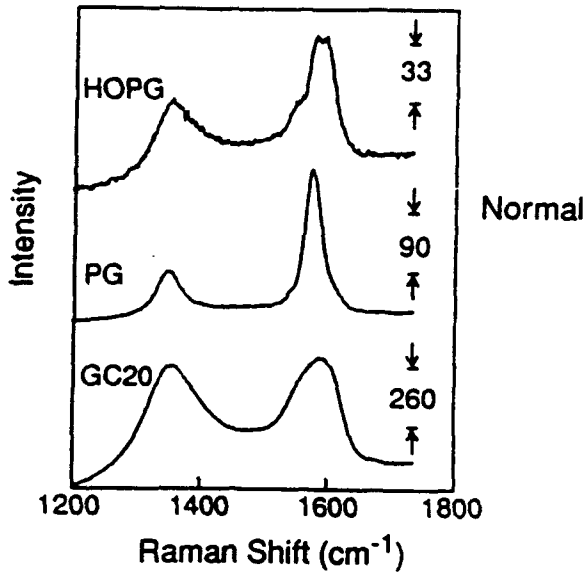

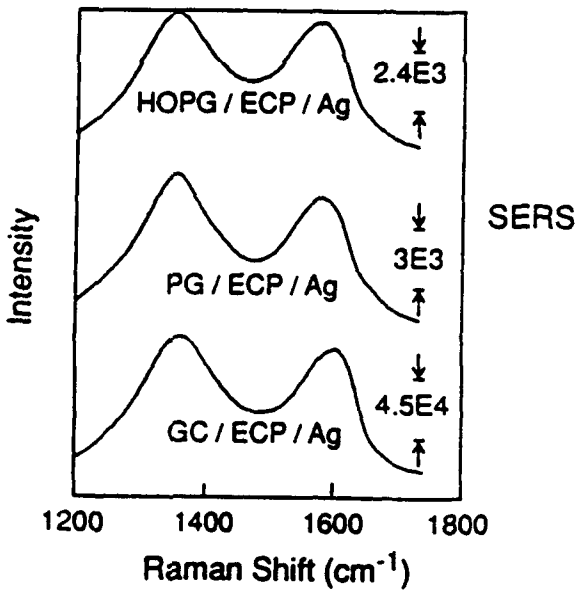

1. Raman spectra of oxidized carbon surfaces before (Normal) and after (SERS) deposition of silver metal. PG=pyrolytic graphite, HOPG= highly ordered pyrolytic graphite. Note both enhancement and surface selectivity following Ag deposition.

These observations are all consistent with our previous hypotheses about the reactivity of graphitic edge plane. HOPG is low in edge plane density and reactivity until damaged by a thermomechanical shock or electrochemical oxidation. GC has plenty of edges, but they need to be exposed by thermal desorption of impurities. As noted later, we have learned much more about the underlying causes of these effects.

2. Enhancement of GC reactivity

The combination of fast, in-situ laser activation (LA) with structural insights from Raman and STM resulted in GC surfaces with unusual electrochemical reactivity, and we have reviewed the extensive literature on this topic [8]. As shown in table 1, laser activated GC yields the highest rate constants yet observed for the commonly studied $Fe(CN)_6^{3/-4}$ benchmark system. This high rate is not accompanied by significant changes in microscopic area, roughness, or capacitance. An unexpected reactivity difference for LA and fractured GC was observed for the dopamine system [9]. Provided the GC surface is clean (as after laser activation), dopamine and other catechols adsorb through their aromatic rings, independent of electrostatic charge. Combined with the kinetic and structural data, these results imply that fractured or laser activated GC supports fast electron transfer and adsorption of certain molecules without the involvement of oxides, provided the surface history from polishing, etc., is removed. The inherent reactivity of GC is the subject of work proposed later.

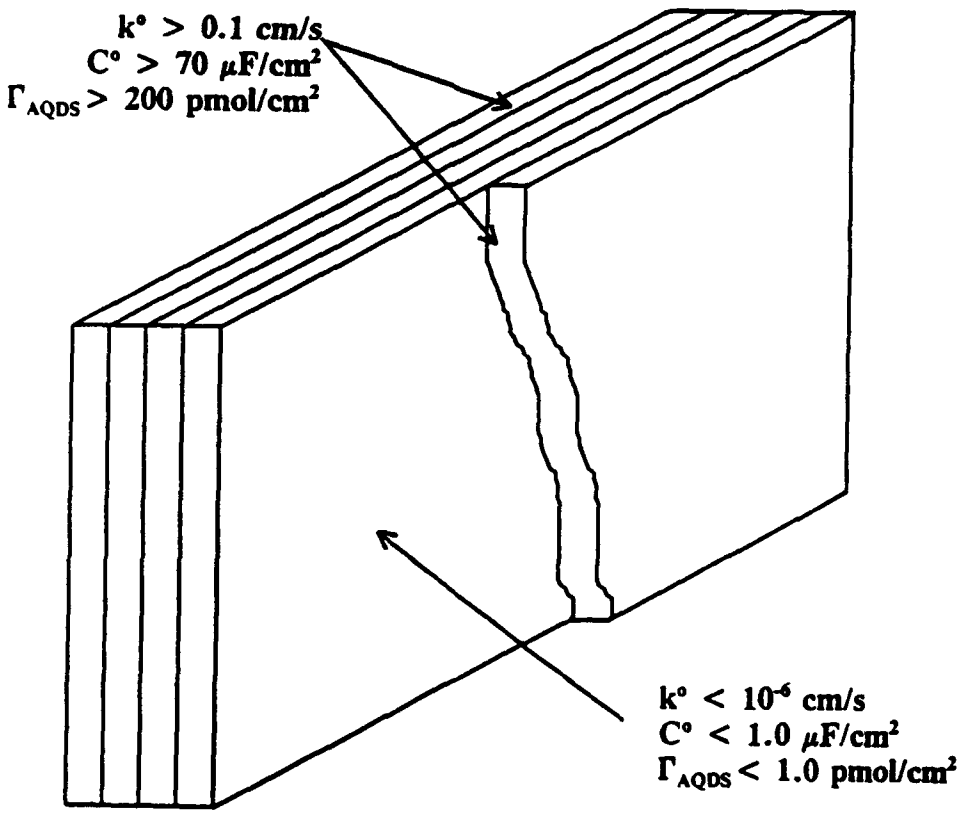

Figure 2. Summary of anisotropic properties of HOPG. k^o is for $Fe(CN)_6^{3/-4}$, 1 M KCl; Γ_{AQDS} is AQDS adsorption in 1 M $HClO_4$. k^o, C^o, Γ were measured on same HOPG surface. From reference [10].

3. Anisotropy of graphite reactivity

A major objective of the work proposed for the 1991-94 grant period was understanding the factors controlling electron transfer kinetics at well defined carbon surfaces. The basal plane of HOPG is such a surface, since it is atomically well defined and relatively easy to prepare. Previous work by Yeager and Gerischer revealed an unusually low capacitance for HOPG, but electrode kinetics had not been studied in any detail. After extensive Raman, adsorption, SEM, capacitance and kinetic investigations of HOPG, we concluded that all of its electrochemical properties are very anisotropic [10]. The capacitance, anthraquinonone 2-6 disulfonate (2,6 AQDS) adsorption, and k^o for several redox systems all depend strongly on the number of defects of a given basal plane surface. For 42 different surfaces on which the three observables were measured, C^o, Γ_{AQDS}, and k^o track each other, indicating that all three are controlled by some weighted average of defect and basal plane regions [10]. These anisotropic properties are summarized in Figure 2.

A quantitative comparison of HOPG and GC properties is made in Table 2.

Table 2

	1360/1580 Raman Ratio	Γ_{AQDS} pmol/cm^2	C^o μF/cm^2	$k^o_{Fe(CN)6}$ cm/s	k^o_{IrCl6} cm/s
GC-20 polished	1.8	186	33	0.002	<0.1
GC-20 3x25 MW/cm^2	1.8	336	34	≥0.5	0.55
GC-20 Fractured	1.1	533	>5	0.5	0.5
HOPG validated	<0.005	<1	<1	$<10^{-5}$	0.003
HOPG cleaved	<0.005	1-70	1-6	10^{-5}-10^{-2}	.003-0.05
HOPG edge	1.1	>200	~70	~.1	

Once the importance of defects to observed HOPG kinetics is appreciated, it is possible to approach "perfect" basal behavior by testing a given surface for defects with some known system (in our case $Fe(CN)_6^{3/-4}$). With great care, it was possible to study 13 redox systems on HOPG which had first been "validated" to have very low defect density [11]. The rates observed for such surfaces represent upper limits of the true basal plane rates, and provide useful insight into factors controlling kinetics at carbon. Specifically:

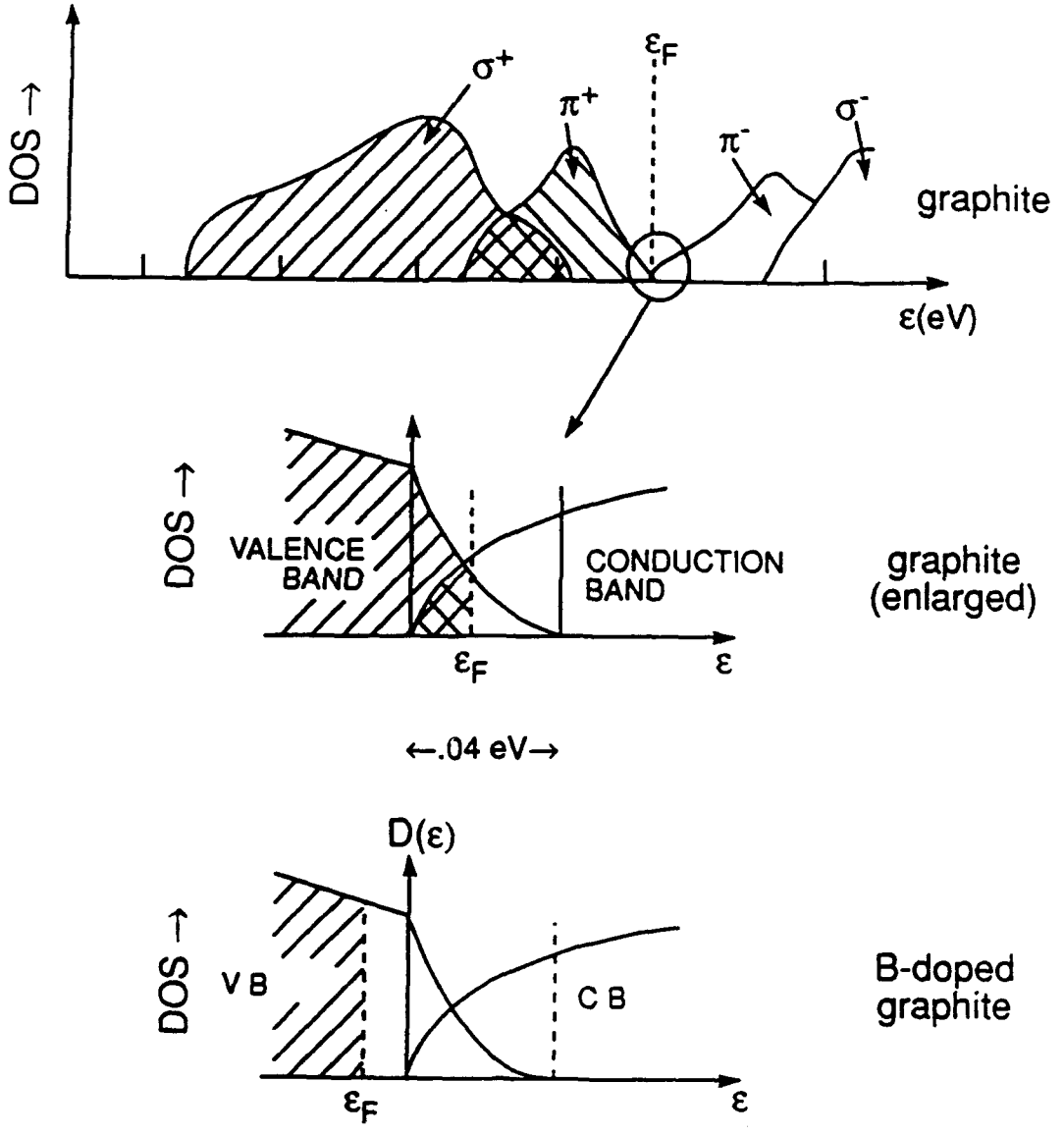

Figure 3A. Calculated density of states (DOS) for HOPG. Second drawing is an enlargement of the overlap between valence and conduction bands. Taken from reference 8a.

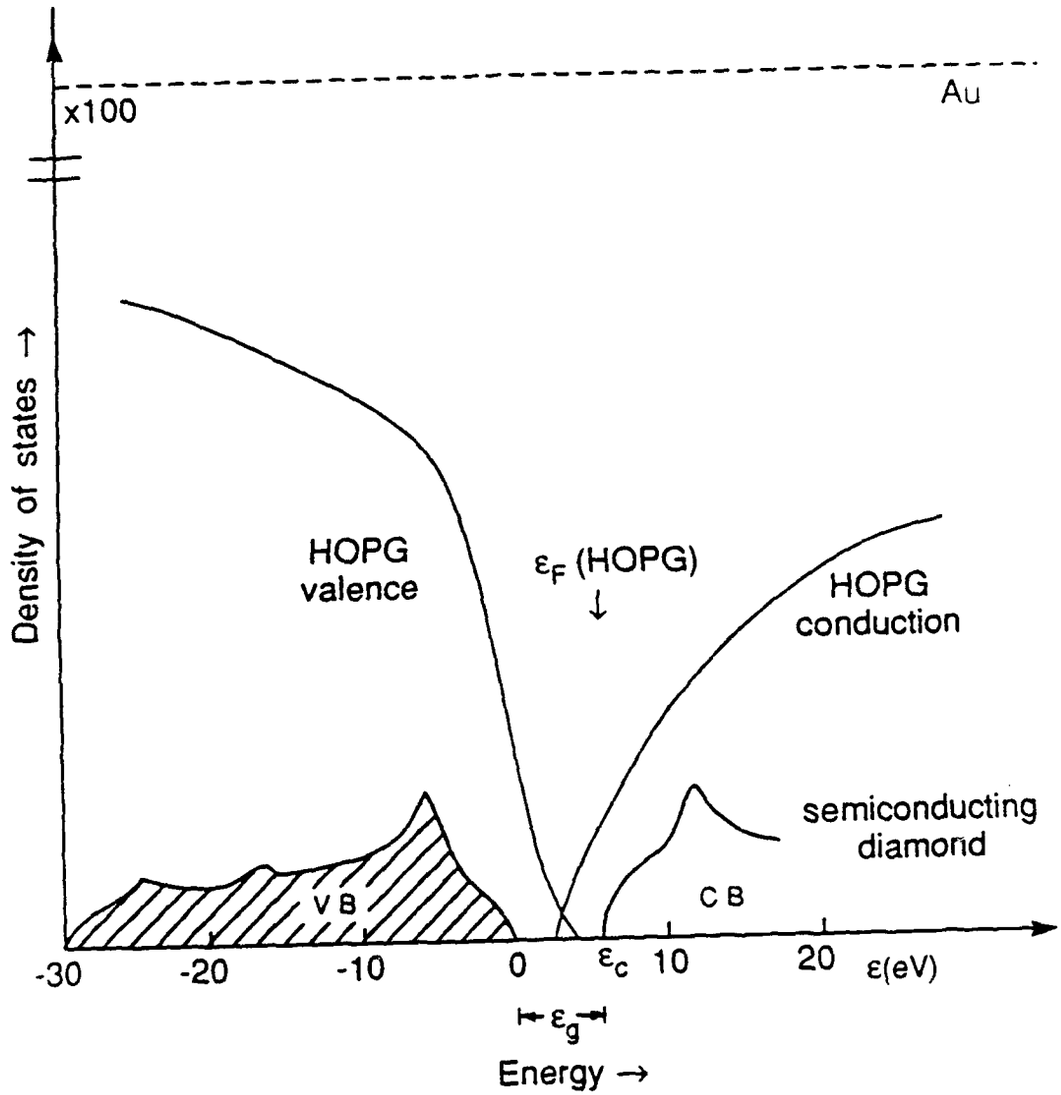

Figure 3B Semiquantitative comparison of DOS for Au, HOPG, and semiconducting diamond. Diamond has a true band gap, while HOPG does not. Gold and most metals have approximately 100x higher DOS than HOPG [11]. Disorder in carbon greatly increases the DOS.

a. All HOPG k^o values were slower than those on GC, usually by 3-5 orders of magnitude.
b. For redox systems believed to involve some specific chemical interactions such as a bridging ligand or ions, proton transfer, etc., the HOPG rate was even slower.
c. k^o on HOPG did not correlate with any hydrophobic or double layer effects, but did track the homogeneous self exchange rate. The observed k^o was much lower than that predicted from Marcus theory.
d. Disorder in the HOPG, either from laser activation or by adventitious defects, greatly increases k^o for all systems studied. It is quite easy to miss the unusual effects of basal HOPG if the surface is even slightly defective.

The origin of the unusual properties of HOPG is important to work proposed below, and appears to depend on two major issues. First, HOPG is a semimetal, with a band structure shown qualitatively in Figure 3. The density of electronic states (DOS) in HOPG is about 1% that of a metal, but still higher than a semiconductor. Although HOPG does not have a band gap, it has a low DOS at the Fermi level, which remains low in the usual potential range for electrochemical solvents. As pointed out by both Gerischer and Yeager, this electronic property leads to a space charge capacitance which lowers the observed capacitance to values much lower than metals (~ 3 vs ~ 30 $\mu F/cm^2$) and semiconductors have lower capacitance still (e.g. ~ 0.1 $\mu F/cm^2$ for Ge). By analogy to Gerischer's theory on charge transfer at semiconductors (Figure 4), the low DOS of HOPG will depress k^o because there will be few states available for e^- transfer at the E^o values we used (+1.0 to -0.8 volts vs SSCE). Thus the semimetal character of HOPG leads to both low capacitance and low k^o. By analogy to semiconductors, disorder in the material increases the DOS at all energies, *increasing both* k^o *and* C^o. (As will be noted later, there is theoretical support for disorder induced electronic changes in HOPG).

The second major factor controlling rates is important for redox systems which involve specific chemical interactions with the surface. HOPG has no dangling bonds or oxides (except at defects), and will not support inner sphere electron transfer requiring such sites. A good example is a group of three aquated ions, $Fe_{aq}^{+2/+3}$, $Eu_{aq}^{+2/+3}$, and $V_{aq}^{+2/+3}$ [12]. These systems exhibit low k^o on either HOPG or clean GC, consistent with their low k_{exc}. However, even slight oxidation of the GC surface greatly increases k^o (by a factor of 500 for $Eu_{aq}^{+2/+3}$); we attribute this enhancement to an oxide dependent inner sphere route, perhaps involving the following structure:

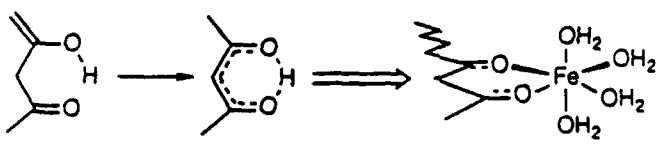

Overall, we conclude that electron transfer at carbon is controlled by an electronic factor, which slows all rates on HOPG, and a surface chemical factor, which is operative for inner sphere systems. Disorder not only changes the electronic factor by increasing the DOS, but it also provides edge or oxide sites for specific chemical interactions. These conclusions are an important step toward understanding what controls ET kinetics at carbon, and they are the basis of much of the proposed work.

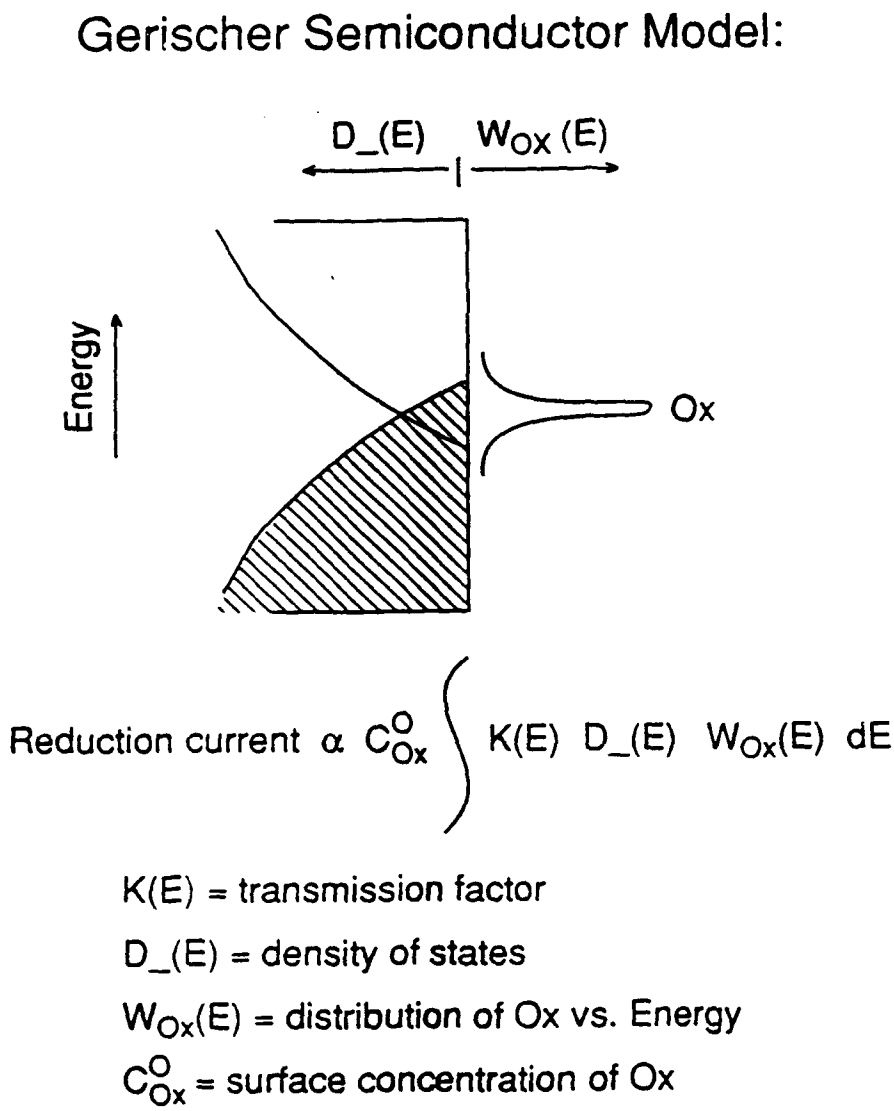

Figure 4. Gerischer model for electrode kinetics at semiconductor electrodes, adapted to HOPG. Low density of charge carriers at favorable energy for e^- transfer to Ox (in this case) reduces rate and current.

Students working on the AFOSR Project

Ronald Rice	Ph.D.	1990	Proctor and Gamble
Yang Wang Alsmeyer	Ph.D.	1991	Eastman Chemical
Mark McDermott	Ph.D.	1993	Iowa State U.
Christie Allred McDermott	Ph.D.	1992	Iowa State U.
Kristin Kneten	Ph.D.	1993	Wittenburg University
Robert Jaworski	Postdoc		Bell Communication Research

Publications resulting from AFOSR support:

1. Yan Wang Alsmeyer, R.L. McCreery, Surface Enhanced Raman Spectroscopy of Carbon Electrodes following Silver Electrodeposition, Anal. Chem., **1991,** 63, 1289.
2. Y.W. Alsmeyer, R.L. McCreery, Surface Enhanced Raman Examination of Carbon Electrodes: Effects of Laser Activation and Electrochemical Pretreatment, Langmuir, **1991**, 7, 2370.
3. R.S. Robinson, Kent Sternitzke, R.L. McCreery, Scanning Tunneling Microscopy of Laser Activated Carbon Electrodes used in studies of Electrochemical Charge Transfer Reactions. J. Vac. Sci. Technol. B **1991**,9, 960.
4. R.S. Robinson, Kent Sternitzke, M.T. McDermott, R.L. McCreery, Morphology and Electrochemical Effects of Defects on Highly Ordered Pyrolytic Graphite, J. Electrochem. Soc., **1991,** 138, 2412
5. R.J. Rice, R.L. McCreery, Effects of Wavelength, pulse duration, and power density on laser activation of glassy carbon electrodes, J. Electroanal. Chem., **1991,** 310, 127.
6. N.M. Pontikos, R.L. McCreery, Microstructural and Morphological Changes Induced in Glassy Carbon Electrodes by Laser Irradiation, J. Electroanal. Chem., **1992**, 324, 229.
7. M.T. McDermott, C.A. McDermott, R.L. McCreery, Scanning Tunneling Microscopy of Carbon Surfaces: Relationships between Electrode Kinetics, Capacitance, and Morphology for Glassy Carbon Electrodes, Anal. Chem., **1993**, 65, 937.
8. R.L. McCreery, Carbon Electrodes: Structural Effects on Electron Transfer Kinetics, in Electroanalytical Chemistry, A.J. Bard, ed., Dekker, N.Y., **1991**, volume 17, pp 221-374.
9. C. D. Allred, R.L. McCreery, Adsorption of Catechols on Fractured Glassy Carbon Electrode Surfaces, Anal. Chem., **1992,** 64, 444
10. M.T. McDermott, K. Kneten, R.L. McCreery, Anthraquinonedisulfonate Adsorption, Electron-Transfer Kinetics, and Capacitance on Ordered Graphite Electrodes: The Important Role of Surface Defects, J. Phys. Chem., **1992**, 96, 3124.
11. K.R. Kneten, R.L. McCreery, Effects of Redox System Structure on Electron-Transfer Kinetics at Ordered Graphite and Glassy Carbon Electrodes, Anal. Chem., **1992**, 64, 2518.
12. C.A. McDermott, K.R. Kneten, R.L. McCreery, Electron Transfer Kinetics of Aquated

$Fe^{+3/+2}$, $Eu^{+3/+2}$, and $V^{+3/+2}$ at Carbon Electrodes: Inner Sphere Catalysis by Surface Oxides, J. Electrochem. Soc., **1993**, 140, 2593.

13. R.K. Jaworski, R.L. McCreery, Laser Induced Transient Currents on Glassy Carbon Electrodes: Double Layer and Ion Adsorption Effects, J. Electrochem. Soc., **1993**, 140, 1360.
14. W. Huang, R.L. McCreery, Electron Transfer Kinetics of $Fe(CN)_6^{3/-4}$ on Laser Activated and CN^- Modified Pt Electrodes J. Electroanal. Chem., **1992**, 326, 1.
15. K.R. Kneten, R.L. McCreery, Carbon Electrodes, Laboratory Techniques in Electroanalytical Chemistry, Kissinger, P.; Heineman, W.; ed. in press.
16. K.R. Kneten, M.T. McDermott, R.L. McCreery, Anomalously Slow Electron Transfer at Ordered Grahpite Electrodes: Influence of Electronic Factors and Reactive Sites, J. Phys. Chem., in press.
17. R.K. Jaworski, R.L. McCreery, Laser Activation of Carbon Microsdisk Electrodes: Surface Oxide Effects on $Ru(NH_3)_6^{+2/+3}$ Kinetics, J. Electroanal. Chem., in press.
18. R.L. McCreery, Carbon Electrode Surface Chemistry: Optimization of Bioanalytical Performance, Neuromethods: Voltammetric Methods, in press.

Appendices

J. Electroanal. Chem., 310 (1991) 127–138
Elsevier Sequoia S.A., Lausanne

Effects of wavelength, pulse duration and power density on laser activation of glassy carbon electrodes

Ronald J. Rice and Richard L. McCreery

Department of Chemistry, The Ohio State University, 120 W. 18th Ave., Columbus, OH 43210 (USA)

(Received 16 October 1990; in revised form 27 February 1991)

Abstract

The hypothesis that laser activation of glassy carbon (GC) electrodes is thermally driven was investigated by comparing simulated surface temperatures for several lasers and experimental conditions. Assuming no phase changes, the surface temperature vs. time profile for a laser pulse striking a GC electrode was predicted by finite difference simulation. It was predicted that peak surface temperature depends on power density, wavelength, pulse duration and the optical properties of the carbon. Experimentally, laser activation is weakly wavelength dependent for ascorbic acid and $Fe^{2+/3+}$. The surface temperatures required for activation were consistent for different lasers, supporting the conclusion that laser activation is thermally driven. Furthermore, predicted surface temperatures during activation were below the melting point of carbon but well above the boiling point of water. The results should be useful for predicting the effectiveness of different laser conditions on electron transfer activation.

INTRODUCTION

Laser effects on solids have been examined in a variety of contexts, including laser desorption mass spectrometry, laser welding and surgery, and laser induced melting of semiconductors. Of particular relevance to the present discussion are laser activation of solid electrodes for enhancing electron transfer kinetics [1–8], and pulsed laser melting of sp^2 carbon materials [10–13]. Our laboratory [1–3,14] and others [6–9] have reported that in-situ or ex-situ laser irradiation can greatly increase the heterogeneous electron transfer rate of several redox systems, particularly on carbon electrodes. The effect is fast, long-lived and repeatable, and can be carried out directly in the solution of interest. Activation has been attributed to formation of edge plane defects on highly ordered pyrolytic graphite (HOPG) electrodes [4] and to the removal of chemisorbed and/or physisorbed impurities on glassy carbon (GC) [14]. A variety of lasers, pulse durations and peak power densities have been employed in our lab and others for electrochemical activation, including

0022-0728/91/$03.50

Nd : YAG (1064 nm, 9 ns and 532 nm, 7 ns) [1,14], N_2 (337 nm, ~ 4 ns) [6,15], and iodine (1513 nm, 150 μs) [7]. With proper selection of parameters, laser activation of GC results in electron transfer rates which meet or exceed those achieved by the best ex-situ techniques such as ultraclean polishing and thermal treatments [14,16,17]. For completely different reasons, pulsed laser effects on graphite have been examined, with the objective of forming and characterizing liquid carbon [10–13]. A phase transition to a metallic liquid state at ca. 4300 K has been reported when HOPG is irradiated with pico- and nanosecond laser pulses. The process was concluded to be completely thermally driven with rapid thermal expansion of the graphite layers followed by melting at 4300 K, Melting was observed when the energy density of a 694 nm, 30 ns ruby laser pulse exceeded 0.63 J/cm^2 [10], Simulations of peak surface temperature and melt depth were consistent with experimental observations.

If laser activation of electron transfer is also thermally driven, several questions arise about the activation mechanism and the effect of experimental conditions. Does the power density required for activation depend on laser wavelength and pulse duration? Is melting involved in activation? Is the same activation threshold expected for in-situ vs. ex-situ activation and for HOPG vs. GC? The questions were addressed by simulating the surface temperature of GC and HOPG under various irradiation conditions, and correlating such simulations with observed activation thresholds. Although significant assumptions are required to carry out the simulations, they do provide useful insights into the factors affecting the activation process.

THEORY

The variables which control the surface temperature of the laser irradiated carbon can be classified into three groups: those relating to the electrode materials, those of the laser, and those of the medium in which irradiation occurs. Carbon material variables include the real and imaginary parts of the refractive index (n and k), the heat capacity, density and thermal conductivity (C_p, ρ and K), and the melting point and heat of fusion. Laser variables are wavelength (λ), FWHM duration (t_p), power density (I_0), angle of incidence, and spatial beam uniformity. For illumination in an optically transparent ($k = 0$) medium, the medium's refractive index will affect electrode reflectivity, and its boiling point and heat of vaporization may be important. In order to make the temperature simulation tractable, several approximations will be made. First, n, k, ρ, C_p and K for carbon were assumed to be independent of temperature and equal to their values at 298 K. It is known that C_p, K, and ρ vary significantly with T for HOPG due to thermal expansion [10]. For example, the c-axis thermal conductivity decreases by 50%, and the heat capacity increases by 21% from 298 to 1000 K. These effects should be smaller for GC due to smaller thermal expansion than for HOPG, and in any case are difficult to incorporate into the simulation. The second approximation is to ignore phase changes of carbon or solvent, including melting, vaporization, or

plasma formation. Below a carbon surface temperature of 4300 K in air or vacuum, this assumption is reasonable if the heat of possible desorption of surface layers is negligible. Given that the average ablation rate of GC for Nd : YAG pulses is a few Å per pulse for typical conditions [3], there appears to be negligible heat loss through carbon ablation. In a solvent, it is likely that the heated surface will vaporize the solvent, resulting in a lower than predicted temperature. Once vaporized, however, the gaseous solvent will have low thermal conductivity and the surface temperature may rise well above the solvent boiling point. Any phase change (carbon melting, solvent vaporization, or desorption) will require heat, so a simulation ignoring these factors leads to an upper limit for surface temperature. A third assumption involving the electrode material is that all heat is conducted away from the surface by the carbon, since its thermal conductivity is high compared to the gas or solvent. Even in a high thermal conductivity solvent like water, K is less than 10% that of GC (5.7×10^{-3} vs. 8.7×10^{-2} W/cm K). Fourth, the laser beam is assumed to be spatially homogeneous across the irradiated electrode and its temporal profile is assumed gaussian. The latter is a reasonable assumption for most pulsed lasers, with the peak power (I_0) being defined as the total pulse energy divided by the FWHM pulse width (t_p).

The approach to simulating temperature vs. time transients on laser irradiated carbon is based on an explicit finite difference calculation [18] similar to that used for diffusion problems, and resembles the approach used by Steinbeck et al. [10], As shown schematically in Fig. 1, the distance into the solid electrode is divided into

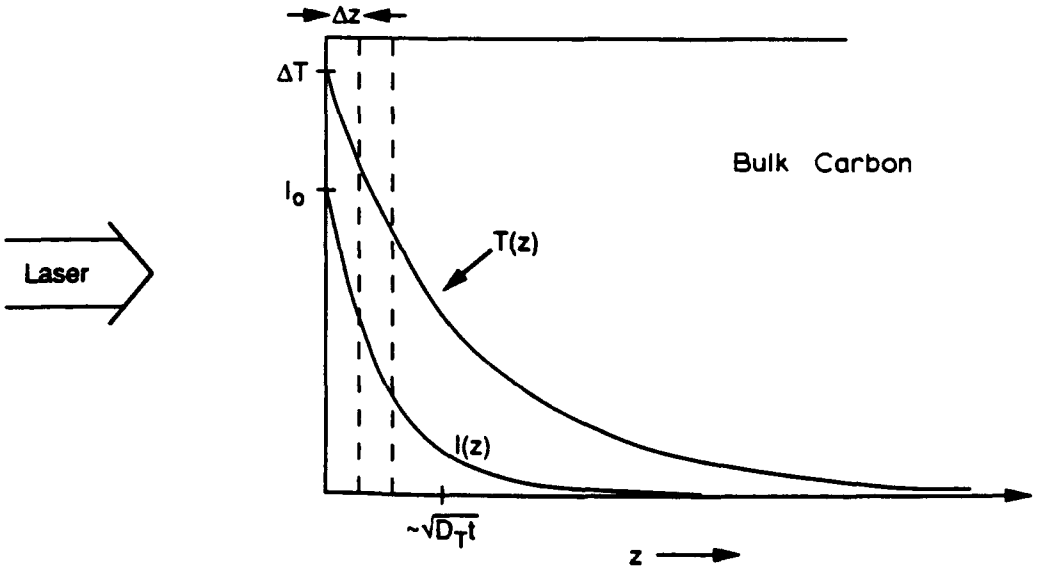

Fig. 1. Laser intensity and temperature profiles within carbon electrode during laser pulse. Thermal penetration depth is approximately $\sqrt{D_T t}$, where t is the time after the laser pulse. ΔT is the peak surface temperature.

increments and the temperature in each increment is simulated with respect to time. The laser beam penetrates the solid according to eqn. (1),

$$I(z, t) = I(0, t)(1 - R)\, e^{-4\pi kz/\lambda} \tag{1}$$

where $I(0, t)$ is the surface irradiance, R the reflectivity, k the imaginary part of the refractive index of the carbon, z the depth and λ the laser wavelength. Since k is fairly large for sp^2 carbon materials, the light penetrates typically less than 1000 Å before 50% attenuation. The heat deposited in each distance increment is the derivative of the intensity, and will also track the time profile of the laser pulse.

During and after the laser pulse, heat is conducted away from the surface into the solid. The thermal diffusivity D_T ($= K/\rho C_p$) has units of cm^2/s and governs thermal diffusion. It is necessary to define a parameter d which relates the average distance of thermal diffusion during the laser pulse to the penetration depth of the laser light:

$$d = (D_T t_p)^{1/2}/\lambda \tag{2}$$

Along with the dimensionless thermal diffusion coefficient ($D_T\, \Delta t/\Delta z^2 = 0.45$, by analogy to the diffusion parameter for electrochemical simulations), d and k are the only parameters required to calculate a dimensionless surface temperature vs. time profile, with dimensionless time being defined as t/t_p. The dimensionless temperature θ is given by eqn. (3) [18],

$$\theta = \frac{(\Delta T)\rho C_p D_T^{1/2}}{I_0(1 - R)t_p^{1/2}} \tag{3}$$

where I_0 is the peak laser irradiance (W/cm^2). In each time increment the heat deposited in each distance increment is calculated from eqn. (1), then heat is propagated into the solid. The resulting θ vs. t/t_p plots for each distance increment may be converted to ΔT vs. t at any depth z, but only surface values are reported here. A typical θ vs. t/t_p plot is shown in Fig. 2, along with axes showing ΔT vs. t for a particular set of conditions. The optical properties of GC (n and k) used to calculate Fig. 2 and Table 1 are from the literature [19,20], and the necessary thermal constants ($K = 0.0870$ J/cm s K, $C_p = 1.26$ J/g K, and $\rho = 1.48$ g/cm^3) were obtained from the Tokai product literature. R was calculated from standard expressions assuming normal incidence and known values of GC and solvent n and k. For GC, R ranged from 0.20 (1064 nm) to 0.11 (265 nm). The approach was partially validated by comparison to a simpler calculation by Ready [22] which assumed that the penetration depth of the laser was negligibly small. When the present calculation was performed for large k (corresponding to surface absorption of the laser) the ΔT vs. t curves agreed with Ready's approach to better than 1%.

Under the constraints of the assumptions noted above, eqns. (1)–(3) and Fig. 2 permit some useful predictions before extensive calculations are made. First, the surface temperature change ΔT should be proportional to laser power density. This prediction should apply up to the temperature where phase changes occur, particu-

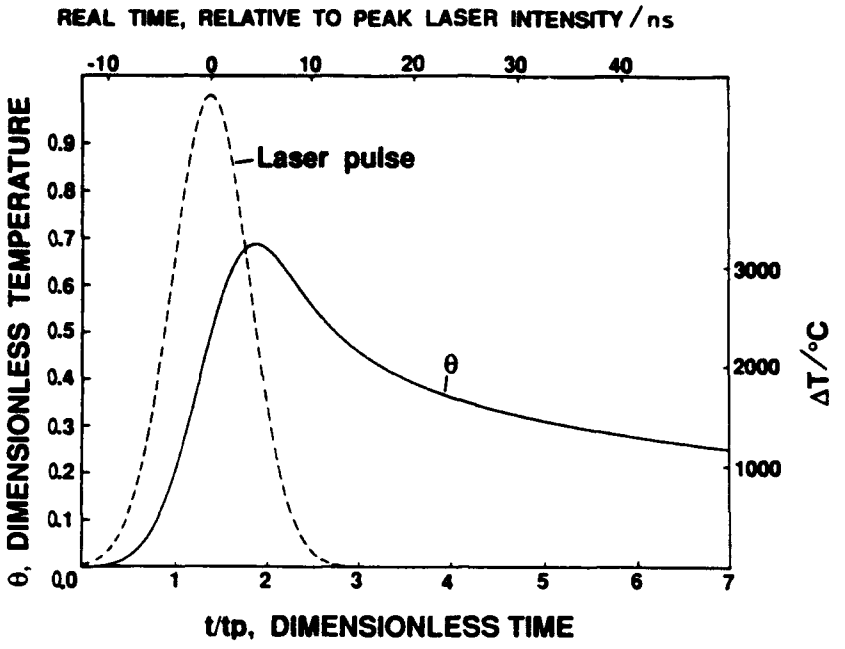

Fig. 2. Laser pulse intensity (— — —) and θ (———) as functions of time. Left and lower axes are dimensionless temperature and time, upper and right axes are the corresponding real time and temperature for a 9 ns, 25 MW/cm^2, 1064 nm laser pulse applied to GC in air. Simulation parameters: $k = 0.966$, $D_T = 0.0467$ cm^2/s.

larly melting of the carbon. Second, ΔT is proportional to $(1 - R)$, since less reflective materials will absorb more heat. Since R will be lower in water than in air, we would predict a higher activation threshold power density in air. Third, ΔT will depend on D_T and t_p, but the dependence is not obvious since these parameters are involved in both eqns. (2) and (3). They will be discussed further below. The principle qualitative conclusion to draw from the theoretical discussion so far is the dependence of ΔT on several variables, including D, λ, t_p, R, I_0, ρ and C_p. These variables must be considered when using laser activation with different materials, solvents and lasers.

The effect of laser wavelength on θ is shown in Fig. 3, for parameters appropriate to GC, t_p was fixed at 9 ns, but λ was varied from 308 to 1064 nm for which k equals 0.725 (308 nm), 0.711 (532 nm), and 0.966 (1064 nm) [20]. The curve corresponding to surface adsorption (large k) is shown for comparison. Notice that the peak θ (θ_p), increases for shorter λ, but not greatly. Since k is varying slowly with λ, this effect is due mainly to smaller penetration depth as λ is decreased (eqn. 1), thus depositing heat in a thinner layer near the surface.

Table 1 lists the peak values of θ and ΔT simulated for a variety of experimental conditions. The results are useful for predicting the effects of t_p, λ, etc. on ΔT, but ΔT values above 4000 K are suspect due to probable melting of carbon at 4300 K. However, since ΔT is linear with power density (ignoring melting) the tabulated ΔT_p values are useful for scaling to lower power densities. Some entries are artificial in

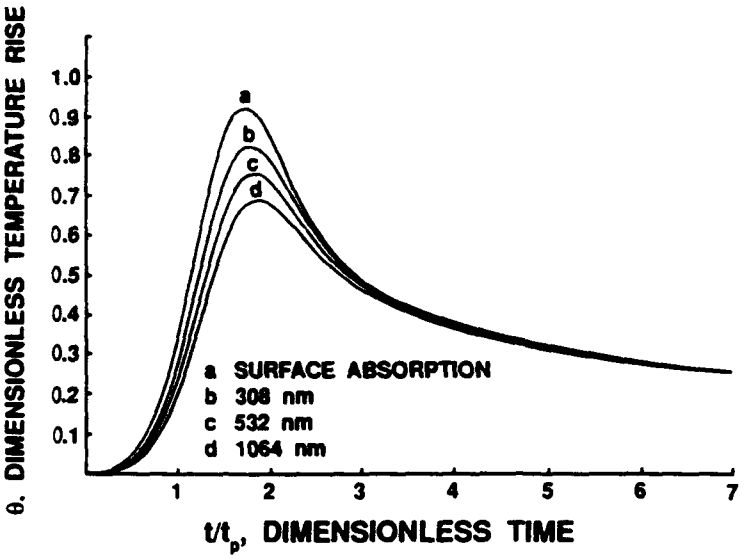

Fig. 3. Effect of laser wavelength on θ for GC. t_p was 9 ns and D_T was 0.0467 cm^2/s in all cases. Curve (a) is for surface adsorption with no laser penetration, and remaining curves are as follows: (b) $\lambda = 308$ nm, $k = 0.725$; (c) 532 nm, $k = 0.711$; (d) $\lambda = 1064$ nm, $k = 0.966$.

order to fix certain variables. For example, a Nd:YAG laser cannot normally sustain 25 MW/cm^2 for 100 ns (group B), but the entry is present to show the effect of pulse duration at constant power density. Group A of Table 1 lists explicitly the effect of power density, and predicts a peak surface temperature for the Nd:YAG case at 25 MW/cm^2 of 3230 K. These conditions are typical of several previous experiments with laser activation [1–3,5], and 25 MW/cm^2 is adequate for GC activation for most redox reactions. Group B shows the effect of pulse duration. The first three entries show the expected increase in ΔT with longer pulses, provided the power is constant. When pulse energy is constant rather than power, shorter pulses produce higher surface temperature since less time is allowed for thermal diffusion. Group C shows the effect of laser wavelength on ΔT_p, for constant t_p and I_0. Since k varies slowly over most of the λ range considered, most of the effect on ΔT stems from the smaller penetration depth at shorter wavelength. The resulting increase in heat deposition near the surface leads to higher ΔT_p for shorter wavelength.

Group D of Table 1 shows simulated ΔT_p results for conditions similar to those used in several reports on laser activation. ΔT_p for activation in water and air are shown, but the only difference between the two media is assumed to be the different $(1 - R)$ value caused by varying refractive index. Solvent vaporization or surface chemical effects are ignored. For the Nd:YAG laser (1064 nm) the 10–25 MW/cm^2 power density range leads to $\Delta T = 1300$–3300 K. A ruby laser (694 nm) at the same power produces larger ΔT due to greater t_p. The iodine (1513 nm) laser's long t_p yields high ΔT at lower I_0, with 0.15 MW/cm^2 yielding a ΔT_p comparable to a 25 MW/cm^2 Nd:YAG laser. The short pulse of the N_2 laser (337 nm) produces a

TABLE 1

Peak values of θ and ΔT simulated for a variety of experimental conditions

	λ/nm	t_p/ns	k	I_0/MW cm^{-2}	θ_p	ΔT_p/K	
						H_2O	Air
Glassy carbon (ρ = 1.48 g/cm^3, C_p = 1.26 J/g K, D_T = 0.0467 cm^2/s)							
A	1064	9	0.966	10	0.686		1290
	1064	9	0.966	25	0.686		3230
	1064	9	0.966	50	0.686		6460
	1064	9	0.966	100	0.686		12900
B	1064	100	0.966	25	0.835		13100
	1064	9	0.966	25	0.686		3230
	1064	0.1	0.966	25	0.203		101
	1064	100	0.966	2.25	0.835		1180
	1064	0.1	0.966	2250	0.203		9090
	1064	0.004	0.966	1000	0.0493		9810
C	1064	9	0.966	25	0.686		3230
	694	9	0.77	25	0.721		3580
	532	9	0.711	25	0.750		3790
	337	9	0.70	25	0.804		4160
	308	9	0.725	25	0.816		4270
	265	9	0.760	25	0.831		4350
D	1064	9	0.966	25	0.686	3733	3230
	1064	9	0.966	10	0.686	1490	1290
	694	30	0.77	25	0.802	8290	8100
	694	30	0.77	10	0.802	3320	3240
	1513	150000	0.958	0.4	0.902	8771	8443
	1513	150000	0.958	0.15	0.902	3290	3170
	532	7	0.711	25	0.731	3530	3260
	337	4	0.70	25	0.755	2780	2610
	337	5	0.70	19	0.771	2420	2261
	308	17	0.75	15	0.835	3810	3569
	265	7	0.76	15	0.820	2400	2270
HOPG (ρ = 2.25 g/cm^3, C_p = 1.48 J/g K, D_T (c-axis) = 0.027 cm^2/s)							
E	1064	9	1.52 [a]	25	0.718		2180
	1064	9	1.52	37	0.718		3230
	1064	9	1.52	45	0.718		3920
	694	30	1.52	21	0.835		3890
	532	0.02	1.52	7000	0.214		8570

[a] Calculated from ref. 23.

smaller ΔT_p than the Nd:YAG even though the penetration depth is smaller. The XeCl excimer laser (308 nm) results in a 3100 K ΔT for 15 MW/cm^2 power density.

Finally, predictions of ΔT for illumination of the basal plane of HOPG are given in group E. Based on published data [19], k for HOPG varies slowly in the 500–1064 nm range, and is assumed equal to the value at 515 nm (1.52). Differences

in $(1 - R)$, D_T, and k for HOPG compared to GC lead to significantly smaller ΔT_p for the same conditions, with a 25 MW/cm^2 Nd:YAG pulse producing a 2200 K rather than 3200 K temperature excursion. Our laboratory has reported a damage threshold for the Nd:YAG fundamental on HOPG of 45 MW/cm^2 [4,5] corresponding to a ΔT_p of 3920 K. Steinbeck et al. [10] note a threshold of 0.63 J/cm^2 for a ruby laser (694 nm, 30 ns), corresponding to 3890 K. Despite differences in I_0, and λ, and t_p, the laser damage to HOPG occurs at similar ΔT_p values close to the melting point of the carbon. Before this correlation is considered firm, however, note that the 140 mJ/cm^2 damage threshold reported by Malvezzi et al. [13] for 20 ps pulses on HOPG corresponds to a much higher surface temperature, shown in the last entry of Table 1.

EXPERIMENTAL

Except for the choice of laser, the activation experiments were conducted with the apparatus described previously [1,3]. The Nd:YAG fundamental (1064 nm, 9 ns) and second harmonic (532 nm, 7 ns) from a Quantel 580-10 and the fundamental of a XeCl excimer (308 nm, 17 ns) were directed onto a GC electrode defined by a teflon washer on a GC disk. Power density was measured with a Scientech CW thermal power meter placed after the teflon aperture which defined the electrode diameter (0.9 mm). With the laser operating at ca. 10 Hz, the power density equalled the average power passing through the aperture divided by the repetition rate, pulse width and aperture area. The manufacturer's stated pulse widths were verified with a fast photodiode and 400 MHz oscilloscope. As noted previously, the power densities stated here are $\pm 20\%$ due to spatial and shot-to-shot power variation. Power density measurements were made with the cell window in place, but losses due to solvent absorption were ignored.

Passage of the laser beam through the teflon aperture produced Fresnel diffraction and accompanying power density fluctuation at the electrode. This effect leads to a ca. $\pm 20\%$ spatial variation in power density which is largest nearest the edge of the illuminated area. For ordered materials such as HOPG, this phenomenon causes variable laser damage and was avoided by laser activation in the absence of any aperture. As will be shown below, the Fresnel diffraction effect is minor compared to effects of laser wavelength, and will be ignored.

All laser activation procedures involved three laser pulses delivered to a freshly polished electrode (0.05 μm Buehler alumina, on Texmet polishing cloth) in the solution of interest. Although ultraclean polishing has been demonstrated to lead to high electron transfer rates [16], the conventional procedure was used here to best illustrate laser effects. Repolishing after each activation experiment eliminated cumulative effects of repeated activation. Test redox systems included ascorbic acid (AA) in pH 7.0 phosphate buffer and $Fe^{2+/3+}$ [from $Fe(NH_4)_2(SO_4)_2$] in 1 M H_2SO_4. The experimental approach involved observation of AA and $Fe^{2+/3+}$ voltammograms as a function of laser wavelength and power density. GC was Tokai GC-20 in all cases.

RESULTS AND DISCUSSION

The effect of pulsed lasers on AA oxidation at GC has been reported previously, with 1064 nm irradiation of 25 MW/cm^2 or higher power density producing a large negative shift of E_p [1]. Similar large increases in electron transfer rate were observed here for $Fe^{2+/3+}$, as shown in Fig. 4. ΔE_p decreases from ca. 700 mV to ca. 150 mV following 30 MW/cm^2 laser pulses. The effects of power density and wavelength on $E_{p/2}$ for AA are shown in Fig. 5. Below 5 MW/cm^2, the laser has no observable effect, while above 25 MW/cm^2 $E_{p/2}$ has reached a limiting value close to that expected for reversible charge transfer. There is a modest but real effect of laser wavelength on activation, with shorter wavelengths activating at lower power density. If one defines a threshold activation power density arbitrarily as that where $E_{p/2}$ shifts halfway from its initial to final value, the threshold is 6, 8, and 11 MW/cm^2 for 308, 532, and 1064 nm light, respectively. A similar plot of ΔE_p for $Fe^{2+/3+}$ is shown in Fig. 6 from which approximate threshold power densities of 10, 16, and 17 MW/cm^2 for 308, 532, and 1064 nm light can be determined.

Based on the simulations listed in Table 1, group D, the shorter wavelength laser is expected to yield a higher surface temperature. The simulated ΔT_p values for the experimental conditions used here are listed in Table 2. Several conclusions are available from the combination of experimental thresholds and simulated temperatures listed. First, activation of GC for $Fe^{2+/3+}$ and AA requires temperatures well below the melting point at ca. 4300 K. Since the simulated temperatures are upper limits for the power densities listed, melting is very unlikely. Second, the ΔT_p values compare well for a given redox system despite variations in λ and t_p. This consistency provides support for a thermal mechanism for laser activation, with a

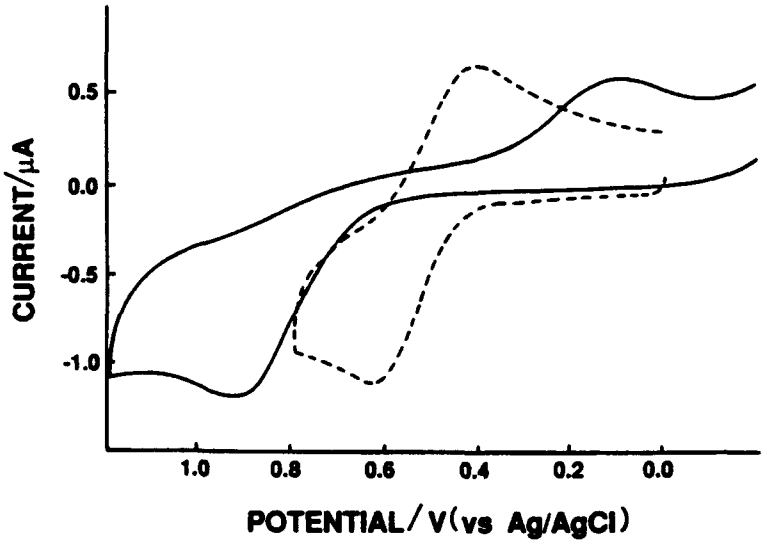

Fig. 4. Voltammograms of 1 mM $Fe^{3+/2+}$ in 1 M H_2SO_4, 100 V/s. (———) Polished surface, (— — —) after three 1064 nm, 30 MW/cm^2 laser pulses delivered in situ.

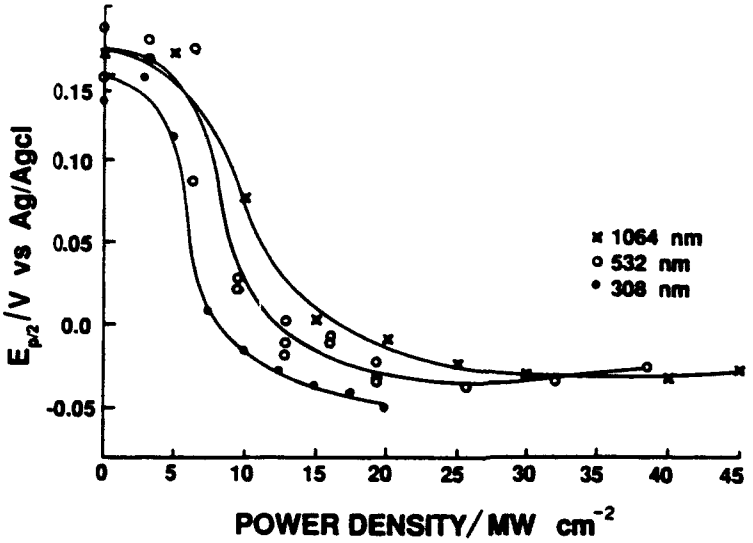

Fig. 5. Half peak potential for ascorbic acid oxidation on GC-20 in pH 7.0 phosphate buffer. Each point was determined from a freshly polished surface which was laser activated at the wavelengths and power densities indicated. Smooth curves are for clarity and do not imply any fit to the results. Scan rate was 100 mV/s.

fairly weak dependence on laser wavelength. Third, the activation temperatures for AA differ significantly from those for $Fe^{2+/3+}$. Although few details are available on laser activation of $Fe^{2+/3+}$ on GC, the higher temperature required may imply a different activation mechanism from that of AA. Although conjecture at this point, it is possible that $Fe^{2+/3+}$ requires surface chemical changes beyond surface cleaning. Fourth, the 20–25 MW/cm^2 (at 1064 nm) power densities used in previous investigations are well above the thresholds observed for GC, and imply ΔT_p values

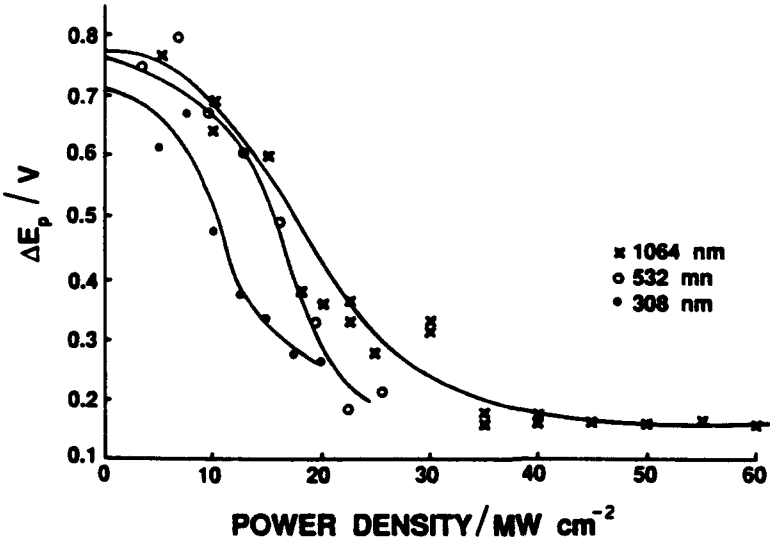

Fig. 6. ΔE_p for $Fe^{2+/3+}$ in 1 M H_2SO_4 in same format as Fig. 5.

TABLE 2

Simulated threshold ΔT_p for GC, in water

System	λ/mm	t_p/ns	I_0 (threshold) [a]/MW cm^{-2}	ΔT_p [b]/K
AA	308	17	6	1524
	532	7	8	1130
	1064	9	11	1620
$Fe^{2+/3+}$	308	17	10	2540
	532	7	16	2260
	1064	9	17	2530

[a] Observed laser power density producing an $E_{p/2}$ or ΔE_p value midway between the fully activated and unactivated values.

[b] Simulated surface temperature change for the experimental conditions present at threshold.

of 2500–3300 K. Finally, laser power densities above those required to reach the activation temperatures may be unnecessary or even counterproductive. Excessive laser power may lead to high background or extensive surface damage. Using the temperature simulation as a guide, these effects can generally be avoided.

As noted earlier, higher laser powers are required to heat basal plane HOPG, due mainly to higher reflectivity and density. The 45 MW/cm^2 damage threshold for 1064 nm, 9 ns pulses produces a comparable ΔT_p to the 30 ns, 21 MW/cm^2, 694 nm ruby laser pulses required to initiate melting of HOPG [10]. Although melting may occur during laser induced damage of HOPG, it may not be required. An alternative mechanism involves constrained thermal expansion of the heated graphite which can occur at temperatures below the melting point [14]. The significantly higher simulated temperatures required to activate or damage HOPG may imply a different activation mechanism for HOPG vs. GC.

Although laser activation of Pt electrodes has been demonstrated [2], it has not been studied in detail. Nevertheless, it is useful to compare predicted surface temperatures for Pt vs. GC electrodes. Based on physical constants for Pt at room temperature [24], the thermal diffusivity (0.251 cm^2/s) is much higher than that of GC (0.0467 cm^2/s) as is its reflectivity (ca. 70% rather than 15%). Primarily because of these differences, the laser power required to heat a Pt surface is significantly higher than that for GC. For example, a 1064 nm, 9 ns, 25 MW/cm^2 pulse is predicted to heat a Pt surface by 630 K, while 100 MW/cm^2 would produce a 2500 K surface temperature excursion (ignoring melting). There is no assurance that the activation mechanisms are similar on Pt and GC, but the point remains that higher laser power densities are required to heat a more reflective, higher thermal conductivity material.

CONCLUSIONS

While there are obvious limitations to the simulations presented here, the predicted ΔT_p values do illustrate the effects of laser wavelength, pulse duration, and power density on surface temperature. Since phase changes are ignored in the simulation, the ΔT_p values should be most reliable for activation in air or inert gas

and ΔT_p values below 4300 K. The most significant experimental observation is the weak dependence of activation on laser wavelength. This observation is consistent with a completely thermally driven activation mechanism, and rules out photochemical effects in the wavelength range examined. It is important to note that different lasers produce markedly different ΔT_p values for a given power density, and one should not assume that a threshold power density for activation will apply across all laser parameters. The current results imply that the peak surface temperature controls activation rather than power density per se. It appears that AA activation requires a ΔT_p of ca. 1500 K, even if λ, t_p or I_0 are varied. The temperature simulations are consistent with our previous conclusion that laser activation of GC involves primarily surface cleaning while activation of HOPG requires creation of edge plane sites [14]. The lower temperatures required for GC activation (1500–2500 K) may be adequate for surface cleaning but insufficient for graphite lattice damage which does not occur until ca. 4000 K. This possibility is corroborated by the observation that the Raman spectrum of GC does not change upon laser activation [14], while that of HOPG does [4]. Finally, the nitrogen, iodine, and YAG lasers used in several investigations of laser activation are predicted to lead to quite different surface temperature excursions. Variables of pulse duration, power density, and wavelength should be considered when choosing activation conditions.

REFERENCES

1 M. Poon and R.L. McCreery, Anal. Chem., 58 (1986) 2745.
2 M. Poon and R.L. McCreery, Anal. Chem., 59, (1987) 1615.
3 M. Poon and R.L. McCreery, Anal. Chem., 60, (1980) 1725.
4 R.J. Bowling, R.T. Packard and R.L. McCreery, J. Am. Chem. Soc., 111 (1989) 1217.
5 R.J. Rice and R.L. McCreery, Anal. Chem., 61 (1989) 1637.
6 L. Bodalbhai and A. Brajter-Toth, Anal. Chem., 60 (1988) 2557.
7 K. Stulik, D. Brabcova and L. Kavan, J. Electroanal. Chem., 250, (1988) 173.
8 R. Alkire and M. Feldman, J. Electrochem. Soc., 135 (1988) 1850.
9 T. Strein and A.G. Ewing, Anal. Chem., 63 (1991) 194.
10 J. Steinbeck, G. Braunstein, M.S. Dresselhaus, T. Venkatesan and D.C. Jacobson, J. Appl. Phys., 58 (1985) 4374.
11 J.S. Speck, J. Steinbeck and M.S. Dresselhaus, J. Mater. Sci., 5 (1990) 980.
12 J. Heremans, C.H. Olk, G.L. Esley, J. Steinbeck and G. Dresselhaus, Phys. Rev. Lett. 60 (1988) 452.
13 A.M. Malvezzi, N. Bloembergen and C.Y. Huang, Phys. Rev. Lett., (1986) 146.
14 R. Rice, N. Pontikos and R.L. McCreery, J. Am. Chem. Soc., 112 (1990) 4617.
15 K.D. Sternitzke and R.L. McCreery, Anal. Chem., 62 (1990) 1339.
16 I.F. Hu, D.H. Karweik and T. Kuwana, J. Electroanal. Chem., 188 (1985) 59.
17 R.L. McCreery, in A.J. Bard (Ed.), Electroanalytical Chemistry, Vol. 17, Marcel Dekker, New York, 1991, pp. 221–314.
18 R.J. Rice, M.Sc. Thesis, The Ohio State University, 1987.
19 E.A. Taft and H.R. Phillip, Phys. Rev., 138 (1965) A197.
20 M.W. Williams and E.T. Arakawa, J. Appl. Phys., 43 (1972) 3460.
21 W.G. Driscoll, in W. Vaughn (Ed.), Handbook of Optics, McGraw-Hill, New York, 1978, p. 10–10.
22 J.F. Ready, J. Appl. Phys., 36 (1963) 462.
23 N. Wada and S. Solin, Physica, 105B (1981) 353.
24 R.C. Weast (Ed.), CRC Handbook of Chemistry and Physics, 66th ed., CRC Press, Boca Raton, FL, 1985.

J. Electroanal. Chem., 324 (1992) 229–242
Elsevier Sequoia S.A., Lausanne
JEC 01890

Microstructural and morphological changes induced in glassy carbon electrodes by laser irradiation

Nicholas M. Pontikos and Richard L. McCreery *

Department of Chemistry, The Ohio State University, 120 West 18th Ave., Columbus, OH 43210 (USA)

(Received 26 July 1991; in revised form 9 October 1991)

Abstract

Raman spectra, phenanthrenequinone adsorption, differential capacitance and scanning electron micrographs on fractured and polished glassy carbon (GC) surfaces were monitored before and after pulsed laser irradiation of varying power density. At power densities below 30 MW/cm^2, the Raman spectra, Γ_{PQ}, C°_{dl} and SEM appearance of polished surfaces changed slightly with laser activation. However, the Raman spectra of fractured GC indicated increased disorder during laser irradiation. After vigorous laser treatment, the Raman spectrum became similar to that of the polished surface, but Γ_{PQ} and C°_{dl} on the fractured surface did not change greatly at power densities below 30 MW/cm^2. At higher power densities, both polished and fractured surfaces showed significantly higher Γ_{PQ} and C°_{dl}, and the SEMs showed evidence of local melting. After 70 MW/cm^2 laser treatment, the fractured and polished surfaces were quite similar. The results support a mechanism based on thermomechanical shock below about 30 MW/cm^2 and local melting above this threshold.

INTRODUCTION

The selection of an appropriate carbon material for a specific electrochemical application is complicated due to the difficulty in predicting its electrochemical behavior, specifically the heterogeneous electron transfer rate constant k° [1,2]. A significant body of literature has been devoted to the explanation of the many factors which affect k° on a variety of carbon surfaces, with glassy carbon being the most widely studied carbon material in the context of electrode kinetics [2–11]. The use of glassy carbon (GC) as an electrode material is widespread due to its wide potential range, relatively low cost, low porosity, chemical inertness, and availability. However, electrochemical applications of GC are complicated by the

* To whom correspondence should be addressed.

fact that its behavior is highly dependent on its surface history. The mechanisms of pretreatment procedures for GC activation toward electron transfer and the subsequent passivation during use are not completely understood.

Several surface pretreatment procedures have been developed for enhancing $k°$ on glassy carbon. They include polishing [5,6], chemical and electrochemical pretreatment [12–15], vacuum heat treatment [7,16], thermal and rf plasma treatments [7,8,17,18], and laser activation [3,10,11,19]. These methods produce carbon surfaces which show increases in $k°$ by factors of 10 to 1000 relative to conventionally polished surfaces for benchmark systems such as $Fe(CN)_6^{3-/4-}$ [1,5]. The mechanism of these increases in $k°$ remains an active area of research. Kuwana et al. and Wightman et al., proposed that active sites exist on carbon and that the removal of impurities such as polishing debris and surface oxygen expose these sites [5,7,20–22], while others propose that oxygen functionalities enhance $k°$ for certain redox systems [15,23]. Considering the problem generally, the determination of which surface variables affect GC electrode behavior is complex because several electrochemical observations are affected by more than one independent surface variable. For example, $k°$, capacitance, and adsorption each depend on the independent variables of surface roughness, surface edge plane density, and surface coverage of oxides or impurities. Since pretreatment procedures such as polishing and electrochemical pretreatment affect more than one independent surface variable, the mechanism of activation is difficult to determine.

In several previous reports, the number of surface variables was reduced by starting with the basal plane of highly ordered pyrolytic graphite (HOPG) [24–26]. For this case, it was concluded that $k°$ for $Fe(CN)_6^{3-/4-}$ was much larger on graphitic edge plane than on basal plane, and the observed $k°$ was determined primarily by the fractional coverage of edge plane on the surface. A subsequent study of GC also sought to reduce the number of surface variables by examining $k°$ on a GC surface created by fracturing in the electrolyte solution. This surface did not undergo any intentional pretreatment, yet exhibited a high (0.5 cm/s) $k°$ for $Fe(CN)_6^{3-/4-}$ in 1 M KCl [3]. In the current investigation, the fractured GC surface was examined in more detail, and compared with a conventionally polished surface. By observing Raman spectra, phenanthrenequinone (PQ) adsorption, capacitance, and $k°$, we sought to gain a better understanding of GC surface variables which affect electrode kinetics.

EXPERIMENTAL

Raman spectra of GC surfaces were obtained in air with 514.5 nm light and a Spex 1403 spectrometer. The spectral bandpass was 10 cm^{-1}, and typical laser power at the sample was between 50 and 70 mW. Laser activation was performed using a Quantel (Continuum) model 580–10 Nd:YAG laser delivering 9 ns pulses at 1064 nm. Laser pulses were delivered in groups of three unless otherwise noted, in order to average spatial and temporal variations. Power density was determined by measuring the average power through a 1.4 mm metal aperture. The electro-

chemical cell used for all experiments was constructed of Teflon with a BK-7 quartz window (> 95% transmittance) to allow the 1064 nm laser radiation to impinge upon the GC-20 electrode in solution.

GC-20 working electrodes were fabricated from a Tokai GC-20 plate by first diamond sawing the carbon then sanding the piece obtained into a small rectangle of approximate dimensions $0.05 \times 0.05 \times 1.0$ cm. The carbon microrod was then mounted onto a conducting surface and coated with Eccobond Epoxy (Emerson & Cuming, Inc., Woburn, MA) as opposed to the Torr Seal (Varian) used previously [3]. Prior to each use, the glassy carbon electrode was polished with slurries of 1.0, 0.3, and 0.05 μm alumina in Nanopure (Barnstead, Boston, MA) water on microcloth (Buehler), then sonicated briefly to remove polishing debris. A Bioanalytical Systems (BAS) Ag/AgCl/3 M NaCl electrode was used as the reference, while a platinum wire served as the auxiliary electrode. Prior to fracturing, the Eccobond epoxy was filed away to expose a short GC "post", which was scored and fractured in solution such that the end of the post became the active surface. Typical areas, as measured by single step chronoamperometry of $Fe(CN)_6^{4-}$ in 1 M KCl, were on the order of 0.005 cm^2 for the exposed GC-20 face. These small electrodes were necessary in order to ensure a "mirror" region upon fracturing [3].

Electrochemical measurements were performed using customized computer software and a Scientific Solutions Labmaster analog interface board which controlled an Advanced Idea Mechanics model 18709 potentiostat (Columbus, OH). The potentiostat was driven by a triangular potential vs. time ramp from a Tektronix 501A function generator. Apparent capacitance was measured by the method of Gileadi [27,28] which involved applying a 100 Hz, 20 mV peak-to-peak triangle wave centered on 0.0 V vs. Ag/AgCl from the Tektronix function generator and recording the current response on a Lecroy 9400A digital oscilloscope. The area used in the calculation of capacitance and PQ adsorption was determined by chronoamperometry of $Fe(CN)_6^{4-}$ on a 1 to 5 s time scale. Background corrected current vs. $t^{-1/2}$ plots were linear.

Phenanthrenequinone (PQ) was recrystallized three times from benzene prior to use. The magnitude of PQ adsorption was determined by the method of Anson [29], using a 10^{-6} M solution in 1 M $HClO_4$. The area of the PQ reduction voltammetric peak above background (obtained at 100 mV/s) was used to determine the adsorbed charge, Q_{ad}, and Γ_{PQ} was calculated based on the chronoamperometric area.

RESULTS

Raman spectra of carbon have been examined previously and found to be quite sensitive to the microstructure of the sp^2 carbon material [1,3,30–32]. GC-20 has a strong 1360 cm^{-1} band which is negatively correlated with the size of the graphitic planes. This band becomes active due to a symmetry breakdown at the graphitic edges. Tuinstra and Koenig reported a linear correlation between the reciprocal of

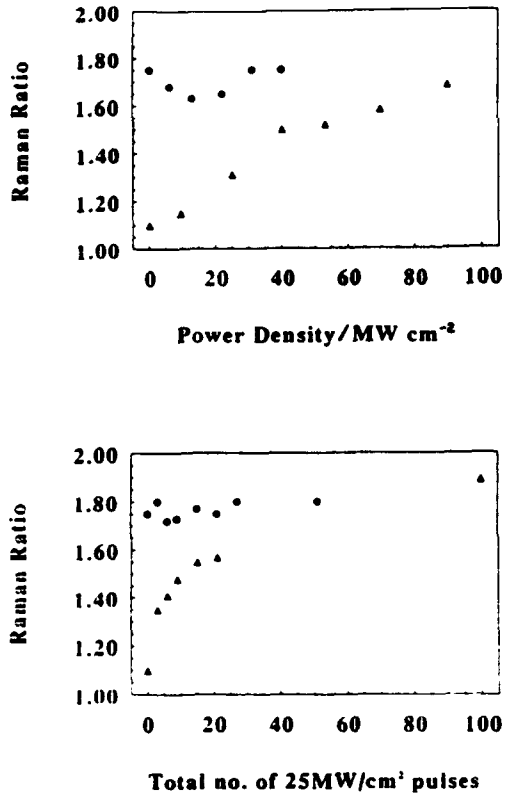

Fig. 1. Raman intensity ratio of GC-20 vs. power density (top) and successive 25 MW/cm^2 pulses (bottom). ● Polished surfaces, (▲) fractured surfaces. For the top plot, a freshly fractured GC surface was used for each triangular point.

the microcrystallite size ($1/L_a$) and the 1360/1582 Raman intensity ratio, with larger ratios implying more graphitic edges and smaller microcrystallites [32]. For glassy carbon, we demonstrated that the 1360/1582 intensity ratio is sensitive to pretreatment procedures [3,30]. Specifically, fracturing a GC-20 microrod produces an intensity ratio of 1.1, while polishing increases this ratio to 1.8, implying mechanical generation of smaller microcrystallites.

A fractured surface was observed first since it is initially free of surface contaminants and presumably representative of the unmodified bulk GC. The top plot in Fig. 1 summarizes the results for varying power density. Each data point was obtained by starting with a freshly fractured GC surface, then exposing the surface to three laser pulses. The 1360/1582 Raman intensity ratio increases for a fractured surface with increasing Nd:YAG power density, indicating that microstructural changes are occurring. Although the intensity ratio starts at a higher value for the polished surface, it shows little change with laser activation, implying that no major additional microstructural changes are induced. The bottom graph in Fig. 1 shows polished and fractured surfaces exposed to successive 25 MW/ cm^2 Nd:YAG pulses. The pulses were delivered in groups of three followed by acquisition of Raman spectra with the sequence being repeated until 99 pulses had

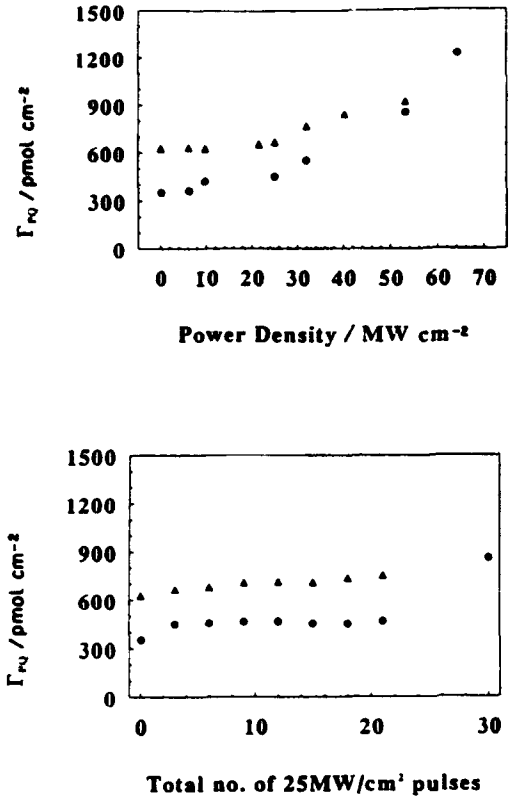

Fig. 2. Adsorption of phenanthrenequinone vs. power density (top) and successive 25 MW/cm^2 pulses (bottom). Electrodes were encapsulated in Eccobond epoxy. (●) Surfaces which were polished prior to laser irradiation, (▲) surfaces which were initially fractured.

been delivered. These results indicate that the Nd:YAG laser causes microstructural changes for a fractured surface, at least to a depth comparable to the Raman sampling depth of ca. 30 nm [33]. Apparently laser activation of a surface already modified by polishing has little further effect on the carbon microstructure, at least to any extent observable with Raman spectroscopy.

The effects of laser activation on phenanthrenequinone (PQ) adsorption and the differential capacitance of fractured and polished surfaces are shown in Figs. 2 and 3. Γ_{PQ} (pmol/cm^2) was determined voltammetrically via the equation

$$Q_{ads} = nFA_g\Gamma_{PQ} \tag{1}$$

where Q_{ads} is the integral of the background corrected voltammetric peak for adsorbed PQ, n is 2, F is the Faraday constant, A_g is the chronoamperometric area, and Γ_{PQ} is the equilibrium coverage of PQ. Note that Γ_{PQ} is based on chronoamperometric area and makes no presumptions about microscopic area. The differential capacitance was determined via the equation

$$I_{p-p} = 2\nu A_g C_{dl}^{\circ} \tag{2}$$

where I_{p-p} is the peak-to-peak current due to double layer charging in response to an imposed 20 mV p – p triangle wave, ν is the slope of the triangle wave, A_g is chronoamperometric area, and C°_{dl} is the double layer capacitance ($\mu F/cm^2$).

Referring first to Fig. 2, it is apparent that Γ_{PQ} increases slightly with laser irradiation below 25 MW/cm^2 for either polished or fractured surfaces. Note that Γ_{PQ} starts at ca. 600 pmol/cm^2 for the fractured surface, about twice the value on the polished surface. For repetitive 25 MW/cm^2 pulses, Γ_{PQ} on either surface increases by at most 40% over initial values. In addition, the fractured surface exhibits consistently higher Γ_{PQ} for all conditions except high power densities. Γ_{PQ} for both fractured and polished GC increases significantly with laser activation, by more than a factor of 3 for polished GC at high power density. The Γ_{PQ} values reported here are significantly higher than those reported previously [3] for GC encapsulated in Torr-seal epoxy. We attribute this difference to reduced contamination of the surface by the Eccobond epoxy compared to Torr-seal, for several reasons. Γ_{PQ} was comparable to the Eccobond values when the GC was encapsulated in compression molded Kel-F prior to fracturing. Dopamine adsorption on fractured GC decreased with time after fracture for Torr-seal encapsulation, but was much more stable for Eccobond [34]. It is possible that the seal between Eccobond and GC is prone to microcracks, increasing the effective adsorption area. However, this possibility is quite unlikely. Optical microscopy of the Eccobond/GC seal revealed no cracks, and Γ_{PQ} was quite reproducible. As noted below, fast cyclic voltammograms of $Fe(CN)_6^{3-/4-}$ had the expected shape for planar diffusion without any cracks. Finally, large cracks are ruled out by the good agreement between the geometric and chronoamperometric areas.

Similar behavior was observed for capacitance, shown in Fig. 3. At 25 MW/cm^2 or below, capacitance is not affected greatly by laser irradiation, but the fractured surface always exhibits higher C°_{dl} than the polished surface. In addition, repetitive 25 MW/cm^2 pulses increase capacitance by about 50%, as noted in a previous report [3]. Above 25 MW/cm^2, C°_{dl} for the polished surface increases markedly. Although the C°_{dl} values for the polished surface before and during laser activation are similar to those reported previously [3], the fractured C°_{dl} values are somewhat higher (55 vs. 36 $\mu F/cm^2$), probably because of the difference in the encapsulation material mentioned earlier.

Scanning electron micrographs of polished and fractured surfaces are shown in Figs. 4 and 5, respectively. In all cases, the samples were gold coated before SEM. Micrographs obtained at lower magnification were featureless, and resembled images reported previously by Kazee et al. [35], and by our laboratory [10]. The fine structure apparent in Figs. 4 and 5 may not have been visible in previous work because the current samples were gold coated or because of differences in polishing procedures. The apparent fissures in Fig. 4a are discussed in more detail below. In Fig. 4b, following 40 MW/cm^2 laser activation, new features are observed which were not observed following 25 MW/cm^2 irradiation. After 70 MW/cm^2 the surface is characterized by occasional large defects (visible at the right) in a sea of small (~ 0.1 μm) nodules. Thus major morphological changes

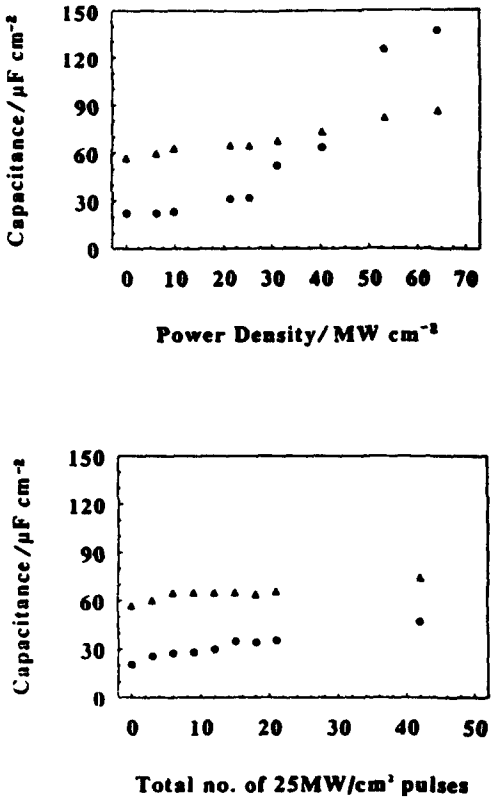

Fig. 3. Apparent capacitance vs. power density (top) and successive 25 MW/cm^2 pulses (bottom). (●) surfaces which were initially polished, (▲) surfaces which were initially fractured.

occurred to the polished surface between 25 and 70 MW/cm^2, starting below 40 MW/cm^2. The fractured surface of Fig. 5a exhibits nodules of GC distributed fairly homogeneously. No obvious changes are apparent upon laser activation at 40 MW/cm^2 (Fig. 5b) and 70 MW/cm^2 (Fig. 5c). Manual measurement of the nodules revealed an average diameter for the fractured surface of 0.16 ± 0.05 μm ($N = 109$), which decreased to 0.09 ± 0.03 μm ($N = 100$) upon 70 MW/cm^2 laser activation.

The SEMs appear to reveal microcracks on the polished surface, as well as small fissures between nodules on the fractured surface. It is reasonable to suspect that these apparent cracks will affect voltammetric peak shapes, since electroactive species in the cracks will undergo thin layer rather than semi-infinite diffusion. This possibility was tested by comparing voltammograms for $Fe(CN)_6^{3-/4-}$ (1 M KCl) at 100 V/s with simulated curves calculated assuming linear diffusion, with the results shown in Fig. 6. The background current decreased somewhat when the solution was changed from $Fe(CN)_6^{3-/4-}$ to blank electrolyte, so the background subtraction was not completely effective. Nevertheless, the voltammograms for both the fractured and 70 MW/cm^2 surfaces have shapes very close to that simulated for a $k°$ of 0.4 cm/s. The predicted peak current for planar diffusion is

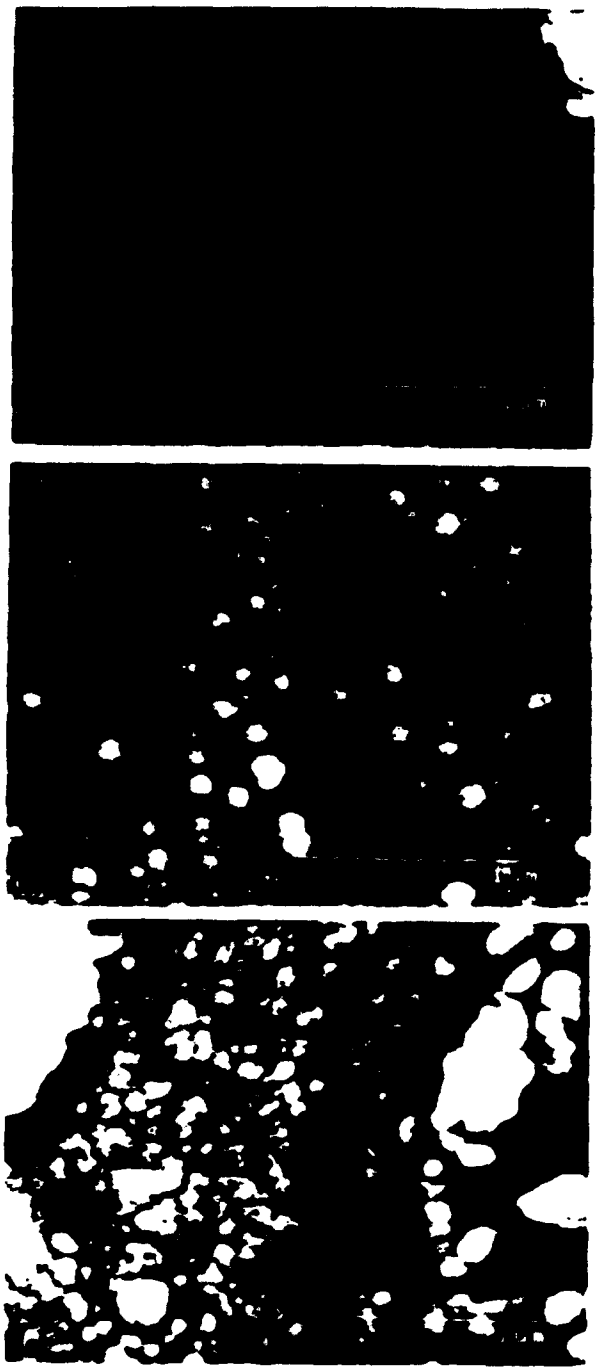

Fig. 4. Scanning electron micrographs of polished and laser irradiated GC-20 surfaces. (a) Freshly polished, (b) polished + three 40 MW/cm^2 Nd:YAG pulses, (c) polished + three 70 MW/cm^2 Nd:YAG pulses.

32 μA for the conditions of Fig. 6a, and the observed value is 35 μA. Thus the apparent microcracks or nodules did not cause an observable deviation from planar electrode behavior. In addition, semi-integration of either voltammogram in

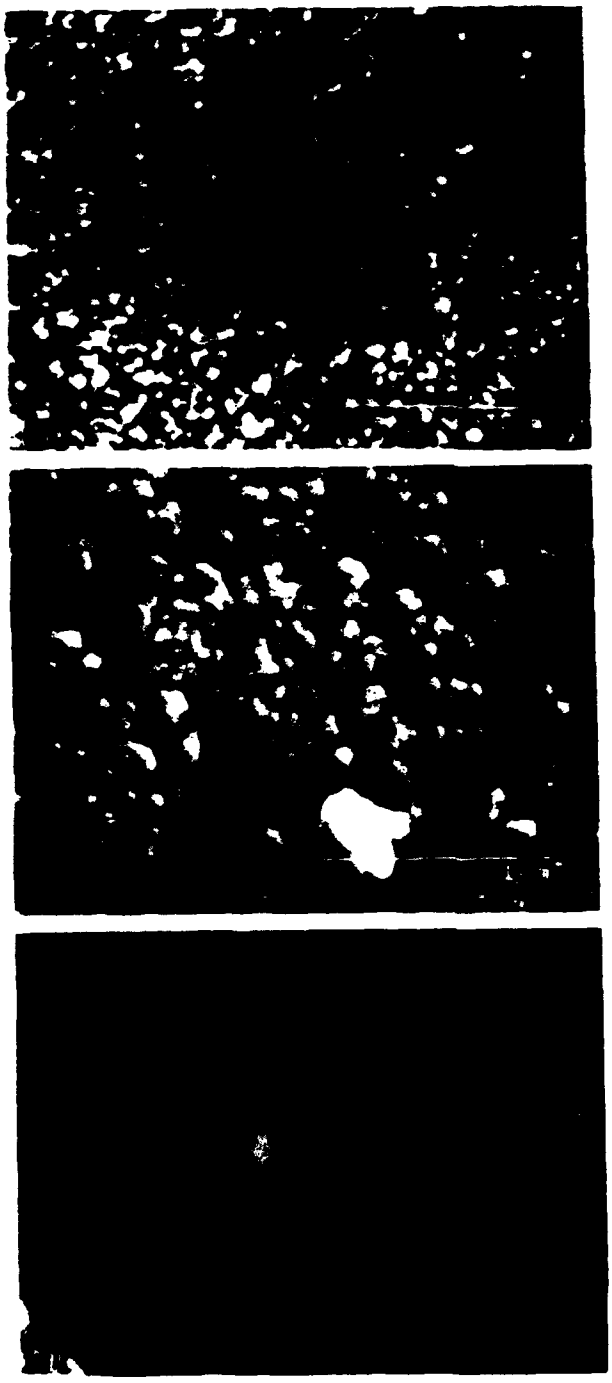

Fig. 5. Scanning electron micrographs of fractured and laser irradiated GC-20 surfaces. (a) Fractured, (b) fractured + three 40 MW/cm^2 Nd:YAG pulses, (c) fractured + three 70 MW/cm^2 Nd:YAG pulses.

Fig. 6 yielded the expected sigmoidal shape [36], with no indication of adsorption or thin layer behavior. Both voltammetry and semi-integration are consistent with an SILD assumption for the conditions employed.

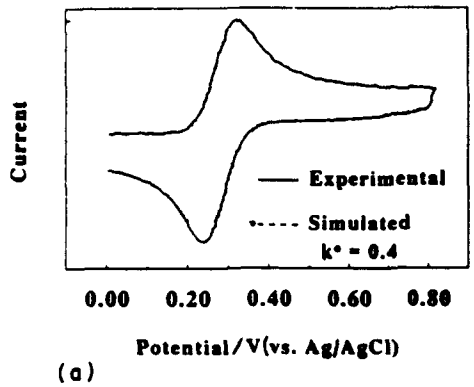

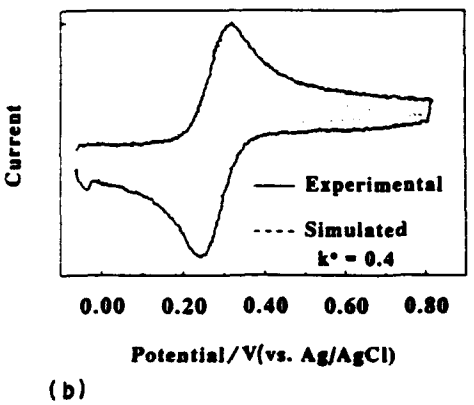

Fig. 6. Comparison of experimental (———) and simulated (- - - - -) voltammograms for $Fe(CN)_6^{3-/4-}$ in 1 M KCl, 100 V/s. Background on experimental curves resulted from incomplete background subtraction caused by a changing background current. (a) Fractured GC-20; (b) fractured + three 70 MW/cm^2 laser pulses. Simulated and experimental current scales were arbitrarily adjusted to be equal before comparison.

DISCUSSION

As noted earlier, a difficulty in relating carbon surface structure to reactivity is the separation of variables dealing with microstructure, roughness, and cleanliness. The common dependent variables such as $k°$, background current, and capacitance depend on more than one of the independent variables dealing with the surface, so one must attempt to monitor these surface variables with some other observables. The Raman intensity ratio of Fig. 1 is a good example, since the L_a and L_c microcrystallite sizes are in the region of 2.5–10.0 nm, and would not be expected to depend on surface cleanliness or roughness. Thus changes in Raman intensity ratio indicate primarily carbon microstructure with little interference from other variables. Figure 1 confirms that the microstructure of the polished surface is already altered from the fractured surface, and is not modified further by the laser. In contrast, the Raman ratio indicates a decrease in L_a with laser treatment of the fractured surface for either repetitive 25 MW/cm^2 pulses or increasing power

density. With extensive or high powered laser treatment, the Raman ratio for the fractured surface approaches that of the polished surface. Thus as far as carbon microstructure is concerned, the nature of the surface following extensive laser activation does not appear to depend on whether the surface was initially fractured or polished.

One would expect Γ_{PQ} to depend on both microscopic surface area and surface cleanliness. However, the fact that Γ_{PQ} does not increase greatly for laser activation in the 0–25 MW/cm^2 power density range implies that cleanliness is not a major factor affecting Γ_{PQ}. Since 25 MW/cm^2 laser pulses increase k° for $Fe(CN)_6^{3-/4-}$ by at least two orders of magnitude for a polished surface, one would presume that the surface is cleaned significantly by the laser [30]. Apparently PQ adsorbs strongly enough that adsorbed impurities, at least those affected by the laser, have only minor effects on Γ_{PQ}. This argument leads to the conclusion that Γ_{PQ} is primarily a measure of surface roughness. Operating under this assumption, the results shown in Fig. 2 lead to two conclusions. First, surface roughness does not change greatly for up to twenty-one 25 MW/cm^2 laser pulses or up to ca. 30 MW/cm^2 power density. This conclusion is consistent with the SEM results, which show minor changes in surface morphology for these conditions. Second, the fractured surface has a higher roughness factor than the polished surface. In relative terms, the fractured surface has a microscopic area about 1.8 times the polished surface. On an absolute scale, the ideal monolayer coverage for PQ on a flat surface, based on Van der Waals radii, is 177 pmol/cm^2 [37]. Therefore the observed roughness factor for the polished surface is about 1.9, while for the fractured surface it is about 3.5. Laser irradiation above 30 MW/cm^2 increases the roughness factor significantly for both surfaces. It is obvious that the roughness factor is strongly dependent on surface preparation and history.

The changes in capacitance are similar to those in Γ_{PQ}, although one would expect C°_{dl} to depend on additional surface variables such as oxides, electrolyte adsorption, etc. As with Γ_{PQ}, the initial C°_{dl} for the fractured surface is about twice that of the polished surface. C°_{dl} increases more rapidly during laser activation of the polished surface compared to the fractured surface, and this increase correlates with electron transfer activation. However, major increases in C°_{dl} were not observed until laser powers of 30 MW/cm^2 and above were delivered.

The voltammetry of Fig. 6 indicates that any surface roughness or heterogeneity is small on the scale of a diffusion layer at 100 V/s. For the time required to scan from the foot of the reduction wave to its peak (1 ms), $\sqrt{Dt}$ is about 0.70 μm. Thus the approximate diffusion layer thickness is much greater than the surface structural features observable by SEM (0.1 μm), even at the fairly high scan rates employed. As a consequence, the microscopically rough surfaces of either polished or fractured GC do not affect planar diffusion significantly.

Based on electrochemical, Raman, and SEM results, a model of the GC surface may be formulated. As shown in Fig. 5a, the fractured GC surface consists of nodules with a mean diameter of 0.16 μm. These nodules are presumably present throughout the material. and were formed when the original GC was fabricated. In

work to be reported elsewhere, we have observed such nodules with scanning tunneling microscopy on fractured GC [38]. On the basis of Fig. 4A, the polishing process flattens the exposed hemisphere of each nodule to yield relatively flat structures. The cracks between nodules presumably contribute to the microscopic area, but are not large or deep enough to contribute to the observed voltammetry. Since the surface area of a hemisphere is twice the area of a circle with the same radius, an idealized case of closely packed hemispheres would have twice the microscopic area of a collection of closely packed circles, ignoring voids. This ideal case is clearly oversimplified, but it does demonstrate that a surface consisting of nodules has a larger microscopic area than a flat surface, by approximately the ratio observed for Γ_{PQ} and C°_{dl}.

Up to 25 MW/cm^2, laser irradiation has relatively minor effects on Γ_{PQ}, C°_{dl} and SEM appearance, but it does increase the Raman intensity ratio. On the basis of the intensity ratio, the a-axis microcrystallite size decreases from ca. 5.0 nm in the fractured case to roughly 2.5 nm upon laser activation [32]. Apparently this scale is too small to affect C°_{dl} or Γ_{PQ} significantly, since these electrochemical variables do not track the Raman ratio. The laser induced microstructural changes are presumably caused by thermally induced mechanical shock during the rapid heating accompanying laser activation. Thus at 25 MW/cm^2 and below, the results are consistent with a laser activation mechanism based on surface cleaning.

At 30 MW/cm^2 and above, obvious changes are apparent in the SEMs, C°_{dl} and Γ_{PQ}. In Fig. 4b (40 MW/cm^2) nodules are apparent, and in Fig. 4c (70 MW/cm^2) they are dominant. For the fractured surface, the nodules are apparent with or without laser treatment, but they do decrease in size upon 70 MW/cm^2 irradiation. Based on a simple model ignoring phase changes, we showed previously that 25 MW/cm^2 pulses will cause a maximum surface temperature excursion of about 3700 K, and that this excursion is linear in power density [39]. Since the melting point of graphite is estimated at 4300 K, laser pulses of 30 MW/cm^2 and higher power density should be able to melt the GC surface. Melting should distort the polished surface and possibly revert the surface back to nodules. For a fractured surface, melting and resolidifying causes no obvious structural changes, but does reduce nodule size. The main conclusion is that the changes in C°_{dl} and Γ_{PQ} starting at 30 MW/cm^2 are likely to be due to localized melting induced by the laser. Since power densities well below this melting threshold are adequate for activation of electron transfer, melting is probably not directly relevant to electron transfer activation. However, melting leads to obvious morphological and electrochemical changes, and is an important phenomenon for a general understanding of laser effects on carbon electrodes.

From an electroanalytical perspective, it is obvious that it is possible to overdo laser activation with high power densities, leading to high capacitive background and high microscopic area. On the other hand, laser treatment at 25 MW/cm^2 and below leads to major increases in k° without obvious surface structural changes [3,10] From a mechanistic standpoint, the results at 25 MW/cm^2 and below demonstrate that laser activation of k° does not require roughness or microstruc-

tural changes, and must involve a phenomenon not probed by Γ_{PQ}, Raman, or SEM, probably involving removal of surface impurities.

ACKNOWLEDGEMENTS

This work was funded by The Air Force Office of Scientific Research. The authors thank Christie Allred for development of the software to control the Lecroy oscilloscope and for useful discussions concerning this work. We also acknowledge preliminary experiments by Ronald Rice which indicated nodules on fractured GC, plus the valuable assistance of Clare McDonald in obtaining SEM images.

REFERENCES

1 K. Kinoshita, Carbon: Electrochemical and Physicochemical Properties, Wiley, New York, 1988.
2 R.L. McCreery, in A.J. Bard (Ed.), Electroanalytical Chemistry, Vol. 17, Marcel Dekker, New York, 1991, pp. 221–374.
3 R.J. Rice, N.M. Pontikos and R.L. McCreery, J. Am. Chem. Soc., 112 (1990) 4618.
4 R.N. Adams, Electrochemistry at Solid Electrodes, Marcel Dekker, New York, 1969.
5 I.F. Hu, D.H. Karweik and T. Kuwana, J. Electroanal. Chem., 188 (1985) 59.
6 G.N. Kamau, W.S. Willis and J.F. Rusling, Anal. Chem. 57 (1985) 545.
7 D.T. Fagan, I.F. Hu and T. Kuwana, Anal. Chem., 57 (1985) 2759.
8 R.M. Wightman, M.R. Deakin, P.M. Kocach, W.G. Kuhr and K. Stutts, J. Electrochem. Soc., 131 (1984) 1578.
9 L.J. Kepley and A.J. Bard, Anal. Chem., 60 (1988) 1459.
10 M. Poon and R.L. McCreery, Anal. Chem., 58 (1986) 2745.
11 M. Poon and R.L. McCreery, Anal. Chem., 59 (1987) 1615.
12 R.C. Engstrom, Anal. Chem., 54 (1982) 2310.
13 R.C. Engstrom and V.A. Strasser, Anal. Chem., 56 (1984) 136.
14 G.E. Cabaniss, A.A. Diamantis, W.R. Murry Jr., R.W. Linton and R.J. Meyer, J. Am. Chem. Soc., 107 (1985) 1845.
15 L. Falat and H.Y. Cheng, J. Electroanal. Chem., 157 (1983) 393.
16 R.M. Wightman, E.C. Park, S. Borman and M.A. Dayton, Anal. Chem., 50 (1978) 1410.
17 C.W. Miller, D. Karweik and T. Kuwana, Anal. Chem., 53 (1979) 2319.
18 J. Evans and T. Kuwana, Anal. Chem., 51 (1979) 358.
19 M. Poon and R.L. McCreery, Anal. Chem., 60 (1988) 1725.
20 K.J. Stutts, P.M. Kovach, W.G. Kuhr and R.M. Wightman, Anal. Chem., 55 (1983) 1632.
21 I.F. Hu and T. Kuwana, Anal. Chem., 58 (1986) 3235.
22 P.M. Kovach, M.R. Deakin and R.M. Wightman, J. Phys. Chem., 90 (1986) 4612.
23 J.F. Evans and T. Kuwana, Anal. Chem., 49 (1977) 1632.
24 I. Marcos and E. Yeager, Electrochim. Acta., 15 (1970) 953.
25 R. Bowling, R.T. Packard and R.L. McCreery, Langmuir, 5 (1989) 683.
26 R.J. Bowling, R.T. Packard and R.L. McCreery, J. Am. Chem. Soc., 11 (1989) 1217.
27 E. Gileadi and N. Tshernikovski, Electrochim. Acta., 16 (1971) 579.
28 E. Gileadi, N. Tshernikovski and M. Babai, J. Electrochem. Soc., 119 (1972) 1018.
29 A.P. Brown and F.C. Anson, Anal. Chem., 49 (1977) 1589.
30 R.J. Rice, C.D. Allred and R.L. McCreery, J. Electroanal. Chem., 263 (1989) 163.
31 M. Nakamizo and K. Tamai, Carbon, 22 (1984) 197.
32 F. Tuinstra and J.L. Koenig, J. Phys. Chem., 53 (1970) 1126.
33 Y.W. Alsmeyer and R.L. McCreery, Anal. Chem., 63 (1991) 1289.

J. Electroanal. Chem., 326 (1992) 1–12
Elsevier Sequoia S.A., Lausanne
JEC 01924

Electron transfer kinetics of $Fe(CN)_6^{3-/4-}$ on laser-activated and CN^--modified Pt electrodes

Wenhua Huang and Richard McCreery *

Department of Chemistry, The Ohio State University, 120 West 18th Avenue, Columbus, OH 43210 (USA)

(Received 26 July 1991; in revised form 25 October 1991)

Abstract

The heterogeneous electron transfer rate constant $k°$ for $Fe(CN)_6^{3-/4-}$ was measured by fast voltammetry at Pt microdisk electrodes with radii from 10 to 50 μm. The observed $k°$ was dependent on electrode pretreatment, but in many cases exceeded the previously reported maximum value of 0.24 cm/s for 1 M KCl electrolyte. When the electrode was polished with alumina in a slurry made with 10 mM KCN, and the 1 M KCl also contained 3 mM KCN, $k°$ was invariant with scan rate and electrode radius for the range of 200–1000 V/s and 10–50 μm, with a value of 0.55 ± 0.07 cm/s. If KCN was absent from the electrolyte, $k°$ decreased with time to below 0.10 cm/s. Laser activation of the Pt electrodes in situ produced reproducibly high $k°$ values of approx. 0.5 cm/s which varied slightly with laser power density up to 75 MW/cm^2. Above this level $k°$ increased up to approx. 1.2 cm/s, but this increase is attributed to a laser-induced increase in microscopic surface area. The observations support a mechanism for electrode passivation based on $Fe(CN)_6^{3-/4-}$ decomposition to a Prussian blue like film. This process can be prevented by initial saturation of the Pt surface with CN^-, resulting in a high stable $k°$.

INTRODUCTION

The $Fe(CN)_6^{3-/4-}$ redox couple has been used extensively as a benchmark system for studying electrode kinetics and diffusion, and for characterizing electroanalytical techniques [1–11]. Considered superficially, $Fe(CN)_6^{3-/4-}$ is a quasi-reversible well-behaved redox system with an $E_{1/2}$ suitable for Pt, Au and carbon electrodes in aqueous electrolytes such as 1 M KCl. For this reason, it has served as a test system for numerous examinations of solid electrode preparation and modification, most notably Pt [1–4] and glassy carbon (GC) [12–14]. Unfortunately,

* To whom correspondence should be addressed.

$Fe(CN)_6^{3-/4-}$ is significantly more complex than a superficial examination indicates. The heterogeneous electron transfer rate constant $k°$ cm/s depends strongly on cation and anion identity and concentration, with the cation effect being more pronounced [11]. Peter et al. [2] attributed the increase in $k°$ with potassium ion concentration to the involvement of K^+ in the transition state for electron transfer. A second complication is the chemisorption and decomposition of $Fe(CN)_6^{3-/4-}$ on Pt surfaces, indicated by Fourier transform IR (FTIR), radiochemical, UV–Vis and electrochemical results [1,3,5]. Galus and coworkers [1,4] noted that $k°$ can be increased by adding free CN^- to the electrolyte, preventing $Fe(CN)_6^{3-/4-}$ chemisorption. Goldstein and Van De Mark [11] noted that large $k°$ values were observed when halides were chemisorbed onto the surface, and associated this effect with the observed anion dependence of $k°$. An additional issue does not involve the $Fe(CN)_6^{3-/4-}$ system directly, but has an important effect on observed $k°$ values. The highest literature values for $k°$ on Pt in 1 M KCl are in the range of 0.1–0.24 cm/s, but in many cases these values are at or near the upper limit of the instrumental technique employed. Most previous detailed kinetic examinations were performed with conventionally sized Pt, Au or carbon electrodes having areas of about 0.05 cm^2 or larger, and are subject to ohmic potential errors under the transient conditions required to measure large $k°$ values. With the advent of ultramicroelectrodes, these ohmic potential errors can be greatly reduced, such that fast scan voltammetry can yield more reliable $k°$ values above 0.2 cm/s [16–18]. In some cases reported in the literature, the observed $k°$ values were acknowledged to be lower limits owing to instrumental limitations [14,15]. When the actual $k°$ is 0.1 cm/s or greater, comparisons of various conditions or electrodes are difficult with voltammetry or rotating-disk techniques on conventional electrodes with areas greater than about 0.05 cm^2.

Several $k°$ values for $Fe(CN)_6^{3-/4-}$ from the literature are listed in Table 1 for various electrode materials, pretreatments and electrolytes. The wide variation in $k°$ on Pt for different pretreatments, with the highest $k°$ observed on a "macroelectrode" in 1 M KCl being 0.22–0.24 cm/s, should be noted. In our previous work on GC electrodes, we observed $k°$ values of > 0.5 cm/s following laser activation of electrodes with areas of approx. 2×10^{-3} cm^2 [13]. In order to compare $k°$ on GC with that on Pt, it is necessary to reconsider the Pt rates using fast scan rates and microelectrodes under conditions where the complications of chemisorption and electrolyte effects are removed or controlled. In addition, we sought to evaluate laser activation on Pt to compare with the dramatic effects on GC. These fairly specific objectives not only serve to clarify the suitability of $Fe(CN)_6^{3-/4-}$ as a benchmark redox system, but also bear on the broader question of the surface chemistry accompanying $Fe(CN)_6^{3-/4-}$ electron transfer on Pt and GC.

EXPERIMENTAL

A LeCroy 8400-A digital oscilloscope was used to record voltammograms before transfer to a 286 based personal computer with a locally written program. A

TABLE 1

$k°$ for $Fe(CN)_6^{3-/4-}$ under various conditions

Electrode	Pretreatment	Electrolyte	$k°$/cm s^{-1}	Reference
Pt	HNO_3	1 M KCl	0.02 ± 0.007	11
Pt	Flame	1 M KCl	0.22 ± 0.01	11
Pt	HNO_3, flame	1 M KCl	0.23 ± 0.23	11
Pt	$HClO_4$, redn in KCl	1 M KCl	0.24	10
Pt	$HClO_4$ only	1 M KCl	0.028	10
Pt	Potential cycling	1 M KCl	0.10	2
Pt/CN	Potential cycling	1 M KCl/0.01 M NaCN	> 0.1	1
Pt/I	Potential cycling	1 M KCl	> 0.1	1
Au	Potential cycling	1 M KCl	0.10	15
GC	Laser activation	1 M KCl	> 0.5	13
GC	Fractured	1 M KCl	0.5	13
Pt, $r_0 = 10\ \mu m$	Case 1 [a]	1 M KCl	0.24 ± 0.04	This work
Pt, $r_0 = 10\ \mu m$	Case 2 [b]	1 M KCl/5 mM CN^-	0.42 ± 0.03	This work
Pt, $r_0 = 10\ \mu m$	Case 3 [c]	1 M KCl/5 mM CN^-	0.56 ± 0.07	This work
Pt, $r_0 = 10\ \mu m$	50 MW/cm^2 laser activation	1 M KCl/5 mM CN^-	0.46	This work

[a] Polished in a Nanopure water + Al_2O_3 slurry, sonicated in Nanopure water. Electrolyte contained no KCN.

[b] Polished in a Nanopure water + Al_2O_3 slurry, sonicated in Nanopure water. Electrolyte contained 5 mM KCN.

[c] Polished in 10 mM KCN + Al_2O_3 slurry, sonicated in 10 mM KCN. Electrolyte contained 5 mM KCN.

Tektronix FG 501A 2 MHz function generator was triggered by the computer to output a triangular potential sweep to a three-electrode potentiostat. Both the potential sweep and the cell current were monitored simultaneously by the digital oscilloscope, and then converted to I versus E curves by the computer. A low-pass filter (Krohn-hite model 3200) was used to filter out high frequency noise, with the RC set according to the $RCn\nu < 4$ mV criterion [16]. Electrodes with radii of 10, 25 and 50 μm were made by sealing the same nominal radius Pt wire (Goodfellow Metals) in type 0120 potash soda lead glass (Corning) followed by annealing. A 12.5 μm radius electrode was obtained commercially from Electrosynthesis Corporation. Either polishing and sonicating or in-situ laser activation was employed to prepare the electrode surface. In the first approach, the electrode was immersed in 18 M H_2SO_4 for 30 min and then rinsed with Nanopure water (Sybron Barnstead, 16 MΩ/cm). After that, the electrode was polished conventionally with 180 grit SiC paper (Buehler) followed by 1.0, 0.3 and 0.05 μm alpha alumina (Buehler) in a slurry with either Nanopure water or 0.01 M CN^- solution (as noted below) on a Buehler polishing cloth for 5 min in each polishing medium. Immediately after polishing, the electrode was sonicated in either Nanopure water or 0.01 M CN^- solution for 5 min in order to remove the alumina particles. For laser activation, a

Nd:YAG laser (1064 nm) was used as described previously [8,9,13]. A He + Ne pilot beam coincident with the Nd:YAG beam was used to center the laser on the electrode. The Nd:YAG laser beam has a diameter of 6 mm and output power densities in the range of 5–100 MW/cm^2 at the electrode surface. The electrochemical cell used has been described previously [9]. It was constructed from Teflon and was able to accept different size electrodes. The laser beam passed through a quartz window and the solution of interest before impinging on the electrode. Cyclic voltammograms (CVs) were recorded four times during each trial (3 s between each scan) and their average was stored for subsequent data processing.

Scanning electron microscopy (SEM) was performed with a Hitachi S-150 scanning electron microscope at an acceleration voltage of 25 kV. Three electrodes were made and polished at the same time preceding SEM examination. After sonicating, one electrode was laser activated with three laser pulses at 75 MW/cm^2. Another electrode was activated with 60 laser pulses at 50 MW/cm^2 followed by three pulses at 75 MW/cm^2. All three electrodes were gold-coated before the SEM examination.

KCl, $K_4Fe(CN)_6$, KI, KBr and KCN (all AR grade) were obtained from Mallinckrodt and used without further purification. All solutions were made fresh daily with Nanopure water and were degassed with argon for 10 min. Because of the possibility of toxic HCN formation, neither KCN nor $K_4Fe(CN)_6$ solutions were exposed to acidic solutions or reagents.

RESULTS

CVs obtained with a Pt microdisk electrode ($r_0 = 10$ μm) at 600 V/s in the presence and absence of 5 mM CN^- are compared in Fig. 1. Figure 1(a) shows the background and $Fe(CN)_6^{3-/4-}$ CVs with CN^- present, while Fig. 1(b) is for the case with CN^- absent. Note that the background current is higher without CN^-, with an apparent wave at about +0.6 V which is attributable to electrode surface oxidation or $Fe(CN)_6^{3-/4-}$ degradation. Figures 1(c) and 1(d) show background subtracted CVs with CN^- present (c) and absent (d). The broken curves show simulated CVs for $\alpha = 0.5$, $T = 21$°C, and $k° = 0.60$ cm/s (c) and $k° = 0.15$ cm/s (d). Note that the agreement of theory and experiment is quite good with CN^- present, and that the CV exhibits excess current in the absence of CN^- that was not subtracted as background current. It should also be noted, that the value of 0.60 cm/s for $k°$ exceeds the previously reported maximum of 0.24 cm/s for Pt in 1 M KCl. As will be discussed later, it is significant that the value of 0.24 cm/s was obtained under conditions conducive to Cl^- chemisorption.

$k°$ values for three different pretreatments and electrolytes are listed in Table 2 for scan rates ranging from 10 to 950 V/s. In the range from 200–1000 V/s, $k°$ shows no obvious trends but does exhibit random error. The low values of $k°$ observed below 200 V/s are probably due to nonplanar diffusion on the microdisk electrode. At 200 V/s, the p function [19], defined as $p = (nFr_0^2\nu/RTD)^{1/2}$, is 33.

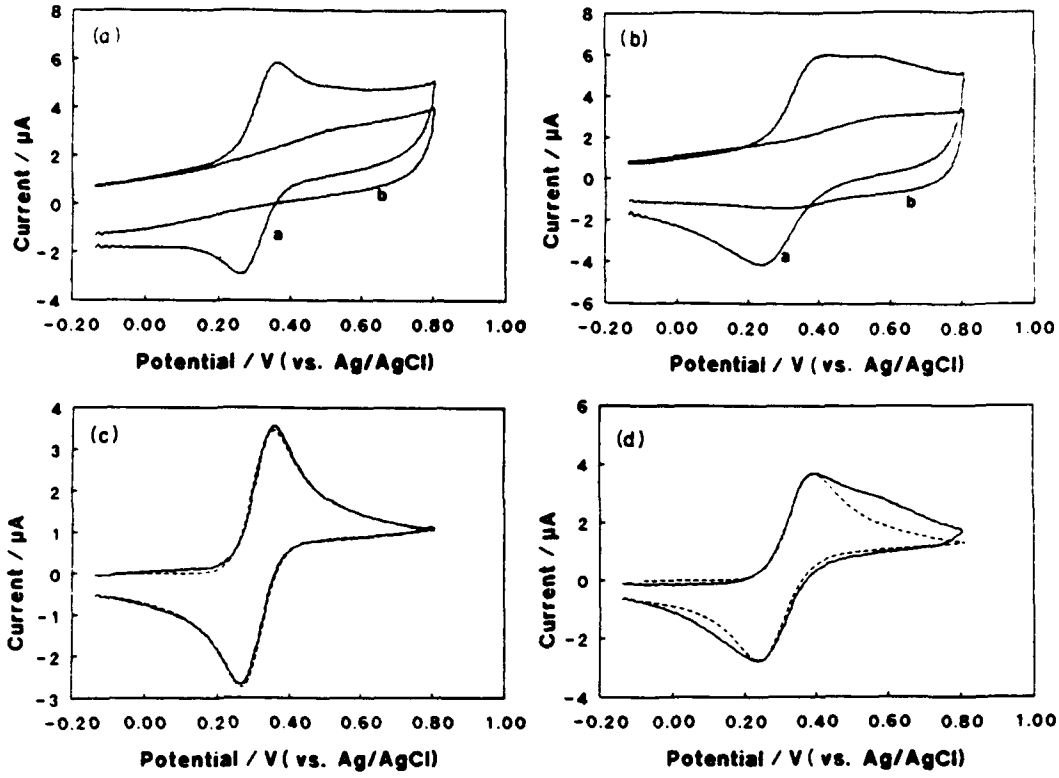

Fig. 1. CVs of $Fe(CN)_6^{3-/4-}$ in 1 M KCl at a Pt microdisk ($r_0 = 10$ μm) at 600 V/s: (a) signal (curve a) and background (curve b) in the presence of 5 mM KCN; (b) without KCN. The solid curves in (c) and (d) are the difference between the signal and background of (a) and (b) respectively. The broken curves are simulated CVs for $\alpha = 0.5$, $T = 21°C$, $k° = 0.60$ cm/s (in (c)) and $k° = 0.15$ cm/s (in (d)).

As ν or p decreases, nonplanar diffusion will distort the CV significantly, and the Nicholson and Shain [20] approach to determining $k°$ from ΔE_p will be in error. For this reason, all kinetic data reported here were obtained for conditions where p exceeded 33. It should also be noted that $k°$ for case 3 in Table 2 varies only slightly with r_0, ranging from 10 to 50 μm. Since ohmic potential errors scale linearly with r_0, the constant $k°$ observed implies little ohmic error.

The time course of $k°$ for various conditions is shown in Fig. 2. In the absence of added CN^-, $k°$ starts at a level comparable with the highest literature values (0.21 cm/s) and then decays over a 70 min period to approx. 0.01 cm/s (curve D). An electrode which was polished and sonicated in CN^- solution starts higher (0.43 cm/s), but also decays to less than 0.1 after 70 min (curve C). Polishing and sonicating in CN^- plus voltammetry in 3 mM CN^- yields a large $k°$ which decays only slightly with an average for 0–70 min of 0.53 ± 0.06 cm/s (curve A). Finally, an electrode polished and sonicated in Nanopure water preceding voltammetry in 3 mM CN^- and 1 M KCl shows a slight increase in $k°$ with time, and an average of 0.40 ± 0.03 cm/s for the 70 min period (curve B).

It is clear from Table 2 and Fig. 2 that the largest and most stable $k°$ values for $Fe(CN)_6^{3-/4-}$ are obtained when CN^- is present during polishing, sonication and

TABLE 2

Observed $k°$ for $Fe(CN)_6^{3-/4-}$ under various conditions

ν/V s^{-1}	$k°$/cm s^{-1}		
	$r_0 = 10\ \mu$m		
	Case 1 [a]	Case 2 [a]	Case 3 [a]
10	0.070		
40	0.128	0.232	0.240
100	0.144	0.142	0.248
150	0.160	0.227	0.145
250	0.186	0.413	0.477
330	0.235	0.394	0.570
420	0.170	0.413	0.582
530	0.280	0.482	0.556
630	0.258	0.388	0.635
700	0.243	0.394	0.605
840	0.267	0.457	0.622
950	0.258	0.432	0.438
Mean for 250–950 V/s	0.24 ± 0.04 [b]	0.42 ± 0.03 [b]	0.56 ± 0.07 [b]
$r_0 = 12.5\ \mu$m, mean for 250–950 V/s			0.56 ± 0.10 [b]
$r_0 = 25\ \mu$m, mean for 250–950 V/s			0.53 ± 0.08 [b]
$r_0 = 50\ \mu$m, mean for 250–950 V/s			0.54 ± 0.10 [b]

[a] As defined in Table 1.
[b] Standard deviation.

voltammetry. Table 3 shows the dependence of $k°$ determined at 600 V/s on CN^- concentration in the electrolyte used for voltammetry. Although 3 mM yields the highest $k°$, the random error is significant compared with the changes observed for varying $[CN^-]$. It is sufficient to say that a range of $[CN^-]$ from 1 to 10 mM yields comparable $k°$ values. The same polishing and sonicating procedure was also carried out with Br^- and I^- instead of CN^-, but high and stable $k°$ values were not obtained. $k°$ decreased with time for the Br^-- and I^--containing electrolytes.

Based on previous experience with GC electrodes, laser activation may provide an attractive alternative to polishing for increasing $k°$ on Pt electrodes. We have shown previously that intense short (approx. 25 MW/cm^2, 9 ns) Nd:YAG laser pulses delivered to GC in situ results in large increases in $k°$ for a variety of redox systems, including $Fe(CN)_6^{3-/4-}$ [8,9,13]. The technique avoids sometimes tedious polishing and prevents exposure of the electrode to air. Laser activation was attempted for the $Fe(CN)_6^{3-/4-}$ system on Pt in 5 mM CN^- + 1 M KCl. The electrodes had been polished and exposed to laboratory air for several days, but were not otherwise pretreated before placing in the laser activation cell. Laser

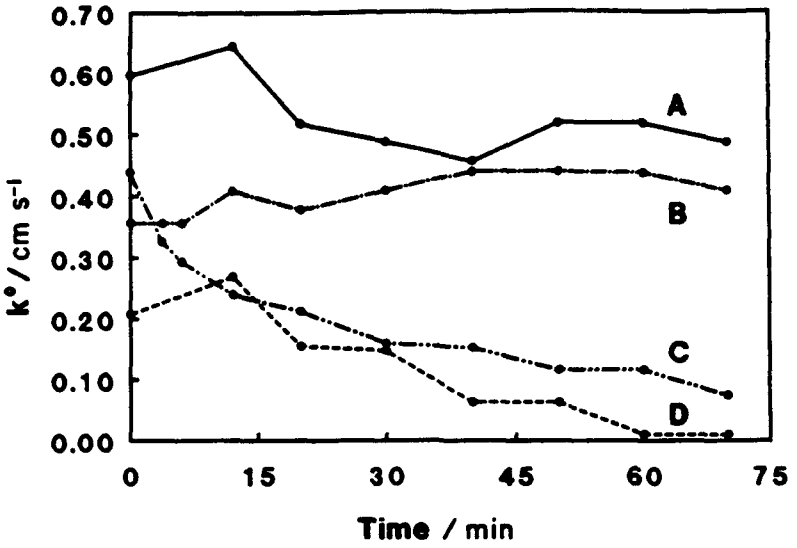

Fig. 2. $k°$ (determined at 600 V/s) versus time after exposure of a Pt microdisk ($r_0 = 10\ \mu m$) to a 10 mM $Fe(CN)_6^{4-}$ + 1 M KCl solution under various conditions: curve A; polished and sonicated in 10 mM KCN, voltammetry in 5 mM KCN; curve B, polished and sonicated in water, voltammetry in 5 mM KCN; curve C, polished and sonicated in 10 mM KCN, electrolyte did not contain KCN; curve D, polishing, sonication and voltammetry in the absence of CN^-.

TABLE 3

Effect of CN^- concentration on $k°$ determined at 600 V/s

Electrode pretreatment	$[CN^-]$ in electrolyte/mM	$k°$/cm s^{-1}
Polished + sonicated in Nanopure water	0	0.24 ± 0.04
Polished + sonicated in 10 mM CN^- solution	0	0.40 ± 0.03
Polished + sonicated in 10 mM CN^- solution	1	0.46 ± 0.05
Polished + sonicated in 10 mM CN^- solution	3	0.56 ± 0.07
Polished + sonicated in 10 mM CN^- solution	5	0.53 ± 0.08
Polished + sonicated in 10 mM CN^- solution	7	0.46 ± 0.09
Polished + sonicated in 10 mM CN^- solution	10	0.38 ± 0.08
50 MW/cm^2 laser activation	5	0.57
60 MW/cm^2 laser activation	5	1.04
75 MW/cm^2 laser activation	5	1.19
50 MW/cm^2 laser activation	5 mM Br^-	0.25 [a]
50 MW/cm^2 laser activation	5 mM I^-	0.21 [a]

[a] Highest values observed after laser activation, decreased with time.

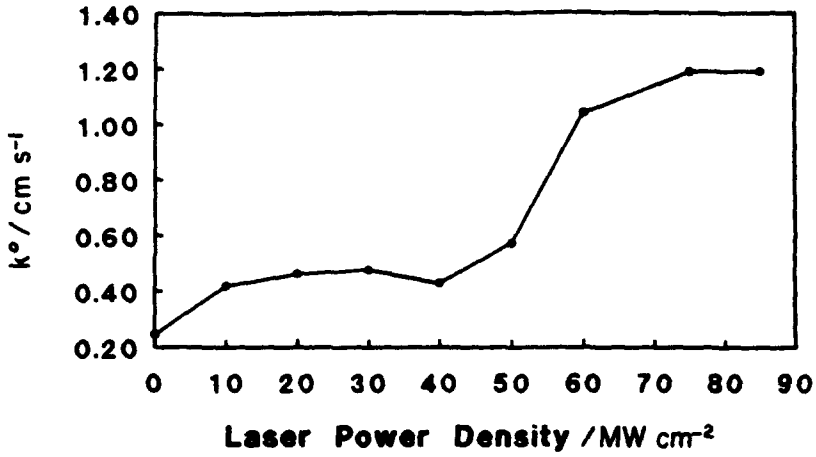

g. 3. $k°$ determined in 5 mM KCN + 1 M KCl following in-situ laser activation at increasing power ensities. Three laser pulses were delivered at each power, and the activation was cumulative starting at low power.

activation at various power densities yielded the results shown in Fig. 3. Laser activation was cumulative in this case, with three laser pulses delivered for each power density as power was increased. For power densities from 10 to 50 MW/cm^2, the observed $k°$ was fairly constant with an average of 0.49 ± 0.05 cm/s. Above 50 MW/cm^2, $k°$ increased significantly to a maximum of 1.19 cm/s at 75 MW/cm^2.

The time course of $k°$ following laser activation was also examined for 25, 50 and 75 MW/cm^2 pulses, as shown in Fig. 4. In all cases, the initial electrode had been partially passivated by long exposure (> 1 day) to laboratory air preceding

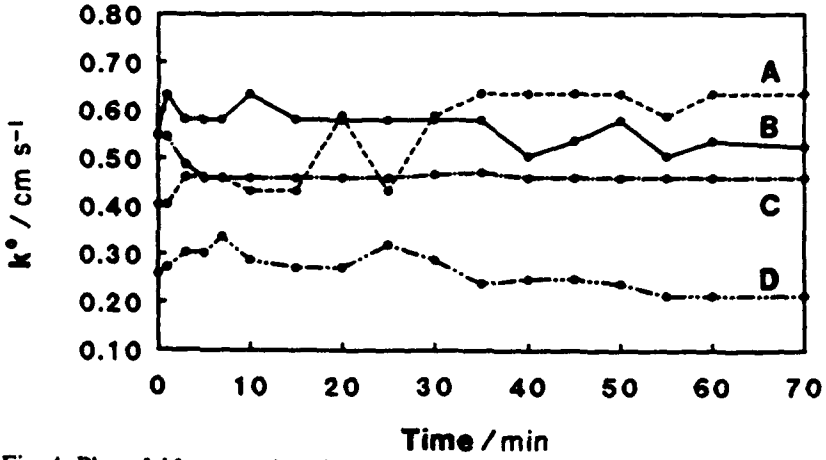

Fig. 4. Plot of $k°$ versus time for a laser-activated electrode following three laser pulses at laser powers of 50 MW/cm^2 (curve A), 75 MW/cm^2 (curve B) and 25 MW/cm^2 (curve C). The analyte solution is 10 mM $Fe(CN)_6^{4-}$ with 5 mM CN^- + 1 M KCl. Curve D is same as curve A without CN^- present.

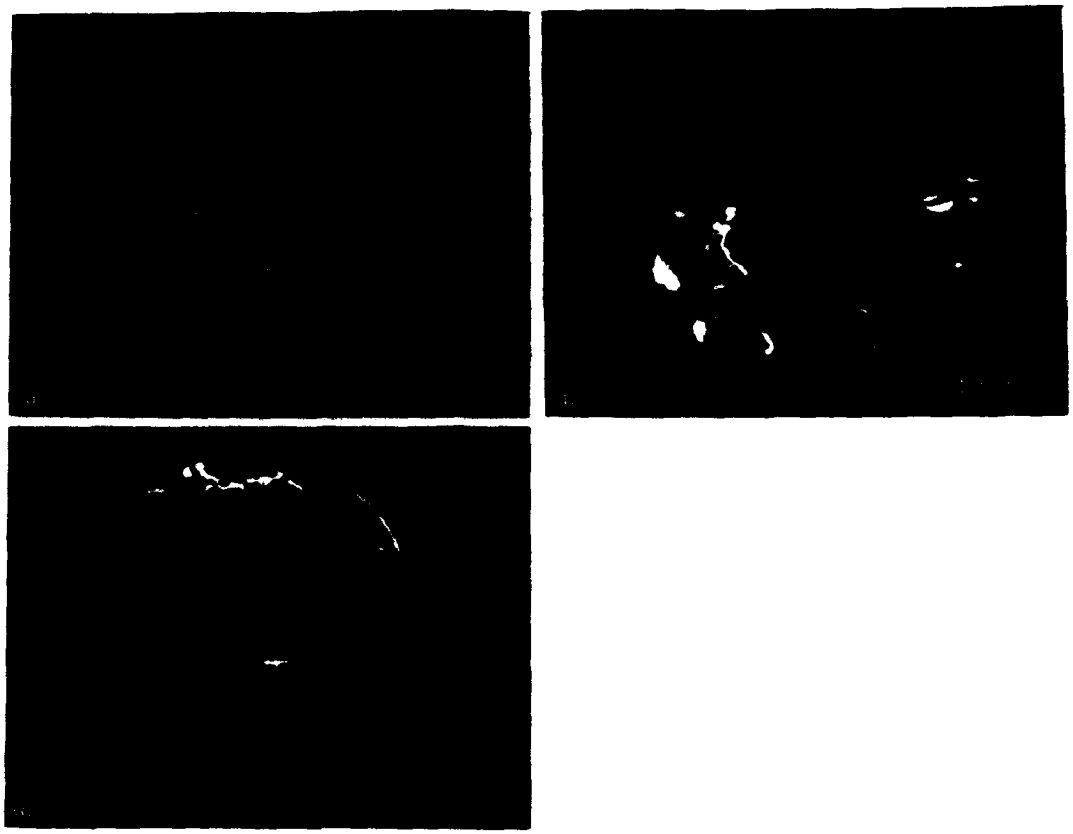

Fig. 5. Scanning electron micrographs of polished Pt microdisk electrodes following various degrees of laser activation in 1 M KCl: (a) initial; (b) after three 75 MW/cm^2 pulses; (c) after sixty 50 MW/cm^2 pulses and three 75 MW/cm^2 pulses.

laser activation, and exhibited an initial $k°$ of less than 0.2 cm/s. In the presence of 5 mM CN^-, $k°$ was quite stable following laser activation, at least for 70 min. The 75 MW/cm^2 pulse did not result in a $k° > 1.0$ cm/s in this case because the activation was not cumulative as in Fig. 3 (see below). In the absence of CN^- (curve D), laser activation did not result in as high a $k°$ value, and $k°$ values decreased with time for at least 70 min.

Scanning electron micrographs of the Pt microdisk before and after laser activation are shown in Fig. 5. After polishing, the surface exhibits polishing scratches but is otherwise fairly smooth. Three 75 MW/cm^2 laser pulses induce some surface roughening but polishing scratches are still visible. Extensive activation (sixty pulses at 50 MW/cm^2 plus three pulses at 75 MW/cm^2) caused obvious surface roughness plus some pits and possibly fissures. Higher magnification scanning electron micrographs of the surface of Fig. 5(c) exhibit small (approx. 0.1 μm) nodules, apparently solidified from molten Pt. Such nodules were absent on the polished surface. Electrodes treated with the same procedure yielding Fig. 5(c) exhibited $k°$ values of 1.21 ± 0.15 cm/s, comparable with the highest rates in Fig. 3.

DISCUSSION

The first conclusion from the current results is quite practical. The $k°$ values observed here with microdisk electrodes are significantly higher than those reported in the literature. Since previous studies use relatively "large" electrodes, the observed $k°$ values are subject to a downward bias due to ohmic potential errors. The constancy of $k°$ with scan rate in the range 200–1000 V/s and with electrode radius, plus the ability to measure rates of 1.2 cm/s for certain conditions support the conclusion that the $k°$ values of approx. 0.5 cm/s are reliable, and not just another lower limit. The results indicate that the observed $k°$ values are not instrumentally limited. Resolution of the pragmatic issues of instrumental limits on $k°$ and electrode cleanliness is a prerequisite to more fundamental questions about the factors which determine electron transfer rates. Before electron transfer mechanisms can be elucidated, one must have confidence in measurement techniques and surface preparation. The high stable $k°$ values observed here reduce concern about surface cleanliness and preparation, and permit more reliable comparison of $Fe(CN)_6^{3-/4-}$ kinetics on Pt electrodes with those on other surfaces.

Given the previous reports by Galus and coworkers [1,4], it is not surprising that CN^- stabilizes $k°$ and prevents degradation of electrode performance. Galus proposed that CN^- forms a protective layer by occupying chemisorption sites, similar to I^-, and both CN^-- and I^--treated surfaces yielded $k°$ values for $Fe(CN)_6^{3-/4-}$ above the instrumental limit of 0.1 cm/s. If this model is correct, a small solution concentration of strongly adsorbing I^- or CN^- will be sufficient to saturate the surface and prevent $Fe(CN)_6^{3-/4-}$ chemisorption. This observation should be considered in the light of spectroscopic data indicating formation of a Prussian blue like film in the absence of CN^-. In addition, Bocarsly and coworkers [21,22] have demonstrated chemisorption of $Fe(CN)_6^{-3/-4}$ onto nickel surfaces, and Wieckowski and Szklarczyk [3] noted that CN^- can be bonded at both ends to yield the chemisorbed species

$$Pt—N \equiv C—Fe(CN)_5^{3-}$$

All these reports are consistent with the conclusion that excess CN^- in solution can saturate the Pt surface and prevent $Fe(CN)_6^{3-/4-}$ chemisorption. Since 3 mM (or less) of free CN^- is apparently enough to prevent chemisorption of 10 mM $Fe(CN)_6^{3-/4-}$, the equilibrium constant for CN^- adsorption must be significantly higher than that of $Fe(CN)_6^{3-/4-}$. A slight extension of this model involves events occurring after $Fe(CN)_6^{3-/4-}$ chemisorption. It is possible that the $Fe(CN)_5(H_2O)^{3-}$ desorbs, leaving CN^- behind, and then reacts with solution $Fe(CN)_6^{3-/4-}$ to produce Prussian blue or a related material [6,23]. This reaction leads to a passivating film which eventually impedes electron transfer and decreases $k°$. Although the current data do not test directly for the presence of chemisorbed $Fe(CN)_6^{3-/4-}$, it is clear that chemisorbed CN^- prevents $Fe(CN)_6^{3-/4-}$ decomposition. By polishing and sonicating the Pt electrode in CN^- solution, the presaturation of the surface may be particularly effective, leading to high stable $k°$ values.

Even a partially passivated electrode exhibiting a low $k°$ can be reactivated by sonicating in 10 mM KCN.

Below 50 MW/cm^2, laser activation of Pt in the $Fe(CN)_6^{3-/4-}$ + CN^- + KCl medium appears straightforward, resulting in $k°$ values of comparable magnitude and stability to the polished values. Based on a simple numerical simulation, the peak temperature excursion for the Pt surface activated by a 50 MW/cm^2, 9 ns, 1064 nm laser pulse has an upper limit of approx. 1260°C [24]. Thus the rapid surface heating of the electrode would be expected to desorb impurities and present an initially clean surface to the solution. With CN^- present, this surface should rapidly saturate with chemisorbed CN^- and a high $k°$ should result. The stability of $k°$ following laser activation is presumably attributable to the same phenomenon that occurs when CN^- is present during polishing. After numerous pulses in the 20–50 MW/cm^2 range plus several above 50 MW/cm^2, the observed $k°$ increases above 1.0 cm/s. Scanning electron micrographs of a similarly treated electrode show significant roughness and surface damage, perhaps from melting or surface ablation. It is quite likely that the increase in $k°$ is a microscopic area effect, implying that the heavily activated surface has a microscopic area roughly twice that of the initial surface. Without an independent measure of microscopic area, it would be risky to conclude that the heavily laser treated surface is more inherently active than the other cases. This uncertainty about area applies to any solid electrode, so that comparisons of rate constants should be made for surfaces of comparable roughness when possible. For this reason, our polishing procedure was conventional with the exception of the presence of CN^-.

Table 1 combines several literature values for $Fe(CN)_6^{3-/4-}$ in 1 M KCl with current results. Recognizing that instrumental limitations and surface impurities usually result in *low* $k°$ values, the entries in Table 1 represent lower limits of the true values. Several points about Table 1 deserve special note. First, the highest $k°$ values observed (ignoring the roughened surface) fall in a fairly narrow range from 0.1 to 0.6 cm/s, even for quite different electrode surfaces. Second, the Pt/CN^- values reported here are comparable with the highest results obtained on fractured or laser-activated GC [13]. On the basis of the Marcus theory correlating $k°$ with homogeneous self-exchange rates, $k°$ for $Fe(CN)_6^{3-/4-}$ should be in the region of 1–10 cm/s, within an order of magnitude of 0.5 cm/s [4,14]. Third, an inner-sphere electron transfer mechanism based on a CN^- or K^+ bridge between the surface and the $Fe(CN)_6^{3-/4-}$ redox center appears unlikely given the data in Table 1. Occupation of Pt surface sites by CN^- has a minor effect (a factor of 2) on the initial $k°$ before any degradation. If a K^+ or CN^- bridge to the Pt surface (or Pt/Cl surface) were important to electron transfer, one would expect that intentional CN^- chemisorption should markedly change the observed $k°$. To carry this logic further with reference to Table 1, $k°$ is not greatly different for Pt/Cl, Pt/CN, Pt/I, Au, GC (laser) and GC (fractured). If a K^+ or CN^- bridge were involved in electron transfer to $Fe(CN)_6^{3-/4-}$, the effect would be very insensitive to surface identity. A more likely conclusion is that the electron transfer does not depend on a bridging group, and that the effect of chemisorbed anions (other than

to prevent film formation) is quite small, perhaps involving double-layer modification or alteration of the distance of closest approach of the redox center. Whatever the effects of anion adsorption on a bridging process, they are very much smaller than the effects of surface cleanliness and instrumental factors. If a bridging or adsorption mechanism is operative, its mechanism would have to be compatible with a small effect of anion or electrode identity. The present results do not rule out an inner-sphere mechanism for $Fe(CN)_6^{3-/4-}$ electron transfer, but they do indicate an insensitivity to electrode surface composition.

ACKNOWLEDGMENTS

This work was supported by the Air Force Office of Scientific Research. The authors thank Dennis Evans for providing CV simulation software.

REFERENCES

1 J. Kawiak, P. Kulesza and Z. Galus, J. Electroanal. Chem., 226 (1987) 305.
2 L.M. Peter, W. Durr, P. Bindra and H. Gerischer, J. Electroanal. Chem., 71 (1976) 31.
3 A. Wieckowski and M. Szklarczyk, J. Electroanal. Chem., 142 (1982) 157.
4 J. Kawiak, T. Jedral and Z. Galus, J. Electroanal. Chem., 145 (1983) 163.
5 S. Pons, M. Datta, J.F. McAller and A.S. Hinman, J. Electroanal. Chem., 160 (1984) 369.
6 D. Ellis, M. Eckhoff and V.D. Neff, J. Phys. Chem., 85 (1981) 1225.
7 K. Itaya, T. Ataka and S. Toshima, J. Am. Chem. Soc., 104 (1982) 4767.
8 M. Poon and R. McCreery, Anal. Chem., 59 (1987) 1615.
9 M. Poon and R. McCreery, Anal. Chem., 58 (1986) 2745.
10 P.H. Daum and C.G. Enke, Anal. Chem., 41 (1969) 653.
11 E.L. Goldstein and M.R. Van De Mark, Electrochim. Acta, 27 (1982) 1079.
12 I.F. Hu, D.H. Karweik and T. Kuwana, J. Electroanal. Chem., 188 (1985) 59.
13 R. Rice, H. Pontikos and R. McCreery, J. Am. Chem. Soc., 112 (1990) 4617.
14 R.L. McCreery, in A.J. Bard (Ed.), Electroanalytical Chemistry, Vol. 17, Marcel Dekker, New York, 1991, pp. 221–374.
15 J. Kuta and E. Yeager, J. Electroanal. Chem., 59 (1975) 110.
16 D.O. Wipf, E.W. Kristensen, M.R. Deakin and R.M. Wightman, Anal. Chem., 60 (1988) 306.
17 R.M. Wightman and D.O. Wipf, in A.J. Bard (Ed.), Electroanalytical Chemistry, Vol. 15, Marcel Dekker, New York, 1989.
18 J.O. Howell and R.M. Wightman, Anal. Chem., 56 (1984) 524.
19 K. Aoki, K. Akimoto, K. Tokuda, H. Matsuda and J. Osteryoung, J. Electroanal. Chem., 171 (1984) 219.
20 R.S. Nicholson and I. Shain, Anal. Chem., 36 (1964) 706.
21 B.W. Pfenning and A.B. Bocarsly, Inorg. Chem., 30 (1991) 666.
22 C. Hidalgo-Luangdilok and A.B. Bocarsly, Inorg. Chem., 29 (1990) 2894.
23 L.M. Siperko and T. Kuwana, J. Electrochem. Soc., 133 (1986) 2349.
24 R.J. Rice and R.L. McCreery, J. Electroanal. Chem., 310 (1991) 127.

Reprinted from Analytical Chemistry, 1991, 63.

Surface-Enhanced Raman Spectroscopy of Carbon Electrode Surfaces Following Silver Electrodeposition

Yang Wang Alsmeyer and Richard L. McCreery*

Department of Chemistry, The Ohio State University, 120 W. 18th Avenue, Columbus, Ohio 43210

Electrodeposition of Ag particles on glassy carbon (GC) resulted in up to a 100-fold enhancement of Raman scattering from the carbon substrate. The enhancement was a maximum when 0.21 μmol/cm² of Ag was deposited and was greater when small (~400-Å) Ag particles were present. Although the enhancement of carbon scattering was large, it was fragile, decaying with time after Ag deposition. On the basis of surface-enhanced Raman theory, the sampling depth of the enhanced spectra is approximately 20 Å, compared to ca. 250 Å for conventional Raman of GC. SERS spectra of GC and pyrolytic graphite (PG) exhibited a stronger "disorder" band, either because the method is more surface selective or because the Ag preferentially deposits on electrochemically active surface defects. The approach was used to examine cleaved and laser-activated PG surfaces and polished highly oriented PG (HOPG), and it was demonstrated that laser damage is more extensive on the surface than the normal Raman spectrum implies.

INTRODUCTION

The wide variety of surface preparation procedures for carbon electrodes leads to quite variable electrochemical performance (*1–3*). Electron-transfer rates, adsorption, and background current all depend strongly on surface history, with variations of several orders of magnitude in k^0 being observed even for allegedly simple redox systems (*4–13*). While a comprehensive understanding of the variables that affect electrode kinetics on carbon is not yet available, it is clear that surface cleanliness and carbon microstructure are of major importance. Unfortunately, the process of relating surface structure to electron-transfer activity has been hindered by the lack of adequate probes of carbon surface structure at the molecular level. Without such probes, conclusions about surface pretreatment effects on electrochemical behavior are necessarily indirect and provide limited structural insight.

In several previous reports, we discussed the relationship between the Raman spectra of carbon materials and their electron-transfer activity (*13–15*). A correlation between the 1360-cm^{-1} "disorder" (D) band of carbon and electron-transfer kinetics for $Fe(CN)_6^{3-/4-}$ and dopamine was noted, indicating that graphitic edges associated with disorder are important to fast electron transfer. Through correlation of k^0 for $Fe(CN)_6^{3-/4-}$ with capacitance and D band intensity, it was possible to hypothesize that the electron-transfer rate is directly proportional to the surface fractional edge plane density, f_e (*15*). Thus, the Raman spectrum of carbon electrodes provides structural information on at least one of the surface variables that determine k^0 on carbon electrodes.

Although conventional Raman spectroscopy has been a very useful probe of carbon structure, it should be recognized that the sampling depth is significantly greater than UHV surface analytical techniques such as Auger and XPS. The photon penetration and escape depths for Raman are usually greater than the electron escape depths relevant to XPS and Auger, leading to lower surface selectivity for the optical probe. For carbon probed with a visible laser at normal incidence, the sampling depth is ca. 300 Å (*3*) and should be somewhat less at non-normal incidence. Although this sampling depth is fairly small due to the opacity of carbon, it is still large compared to the electrochemically relevant depths of a few tens of angstroms. Thus, a pretreatment procedure that affects only a few atomic layers of a carbon surface may not be detected by a normal Raman probe due to a relatively large signal from the several hundred angstroms of bulk carbon.

The current work was initiated to decrease the effective sampling depth of Raman spectroscopy by exploiting the surface enhanced Raman effect (SERS). Although SERS has been studied extensively because of its high sensitivity and surface selectivity (*16*), the vast majority of work has been carried out on Ag, Au, and Cu substrates. Carbon itself is not a suitable SERS substrate due to its unsuitable optical and electronic properties, and any enhancement on carbon would be very small. In order to exploit SERS for examining carbon materials, we used an approach that is similar to that of Pemberton (*17*) in which small, SERS active Ag particles were electrodeposited on Pt surfaces. As was observed for vapor-deposited Ag particles (*18–20*), the material near the Ag particles exhibited enhanced Raman due to the electromagnetic field enhancement by the Ag. Thus, the carbon electrode material near an electrodeposited Ag particle of suitable size should exhibit enhanced Raman within a few tens of angstroms of the Ag (*16b, 20*). Since such Raman enhancement distances are much less than the 300-Å normal Raman sampling depth, the SERS technique should be more surface selective than conventional Raman. In this paper, we will discuss the deposition technique, enhanced spectroscopy, and applications to several carbon electrodes.

EXPERIMENTAL SECTION

A schematic diagram of the instrument is shown in Figure 1. The spectrometer and collection optics have been described previously (*21*), and the band reject (Pomfret optics, Orange, VA) and band-pass (Oriel) filters were both centered on the 514.5-nm laser line. The cell was designed both to hold a variety of electrode materials and to properly orient the incident beam, electrode surface, and collection optics. The beam impinged on the electrode at an angle of 75 ± 5° to the surface normal with the polarization parallel to the electrode surface. An Ag wire quasi-reference electrode (QRE) and Pt auxiliary electrode were inserted in the solution out of the optical path at opposite sides of the cell. The working electrode is shown in Figure 2. Teflon plumber's tape was used to seal the holder to the carbon electrode material. It was important to avoid strain on the carbon during mounting, particularly for graphite samples, so the soft Teflon tape gasket was preferable to an O-ring.

Coarse optical alignment was carried out with a dummy glassy carbon (GC) electrode positioned in the cell with solution present. Laser scatter was strong enough from GC to permit orientation of the electrode and incident beam such that the scattered light was imaged on the entrance slit. Then the electrode position and collection lens were adjusted to maximize the D band intensity for a Raman spectrum of the GC. It was important to have solution present to produce the same focusing conditions present during the experiment. Once an adequate signal from the dummy

* Author to whom correspondence should be addressed.

0003-2700/91/0363-1289$02.50/0

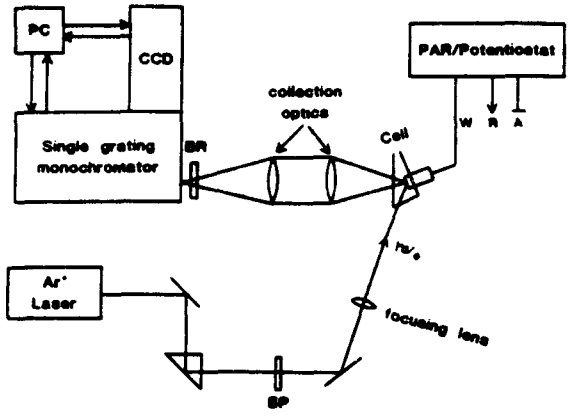

Figure 1. Schematic diagram of the experimental apparatus. Reference and auxiliary electrodes were placed on opposite sides of the working electrode. BR and BP are band reject and band-pass filters. Laser power at sample was ~10 mW, entrance slit width was 125 μm.

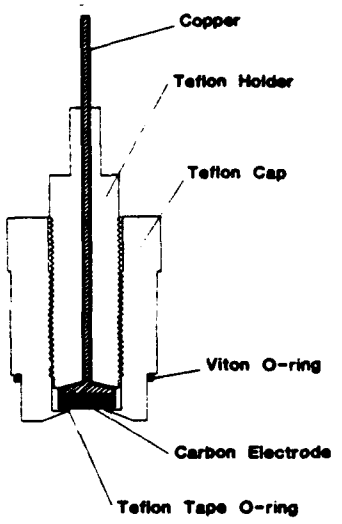

Figure 2. Detail of electrode holder. Entire assembly could be removed from cell without major disturbance of optical alignment. Teflon tape seal minimized pressure on carbon sample.

GC electrode was obtained, the GC was replaced with the electrode to be studied. The cell design permitted removal and replacement of the working electrode assembly with minimal disturbance to its position. With the new electrode in place, the Raman intensity was again maximized on the D band for GC or the E_{2g} band for pyrolytic graphite (PG) or highly oriented PG (HOPG).

After significant trial and error, the optimum Ag deposition conditions for maximum SERS intensity were determined. The solution was 0.5 mM $AgNO_3$ plus 0.1 M $NaClO_4$ or 0.1 M $NaNO_3$ in Nanopure (Barnstead) water. In this medium, the Ag wire QRE had a potential of 0.332 V vs SCE. The QRE was preferable to a conventional reference electrode because of lack of contaminants, particularly chloride ion. Constant current from a PAR 173 galvanostat was used to deposit Ag, in order to easily control the total amount deposited. For a current of 20 μA on a 0.12–0.38 cm^2 electrode area, the deposition potential ranged from −0.4 to −0.6 V vs QRE. Larger current densities resulted in more negative potential excursions and were avoided. Deposition times were varied as described below but were typically 1–5 min. Carbon materials were Tokai GC-20 glassy carbon, pyrolytic graphite from Pfizer, and HOPG from Union Carbide (ungraded material from Arthur Moore).

The spectrometer shown in Figure 1 is a modification of a previous design (*21*). A 200 line/mm grating in the ISA 640 spectrograph operated in second order produced a ca. 800-cm^{-1} Raman shift range when centered at 1340 cm^{-1} relative to the 514.5-nm Ar^+ laser. The detector was a 1-cm × 1-cm CCD, which

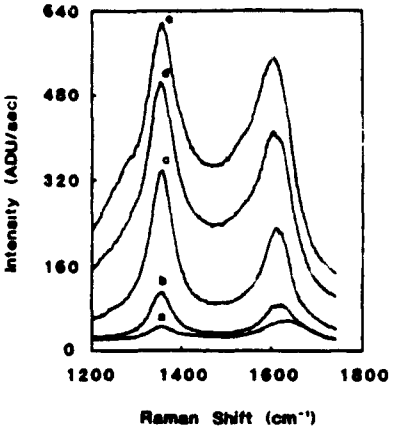

Figure 3. Raman spectra of polished GC-20 before and during Ag deposition. 5-s CCD integration times, laser off during deposition. Spectrum a is of the initial GC surface in solution but before deposition. Curves b–e are after Ag deposition as follows: b, 0.041 μmol/cm^2; c, 0.099 μmol/cm^2; d, 0.145 μmol/cm^2; e, 0.248 μmol/cm^2.

was binned to become a 512 × 1 detector. Laser power at the sample surface was 10 MW on a 50-μm × 2-mm focal spot. The laser light was kept off except during spectrum acquisition to minimize any photodegradation effects during deposition and observation. The beam waist at the electrode was relatively wide ~50 μm, thus keeping the power density relatively low. The typical CCD integration time was 5 s, with neglible dark counts for the CCD cooled to −110 °C. The Raman shift range was calibrated with a neon lamp each time the grating was repositioned. Intensities are expressed as CCD analog/digital converter units per second of integration, with each A/D unit corresponding to approximately 15 photoelectrons.

The overall experimental sequence was as follows: the cell and dummy GC electrode were aligned relative to the laser and spectrometer in the presence of solution, using both elastic scatter (crude alignment) and the carbon Raman bands (fine tuning). The GC electrode was replaced with the test electrode, and the alignment was fine tuned. Once alignment was complete, an initial spectrum was obtained (5-s integration time). With the laser off, Ag was deposited with constant current until the desired average film thickness was achieved. The working electrode was disconnected, the laser turned on, and the spectrum acquired immediately. Successive spectra at various Ag thicknesses were often obtained, with the laser on only during spectrum acquisition.

RESULTS

Raman spectra obtained before and after Ag deposition on conventionally polished GC are shown in Figure 3. The peak intensities increase by factors of up to 100 upon deposition depending on Ag coverage. The integrated intensity ratio of the D to E_{2g} bands increases from 1.25 to a maximum of 2.0 upon Ag deposition. The changes in shape of the E_{2g} peak at ~1600 cm^{-1} are due mainly to interference by water in the initial spectrum. Once the SERS intensity becomes large, the H_2O signal becomes insignificant compared to the carbon E_{2g} band. The absolute D band intensity (1360 cm^{-1}) and baseline are compared in Figure 4 as functions of Ag deposition time. For the polished GC surface, the maximum SERS intensity is reached at an average Ag coverage of 2.1×10^{-7} mol/cm^2, based on the geometric electrode area.

SEM's of the polished GC surface are shown in Figure 5A–E at two coverages and magnifications. On low magnification (A and C), a distribution of "large" Ag particles with diameters of ca. 2500 Å is apparent, plus numerous smaller particles visible upon close inspection. Higher magnification (B and D) reveals numerous particles in the 100–1000-Å range, with a higher density of small particles for the higher Ag coverage. As shown in Figure 5E, Ag on freshly cleaved HOPG leads to relatively large particles and clusters of ca. 1000-Å particles

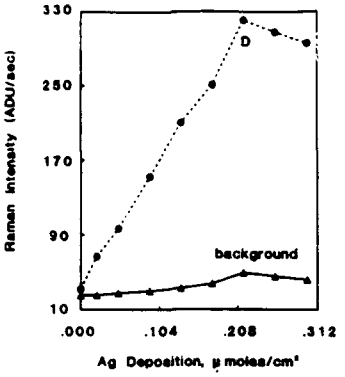

Figure 4. Raman intensities of D band (1354 cm^{-1}) and baseline during Ag deposition.

but few isolated small particles. In Figure 5F, a high density of small Ag particles is apparent on mechanically damaged regions of polished HOPG.

As shown in Figures 6 and 7, the SERS signal decays with time, whether or not the laser is on continuously. Although the signal degradation can be serious on a several minute time scale, the spectra are strong enough and the CCD fast enough to obtain excellent spectra in 5 s after deposition. Furthermore, the reproducibility of signal strength is fairly poor, with peak intensities having a standard deviation of 50% for N = 10. Thus, quantitative conclusions based on absolute intensity will be difficult in any case, and the signal decay must be considered in the experimental design.

Although the polished GC surfaces used for Figures 3–7 demonstrate that SERS can be used to enhance substrate scattering, structural inferences are more straightforward with more ordered HOPG samples. Raw spectra obtained from HOPG, which was lightly polished with 0.05-μm alumina, are shown in Figure 8. The E_{2g} band at 1582 cm^{-1} is the only graphite feature visible above the H_2O background before Ag deposition. As Ag is deposited, the D and E_{2g} bands become prominent, and the D/E_{2g} intensity ratio increases. The trend is more clear after the water background is subtracted, as in Figure 9. The D band is not apparent before Ag deposition but is prominent after 3.6×10^{-8}–2.5×10^{-7} mol/cm^2 of Ag has been deposited. On the basis of an equivalent monolayer coverage of ca 350 μC/cm^2 (*17*, *22*) or 3.6×10^{-9} mol/cm^2, the SERS effect begins at 10 average monolayers and is most prominent for 70 average monolayers of Ag. The integrated

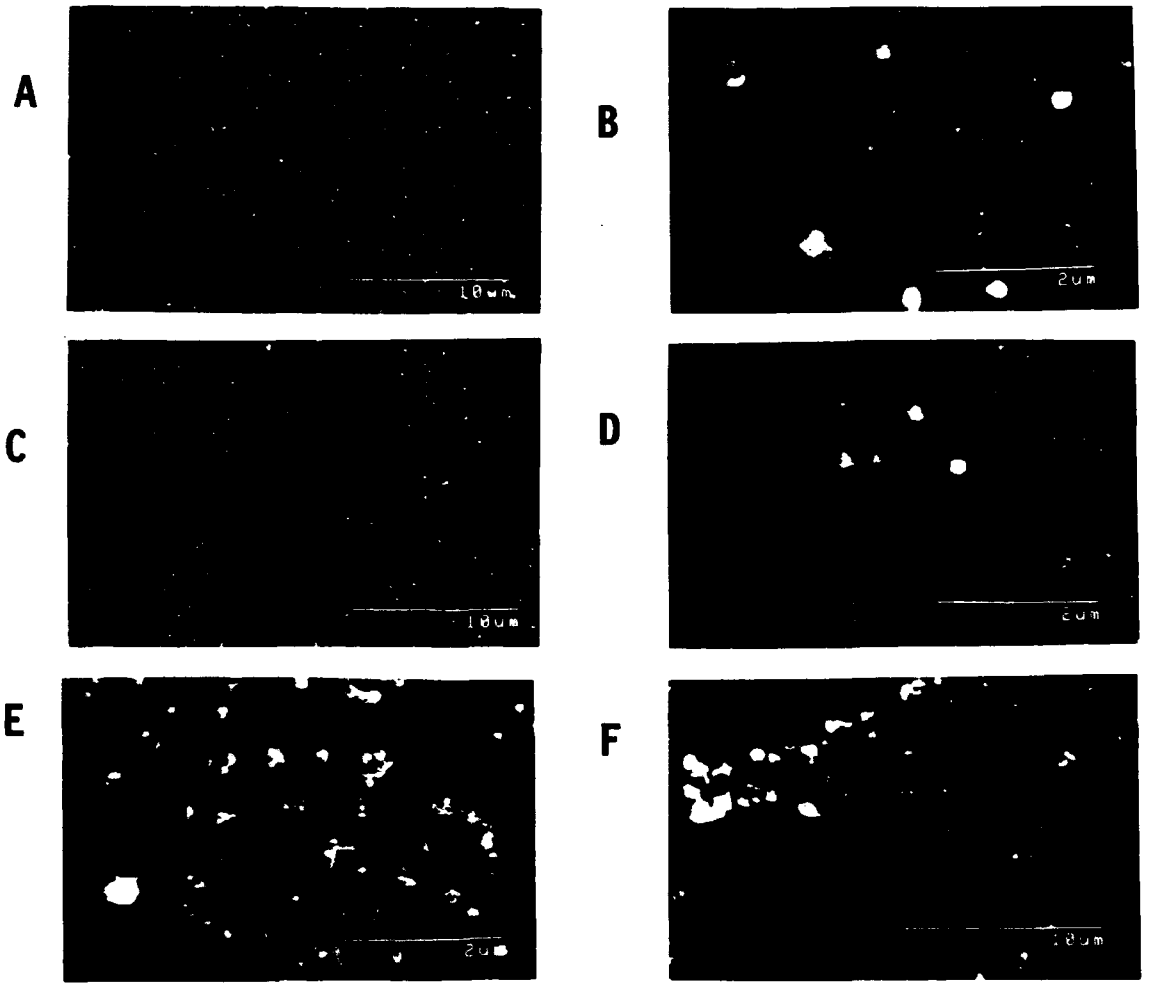

Figure 5. SEM's of GC (A–D) and HOPG (E, F) surfaces after Ag deposition. A and B are after 0.04 μmol/cm^2 C and D after 0.12 μmol/cm^2. E was obtained after Ag deposition on freshly cleaved HOPG and F after deposition on lightly polished HOPG.

and ECP surfaces due to selective adsorption, the adsorption mechanism for the two surfaces is fundamentally different. The current results are relevant to the area of voltammetric

(8) Poon, M.; McCreery, R. L. *Anal. Chem.* **1986**, *58*, 2745.
(9) Poon, M.; McCreery, R. L.; Engstrom, R. *Anal. Chem.* **1988**, *60*, 1725.
(10) Rice, R. J.; Pontikos, N. M.; McCreery, R. L. *J. Am. Chem. Soc.* **1990**, *112*, 4617.

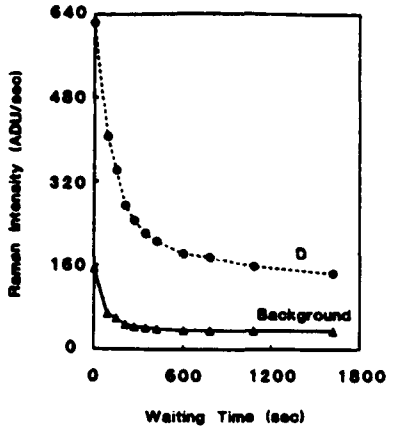

Figure 6. Decay of the D band and background Raman signals with time after Ag deposition was completed. Electrode remained in solution with laser on continuously. Initial Ag coverage was 0.24 μmol/cm^2.

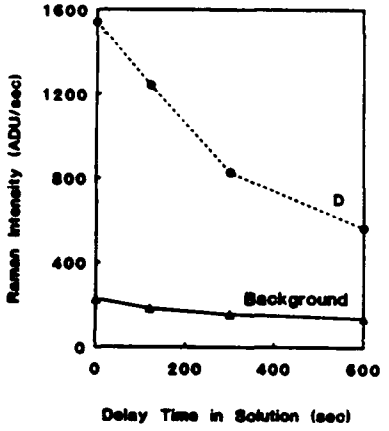

Figure 7. Decay of Raman intensity with time after Ag deposition. Conditions same as Figure 6, but Ar^+ laser was turned off between spectra.

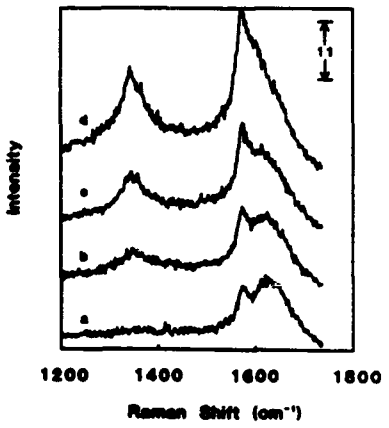

Figure 8. In situ Raman spectra of lightly polished HOPG before and after Ag deposition. Scale indicates ADU/s for all four spectra. Spectrum a, 0 μmol/cm^2 of Ag; b, 0.041 μmol/cm^2; c, 0.12 μmol/cm^2; d, 0.25 μmol/cm^2.

D/E_{2g} intensity increases from near 0 to 0.73 upon Ag deposition. Not only is the D/E_{2g} intensity ratio much higher after Ag deposition, but there is also a shoulder on the high-frequency side of the E_{2g} mode, a feature associated with delamination of the graphite and increased d_{002} spacing (*13*).

As noted earlier, enhanced Raman scattering was not observed following Ag deposition on cleaved HOPG, apparently because the particle size is unsuitable for SERS. However,

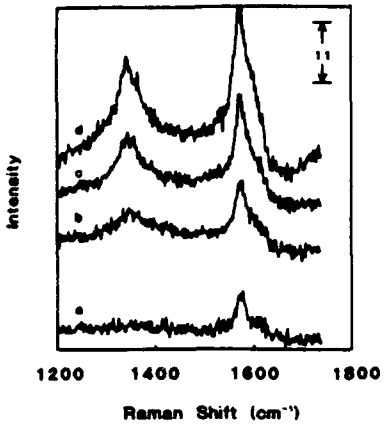

Figure 9. Same as Figure 8 but with H_2O background subtracted.

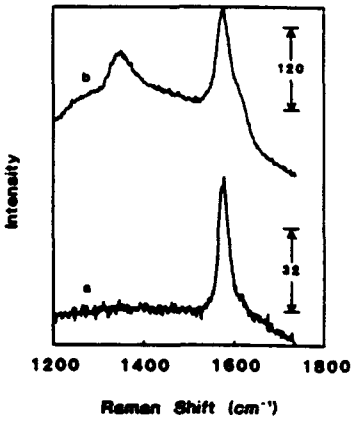

Figure 10. Raman spectra of cleaved PG basal plane. PG was cleaved in solution, and both spectra are corrected for H_2O background. Scale indicates ADU/s for each spectrum. Spectrum a is before Ag deposition, b is after 0.41 μmol/cm^2 of Ag was electrodeposited.

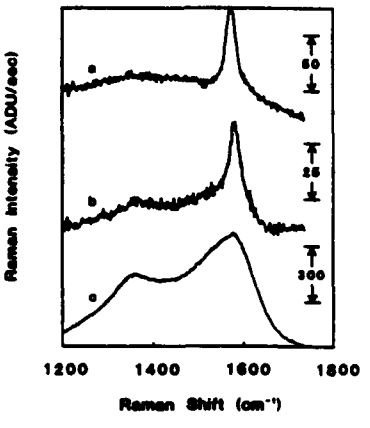

Figure 11. Raman spectra of cleaved PG, with relative scales indicated in ADU/s. Spectrum a is cleaved basal plane before Ag deposition. Spectrum b is same surface after three 50 MW/cm^2 Nd:YAG pulses were delivered in air. Spectrum C is the surface of curve b following deposition of 0.12 μmol/cm^2 of Ag.

pyrolytic graphite (PG) is similar to HOPG except it is not subjected to the final pressure annealing. It is less ordered than HOPG, with smaller microcrystallite sizes, but retains the macroscopic and microscopic layered structure. Figure 10 shows Raman spectra of the freshly cleaved basal plane of PG before and after Ag deposition. Unlike the data of Figures 8 and 9, the PG surface was not scratched or pretreated in any way. The D band is unobservable in the normal

Raman spectrum but increases in intensity upon Ag deposition. Figure 11 shows the effect of pulsed Nd:YAG laser irradiation on the PG spectrum. Laser treatment without Ag deposition causes a slight increase in D band intensity, sufficient to elevate the band above background. Following Ag deposition, the D band is much stronger, and the spectrum is similar to that for quite disordered sp^2 carbon. As with earlier experiments, Ag deposition greatly increases the absolute Raman intensities.

As noted in the Introduction, the surface selectivity of Raman scattering will be dependent on effective sampling depth. The normal Raman sampling depth may be estimated from the optical properties of GC and HOPG, using a modification of the approach of Wada and Solin (*23*) and Loudon (*24, 25*). The observed Raman signal at a particular sample depth, $R(z)$, will be related to the local laser intensity as it penetrates the solid, $I_L(z)$, and the attenuation of Raman scattering intensity as it leaves the solid. Therefore, the observed Raman sampling depth will be significantly smaller than the laser penetration depth. At normal incidence,

$$I_L(z) = I_0(1 - r)e^{-4\pi k_L(z/\lambda_L)} \quad (1)$$

$$R(z) = \gamma I_L(z)e^{-4\pi k_R(z/\lambda_R)} \quad (2)$$

where I_0 is the incident laser intensity, z the sample depth, and γ a constant incorporating the Raman scattering cross section, number density, etc. k_R and k_L are the absorption coefficients of the carbon at the Raman and laser photon wavelengths, λ_R and λ_L, and r is the reflectivity. After approximating that the scattered and laser wavelength are sufficiently close to each other to equate, the normal incidence Raman signal at a particular z becomes

$$R(z) = I_0(1 - r)\gamma e^{-8\pi k_L(z/\lambda_L)} \quad (3)$$

The total observed Raman scattering is proportional to the integral of eq 3 over the depth variable z. We will arbitrarily define the sampling depth, z_{63}, as the sample thickness that will generate 63% $(1 - e^{-1})$ of the Raman signal observed for a sample of infinite thickness. Integration of (3) leads to

$$S(z) = S_{max}(1 - e^{-8\pi k_L(z/\lambda_L)}) \quad (4)$$

$$S_{max} = \frac{I_0(1 - r)\gamma\lambda_L}{8\pi k_L} \quad (5)$$

where $S(z)$ indicates the total Raman signal for a sample of thickness z. Setting $S(z)/S_{max} = 1 - e^{-1}$ permits determination of z_{63} for normal incidence:

$$z_{63} = \frac{\lambda_L}{8\pi k_L} \quad (6)$$

For GC with a 515-nm laser at normal incidence ($k_L = 0.70$) (*26*), z_{63} is 291 Å, while for the HOPG basal plane ($k_L = 1.52$ at 515 nm) (*23*), z_{63} is 135 Å. Thus, 63% of the total Raman signal for GC at normal incidence is derived from the carbon within 290 Å of the surface (*3*). Obviously the sampling depth varies with λ_L and to a much smaller degree on the Raman shift, $\Delta\nu$.

For the geometry of Figure 1, with non-normal laser incidence and near-normal collection optics, the situation is more complex. $I_L(z)$ will vary with the incident angle, θ_i, and this dependence was predicted by using classical treatments (*27*). $I_L(z)$ was calculated by using the transmittance of a thin carbon film for light polarized parallel to the electrode surface. The "thick film" model (eq 27 in ref 27) was used to avoid any interference effects, and the film thickness was gradually increased to calculate I_L as a function of z. The resulting $I_L(z)$ curve was substituted into eq 2 and z_{63} was determined by numerical integration. The results are shown in Table I, along with the calculated reflectivity. In all cases, the electrode was assumed to be immersed in water ($n = 1.33$). The calculation was compared to one based on the mean-square electric field predictions of Porter et al. (*28*) to calculate $I_L(z)$, with identical results.

Table I. Calculated Reflectivity and Raman Sampling Depth

θ_i	reflectivity[b]	z_{63},[c] Å
Glassy Carbon ($n = 1.79$, $k = 0.70$,[a] $\lambda_L = 515$ nm)		
0°	0.0688	291
30	0.0997	281
45	0.1493	270
60	0.2612	260
75	0.5004	252
85	0.7924	250
89	0.9545	250
HOPG ($n = 1.79$, $k = 1.52$,[d] $\lambda_L = 515$ nm)		
0	0.2093	135
75	0.6820	125

[a] From ref 26. [b] Sample immersed in water ($n = 1.33$) in all cases. [c] Sample depth yielding 63% of maximum Raman signal. [d] Calculated from ref 23.

DISCUSSION

Considering the normal Raman experiment first, several useful observations are available from the results. The effective sampling depth z_{63} is 250–300 Å for GC, and is weakly dependent on the angle of incidence. Although surface selectivity can be improved somewhat at glancing incidence over normal incidence, the sampling depth still exceeds 200 Å. It should be noted that z_{63} decreases with decreasing λ_L and is smaller for the more strongly absorbing HOPG. The reflectivity is strongly θ_i dependent, with higher angles of incidence coupling significantly less light into the solid sample and reflecting more. At the 75° angle employed in the current experiments, 50% of the laser light enters the GC and 32% penetrates HOPG. The polarization parallel to the electrode surface was chosen partly because of past experience with solution scatterers (*29*) but principally to maintain the induced dipole axis perpendicular to the axis of the collection optics. Thus, the optical geometry corresponds to parallel polarization in the conventional Raman terminology. Based on results and theory for IR reflection/absorption spectroscopy (*28*), the normal Raman sampling depth and sensitivity may vary with incidence polarization, but these effects were not examined further in the present case.

The normal Raman spectra of various carbon electrode materials have been reported previously (*3, 13*) and are relevant here only as initial spectra preceding Ag deposition. As expected, the cleaved HOPG and PG normal Raman spectra show minimal D band intensity due to their ordered structures, while for GC the D band is the most intense band observed. As noted in a previous report, polishing can affect the D/E_{2g} intensity ratio for GC, indicating that polishing affects several hundred angstroms of substrate near the surface (*30*).

The results support several useful conclusions about the SERS experiment following Ag deposition. First, Ag deposition on GC results in an up to 100-fold enhancement of the carbon Raman signal. Second, although the enhancement is always large, its magnitude is only semiquantitatively reproducible and strongly dependent upon deposition time and conditions. Third, the SERS enhancement is a maximum at an average Ag coverage of 0.21 mol/cm² for GC. This value corresponds to about 10–70 equivalent monolayers. Fourth, the Ag deposit occurs as 400–4000-Å particles, and the density and size distribution vary significantly with carbon substrate type and Ag deposition time. Fifth, the SERS enhancement

is large but fragile, with degradation of the effect occurring on a several minute time scale following Ag deposition.

Although the quantitative irreproducibility and instability of the SERS effect on carbon electrodes are problematic, the utility of the method is determined by conclusions about surface selectivity. In several of the cases examined, the SERS spectrum differs qualitatively from the normal Raman spectrum, in addition to being more intense. For polished GC, the D/E_{2g} intensity increases with Ag deposition, implying greater carbon disorder near the surface. For both cleaved PG and lightly polished HOPG, the D band intensity increased greatly with Ag deposition. Two explanations for these observations arise, both of which provide insight into the electrochemical consequences of carbon surface structure. First, the SERS enhancement length may be short enough (e.g., < 50 Å) to be more surface selective than normal Raman, thus revealing more surface defects or damage. For example, the polished surface of the GC should be more disordered than the bulk (*31*), and the SERS spectrum should exhibit a higher D band intensity. Similarly, lightly polished HOPG will be most disordered at its surface. The normal Raman spectrum of polished HOPG reveals no D band intensity because it samples >100 Å into the material, whereas the SERS spectrum reveals the D band and associated surface disorder. A second explanation of higher D band intensity is enhanced electrodeposition at surface defects, leading to Ag particles primarily at defects sites. On the basis of other redox systems, electron transfer to Ag^+ should be faster at edge plane defects than at the basal plane (*3*, *13*, *15*), and these defects will exhibit higher D band intensity. Such an effect has been proposed to explain Cu electrodeposition on GC, as observed by SEM (*31*). This hypothesis retains the surface selectivity mentioned earlier but further states that Ag deposition and accompanying enhanced Raman is selective for defect sites, particularly graphitic edges. The relative importance of general surface selectivity and selective defect enhancement may be carbon substrate dependent.

On the basis of the theory for the SERS enhancement factor, a rough estimate of the SERS sampling depth may be made. The enhancement factor (EF) is a maximum at the Ag particle surface, with its magnitude strongly dependent on particle shape and size (*16*, *20*, *32*). For Ag spheres and λ_L = 515 nm, the maximum enhancement on the Ag surface decreases rapidly as the radius increases above a few 100 Å. Of greater relevance to the current work is the dependence of EF on distance away from the Ag particle surface. There is general agreement that the EF is proportional to $(a/d)^{12}$, where a is the Ag sphere radius and d is the distance of a scatterer from the particle center (*16*, *20*). Since the number of scatterers at a particular distance from a particle increases with d^2, the overall distance dependence of the Raman scattering becomes $(a/d)^{10}$. This prediction has been confirmed experimentally for polymer films deposited on Ag islands or Ag deposited on rough films (*20*).

The correlation of SERS intensity with the presence of small particles observed in the SEM's of Ag deposited on GC and HOPG confirms the importance of ca. 400-Å diameter particles for intense SERS. The 4000-Å particles observed on HOPG did not produce observable enhancement, and the Raman intensity roughly tracked the population of ca. 400-Å particles. Thus, it appears that the observed SERS effect is derived predominately from ca. 400-Å particles. For a = 200 Å, $(a/d)^{10}$ equals 0.38 for d = 220 Å and 0.11 for d = 250 Å. Thus, the Raman intensity has decreased by 62% when the scatterer is 20 Å from the surface of a 400-Å diameter Ag particle, and 89% at 50 Å away. These predictions are consistent with the 35–50-Å enhancement lengths observed by Murray and Allara for enhancement of a polymeric scatterer near rough Ag films (*20*). The predictions should onl considered as guides since the Ag particles cover a rang sizes and shapes, but a SERS sampling depth of a few te of angstroms is consistent with both theory and experimen The 25–50-Å enhancement length will be further decre by the absorption of enhanced laser light and scatt photons by the carbon. For example, the product of (a/a) and $\exp(-8\pi kz/\lambda)$ from eq 4 leads to a z_{95} sampling depth 22 Å for a = 200 Å, d = 220 Å, and k = 0.70 and 20 Å f = 1.52. Although approximate due to variations in Ag par size, 20 Å is the best estimate of the SERS sampling dept and is consistent with the estimate of Ishida et al. (*19*) f vapor-deposited Ag.

We have already seen the surface and defect selectivi SERS over normal Raman for GC and polished HOP Figures 10 and 11 provide a further example of partic relevance to electrochemical effects of carbon surface struc In Figure 10, it was clear that Ag deposition enhanced t band scattering from cleaved PG. In Figure 11, the norm Raman spectrum of cleaved PG showed increased D inter following Nd:YAG irradiation. The spectrum of Figure indicates moderate disorder, with a microcrystallite siz ca 150 Å based on the D/E_{2g} intensity ratio (*33*). Upon deposition, however, the D/E_{2g} ratio is much higher and spectrum indicates much greater disorder. The normal Ra spectrum is probing at least 100 Å into the surface, and it n contributions from both the laser-damaged surface layer a undamaged substrate. Since the SERS experiment is surface selective, the SERS spectrum reflects primarily laser-damaged region near the surface. Apparently the las damage depth is less than ~130 Å but deeper than the ~20 SERS sampling depth. These results indicate that no Raman underestimates laser-induced surface damage be of insufficient surface selectivity. A examination of laser a electrochemically induced surface damage on HOPG will presented later.

In summary, SERS following electrodeposition of A carbon electrodes improves surface selectivity for Ram spectroscopy from a few hundred to a few tens of angstr Although the absolute SERS intensities vary significantly conditions and time after deposition, changes in relativ tensity and appearance of the spectrum can be useful f deducing surface structural features.

ACKNOWLEDGMENT

We thank Marc Porter and Darwin Popenoe of Iowa Sta University for providing the computer program to confirm laser penetration depth.

Registry No. GC, 7440-44-0; PG, 7782-42-5; Ag, 7440-22- $NaClO_4$, 7601-89-0; $NaNO_3$, 7631-99-4.

LITERATURE CITED

(1) Kinoshita, K. *Carbon: Electrochemical and Physicochemical Pro ties*; Wiley: New York, 1988.
(2) Randin, J.-P. In *Encyclopedia of Electrochemistry of the Elemer* Bard, A. J., Ed.; Dekker: New York, 1976; Vol. 7, pp 1–291.
(3) McCreery, R. L. In *Electroanalytical Chemistry*; Bard, A. J., Ed.; ker: New York, 1991; Vol. 17.
(4) Stulik, K. J.; Kovach, P. M.; Kuhr, W. G.; Wightman, R. M. *An Chem.* **1988**, *55*, 1632.
(5) Fagan, D. T.; Hu, I. F.; Kuwana, T. *Anal. Chem.* **1985**, *57*,
(6) Hu, I. F.; Kuwana, T. *Anal. Chem.* **1986**, *58*, 3236.
(7) Hu, I. F.; Karweik, D. H.; Kuwana, T. *J. Electroanal. Chem.* *188*, 59.
(8) Rice, R. J.; Pontikos, N. M.; McCreery, R. L. *J. Am. Chem. So* **1990**, *112*, 4617.
(9) Engstrom, R. C.; Strasser, V. A. *Anal. Chem.* **1984**, *56*, 136.
(10) Cabaniss, G. E.; Diamantis, A. A.; Murphy, W. R., Jr.; Linton, Meyer, T. J. *J. Am. Chem. Soc.* **1985**, *107*, 1845.
(11) Kamau, G. N.; Willis, W. S.; Rusling, J. F. *Anal. Chem.* **1985**, *57*, 5
(12) Thornton, D. C.; Corby, K. T.; Spendel, V. A.; Jordan, J.; Robbat Rutstrom, D. J.; Gross, M.; Ritzler, G. *Anal. Chem.* **1985**, *57*
(13) Bowling, R. J.; Packard, R. T.; McCreery, R. L. *J. Am. Chem.* **1989**, *111*, 1217.
(14) Bowling, R. J.; Packard, R. T.; McCreery, R. L. *Langmuir* **1989**, *5*, 6
(15) Rice, R. J.; McCreery, R. L. *Anal. Chem.* **1989**, *61*, 1637.

Surface Enhanced Raman Examination of Carbon Electrodes: Effects of Laser Activation and Electrochemical Pretreatment

Yan Wang Alsmeyer and Richard L. McCreery*

Department of Chemistry, The Ohio State University, 120 West 18th Avenue, Columbus, Ohio 43210

Received January 2, 1991. In Final Form: April 22, 1991

Surface enhanced Raman spectroscopy (SERS) was used to examine carbon electrode surfaces following electrodeposition of 0.2 μmol/cm² of metallic silver. As demonstrated previously, the resulting ca. 400-Å Ag particles increase the Raman scattering intensity from the carbon substrate by 30–100 times, or larger for special cases. In the current report, the technique was used to characterize the surfaces of laser activated and electrochemically pretreated (ECP) glassy carbon (GC) and highly ordered pyrolytic graphite (HOPG). The SERS spectra were more surface selective than normal Raman and more closely correlated with electrochemical observations. For laser-activated HOPG, the SERS spectra revealed damage to the graphite lattice at lower power densities, and the disorder exhibited in SERS spectra more closely tracked the increase in electron transfer rate. For ECP of GC, HOPG, and pyrolytic graphite, the surface film examined with SERS was indistinguishable for the three substrates. Finally, the damage resulting from ECP of HOPG is consistent with a nucleation and growth mechanism.

Introduction

As noted in numerous reports and reviews,[1-3] the surface history of carbon electrodes has a large effect on electrochemical behavior. Of particular relevance here are the effects of pretreatment procedures on electron transfer kinetics, which vary by several orders of magnitude depending on surface variables. It has been demonstrated by our lab and others that fast electron transfer on carbon surfaces depends on both carbon microstructure and cleanliness.[3-11] In the case of ordered graphite basal plane, such as highly ordered pyrolytic graphite (HOPG), the rates of electron transfer for $Fe(CN)_6^{3-/4-}$ and dopamine increase greatly when microstructural edge plane defects are formed by laser treatment or anodization.[9,10] For disordered materials such as glassy carbon, the defect density is sufficient for rapid electron transfer, but the surface must be cleaned by careful polishing,[7] laser activation,[9,11,12] electrochemical pretreatment,[13-15] etc. When the conditions of high defect density and surface cleanliness are met, GC electrodes exhibit electron transfer rate constants (k°) for $Fe(CN)_6^{3-/4-}$ comparable to those of Pt or Au.[3,7]

Raman spectroscopy has proven to be a useful probe of changes in carbon microstructure caused by surface pretreatment. For example, the presence of the 1360-cm^{-1} "disorder (D)" band correlated with large heterogeneous electron transfer rate constant (k°) for HOPG, and both effects were attributed to the presence of edges of graphite microcrystallites.[9,11] "Disorder" is used here to mean any decrease in long range order from an ideal graphite crystal and, in particular, to the existence of microcrystallites or graphitic edges. Creation of disorder, and therefore the D band, by either laser activation or electrochemical pretreatment (ECP) coincides with large increases in k°. Both Raman spectroscopy[9,10] and scanning tunneling microscopy (STM)[16] imply that ECP proceeds on HOPG by nucleating at defect sites, followed by growth of a damaged region during oxidation. The resulting increase in defect density causes the increase in observed k° and D band intensity.

Although Raman spectroscopy has been valuable for revealing structural changes accompanying ECP and laser treatment of HOPG, an important issue remains. The sampling depth of conventional Raman spectroscopy is ca. 135 Å for HOPG and 290 Å for GC.[3,17] However, the structure of only a few atomic layers (~10 Å) of carbon should determine its electrochemical behavior. Normal Raman provides useful correlations of microstructure and electrochemical effects, but its utility would be increased by improving its surface selectivity. We recently reported a technique based on surface enhanced Raman spectroscopy (SERS) for improving the surface selectivity of Raman spectroscopy for carbon surfaces.[17] Following electrodeposition of Ag particles on the carbon electrode, the carbon Raman scattering was enhanced ca. 50 times when the Ag particle diameter was ca. 400 Å. The enhancement is due to short range chemical interactions between the particles and the carbon or to electromagnetic field enhancement. The latter effect decreases with the 10th power of the distance from the Ag particle, which is a combination of a r^{-12} decrease in the field effect and a r^2 increase in the number of scatterers.[18,19] An estimate of

(1) Kinoshita, K. *Carbon: Electrochemical and Physicochemical Properties*; Wiley: New York, 1988.
(2) Randin, J.-P. In *Encyclopedia of Electrochemistry of the Elements*; Bard, A. J., Ed.; Dekker: New York, 1976; Vol. 7, pp 1–291.
(3) McCreery, R. L. In *Electroanalytical Chemistry*; Bard, A. J., Ed.; Dekker: New York, 1991; Vol. 17.
(4) Stutts, K. J.; Kovach, P. M.; Kuhr, W. G.; Wightman, R. M. *Anal. Chem.* **1983**, *55*, 1632.
(5) Fagan, D. T.; Hu, I. F.; Kuwana, T. *Anal. Chem.* **1985**, *57*, 2759.
(6) Hu, I. F.; Kuwana, T. *Anal. Chem.* **1986**, *58*, 3235.
(7) Hu, I. F.; Karweik, D. H.; Kuwana, T. *J. Electroanal. Chem. Interfacial Electrochem.* **1985**, *188*, 59.
(8) Rice, R. J.; Pontikos, N. M.; McCreery, R. L. *J. Am. Chem. Soc.* **1990**, *112*, 4617.
(9) Bowling, R. J.; Packard, R. T.; McCreery, R. L. *J. Am. Chem. Soc.* **1989**, *111*, 1217.
(10) Bowling, R. J.; Packard, R. T.; McCreery, R. L. *Langmuir* **1989**, *5*, 683.
(11) Rice, R. J.; McCreery, R. L. *Anal. Chem.* **1989**, *61*, 1637.
(12) Bodalbhai, L.; Brajter-Toth, A. *Anal. Chim. Acta* **1990**, *31*, 191.
(13) Engstrom, R. C.; Strasser, V. A. *Anal. Chem.* **1984**, *56*, 136.
(14) Cabaniss, G. E.; Diamantis, A. A.; Murphy, W. R., Jr.; Linton, R. W.; Meyer, T. J. *J. Am. Chem. Soc.* **1985**, *107*, 1845.
(15) Kepley, L. J.; Bard, A. J. *Anal. Chem.* **1988**, *60*, 1459.
(16) Gewirth, A. A.; Bard, A. J. *J. Phys. Chem.* **1988**, *92*, 5563.
(17) Alsmeyer, Y. W.; McCreery, R. L. *Anal. Chem.* **1991**, *63*, 1289.
(18) Murray, C. A.; Allara, D. L. *J. Chem. Phys.* **1982**, *76*, 1290.

0743-7463/91/2407-2370$02.50/0

the sample depth based on field enhancement is approximately 20 Å.[17] Thus for either chemical or field enhancement mechanisms, the improved surface selectivity should provide structural information of greater direct relevance to electrochemical behavior than normal Raman spectroscopy.

We report here the application of SERS to laser and electrochemically pretreated HOPG and GC electrodes. The controlling objective of the experiments is to reveal the relationship between carbon surface structure and the electron transfer rate for $Fe(CN)_6^{3-/4-}$.

Experimental Section

The Raman spectrometer and SERS procedure have been described previously. In all cases, the average Ag coverage was 0.21 μmol/cm² for SERS experiments, and spectra were obtained within 10 s of deposition with a CCD integration time of 5 s in all cases. Laser power at the sample was typically 10 mW on a 50 × 200 μm spot. Where noted, a Spex Raman microprobe with a ca. 5 μm diameter focal spot was used to acquire spatially resolved spectra.

HOPG was ungraded material from Union Carbide (Parma, OH) and was freshly cleaved before each experiment with adhesive tape. The fresh basal plane surface was exposed to air for a few minutes before immersion in electrolyte. For all HOPG and PG experiments described here, only the basal plane was examined. Laser activation was carried out as described previously,[8,20-22] in air with a 9-ns, 1064-nm Nd:YAG pulse, on a freshly cleaved surface immediately before cell assembly and immersion in electrolyte. In order to electrochemically pretreat carbon surfaces gradually, ECP was conducted with linear cyclic sweeps at 50 mV/s starting at −0.1 V vs Ag/AgCl. Unless noted otherwise ECP was conducted in 0.1 M KNO_3. The maximum positive potential was either 1.85 or 1.95 V, as noted below, and cyclic sweeps were repeated in some cases. After the ECP procedure was complete, either the electrode was examined in air with normal Raman spectroscopy (at 515 nm) or the electrolyte was replaced with 1 mM $AgNO_3$ in 0.1 M $NaClO_4$, Ag was electrodeposited, and SERS spectra were acquired. Each ECP and SERS procedure was initiated with a freshly cleaved HOPG surface; no attempts to further modify the surface after Ag deposition were made. GC was polished conventionally with 0.05-μm alumina before ECP, and PG was cleaved before any subsequent procedures.

Heterogeneous electron transfer rate constants (k°) for $Fe(CN)_6^{3-/4-}$ were determined from cyclic voltammetry in 1 M KCl by the method of Nicholson, assuming $\alpha = 0.5$ and $D_{ox} = 7.6 \times 10^{-6}$ cm²/s.

Results and Discussion

Figure 1 shows normal Raman spectra of HOPG basal plane surfaces irradiated in air at various power densities. At 40 and 50 MW/cm², a modest 1360-cm⁻¹ band is observed, while the spectra following 60 MW/cm² or higher activation indicate significant disorder of the graphite lattice. As discussed in detail elsewhere, the D band intensity for graphitic materials correlates with the presence of edges of graphitic domains.[23] Figure 2 shows spectra of HOPG following laser irradiation in air and then electrodeposition of 0.21 μmol/cm² Ag. Raman scattering from H_2O has been mathematically subtracted. The 1360-cm⁻¹ intensity is higher for the SERS spectra following 40 and 50 MW/cm² activation, with severe disorder observed at 50 MW/cm². Figure 3 compares the integrated D/E_{2g} (1360/1582 cm⁻¹) intensity ratio for the normal and SERS spectra for various power densities. Note the D band in the SERS spectra is more intense for the 40 and 50 MW/cm² surfaces, implying that the SERS

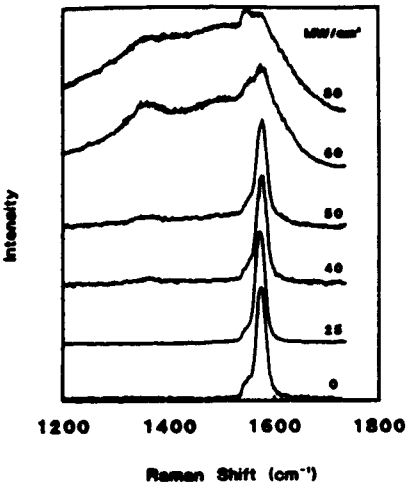

Figure 1. Normal Raman spectra for HOPG obtained in air following laser activation (9 ns, 1064 nm), also in air. Numbers indicate activation laser power density.

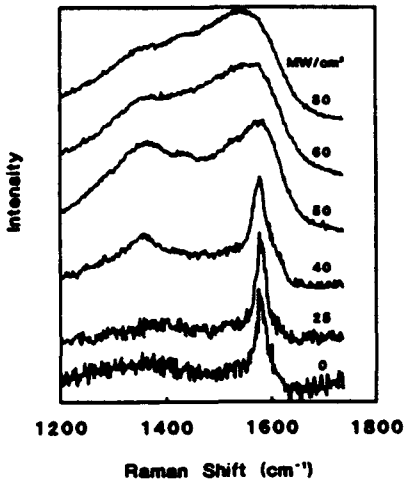

Figure 2. Surface enhanced spectra of laser-activated HOPG obtained in solution following electrodeposition of 0.21 μmol/cm² Ag. Surfaces prepared as in Figure 2 before immersion in Ag deposition solution. Solvent background was subtracted from Raman spectra.

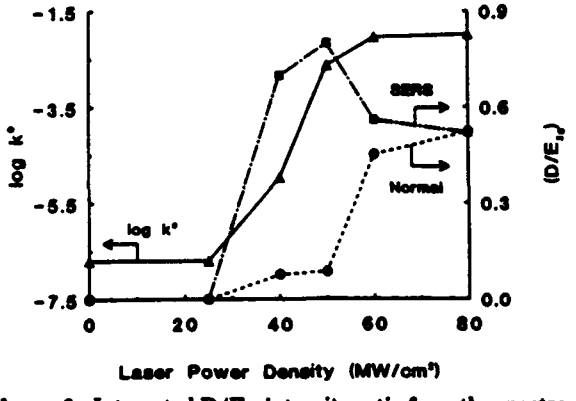

Figure 3. Integrated D/E_{2g} intensity ratio from the spectra of Figures 1 and 2, plotted with the k° for $Fe(CN)_6^{3-/4-}$ obtained following the same laser activation procedure.

(19) For reviews, see (a) Chang, R. K.; Furtak, T. E. *Surface Enhanced Raman Scattering*; Plenum: New York, 1982. (b) Moskovits, M. *Rev. Mod. Phys.* **1985**, *57*, 783. (c) Chang, R. K.; Laube, B. L. *CRC Crit. Rev. Solid State Mater. Sci.* **1984**, *12*, 1.

(20) Poon, M.; McCreery, Richard L.; Engstrom, R. *Anal. Chem.* **1988**, *60*, 1725.

(21) Poon, M.; McCreery, R. L. *Anal. Chem.* **1986**, *58*, 2745.

(22) Poon, M.; McCreery, R. L. *Anal. Chem.* **1987**, *59*, 1615.

(23) Wang, Y.; Alsmeyer, D.; McCreery, R. L. *Chem. Mater.* **1990**, *2*, 557.

technique is more sensitive to laser-induced surface damage. Stated differently, the SERS probe is more sensitive to laser-induced lattice damage because of its greater surface selectivity.

The electron transfer rate constant for $Fe(CN)_6^{3-/4-}$ was also determined following laser irradiation, with the results plotted on a log scale in Figure 3. As reported previously, the observed k° increases sharply following 40–50 MW/cm² laser pulses.[11] Since k° reflects an interfacial process, one would predict that disorder in the first few atomic layers of HOPG would be sufficient to increase the rate. In Figure 3, the appearance of disorder in the SERS spectrum coincides with the increase in k°. The greater surface selectivity (ca. 20 Å)[17] of SERS provides spectra of greater relevance to electron transfer kinetics than normal Raman, which has a sampling depth of >100 Å.[3,17] Thus the laser damage as assessed by normal Raman lags the increase in k°.

The results shown in Figure 1–3 are consistent with previous conclusions on the effects of pulsed lasers on HOPG.[9,11,24–26] The thermomechanical shock or local melting caused by the laser creates defects in the basal plane which are active to electron transfer. Steinbeck et al. considered local melting in some detail and concluded that higher laser powers lead to greater melt depths.[24] It is clear from Figure 2 that 60 MW/cm² pulses cause damage to a depth greater than the normal Raman sampling depth of ca. 100 Å. Similarly, the damage from a 50 MW/cm² treatment extends at least 20 Å (the SERS sampling depth) but less than 100 Å into the HOPG. Due to differences in laser parameters, a direct comparison of the work of Steinbeck et al. with the current results is not possible, except to note that local melting is a distinct possibility for the damage mechanism leading to Figures 1 and 2. Regardless of mechanism, the main points remain: that the SERS spectra correlate more closely with k° and that higher laser powers damage the lattice more deeply.

ECP is considerably more complex than laser activation, since a variety of chemical processes accompany breakup of the graphitic lattice. Although there is general agreement that ECP leads to surface oxides and eventually an electrogenerated graphitic oxide (EGO) film,[13–15,27] the nature of the film is not yet clear. Figure 4 shows normal Raman spectra of HOPG, PG, and GC following ECP. HOPG surfaces were subjected to eight oxidation/reduction cycles (ORC) from −0.1 to +1.95 V vs Ag/AgCl in 0.1 M KNO_3 and GC and PG from −0.1 to +1.85 V. Although all three materials exhibit disorder following ECP, the normal Raman spectra vary with the carbon substrate material. At first glance, one might conclude that the EGO film differs from the three carbon materials. Alternatively, the normal Raman sampling depth (>100 Å) may still be probing the unaffected substrate and diluting the contribution of the EGO layer to the Raman spectrum.

The situation is clarified by the SERS spectra, shown in Figure 5. As expected, all the SERS spectra are much stronger than the normal Raman spectra. In addition, the D and E_{2g} bands for all three carbon materials are essentially identical, implying that the EGO film is similar for the three materials. It is not surprising that extensive

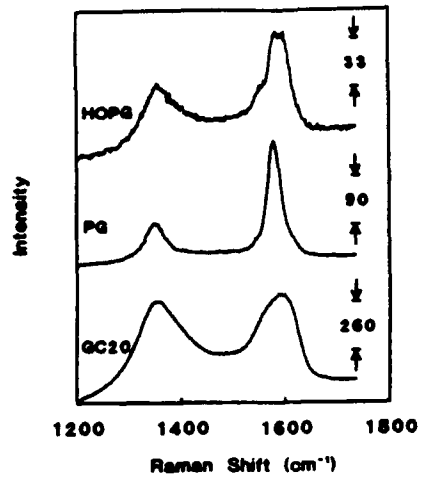

Figure 4. Normal Raman spectra of HOPG, PG, and GC obtained in air following eight oxidation reduction cycles in 0.1 M H_2SO_4. Vertical scales refer to A/D units from the CCD, with ca. 15 photoelectrons/ADU.

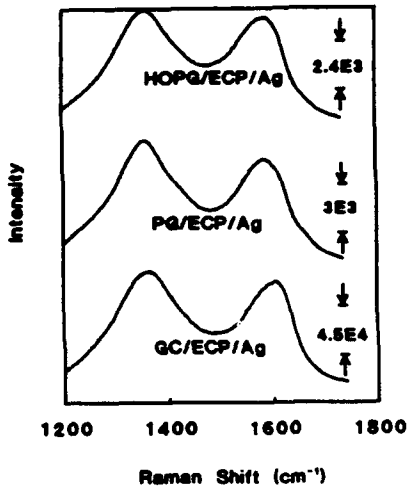

Figure 5. SERS spectra of surfaces prepared as in Figure 4, following deposition of 0.21 μmol/cm² Ag.

oxidation leads to similar films for different carbons, but Figure 5 provides direct evidence. Clearly the SERS experiment is providing higher selectivity for the film vs the substrate than normal Raman. Since the sampling depth for SERS is ca. 20 Å rather than >100 Å, the surface film should contribute more to the spectrum. In addition, Ag may nucleate and deposit more extensively in the film, thus providing greater enhancement in the film rather than the carbon. The fact that an EGO film produced on GC yields consistently more intense SERS may imply that the film is thicker or that it promotes Ag particle nucleation.

ECP of HOPG was examined in greater detail to ascertain the nature of structural damage plus relationships between Raman and electrochemical effects. Freshly cleaved HOPG was then subjected to linear oxidation/reduction scans between −0.1 and +1.95 V vs Ag/AgCl at 50 mV/s in 0.1 M KNO_3. For normal Raman spectra, the HOPG sample was removed from the KNO_3 solution and spectra were obtained in air. SERS spectra were obtained after transfer to 0.1 M $NaClO_4$/0.5 mM $AgNO_3$ and deposition of 0.21 μmol/cm² of Ag^0 at a controlled current of 20 μA. Both normal and SERS spectra were acquired after varying numbers of oxidation reduction cycles (ORC), but each ECP and Raman experiment started with a fresh

(24) Steinbeck, J.; Braunstein, G.; Dresselhaus, M. S.; Venkatesan, T.; Jacobson, D. *J. Appl. Phys.* **1985**, *58*, 4374. *J. Appl. Phys.* **1988**, *64*, 1502.
(25) Speck, J. S.; Steinbeck, J.; Braunstein, G.; Dresselhaus, M. S.; Venkatesan, T. Beam-Solid Interactions and Phase Transformations; Proceedings of the Materials Research Society.
(26) Speck, J. S.; Steinbeck, J.; Dresselhaus, M. S. *J. Mater. Res.* **1990**, *5*, 980.
(27) Besenhard, J. O.; Fritz, H. P. *Angew. Chem., Int. Ed. Engl.* **1983**, *22*, 950.

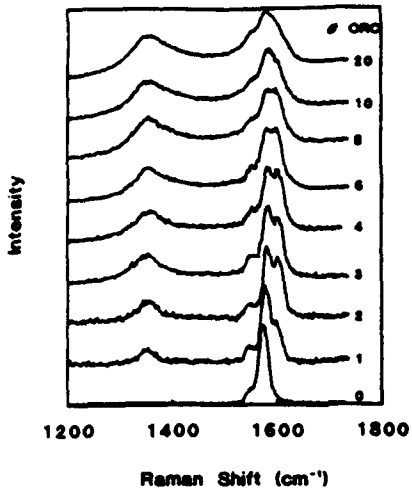

Figure 6. Normal Raman spectra obtained in air for HOPG following varying numbers of ORC's in 0.1 M KNO_3, −0.1 to +1.95 V vs Ag/AgCl.

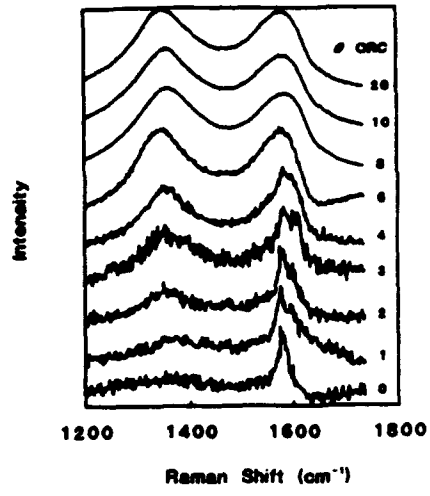

Figure 7. Same as Figure 6, except SERS spectra were obtaine in solution after Ag deposition (0.21 μmol/cm²). Solvent back ground was subtracted.

HOPG surface. Treatment of HOPG with successive cyclic scans is similar to the protocol used by Bard et al.,[15,16] for GC and HOPG, and is more gradual than the ECP procedure originated by Engstrom et al.[13]

The normal Raman spectra shown in Figure 6 reveal several microstructural effects caused by ECP. One ORC to 1.95 V is sufficient to create a 1360-cm^{-1} band, which increases gradually with further oxidation cycles. The effects on the E_{2g} band are more complex, with a 1620-cm^{-1} band appearing initially and then merging with the 1582-cm^{-1} band as the latter shifts upward in $\Delta\bar{\nu}$. The 1620-cm^{-1} band has been attributed to "boundary layer" graphite which occurs in intercalation compounds or when the graphite is delaminated.[9,28] The upward shift in the 1582-cm^{-1} band occurs when the graphite lattice is damaged, specifically as the in-plane microcrystallite size (L_a) is decreased.[23] Thus the progression of Raman spectra with repeated ORC indicates increasing disorder, with the graphite layers separating and fragmenting during ECP. Note also that the eight cycle spectrum of Figure 6 corresponds to the HOPG spectrum of Figure 4 and that subsequent ORC's cause the valley between the D and E_{2g} bands to begin to fill in.

SERS spectra acquired after the same ECP procedure are shown in Figure 7. Although the spectra are qualitatively similar to normal Raman, the D band intensity develops more quickly and the SERS spectra indicate more disorder. Note that the appearance of the spectrum changes negligibly after the eight ORC cycle, implying that the EGO film changes little once the severe disorder exhibited in Figure 5 is reached. The results imply that eight ORC cycles are sufficient to negate the effects of the original carbon microstructure on the EGO film. The D/E_{2g} integrated intensity ratio is plotted as a function of ORC in Figure 8. The SERS ratio exhibits greater disorder with a smaller number of ORC's, due to increased surface selectivity.

The voltammetry of $Fe(CN)_6^{3-/4-}$ in 1 M KCl was examined following the same ECP procedure used for Figures 6–8. Figure 9 shows voltammograms obtained after the first through fourth ORC cycles. Following the second and third cycles, and possibly the first, two voltammetric couples are observed, one exhibiting a high k° and one low. After four cycles the high k° couple is dominant. This behavior is similar, although more pronounced, than that observed for potentiostatic ECP in 0.1 M KNO_3.[9,10] Two couples for a simple, $1e^-$ redox system indicate spatial heterogeneity on a scale greater th

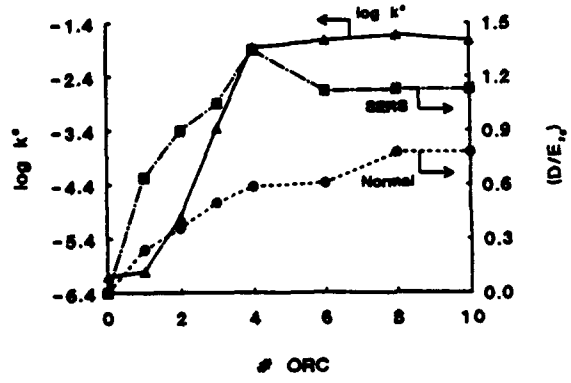

Figure 8. Integrated D/E_{2g} ratios for normal and SERS spectra of Figures 6 and 7, log (k°) for $Fe(CN)_6^{3-/4-}$ is also shown f surfaces prepared identically, but without Ag deposition.

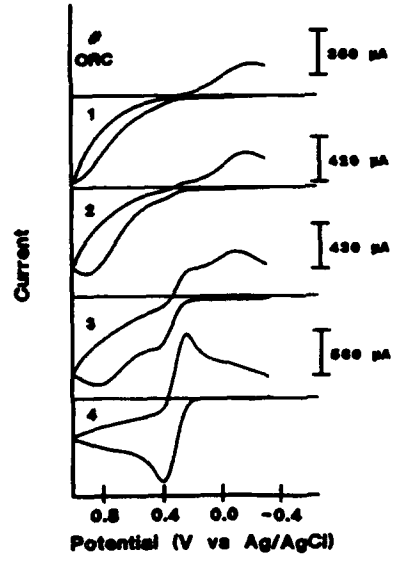

Figure 9. Voltammetry of $Fe(CN)_6^{3-/4-}$ on HOPG basal pla following one to four ORC's. ECP was conducted in 0.1 M KNO_3 (as for Figures 6–8), then the electrolyte was replaced with $Fe(CN)_6^{3-/4-}$ in 1 M KCl.

(28) Dresselhaus, M. S.; Dresselhaus, G. *Adv. Phys.* 1981, *30*, 139.

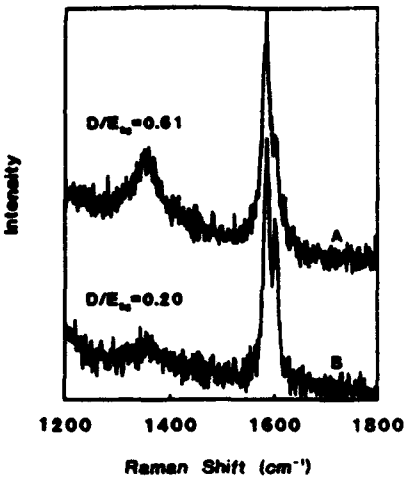

Figure 10. Raman microprobe (spot size ~5 μm) on HOPG following ECP, three ORC's. Probe was translated 60 μm between spectra A and B.

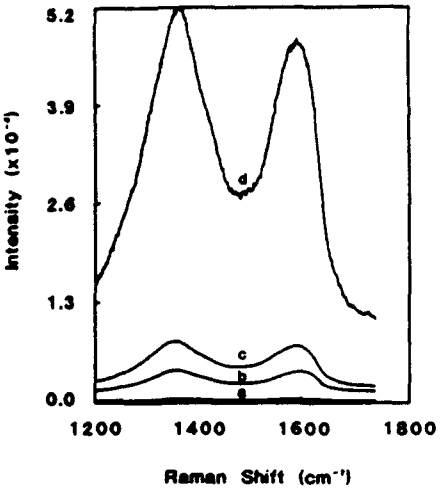

Figure 11. SERS spectra during Ag deposition on polished GC following ECP in 0.1 M H_2SO_4. Amount of Ag deposited was as follows: a, 0 μmol/cm²; b, 0.04 μmol/cm²; c, 0.12 μmol/cm²; d, 0.25 μmol/cm².

$(Dt)^{1/2}$, such that the diffusion fields to high activity and low activity regions are essentially decoupled.[3]

The k° determined from the major couple of voltammograms following ECP is shown in Figure 8. When only the major peak is considered, the k° appears to lag the increases in D band intensity, with significant D band intensity appearing before k° activation. This result is inconsistent with the laser activation experiments, where k° and the SERS derived D/E_{2g} intensity ratio tracked each other.

An explanation for this apparent inconsistency is revealed by Figure 10 and has been noted previously for a different ECP protocol.[9] Figure 10 shows Raman microprobe results for two different spots on an ECP surface following three oxidation/reduction cycles. The damage is quite heterogeneous on the HOPG surface because it originates with a nucleation and growth mechanism. Since the SERS experiment enhances the Raman scattering from damaged regions, a high SERS D band intensity can be observed even though the extent of damage may be small on average. In other words, a small amount of lattice damage can result in a significant D/E_{2g} intensity ratio in the SERS experiment. Since the usual spot size for the SERS spectra (50 × 200 μm) is large on the scale of the surface heterogeneity, spectra obtained with a conventional spectrometer do not exhibit spatial heterogeneity.

For the cyclic voltammetric determination of k°, however, the relevant distance scale is $(Dt)^{1/2}$, not the laser spot size. If the heterogeneity is large on a scale of $(Dt)^{1/2}$, the damaged and undisturbed basal plane surfaces will behave independently, with minimal diffusional crosstalk. If both regions cover a significant fraction of the surface, two sets of voltammetric waves will be observed, one for a high k° and one for a lower k°. If the average coverage of damaged region on the surface is very low, the high k° couple will be buried in the background current. The small, more reversible couple in Figure 9 is consistent with these conclusions. It is due to electron transfer at active, damaged regions, but the average surface coverage of these regions is small until four or more cycles have occurred. The damaged regions are responsible for the large k° couple and the high D/E_{2g} ratio observed in Figure 10A and the SERS spectra.

Returning to Figure 8, the basal plane surface before any ECP has a few defects (roughly one every μm²), the D/E_{2g} ratio is near zero, and k° is very low (ca. 10^{-6} cm/s). After one ORC, a few of the initial defects have become sites for oxidation and the start of EGO formation, with accompanying lattice damage. These sites are apparently much more than $(Dt)^{1/2}$ apart, but there still are many in the 50 μm × 200 μm Raman sampling area. The normal Raman and to a greater extent the SERS spectra exhibit a finite D/E_{2g} ratio due to symmetry breakdown near defects. The average defect density is too low to have an observable effect on the major cyclic voltammetric peaks because the surface is still predominately basal plane. As ECP progresses, more damage sites are created and existing ones grow, thus increasing the D/E_{2g} ratio. Simultaneously, the high k° voltammetric peak increases in size with further ORC. As the density of oxidation sites increases, the distance between them decreases below $(Dt)^{1/2}$, and ΔE_p for the major voltammetric couple decreases. The data do not permit quantitative conclusions about defect size and spacing, except to say that $(Dt)^{1/2}$ is about 8 μm at the scan rate used (10 V/s) and the defect spacing must progress from values much larger than $(Dt)^{1/2}$ to much smaller during the first through fourth cycles.

A final example of the SERS technique for examining ECP is shown in Figures 11–13. Figure 11 shows the progression of SERS spectra during Ag deposition on a GC electrode following ECP in 0.1 M H_2SO_4. Spectrum d is similar to Figure 5 and shows the familiar disordered spectrum. Figure 12 is the same experiment, except the ECP was conducted in 1 M KOH. The spectra of base-treated GC are much weaker but better defined than the acid spectra. Spectra following acid ECP were consistently at least an order of magnitude stronger than the base spectra and always had greater line width. Some insight into the difference is provided by the SEM of Figure 13. The Ag particles formed on the base-treated GC are similar to those on polished GC,[17] with most having diameters of ~400 Å. When Ag deposition was carried out after ECP in acidic or neutral solutions, however, complex fractal structures were observed, indicating quite different growth dynamics.

Several reports in the literature note that dopamine adsorption is much lower when ECP is conducted in base or if an acid-treated surface is washed with base.[29,30] Anjo

(29) Beilby, A.; Carlsson, A. *J. Electroanal. Chem. Interfacial Electrochem.* **1988**, *248*, 283.

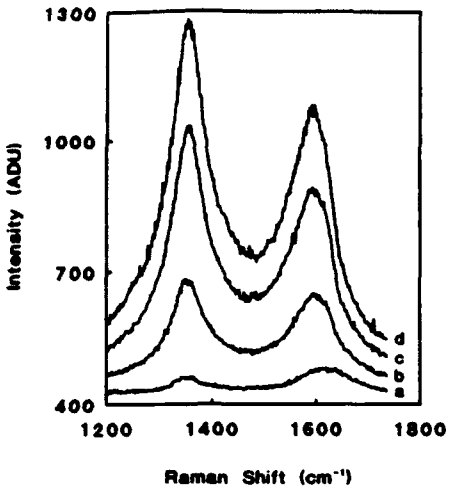

Figure 12. Same as Figure 11, but ECP was carried out in 1 M KOH.

et al., conclude that DA (a cation) is absorbed by the EGO film and that the film is largely removed by base.[30] The SERS results support this hypothesis and are consistent with a process where the GC is oxidized in base but does not form a stable film. Thus the SERS from a base-treated GC electrode is similar to that of a polished surface. However, the stable EGO film formed in acid can ion exchange with Ag^+, thus preconcentrating the Ag^+ in the film. Upon reduction, the Ag forms the complex particles in Figure 13, which apparently promote strong SERS because of their dendritic shape. Thus the difference between the acid- and base-treated GC surface is the stability of the EGO film.

Taken as a whole, the SERS and electrochemical results for ECP surfaces provide several useful insights. First, ECP of any of the carbon materials examined (HOPG, PG, and GC) leads to EGO films which are indistinguishable by SERS. Second, the Raman spectra of the films still exhibit the usual *D* and E_{2g} bands observed for all sp^2 carbon lattice, but the bands are significantly broader than

(30) Anjo, D. M.; Kahr, M.; Khodabakhsh, M. M.; Nowinski, S.; Wenger, M. *Anal. Chem.* **1989**, *61*, 2603.

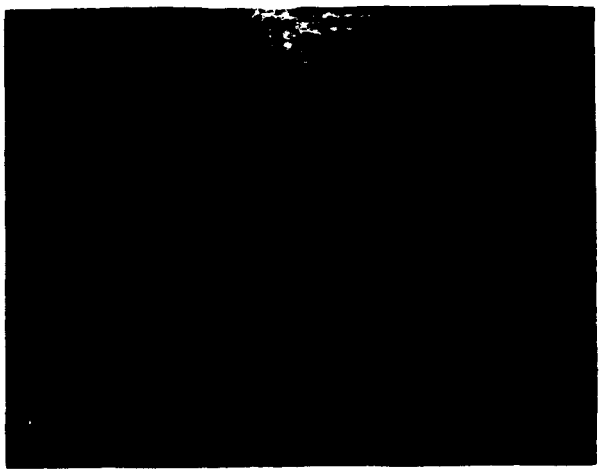

Figure 13. SEM of GC following Ag deposition (0.12 μmol/cm²) after ECP (eight ORC's from −0.1 to +1.85 V) in 1 M H_2SO_4.

usual. Apparently the film contains graphite fragments with small L_a, perhaps formed during oxidative disruption of the carbon surface. This conclusion was also reached following EGO film characterization.[15] Third, treatment with base removes the EGO film formed on GC, with return of the usual GC Raman bands. Fourth, ECP of HOPG proceeds by nucleation and growth, with the oxidation causing localized damage to the graphite lattice. The damaged regions are initially widely spaced compared to $(Dt)^{1/2}$, and the spatial heterogeneity is revealed with both voltammetry and the Raman microprobe. The damaged sites have a high D/E_{2g} ratio and large k° for $Fe(CN)_6^{3-/4-}$. As oxidation proceeds, the damage regions grow together and the spatial heterogeneity vanishes. Fifth, oxidative damage to the graphite planes is accompanied by delamination, and possibly intercalation.

Acknowledgment. This work was supported primarily by the Analytical and Surface Chemistry Division of The National Science Foundation. Laser activation techniques were developed under a grant from the Air Force Office of Scientific Research.

Registry No. C, 7440-44-0; Ag, 7440-22-4; KNO_3, 7758-09-0; KCl, 7447-40-7; graphite, 7782-42-5; ferricyanide, 13408-62-3; ferrocyanide, 13408-63-4.

Reprinted from Analytical Chemistry, 1992, 64.

Adsorption of Catechols on Fractured Glassy Carbon Electrode Surfaces

Christie D. Allred and Richard L. McCreery*

Department of Chemistry, The Ohio State University, 120 West 18th Avenue, Columbus, Ohio 43210

Glassy carbon surfaces exposed by fracturing a glassy carbon rod in the electrolyte solution exhibit fast electron transfer kinetics compared to conventionally polished surfaces, implying that glassy carbon is inherently active toward electron transfer before any intentional surface modification. The adsorption of dopamine and related compounds was examined on fractured glassy carbon surfaces and compared to polished or electrochemically pretreated (ECP) surfaces. While the catechols and ascorbic acid had the anticipated fast electron transfer on fractured glassy carbon, their adsorption behavior differed substantially from that reported for polished, ECP, or vapor-deposited carbon. Dopamine, 4-methylcatechol (4-MC), and dihydroxyphenylacetic acid (DOPAC) adsorbed to similar degrees on fractured glassy carbon, with no apparent discrimination on the basis of adsorbate charge. If the surface was partially oxidized, however, cationic dopamine was preferentially adsorbed over anionic DOPAC or neutral 4-MC. The results support an adsorption mechanism on fractured glassy carbon which is not charge specific and probably involves the catechol ring rather than the side chain. The implications of this finding to the analytical utility of carbon electrodes are discussed.

INTRODUCTION

Pretreatment of glassy carbon (GC) surfaces is a necessary practice for producing electrodes with reproducible characteristics. Although pretreatment provides improved electron transfer capabilities or selectivity for certain sample components, it can also modify the electrode surface in essentially unknown ways. Electrode activity is affected by factors such as chemi- and physisorbed species, microscopic surface area, polishing debris, and active sites such as graphitic edge plane or oxygen-containing functional groups. The changes in these variables with pretreatment along with the assortment of pretreatment procedures utilized make it difficult to define the electrode surface structure for a given experiment. If the goal is a better understanding of the relationship between the GC surface structure and its electrochemical reactivity, it is important to reproduce and characterize the surface structure as much as possible.

Pretreatment procedures generally involve polishing under a variety of conditions, in many cases followed by activation by heat treatment under vacuum or inert atmosphere, laser irradiation, or electrochemical pretreatment procedures (ECP).[1] By comparison of polished surfaces with activated surfaces, several requirements for rapid electron transfer have been proposed. A concern about this approach, however, is that the polished surface which serves as a starting point is not well-defined. Polished surfaces are characterized by polishing debris, loose carbon particles, and various levels of impurities and surface oxides.[2-5] Activation by heat treatment and laser ablation of polished GC surfaces is believed to occur through a cleaning mechanism which exposes or creates active sites on the bulk carbon.[5-11] Activation by electrochemical pretreatment also cleans the surface, but with oxidation of the carbon to an extent depending on the strength of the electrochemical treatment.[12-16] Functional groups generated at the carbon surface during ECP may promote electron transfer by participating in a proton-exchange mechanism, causing electrostatic interactions with redox centers, acting as catalytic sites for adsorption or electron transfer, or decreasing the hydrophobicity of the carbon surface.[17-21] The most pronounced effects of ECP seem to be on complex, multistep redox systems which involve proton transfer or adsorption effects.

The objective of the research discussed here is to clarify the effects of activation procedures and to define better the characteristics of an active carbon surface. For this purpose, the practice of fracturing a glassy carbon rod in solution has been adopted. In this procedure, the surface utilized has had no exposure to polishing abrasives and limited exposure to environmental factors such as oxygen or impurities. Because of its relatively short history, this surface provides a unique starting point where the GC substrate has been modified as little as possible. In this report, catechol voltammetry and adsorption on the fractured surface are discussed. The fractured carbon surface exhibits electron transfer and adsorption behavior significantly different from that which has been observed on polished or pretreated carbon surfaces.

EXPERIMENTAL SECTION

Electrodes used for fracturing were constructured by diamond sawing pieces of GC-20 from a plate (Tokai). These pieces were sanded to yield a post with a cross-sectional area of approximately 0.003–0.006 cm^2. The use of small electrodes for fracturing has been addressed in a previous publication,[10] and it was concluded that small electrode areas are necessary to avoid microcracking during the fracturing process. After sanding, the carbon piece was sonicated in acetone to remove cutting oils and excess carbon particles, then embedded in an epoxy (Eccobond 55, Emerson and Cuming, Inc.), which was cured at 60 °C for 24 h. The epoxy provided mechanical stability and a good seal but also minimized electrode surface contamination compared to other encapsulation materials. The issue of surface fouling is addressed in more detail below. Chronoamperometry was performed after fracturing to obtain the electrode area. To perform chronoamperometry the rod was sanded to a smooth surface, polished conventionally (1.0-, 0.3-, 0.05-μm alumina on polishing cloth), and then placed in a cell with 1 mM $K_4Fe(CN)_6$ in 1 M KCl. The potential was stepped to 0.6 V vs Ag/AgCl and held for 10 s. Chronoamperometry was also performed in 1 M KCl so that curves used for area calculations were always background subtracted. Chronoamperometric areas obtained on polished and fractured surfaces showed good agreement. The fracturing procedure involved filing away the epoxy to expose a protruding tip of approximately 2–3 mm. The GC was scored with a glass-cutting file at the epoxy/GC junction to define a preferential plane for fracturing. The electrode was inserted into the electrochemical cell using Teflon tape as a seal. This cell was flushed a number of times and filled with the analyte solution, and the electrode was fractured by impact from the side, exposing the GC surface. Electrochemical experiments were performed immediately after fracturing and monitored over time. The cell was completed with a Ag/AgCl (3 M NaCl) reference electrode and a platinum auxiliary electrode. For experiments on polished surfaces, Eccobond mounted GC-20 electrodes were sanded with 600-grit silicon carbide paper, polished successively

* Author to whom correspondence should be addressed.

0003-2700/92/0364-0444$03.00/0

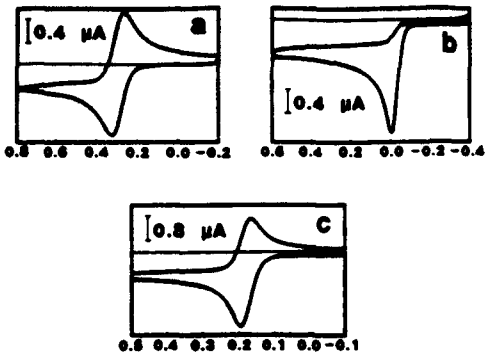

Figure 1. Voltammetry of systems on fractured GC-20. Ferrocyanide in 1 M KCl, ΔE_p = 59 mV, background subtracted (a), ascorbic acid in phosphate buffer pH 7.0, E_p = 0.0 V (b), dopamine in phosphate buffer pH 7.0, ΔE_p = 28 mV (c). Concentrations are approximately 1 mM; ν = 0.1 V/s; potentials vs Ag/AgCl.

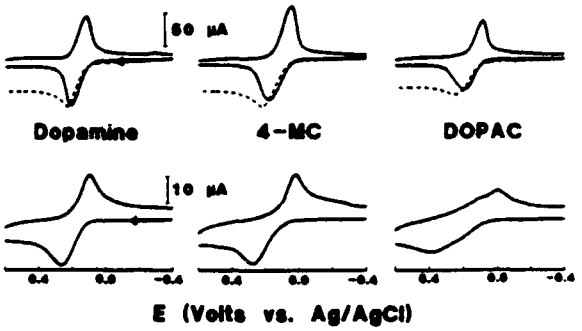

Figure 2. Top: Voltammetry of catechols on fractured GC-20 with associated semiintegrals, not background subtracted; ΔE_p values are DA = 90 mV, 4-MC = 136 mV, DOPAC = 109 mV. Dashed lines are semiintegrals of oxidation scan. Bottom: Catechols on polished GC-20; ΔE_p values are DA = 178 mV, 4-MC = 255 mV, DOPAC = 412 mV. Concentrations are approximately 1 mM; ν = 10 V/s; electrode area for all trials is approximately 0.003 cm²; supporting electrolyte is phosphate buffer pH 7.0.

with 1-, 0.3-, and 0.05-μm alumina, and finally sonicated. All electrochemical experiments were interfaced to a PC and controlled by a locally written program. Linear cyclic voltammetry wave forms were provided by a function generator (Tektronix) which was triggered with a pulse provided by a Labmaster A/D board (Scientific Solutions). A conventional three-electrode potentiostat (Advanced Idea Mechanics, Columbus, OH) was utilized with the RC filter value dictated by $RC\nu < 4$ mV.[22]

Determination of surface coverage Γ (mol/cm²) of catechols was performed by integrating the peak area of cyclic voltammograms plotted on a time axis to obtain charge (Q), and taking $\Gamma = Q/nFA$ where $n = 2$ and A is the chronoamperometric area of the fractured region. Semiintegrals were calculated with the G1 algorithm of Oldham as in previous publications.[23] Capacitance measurements were performed with a 20-mV amplitude input triangular wave, centered on 0.0 V vs Ag/AgCl. The square wave output peak to peak current is proportional to the observed capacitance ($C^o(\mu F/cm^2) = i_{p-p}/2\nu A$) where A = chronoamperometric area.[24,25] Dopamine, 4-methylcatechol, 3,4-dihydroxyphenylacetic acid (DOPAC), and ascorbic acid were obtained from Aldrich. $K_4Fe(CN)_6$ was obtained from Mallinckrodt. The various stock solutions were prepared with 70% $HClO_4$ from GFS Chemicals and mono- and dibasic potassium phosphate from Fisher Scientific and Mallinckrodt. All solutions were prepared daily with Nanopure water, with those at pH 7 prepared immediately before use. Solutions were degassed with argon or nitrogen for approximately 15 min before use.

RESULTS

The hypothesis driving this investigation is that the electrochemical behavior of the fractured surface reflects the bulk GC structure more accurately than polished or otherwise pretreated GC. Previous reports on electrochemistry at fractured GC-30 involved an investigation of electron-transfer rates and capacitance.[10,26] Figure 1 contains representative voltammograms of the benchmark systems $Fe(CN)_6^{3-/4-}$, dopamine (DA) and ascorbic acid (AA) on fractured GC-20. The ΔE_p values and E_p values obtained here are characteristic of fast electron transfer and confirm the results shown in previous publications. It is significant that these three redox systems exhibit fast electron transfer on the fractured surface without any pretreatment, implying that the bulk GC structure is inherently active for charge transfer. A subsequent investigation of adsorption on the fractured surface was performed, and these results constitute the bulk of the observations discussed here.

Dopamine adsorption has been observed frequently at surfaces which have been electrochemically pretreated.[27-33] Adsorption is believed to occur through electrostatic attraction and/or ion exchange between the negatively charged surface oxide layer and the positively charged DA amine group.[27,30,32] This interaction greatly enhances the sensitivity of DA relative to anions such as ascorbate and dihydroxyphenylacetic acid (DOPAC) and is the basis of several in vivo analyses. Because the fractured surface is presumably initially free of oxid functionalities, its adsorption properties may differ substar tially from those of pretreated surfaces. The scan rate used here was 10 V/s to enhance current due to adsorbed species. The results are shown in Figure 2, contrasted with thos obtained at a polished surface. The voltammetry obtaine at the fractured surface exhibited a sharper peak characteristic of adsorbed species, and semiintegration also showed nonsigmoidal behavior indicative of adsorption.[23] The voltan mogram on the fractured surface persisted even after r placement of the dopamine solution with background electrolyte. All indications showed that dopamine adsorptio occurred on the fractured surface immediately after th fracturing process. These results were unexpected based o an electrostatic mechanism. In order to investigate this discrepancy further, 4-methylcatechol (4-MC) and DOPA were also examined. These systems were chosen because their similarity to dopamine in all aspects except side-cha structure and charge. 4-MC and DOPAC possess neutral and negative charges respectively at pH 7, while dopamine is monocation. Voltammetry of these systems at the fractur surface is shown in Figure 2 with voltammetry at polished surfaces for comparison. Cyclic voltammetry and semiintegration at the fractured surface for 4-MC and DOPAC bo indicate that significant amounts of adsorption occurred f these compounds as well as for dopamine. Adsorption through electrostatic interactions with surface oxides on the fractured surface (if present) is not likely since there is no obvio discrimination based on side-chain charge. In addition, t ΔE_p values obtained at the fractured surface for the three compounds are approximately equal while those at the polished surface show a definite trend based on charge (DA 4-MC < DOPAC). The voltammetry obtained at the fractur surface is therefore significantly different from that at the polished surface and is distinct from other reported activat surfaces as well.

Further quantitation of the extent of catechol adsorpti was achieved by reducing the analyte concentration to approximately 10 μM so that current due to diffusing spec was reduced. These results are shown in Figure 3. Volta mograms were obtained as a function of time after fracturi and those shown are for maximum adsorption of the species of interest. The time of maximum adsorption varied pending on the analyte but ranged from 3 to 7 min af fracturing. Almost no Faradaic current was observable a these low concentrations on a polished surface, nor was any of the current in Figure 3 attributable to diffusing spec

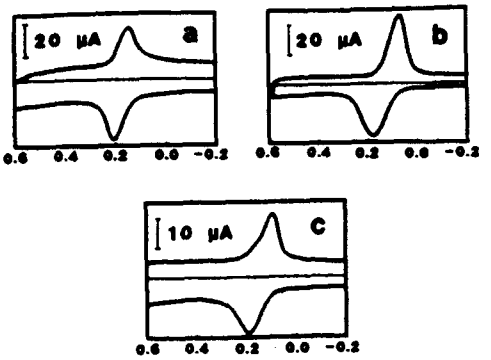

Figure 3. Voltammetry of catechols on fractured GC-20. Dopamine (a), 4-methylcatechol (b), DOPAC (c). Concentrations are 10 μM; ν = 10 V/s; supporting electrolyte is phosphate buffer pH 7.0; potential vs Ag/AgCl.

Table I. Adsorption on GC Surfaces (ν = 10 V/s, C^{bulk} = 10 μM)

	Γ,[a] pmol/cm²	
	pH 7.0	pH 0.8
fractured		
DA	156 ± 42[b] (N = 12)	312 ± 92 (N = 10)
4-MC	312 ± 64 (N = 8)	324 ± 66 (N = 5)
DOPAC	133 ± 44 (N = 10)	280 ± 40 (N = 5)
AA	<15 (N = 3)	42 ± 20 (N = 3)
fractured + ECP[d]		
DA	303 ± 30 (N = 3)	
4-MC	312 (N = 2)	
DOPAC	66 (N = 2)	
fractured + ECP[c]		
DA	493 ± 121 (N = 4)	447 (N = 2)
4-MC	296 (N = 2)	
DOPAC	59 ± 23 (N = 3)	
polished		
DA	9 ± 5 (N = 7)	29 ± 19 (N = 6)
polished + ECP[c]		
DA	503 ± 66 (N = 3)	352 (N = 2)

[a] Based on chronoamperometric area. [b] Standard deviation. [c] ECP conditions: 25 cyclic potential scans 0–1.8 V vs Ag/AgCl, in 0.1 M KNO_3. [d] ECP conditions: Same as c, but in pH 7.0 phosphate buffer.

Table I summarizes Γ (pmol/cm²) values obtained by integrating voltammograms for 10 μM solutions at acidic and neutral pH. At 10 μM concentration and pH 7.0, the largest amount of adsorption observed is for 4-MC, with less observed for DA and DOPAC. At pH 0.8, the differences are less significant, but all three compounds exhibited higher Γ. A specific mechanism of adsorption is not apparent from this data; however, some qualitative observations are evident. At GC surfaces prepared by polishing or ECP, electron transfer and adsorption activity have been observed to vary with the charge of the analyte.[27,30,31,32] At fractured surfaces, significant adsorption occurs for components regardless of their charge, with no preference for cations or anions. This behavior is not indicative of adsorption occurring through an electrostatic mechanism.

An example of how adsorption differs for fractured, polished, and ECP surfaces is shown in Figure 4. Dopamine adsorption at 10 μM concentration is barely observable on polished surfaces, but is prominent for fractured and ECP surfaces. ECP of a fractured surface causes an increase in both dopamine adsorption and background current. Table I summarizes Γ values for ECP treatment.

A factor of some importance in determining the extent of adsorption at the fractured surface is variation of Γ with time after fracture. Peak areas for 10 μM concentrations increased

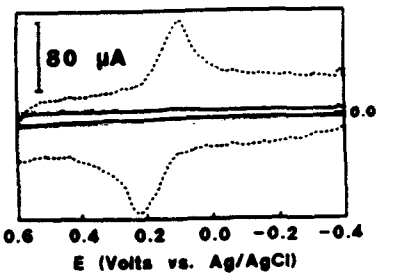

Figure 4. Dopamine voltammetry on polished (solid line), Γ = 11 pmol/cm²; fractured (dotted line), Γ = 178 pmol/cm²; and ECP (dashed line), Γ = 546 pmol/cm² surfaces. ECP procedure is 25 cyclic potential scans, 0–1.8 V vs Ag/AgCl in 0.1 M KNO_3. DA concentration is 10 μM; supporting electrolyte is phosphate buffer pH 7.0; ν = 10 V/s.

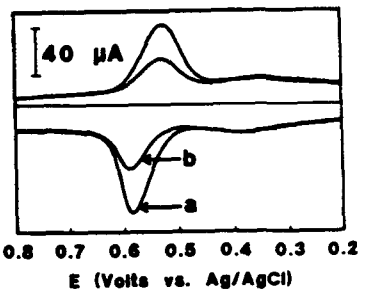

Figure 5. Voltammetry of dopamine on fractured GC-20, 10 μM in 0.1 M $HClO_4$. ν = 10 V/s, before addition of 1,4-dimethoxybenzene (a), immediately after addition of 10 μM 1,4-dimethoxybenzene (b).

for several minutes after the fracturing procedure, reached a constant value for some time, and then slowly decreased. The increase following fracture is at least partly attributable to finite diffusion time at low concentration. If only diffusion-controlled mass transport were operative, a monolayer would require about 6 min to adsorb for 10 μM bulk concentration.[1] The subsequent decrease in charge may be due to competition for adsorption sites by impurities which displace the adsorbed analyte. The effect of impurity competition is pronounced, perhaps due to the weak nature of the analyte adsorption. Initial experiments were performed on electrodes which had been encapsulated in Torr-seal (Varian) epoxy. Voltammetry of 1 mM solutions obtained at such electrodes immediately after fracturing was well-defined and displayed both low peak separations and peak shapes characteristic of adsorption. After a few minutes, however, a large decrease in peak height and a large increase in peak separation were observed. For 10 μM concentrations the adsorption was not even apparent at the Torr-seal electrodes because the time necessary to achieve sufficient analyte adsorption also allowed extensive competition by Torr-seal derived impurities. Obviously care must be taken to minimize impurities, and the epoxy used to fabricate the electrode appears to be a principle source of contamination. The Eccobond epoxy used in this study also contaminates the solution to some extent, though its effects are not as severe as those of Torr-seal. However, interpretation of quantitative results must be qualified accordingly. Modeling of the contamination process was attempted by introducing 1,4-dimethoxybenzene to the analyte solution, with the results shown in Figure 5. With the introduction of 1,4-dimethoxybenzene, the charge due to analyte adsorption did decrease significantly, indicating that the analyte species was displaced from the electrode surface. Although dimethoxybenzene is only a model for adventitious solution impurities, it does demonstrate that catechol adsorption is fairly weak and easily displaced by competitive adsorption of other solution species. Stated differently, catechol adsorption requires a quite clean surface.

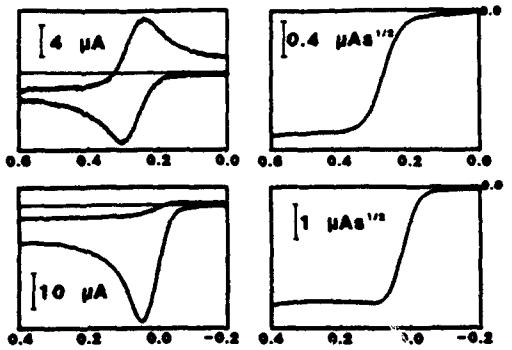

Figure 6. Voltammetry (upper left) of ferrocyanide (ΔE_p = 60 mV) on fractured GC-20 with associated semiintegral (upper right), 1 mM in 1 M KCl, ν = 10 V/s, ascorbic acid on fractured GC-20 (E_p = 0.05 V) (lower left) with associated semiintegral (lower right) 1 mM in phosphate buffer pH 7.0, ν = 10 V/s. CV's are background subtracted. Potentials vs Ag/AgCl.

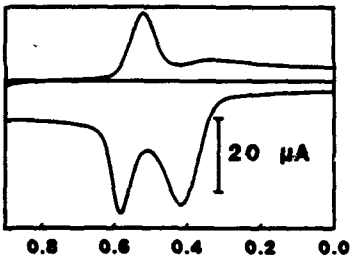

Figure 7. Voltammetry of 1 mM ascorbic acid + 10 μM dopamine on fractured GC-20 in 0.1 M $HClO_4$, ν = 10 V/s. Dopamine ΔE_p = 66 mV, ascorbic acid E_p = 416 mV; potential vs Ag/AgCl.

Since fracturing of glassy materials can lead to microcracking, there is a possibility that the apparent adsorption behavior is due to electrolysis of analyte in cracks. To test this possibility, ascorbate and $Fe(CN)_6^{3-/4-}$ were examined on fractured GC. Figure 6 contains voltammetry and corresponding semiintegrals for $K_4Fe(CN)_6$ and ascorbic acid at pH 7. No indication of adsorption in either the voltammetry or the semiintegrals was observed for $Fe(CN)_6^{3-/4-}$ under any of the conditions employed. For AA, no indication of adsorption on the fractured surface was apparent at pH 7, but weak adsorption was evident in 0.1 M $HClO_4$ for 1 mM AA. No voltammetric signal was observed for 10 μM AA under any conditions. These experiments were performed a number of times through the course of research, but at no time was adsorption at the level observed for the catechols ever observed for AA. A number of other factors also indicate that the voltammetric behavior of catechols is induced by adsorption and not microcracking. Figure 7 shows voltammetry at a fractured surface in a mixture of 1 mM ascorbic acid and 10 μM dopamine. The peak areas are similar for the two components even though the ascorbate is present at a much higher concentration. The behavior shown in Figure 7 persists for about 3–5 min, after which the AA peak broadens, ΔE_p for DA increases, and i_p for DA decreases, apparently due to impurity adsorption from solution. These results indicate preconcentration of the dopamine due to its adsorption at the electrode surface. In addition, capacitance measurements performed at the fractured surface result in almost model square wave behavior in response to an imposed triangle wave potential. If microcracking had occurred, some rounding of the square wave would be expected due to the presence of large RC components at the electrode surface microcracks.

DISCUSSION

The results bear on two distinct questions about GC surface reactivity. First, does the fractured face of GC more greatly reflect the bulk GC properties than a polished or ECP surface? Second, does the adsorption behavior of the fractured su... differ from that of treated GC surfaces? Regarding the fir... question, current results confirm earlier observations ... polishing or ECP substantially alter the GC structure. ... Raman spectra and observed k° for a polished surface ... quite different from the results for a fractured face, with th... Raman spectrum indicating greater disorder on the poli... surface.[10] For all systems studied, electron-transfer kin... are faster on the fractured surface, an effect attributed ... greater surface cleanliness. Furthermore, the k° value for th... fractured face is as high or higher than the highest value ... polished or laser activated surfaces, implying that fract... GC is inherently rich in active sites for electron transfer. Sin... a fractured surface must have initially unsatisfied valence ... it cannot be identical to bulk GC. However, we conclude ... the modification of the bulk structure is minimized for ... turing compared to polishing or laser activation. Th... agreement of theoretical and observed voltammograms ar... the lack of $Fe(CN)_6^{3-/4-}$ or ascorbate adsorption on the ... tured surface indicate nearly ideal behavior with high ele... transfer activity.

The adsorption behavior for DA, 4-MC, and DOPAC on ... varies dramatically depending on how the surface is prep... This behavior is most easily considered for three case... fractured, polished, and electrochemically pretreated GC. Th... fractured surface exhibits classical adsorption at low ... concentration (10 μM) for DA, 4-MC, and DOPAC, but ... ligible adsorption for $Fe(CN)_6^{3-/4-}$ or ascorbic acid. Fu... thermore, the adsorption was independent of the charge ... the adsorbate, although adsorption was significantly hi... in acidic media. Soriaga and Hubbard[34] reported Γ for 4 ... on Pt electrodes to be 267 pmol/cm² for flat orientation ar... 525 pmol/cm² for edge orientation for monolayer adsorptio... Roughness factors for fractured GC are approximately 2–... so the adsorption of catechols is somewhat less than a ... olayer. When the analyte concentration was increased to ... mM, diffusing material was observed on top of a stron... sponse for adsorbed species.

On the polished surface, the electron-transfer kinetics ... creased significantly and adsorption was not observable f... 10 μM concentrations. Even at 1 mM, adsorption appe... weak, but was stronger for DA than for 4-MC or DOP... When a fractured surface underwent ECP in either nitra... or phosphate solution, adsorption for DA *increased* by 2 ... 3 times, 4-MC changed little, and DOPAC *decreased*. Si... ilarly, ECP of a polished surface greatly increased Γ for ... by a factor of approximately 50 (Table I). Thus both th... polished and ECP surfaces exhibited adsorption which di... criminated for adsorbate charge, with the ECP surface ... more pronounced in both magnitude and degree of dis... nation. Thus the adsorption behaviors on polished and EC... surfaces are qualitatively similar but are clearly distinct fro... that on the fractured surface.

The observations are consistent with a qualitatively dis... adsorption mechanism for the fractured surface compared ... polished or ECP surfaces. If adsorption to the fractured ... face occurred through the aromatic catechol ring, it would ... be charge specific and would not occur for ascorbate or ... $(CN)_6^{3-/4-}$. Furthermore, the clean, active fractured surfa... would yield fast electron transfer. When the surface is ... ished, both the adsorption and k°'s are decreased, appar... due to impurity adsorption. Upon ECP, adsorption strongly favors cations, implying an electrostatic mechanism. As note... by several other authors,[28-33] the preference for DA ... ascorbate or DOPAC on the ECP surface is likely due ... ion exchange mechanism, probably at carboxylate groups ... the oxide film. It should be noted that although DA yield... a larger voltammetric response than AA for both fract...

and ECP surfaces due to selective adsorption, the adsorption mechanism for the two surfaces is fundamentally different. The current results are relevant to the area of voltammetric bioanalysis of catechols, particularly in small-animal tissue. In such experiments, a carbon fiber microelectrode is used to detect catechols in the presence of ascorbate after pretreatment by polishing[30-31] or ECP.[27,28,36,37] If the approach is to be successful, the electrode must discriminate heavily for DA over DOPAC or ascorbate, since DA is usually a minority component. The work reported here demonstrates that a fractured and presumably unmodified carbon surface will discriminate for catechols over ascorbate but not for DA over DOPAC. In contrast, a lightly polished carbon fiber microdisk does discriminate for DA over DOPAC,[31] implying that a charge-specific mechanism is operative. This observation implies that the surface of carbon fiber electrodes used thus far for in vivo analysis are partially oxidized, often unintentionally.

ACKNOWLEDGMENT

We thank Nicholas Pontikos for useful discussions and H. Ping Wu for assistance with electrode fabrication. This work was supported by the Air Force Office of Scientific Research, and by an ACS Analytical Division Fellowship to CDA sponsored by Eli Lilly and Company.

REFERENCES

(1) McCreery, R. L. In *Electroanalytical Chemistry*; Bard, A. J., Ed.; Dekker: New York, 1991; Vol. 17.
(2) Fagan, D. T.; Hu, I.; Kuwana, T. *Anal. Chem.* **1985**, *57*, 2759.
(3) Hu, I.; Karweik, D. H.; Kuwana, T. *J. Electroanal. Chem. Interfacial Electrochem.* **1985**, *188*, 59.
(4) Kamau, G. N.; Willis, W. S.; Rusling, J. F. *Anal. Chem.* **1985**, *57*, 545.
(5) Kazee, B.; Weisshaar, D. E.; Kuwana, T. *Anal. Chem.* **1985**, *57*, 2736.
(6) Stutts, K. J.; Kovach, P. M.; Kuhr, W. G.; Wightman, R. M. *Anal. Chem.* **1983**, *55*, 1632.
(7) Wightman, R. M.; Deakin, M. R.; Kovach, P. M.; Kuhr, W. G.; Stutts, K. J. *J. Electrochem. Soc.* **1984**, *131*, 1578.
(8) Poon, M.; McCreery, R. L. *Anal. Chem.* **1986**, *58*, 2745.
(9) Poon, M.; McCreery, R. L.; Engstrom, R. *Anal. Chem.* **1988**, *60*, 1725.
(10) Rice, R. J.; Pontikos, N. M.; McCreery, R. L. *J. Am. Chem. Soc.* **1990**, *112*, 4617.
(11) Strein, T. G.; Ewing, A. G. *Anal. Chem.* **1991**, *63*, 194.
(12) Engstrom, R. C. *Anal. Chem.* **1982**, *54*, 2310.
(13) Engstrom, R. C.; Strasser, V. A. *Anal. Chem.* **1984**, *56*, 136.
(14) Kepley, L. J.; Bard, A. J. *Anal. Chem.* **1988**, *60*, 1459.
(15) Bowling, R. J.; Packard, R. T.; McCreery, R. L. *Langmuir* **1989**, *5*, 683.
(16) Xie, Y.; Sherwood, P. M. *Appl. Spec.* **1990**, *44*, 1621.
(17) Cabaniss, G. E.; et al. *J. Am. Chem. Soc.* **1985**, *107*, 1845.
(18) Deakin, M. R.; Kovach, P. M.; Stutts, K. J.; Wightman, R. M. *Anal. Chem.* **1986**, *58*, 1474.
(19) Nagaoka, T.; Yoshino, T. *Anal. Chem.* **1986**, *58*, 1037.
(20) Bellby, A. L.; Carlsson, A. *J. Electroanal. Chem. Interfacial Electrochem.* **1988**, *248*, 283.
(21) Nagaoka, T.; et al. *Anal. Chem.* **1988**, *60*, 2766.
(22) Howell, J. O.; Kuhr, W. G.; Ensman, R. E.; Wightman, R. M. *J. Electroanal. Chem. Interfacial Electrochem.* **1986**, *209*, 77.
(23) Bowling, R. J.; McCreery, R. L. *Anal. Chem.* **1988**, *60*, 605.
(24) Gileadi, E.; Tehamikovski, N. *Electrochim. Acta* **1971**, *16*, 579.
(25) Babai, M.; Tehamikovski, N.; Gileadi, E. *J. Electrochem. Soc.* **1972**, *119*,
(26) Rice, R.; Allred, C.; McCreery, R. *J. Electroanal. Chem. Interfacial Electrochem.* **1989**, *263*, 163.
(27) Gonon, F. G.; Fombarlet, C. M.; Buda, M. J.; Pujol, J. F. *Anal. Chem.* **1981**, *53*, 1386.
(28) Falat, L.; Cheng, H. Y. *Anal. Chem.* **1982**, *54*, 2111.
(29) Sujaritvanichpong, S.; Aoki, K.; Tokuda, K.; Matsuda, H. *J. Electroanal. Chem. Interfacial Electrochem.* **1986**, *198*, 195.
(30) Michael, A. C.; Justice, J. B. *Anal. Chem.* **1987**, *59*, 405.
(31) Baur, J. E.; Kristensen, E. W.; May, L. J.; Wiedemann, D. J.; Wightman, R. M. *Anal. Chem.* **1988**, *60*, 1268.
(32) Saraceno, R. A.; Ewing, A. G. *Anal. Chem.* **1988**, *60*, 2016.
(33) Anjo, D. M.; Kahr, M.; Khodaishkah, M. M.; Nowinski, S.; Wanger, M. *Anal. Chem.* **1989**, *61*, 2603.
(34) Sortega, M. P.; Hubbard, A. T. *J. Am. Chem. Soc.* **1982**, *104*, 2735.
(35) Pontikos, N.; McCreery, R. L. *J. Electroanal. Chem. Interfacial Electrochem.*, in press.
(36) Gerhardt, G.; Adams, R. N. *Anal. Chem.* **1982**, *54*, 2618.
(37) Nagy, G.; Gerhardt, G.; Oke, A.; Rice, M. E.; Adams, R. N.; Moore, R. B.; Szentirmay, M. *J. Electroanal. Chem. Interfacial Electrochem.* **1985**, *188*, 85.

RECEIVED for review July 25, 1991. Accepted November 6, 1991.

Reprinted from The Journal of Physical Chemistry, 1992, 96.

Anthraquinonedisulfonate Adsorption, Electron-Transfer Kinetics, and Capacitance on Ordered Graphite Electrodes: The Important Role of Surface Defects

Mark T. McDermott, Kristin Knetea, and Richard L. McCreery*

Department of Chemistry, The Ohio State University, 120 W. 18th Avenue, Columbus, Ohio 43210
(Received: October 3, 1991; In Final Form: December 12, 1991)

The adsorption of anthraquinone-2,6-disulfonate, disodium salt (AQDS), was found to be well behaved at glassy carbon (GC) and highly oriented pyrolytic graphite (HOPG) electrodes. On laser-activated GC, the surface excess obeys a Langmuirian isotherm in the concentration range of 5×10^{-6} to 1×10^{-5} M with a saturation coverage of 228 pmol/cm^2. AQDS at untreated HOPG electrodes was studied more extensively. Adsorption at basal plane HOPG was discovered to occur solely on edge plane defects. Defects on basal plane HOPG can be created adventitiously in the cleaving process or can be controlled by laser irradiation at varying power densities. The amount of AQDS adsorbed correlates with laser power density. Surface excess on HOPG also obeys a Langmuir isotherm with the saturation coverage depending on the defect density. On conventionally cleaved HOPG surfaces, the amount of AQDS adsorption correlates with other electrochemical parameters, the magnitudes of which are known to depend on edge plane density. These parameters are the heterogeneous electron-transfer rate constant of the ferri/ferrocyanide redox couple and differential capacitance. A new low differential capacitance of less than 1.0 μF/cm^2 has also been observed on near-perfect basal plane HOPG. The unusual ferrocyanide voltammograms observed on low-defect HOPG are consistent with a potential-dependent transfer coefficient.

Introduction

The widespread use of carbon electrodes in energy conversion, electrosynthesis, and electroanalysis has stimulated a wide variety of research on the relationship between carbon structure and electrochemical behavior.[1,2] While it is recognized that carbon microstructure, surface oxides, and adsorbed films will affect electrode kinetics, capacitance, etc., these structural variables are often difficult to control. Several reports from our group[3-6] and others[7-12] have identified the importance of basal and edge plane graphite regions to electrochemical behavior, and noted that the distribution of edge and basal sites on a carbon surface varies greatly for different carbon substrates and surface preparations. The difficult problem of relating surface structure to electrochemical behavior is significantly simplified by examining a nearly ideal surface, namely, the basal plane of highly ordered pyrolytic graphite (HOPG). The basal plane has a known distribution of carbon atoms and provides a single-crystal analogue of more disordered carbon materials. The purpose of this paper is to characterize the basal plane surface of nearly perfect HOPG and to examine its electrochemical properties.

HOPG is a highly anisotropic material, exhibiting quite different properties on its basal and edge planes. Physical properties of HOPG, such as resistivity, thermal conductivity, thermal expansion, and Young's modulus, display anisotropy with sometimes large differences between the in-plane (a-axis) and out-of-plane (c-axis) directions.[2] Raman spectroscopy of HOPG also depends on this anisotropy, with the ratio of 1360-cm^{-1}/1582-cm^{-1} band intensities correlating with graphitic edge plane density.[4,5] Our group and others have reported anisotropy in the double-layer capacitance (C°)[3,6,7-10] and heterogeneous electron-transfer rate constant (k°)[3,5,6,11,12] for some benchmark redox systems, with both C° and k° being higher for edge vs basal plane HOPG. The density of edge plane sites on HOPG can be increased greatly by illumination with energetic laser pulses, apparently by thermomechanical shock induced by rapid thermal expansion.[3,4,6] We showed that k° of $Fe(CN)_6^{3-/4-}$ correlated with C° for laser-irradiated HOPG, implying that both are related to laser-generated edge plane.[6] Adventitious edge plane defects resulting from the cleaving of HOPG are known to be sites for other phenomena. Eklund et al.[13] have reported intercalation of HSO_4^- through the basal plane of HOPG. They concluded that the intercalant enters through grain boundaries and/or accidental defects on the surface. Damage caused by electrochemical oxidation of basal plane HOPG has been shown by Raman spectroscopy,[4,5] scanning electron microscopy (SEM),[4] and scanning tunneling microscopy (STM) to initiate on edge defects.[14] Chang and Bard observed that defects on freshly exposed basal plane occurred at a density of 0.1–13 μm^{-2} for various samples of HOPG.[15] Snyder et al.[16] used STM to observe polymers preferentially nucleating at step sites on basal plane HOPG. Recently, we have shown that adventitious defects on HOPG electrodes affect electrochemical parameters in ways similar to those created intentionally. A more defective surface as observed by STM exhibits a higher k° for ferri/ferrocyanide and a larger C°.[3] Accidental edge plane defects cause considerable statistical variation in the measurement of these two parameters. The results also indicate strong adsorption of anthraquinone-2,6-disulfonate (AQDS) to edge plane sites and weak adsorption to basal plane. All of these phenomena indicated the importance of edge plane defects to HOPG behavior.

The pronounced anisotropy of HOPG leads to several serious problems when examining electrochemical variables on carbon electrodes. First, capacitance, k°, and adsorption often vary greatly with the proportions of edge and basal plane on the exposed surface, as has been noted previously in some detail.[3,6,17] Thus GC exhibits faster kinetics than HOPG basal plane because of its higher edge plane density. Second, supposedly ordered HOPG

* Author to whom correspondence should be addressed.

(1) Kinoshita, K. *Carbon: Electrochemical and Physicochemical Properties*; Wiley: New York, 1988.
(2) McCreery, R. L. In *Electroanalytical Chemistry*; Bard, A., Ed.; Dekker: New York, 1991; Vol. 17.
(3) Robinson, R. R.; Sternitzke, K.; McDermott, M. T.; McCreery, R. L. *J. Electrochem. Soc.* **1991**, *138*, 2454.
(4) Bowling R.; Packard, R.; McCreery, R. L. *J. Am. Chem. Soc.* **1989**, *111*, 1217.
(5) Bowling R.; Packard, R. T.; McCreery, R. L. *Langmuir* **1989**, *5*, 683.
(6) Rice, R. J.; McCreery, R. L. *Anal. Chem.* **1989**, *61*, 1637.
(7) Morcos, I.; Yeager, E. *Electrochim. Acta* **1970**, *15*, 953.
(8) Randin, J. P.; Yeager, E. *J. Electroanal. Chem.* **1972**, *36*, 257.
(9) Randin, J. P.; Yeager, E. *J. Electrochem. Soc.* **1971**, *118*, 711.
(10) Randin, J. P.; Yeager, E. *J. Electroanal. Chem.* **1975**, *58*, 313.
(11) Wightman, R. M.; Paik E. C.; Borman, S.; Dayton, M. A. *Anal. Chem.* **1978**, *50*, 1410.
(12) Wightman, R. M.; Deakin, M. R.; Kovach, P. M.; Kuhr, P. M.; Stutts, K. J. *J. Electrochem. Soc.* **1984**, *131*, 1578.
(13) Eklund, P. C.; Oik, C. H.; Holler, F. J.; Spolar, J. G.; Arakawa, E. T. *J. Mater Res.* **1986**, *1* (2), 361.
(14) Gewirth, A. A.; Bard, A. J. *J. Phys. Chem.* **1988**, *92*, 5563.
(15) Chang, H.; Bard, A. J. *J. Am. Chem. Soc.* **1991**, *113*, 5588.
(16) Snyder, S. R.; White, H. S.; Lopez, S.; Abruna, H. D. *J. Am. Chem. Soc.* **1990**, *112*, 1333.
(17) Rice, R. J.; Pontikos, N. M.; McCreery, R. L. *J. Am. Chem. Soc.* **1990**, *112*, 4618.

0022-3654/92/2096-3124$03.00/0

basal plane surfaces exhibit quite variable electrochemical behavior, depending on the presence of adventitious (or intentional) defects.[3,6] For example, k° may vary significantly with repeated cleavage of HOPG, due to variations in surface defects from cleave to cleave.[3] Third, any measurement of inherent basal plane properties is likely to be contaminated by the effects of edge plane defects, and this problem is severe when the anisotropy is large. For example, when k° is 0.1 cm/s on the edge and 10^{-7} cm/s on basal plane (approximate values for $Fe(CN)_6^{3-/4-}$),[6] even 0.1% of edge plane defects on a basal surface will yield observed "basal" rate constants about 1000 times too large. Thus any attempt to study electrochemical properties of the ordered HOPG basal plane is likely to be frustrated by the effects of a low level of defects. The long-range goal of the effort presented here is observation of basal plane properties which are uncontaminated by the properties of edge plane defects and thus representative of an ordered carbon surface.

The electrochemical behavior of mono- and disulfonated anthraquinones has been the topic of several investigations, and the adsorption of these sulfonated anthraquinones on metals and carbon has been noted previously.[18-20] Soriaga and Hubbard showed that anthraquinone-2,6-disulfonate (AQDS) adsorbs at platinum electrodes in a close-packed, flat orientation.[18] More recently, He et al.[19] demonstrated that AQDS exhibited a well-behaved, reversible adsorption voltammogram on mercury at bulk concentrations below 10^{-5} M. Brown and Anson examined the adsorption of anthraquinone-2-monosulfonate (AQMS) at pyrolytic graphite (PG) electrodes.[20,21]

The approach used here starts with a more detailed examination of AQDS adsorption on edge plane defects. Once AQDS adsorption is established as a useful quantitative marker of defect density, it can be correlated with other defect-dependent electrochemical variables, including capacitance and k° for $Fe(CN)_6^{3-/4-}$. Such correlations are useful not only for establishing the existence of a nearly defect free basal plane surface, but also for determining the electrochemical properties of an ordered graphite electrode surface.

Experimental Section

All solutions were prepared with distilled water purified with a Nanopure water purification system and degassed with argon. Potassium ferrocyanide was used as received from Mallinckrodt Inc., and solutions of 1 mM $K_4Fe(CN)_6$ in 1 M KCl were prepared daily. Disodium AQDS was obtained from Aldrich and recrystallized from water after filtering through activated charcoal.[19] Solutions of AQDS in 0.1 M $HClO_4$ degrade after 2–3 days and were prepared accordingly. All experiments were conducted at 23 ± 2 °C.

For experiments on GC, a Bioanalytical Systems GC-20 electrode embedded in Kel-F was utilized. The GC electrode was conventionally polished before laser activation and GC experiments were performed in a Teflon cell as previously described.[17] HOPG was either purchased from Union Carbide (Parma, OH) or was a gift from Arthur Moore of Union Carbide. HOPG samples are graded by Union Carbide according to the line width of the X-ray diffraction peak, with greater line width corresponding to smaller microcrystallite size along the a-axis. Grades are as follows: ZYA, ≤0.4°; ZYB, 0.8 ± 0.2°; ZYH, 3.5 ± 1.5°. HOPG surfaces were prepared either by peeling with adhesive tape or by cleaving with a razor blade. Surfaces of "pure" basal plane (very low defects) were obtained by cleaving a thick piece (ca. >5 mm along the c-axis) of HOPG with a razor blade. Since cleaving with adhesive tape imposed curvature on the graphite being removed and to a lesser extent on the sample, the resulting mechanical strain appeared to create defects. Cleaving with the razor blade did not cause curvature and led to low-defect surfaces. Laser activation of HOPG was performed in situ with solution present in a cell described previously.[6] All other electrochemical experiments were carried out in an inverted drop cell. The HOPC was peeled or cleaved and fastened to a conductive metal plate with powdered graphite/nujol paste to assure good electrical contact. A drop of solution was then placed on the fresh basal plane surface. A platinum wire auxiliary electrode and a capillary salt bridge containing a Ag/AgCl (3 M NaCl) reference electrode were lowered into the drop to complete the cell. This type of "cell" eliminates factors such as damage to the surface from an O-ring and impurities from the Teflon cell. Because the solution was placed on the electrode within 10–15 s of peeling or cleaving, surface contamination was minimized. Edge plane HOPG electrodes were imbedded in Torr-Seal (Varian) as previously reported.[6]

Adsorption of AQDS was quantified by measuring the baseline-corrected area under the voltammetric reduction wave as described by Brown and Anson.[21] The diffusion wave for AQDS was too small to interfere with measurements of the adsorption peak and was displaced far away on the potential axis.[3] Adsorption was monitored with time until a constant value was observed, with longer times being required for lower AQDS concentrations. AQDS data are reported here as Γ_{obs}, the observed adsorption in picomoles per square centimeter, and Γ_{sat}, the saturated adsorption at high bulk concentration of AQDS, denoted C_{AQDS}. The observed k° for $Fe(CN)_6^{4-/3-}$ ($D = 6.3 \times 10^{-6}$ cm^2/sec) is reported as k°_{obs} and was calculated from ΔE_p via the method of Nicholson in most cases.[22] Where noted, simulations based on a potential-dependent transfer coefficient according to the approach of Corrigan and Evans[23] were used to determine k°_{obs}. Observed differential capacitance, reported as C°_{obs}, was measured with a 20-mV peak-to-peak, 100-Hz triangle wave centered at 0.0 V vs Ag/AgCl using the method developed by Gileadi et al.[24,25] and used by us previously.[3,6,17] All electrode areas used for calculations were measured by chronoamperometry of 1 mM $Fe(CN)_6^{4-}$ on a 5-s time scale. Cyclic voltammetry and laser activation with a Nd:YAG laser operating at 1064 nm were performed as described previously.[3-6,17]

Results

The voltammetry of 10^{-5} M AQDS at a GC electrode laser irradiated with three 25 MW/cm^2 Nd:YAG pulses is shown in Figure 1A. Laser activation of GC at this power density serves to clean the surface of impurities and polishing debris.[17,26] At this low concentration of AQDS, the peak diffusion current should be approximately 0.01 mA/cm^2 and is negligible on the scale of Figure 1A. The peak current in Figure 1A is directly proportional to scan rate for the wave centered at −0.1 V vs Ag/AgCl. Peak width at half-maximum (pwhm) for this wave is 55 mV, and the cathodic/anodic peak separation is 12 mV at 1 V/s and 5 mV at 100 mV/s. For a reversible adsorption wave, the theoretical pwhm is $90.6/n$, where $n = 2$ for AQDS, and the peak separation is zero.[27,28] The data indicate that at low concentrations AQDS is a quasi-reversible surface-bound redox center at GC electrodes.

An adsorption isotherm was obtained for bulk concentrations of AQDS from 5×10^{-8} to 2×10^{-6} M. Curve A in Figure 2 is the surface excess vs bulk concentration plot for AQDS at a GC electrode. This curve is characteristic of a Langmuir isotherm.[27,28] Peak shape, potential, and half-width do not change with concentration. These results imply minimal interaction between surface-bound molecules at low bulk concentrations and provide strong evidence for an adsorbed species adhering to a Langmuir isotherm. It is clear that AQDS is a well-behaved surface-bound species on laser-activated GC at low bulk concentrations.

(18) Soriaga, M. P.; Hubbard, A. T. *J. Am. Chem. Soc.* **1982**, *104*, 2735.
(19) He, P.; Crooks, R. M.; Faulkner, L. R. *J. Phys. Chem.* **1990**, *94*, 1135.
(20) Anson, F. C.; Epstein, B. *J. Electrochem. Soc.* **1968**, 1155.
(21) Brown, A. P.; Anson, F. C. *Anal. Chem.* **1977**, *49*, 1589.
(22) Nicholson, R. S. *Anal. Chem.* **1965**, *37*, 1351.
(23) Corrigan, D. A.; Evans, D. H. *J. Electroanal. Chem.* **1980**, *106*, 287.
(24) Gileadi, E.; Tshernikovski, N. *Electrochim. Acta* **1971**, *16*, 579.
(25) Gileadi, E.; Tshernikovski, N.; Babai, M. *J. Electrochem. Soc.* **1972**, *119*, 1018.
(26) Pontikos, N. M.; McCreery, R. L. *J. Electroanal. Chem.*, in press.
(27) Laviron, E. *J. Electroanal. Chem.* **1982**, *12*, 53.
(28) Bard, A. J.; Faulkner, L. R. *Electrochemical Methods*; Wiley: New York, 1980.

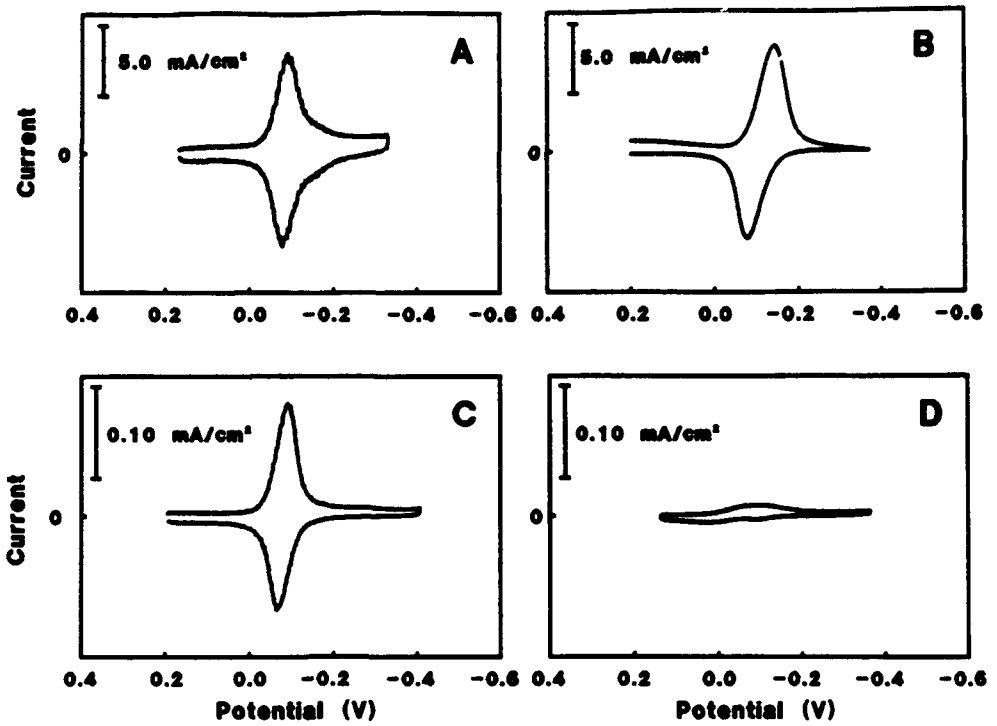

Figure 1. Cyclic voltammetry of 10^{-5} M AQDS at (A) GC electrode activated with three 25 MW/cm² laser pulses; (B) edge plane HOPG; (C) basal plane HOPG with visible defects; (D) basal plane HOPG with few defects. Scan rate = 1 V/s. Potentials are vs Ag/AgCl.

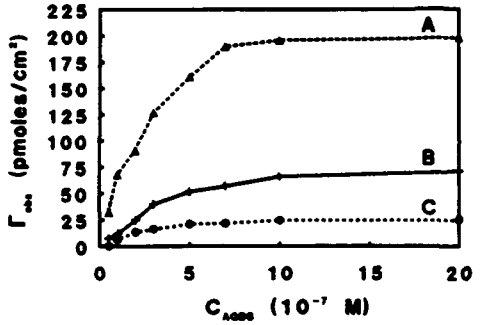

Figure 2. Amount of AQDS adsorbed vs bulk concentration on (A) GC, laser activated at 25 MW/cm²; (B) basal plane HOPG, laser activated at 70 MW/cm²; (C) basal plane HOPG, laser activated at 50 MW/cm². The lines simply connect the points and do not assume any theoretical equation. Adsorption time was at least 20 min.

Parts B–D of Figure 1 were obtained under the same conditions as part A, but with various HOPG surfaces. Voltammogram B is HOPG edge plane (embedded in Torr-Seal), and voltammograms C and D were obtained on two different basal plane surfaces with the inverted drop "cell". Except for current magnitude, the voltammograms in Figure 1 exhibit comparable pwhm and ΔE_p, with the only exception being the slightly larger ΔE_p for HOPG edge plane (possibly due to Torr-Seal contamination). Inspection of the current scales of Figure 1 reveals the effect of edge plane density on the quantity of AQDS adsorbed, since the peak current for an adsorbed species is proportional to the quantity adsorbed. Electrodes rich in edge plane such as GC and edge plane HOPG (Figure 1A,B) yield approximately 50 times greater current than basal plane HOPG with visible defects created in the cleaving process (Figure 1C). The voltammogram of Figure 1D occurred on an HOPG surface which had no visible defects. The absence of a voltammetric wave for AQDS on basal plane indicates either that AQDS does not adsorb on basal plane or that any adsorbed AQDS does not undergo electron transfer to basal plane. In either case, Γ_{obs} increases with greater edge plane density.

Since the voltammograms of Figure 1C,D were obtained on HOPG basal surfaces prepared in the same manner, it is clear that the defect density varies significantly from surface to surface. This conclusion is not surprising, but it does prevent preparation of surfaces with reproducible defect density by conventional cleaving. In order to examine AQDS adsorption on HOPG basal plane more quantitatively, we used laser irradiation to generate reproducibly defective surfaces. In earlier reports, we showed that Nd:YAG laser pulses damaged the HOPG surface at power densities of 45 MW/cm² and higher.[3,6] Furthermore, both capacitance and k°_{obs} for $Fe(CN)_6^{3-/4-}$ increased with increasing laser power, implying a higher density of edge sites. Accordingly, AQDS adsorption was examined on laser-treated HOPG in order to study a more reproducibly damaged surface, with the results shown in Table I. All voltammograms of AQDS on laser-activated HOPG indicated ideal adsorption and were qualitatively very similar to those of Figure 1C. Isotherms for the 50 and 70 MW/cm² cases are shown in Figure 2. While the shapes are comparable to that observed for GC, saturation coverage is lower.

TABLE I: Observed Adsorption of AQDS and k° of $Fe(CN)_6^{3-/4-}$ on Laser-Irradiated Basal Plane HOPG

power density, MW/cm²	Γ_{obs}, pmol/cm²	$k^\circ_{obs}(Fe(CN)_6^{3-/4-})$, cm/s
50	35 (σ = 1.2)	0.042 (σ = 0.0090)
60	44 (σ = 1.1)	0.065 (σ = 0.0092)
70	70 (σ = 1.4)	0.093 (σ = 0.010)
80	82 (σ = 1.7)	0.096 (σ = 0.0046)
90	96 (σ = 2.8)	0.110 (σ = 0.0057)
100	140 (σ = 14)	0.130 (σ = 0.0058)

[a] σ is standard deviation, N = 3 in all cases.

The equation of a Langmuir isotherm can be linearized in the form

$$\frac{C_{AQDS}}{\Gamma_{obs}} = \frac{1}{\Gamma_{sat} b_{AQDS}} + \frac{C_{AQDS}}{\Gamma_{sat}} \qquad (1)$$

where Γ_{obs} is the surface excess of AQDS, Γ_{sat} is the saturation surface excess, b_{AQDS} is the adsorption coefficient of AQDS the on the particular surface, and C_{AQDS} is the bulk concentration. Figure 3 shows the linearized data of Figure 2, and Table II lists the data obtained from the isotherm of AQDS at several electrodes. In the case of HOPG, the saturation coverage is dependent

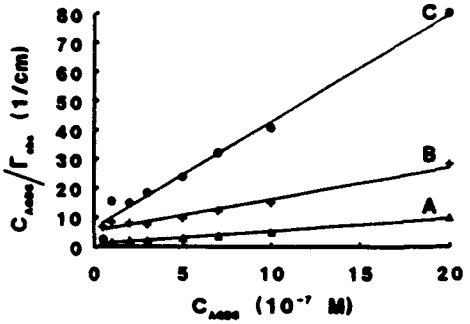

Figure 3. Linearized data from Figure 2. A, B, and C correspond to the same surfaces as in Figure 2. The lines are the least-squares fit to the data, with $r \geq 0.99$ for all lines.

TABLE II: Adsorption Isotherm Results for AQDS[a]

surface	Γ_{obs}, Γ_{sat}, pmol/cm²	b_{AQDS}, cm³/mol	ref
GC, 25 MW/cm²	228	6×10^9	this work
HOPG, 70 MW/cm²	92	2×10^9	this work
HOPG, 50 MW/cm²	28	4×10^9	this work
Hg	94	7×10^9	19
Pt	127[b]		18
PG	140[b]		20

[a] Determined from linearized Langmuir equation as described in text. [b] Not determined from a complete isotherm.

on laser-induced damage. For comparison, saturation coverages for AQDS on other surfaces are also given in Table II. The increase in Γ_{obs} for the series HOPG (basal) < HOPG (laser) < PG < GC is consistent with the increase in disorder and edge plane density for these materials.[2] Although studied in less detail, anthraquinonemonosulfonate and 1,5-AQDS behave quite similarly to AQDS with small differences in Γ due to varying molecular size. The differences in the magnitude of AQDS adsorption on platinum vs mercury have been attributed to a very substantial dissimilarity in surface bonding.[19] On the basis of the approach of Soriaga and Hubbard, the theoretical saturation coverage for AQDS on a flat surface is 132 pmol/cm².[18]

Table I also lists the observed k°_{obs} for $Fe(CN)_6^{3-/4-}$ on laser-treated surfaces, in order to compare with Γ_{obs}. As noted previously, k°_{obs} increases with increasing laser power density above the 45 MW/cm² threshold.[6] The k°_{obs} values observed here follow the same trend as those reported previously,[6] but are consistently higher, probably due to greater cleanliness accompanying irradiation in solution rather than air. In order to make a similar correlation of Γ_{obs} and k°_{obs} on untreated basal plane, it was necessary to measure Γ_{obs} and k°_{obs} on the *same* surface. Thus a voltammogram of $Fe(CN)_6^{3-/4-}$ was acquired on a freshly cleaved surface with the inverted drop "cell", and then the solution was replaced and Γ_{obs} was determined. In addition, C°_{obs} was determined in the $Fe(CN)_6^{3-/4-}$ or AQDS solution. In this way, C°_{obs}, k°_{obs}, and Γ_{obs} were measured on a surface with a given defect density, effectively controlling for variations in defects from surface to surface. The results for 42 basal plane surfaces are listed in Table III, in order of increasing Γ_{obs}. With the exception of the laser-treated surfaces, the Γ, k°_{obs}, and C°_{obs} values listed for a given electrode were determined on the same surface by the inverted-drop approach. Parameters determined on laser-treated surfaces were reproducible from surface to surface, and entries in Table III are averages of three surfaces. Notice that k°_{obs} and C°_{obs} increase monotonically with Γ_{obs}, implying that all three observables are controlled by similar surface effects.

Representative voltammograms obtained with several surfaces exhibiting varying ΔE_p are shown in Figure 4. For $\Delta E_p < 200$ mV, the voltammograms have shapes consistent with conventional Nicholson and Shain theory.[22,29] However, when ΔE_p exceeds 200 mV, distortions from classical behavior are evident, with serious disagreement with theory at ΔE_p of above 300 mV. The scan rate dependence of this distortion is shown in Figure 5 for

TABLE III: Surface Coverage of AQDS, Kinetic Parameters of $Fe(CN)_6^{4-/3-}$, and Differential Capacitance for Basal Plane HOPG

grade/prep.[a]	Γ_{obs}, pmol/cm²	ΔE_p,[b] mV	k°_{obs}, cm/s	C°_{obs}, μF/cm²
U/C	<1.0	1500	8.0×10^{-7}[c]	0.6[d]
U/C	<1.0			0.8[e]
U/C	<1.0			0.9[e]
U/C	<1.0			1.0[e]
U/C	1.0	1020	8.0×10^{-6}[c]	1.4[d]
U/C	1.1	770	6.1×10^{-5}[c]	1.5[d]
U/C	2.1	970	9.2×10^{-6}[c]	1.7[d]
U/C	3.5	740	7.5×10^{-5}[c]	1.5[d]
U/C	8.0			1.8[e]
A/C	11	470	2.8×10^{-6}[c]	
A/C	14	300	0.0014[c]	1.2[d]
A/C	14	130	0.0085	
B/C	24	203	0.0032	2.9[d]
H/C	25	168	0.0049	
B/C	25	165	0.0057	
A/C	26	103	0.015	
A/C	26	95	0.019	
U/C	30	122	0.010	3.1[d]
H/C	34	144	0.0068	3.6[d]
U/L(50)	35	78	0.042	3.4[d]
H/C	38	97	0.018	
H/C	40	122	0.010	
H/C	41	120	0.011	
H/C	41	93	0.020	
U/L(60)	44	84 (5)	0.065	
H/C	45	114	0.012	
H/C	52	100	0.015	
H/C	55	80	0.036	4.2[d]
H/C	56			4.7[e]
H/C	58	106	0.014	5.2[d]
H/C	62			5.3[e]
H/C	64	87	0.025	5.8[d]
H/C	65	83	0.030	
A/C	67	78	0.041	5.8[d]
U/C	69	92	0.021	6.5[d]
U/L(70)	70	79 (5)	0.093	
H/C	73	114	0.012	6.7[d]
U/L(70)	75			8.2[e]
U/L(80)	82	77 (5)	0.096	
H/C	85	85	0.030	
U/L(90)	96	81 (10)	0.110	
U/L(100)	142	76 (10)	0.130	

[a] Grade: U = ungraded; A = ZYA; B = ZYB; H = ZYH. Preparation: C = cleaved; L = laser activated; power density in MW/cm² listed in parentheses. [b] ν = 1.0 V/s unless indicated in parentheses. [c] k°_{obs} calculated by simulation with potential-dependent α; all others from ΔE_p by method of Nicholson. [d] C°_{obs} measured in 1.0 M KCl. [e] C°_{obs} measured in 0.1 M $HClO_4$.

TABLE IV: Voltammetric Results for Single HOPG Basal Surface with Low Defect Density

ν, V/s	ΔE_p, mV	k°_{NS},[a] cm/s	k°_{sim},[b] cm/s	α_0[b]	$d\alpha/dE$[b]
10	1238	4.6×10^{-7}	9.6×10^{-6}	0.50	0.25
5	1132	8.1×10^{-7}	1.1×10^{-5}	0.50	0.27
1	940	2.4×10^{-6}	1.6×10^{-5}	0.49	0.27
0.5	896	2.5×10^{-6}	1.6×10^{-5}	0.50	0.28
0.1	808	2.6×10^{-6}	1.1×10^{-5}	0.50	0.28
0.05	755	3.2×10^{-6}	1.1×10^{-5}	0.51	0.29

[a] Calculated by method of Nicholson,[22] using $D = 6.3 \times 10^{-6}$ cm²/s. [b] Best fit of experimental and simulated voltammograms assuming a potential-dependent α.

ΔE_p = 940 mV (at 1 V/s), and voltammetric results for various scan rates are listed in Table IV. Although there is no doubt that the large ΔE_p indicates slow electron-transfer kinetics, the voltammograms on low-defect surfaces clearly do not exhibit classical behavior.

Discussion

The variations in k°_{obs}, C°_{obs}, and Γ_{obs} for different HOPG basal plane surfaces establish the importance of surface defects in determining electrochemical parameters. AQDS is a useful marker

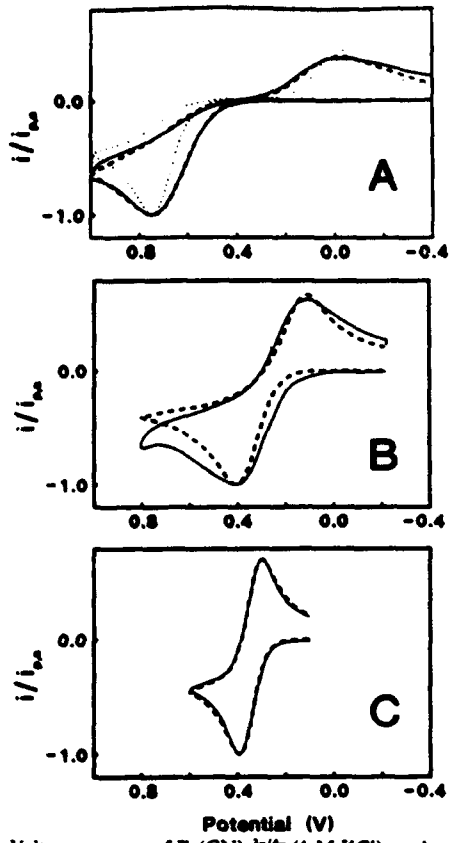

Figure 4. Voltammograms of $Fe(CN)_6^{3-/4-}$ (1 M KCl) on three HOPG basal plane surfaces with different defect density. Solid lines are experimental in all cases. (A) Dashed line, simulated for $k^\circ_{obs} = 6.1 \times 10^{-5}$ cm/s, $\alpha_0 = 0.51$, $d\alpha/dE = 0.30$ V^{-1}; dotted line, simulated for $k^\circ_{obs} = 1.2 \times 10^{-5}$ cm/s, $\alpha = 0.51$, $d\alpha/dE = 0.0$. (B) Dashed line, simulated for $k^\circ_{obs} = 1.4 \times 10^{-3}$ cm s^{-1}, $\alpha_0 = 0.50$, $d\alpha/dE = 0.30$ V^{-1}. (C) Dashed line simulated for $k^\circ_{obs} = 0.018$ cm s^{-1}, $\alpha_0 = 0.50$, $d\alpha/dE = 0.30$. Simulation for $d\alpha/dE = 0.0$ is identical to dashed line. Scan rate = 1.0 V/s in all cases. Potentials are vs Ag/AgCl.

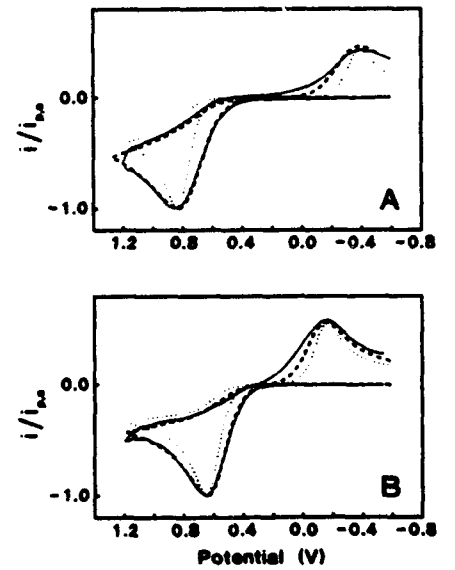

Figure 5. Voltammograms of $Fe(CN)_6^{3-/4-}$ (1 M KCl) on cleaved HOPG at two scan rates on a low defect surface. Solid line is experimental in both cases. (A) 10 V/s; dashed line is simulated for $k^\circ_{obs} = 9.6 \times 10^{-4}$ cm/s, $\alpha_0 = 0.50$, $d\alpha/dE = 0.25$ V^{-1}; dotted line is same, except $k^\circ_{obs} = 4.6 \times 10^{-7}$ cm/s and $d\alpha/dE = 0$. (B) 0.1 V/s, dashed line is simulated for $k^\circ_{obs} = 1.1 \times 10^{-5}$ cm/s, $\alpha_0 = 0.51$, $d\alpha/dE = 0.29$ V^{-1}. Dotted line is simulation for $k^\circ_{obs} = 2.6 \times 10^{-6}$ cm/s, $\alpha_0 = 0.51$, $d\alpha/dE = 0.0$.

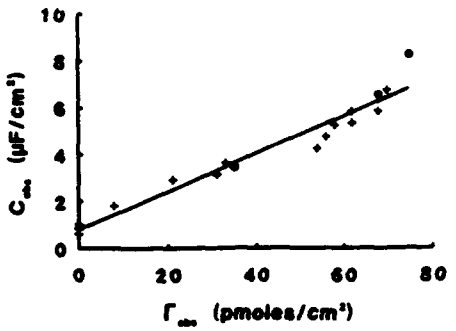

Figure 6. Plot of differential capacitance, C°_{obs}, vs Γ_{obs}. Points are laser surfaces, pluses are cleaved. Line is least-squares fit to all points.

for defect density, with Γ_{obs} ranging from near zero on low-defect basal plane HOPG up to roughly monolayer coverage on GC. Since C°_{obs}, k°_{obs} and Γ_{obs} are all much higher on edge vs basal plane, they should track the edge plane density as indicated by Γ_{obs}. In addition, the observed k°_{obs} should correlate with Γ_{obs}, since both observables depend on edge plane density. In the simplest case, one might propose that the electrode area covered by adsorbed AQDS equals the defect area. However, this proposal is probably oversimplified due to the unkown microscopic details of AQDS adsorption on defects of various size and shape. For now, it is sufficient to conclude that increased Γ_{AQDS} indicates a greater number of edge plane defects. A variety of defects have been reported for HOPG basal plane, including step edges, missing atoms, atomic scale ridges, and fissures.[3,15,29] As stated earlier, Chang and Bard noted a wide variation in defect density observed by STM, ranging from 0.1 to 13 defects/μm^2.[15] In some cases, these defects have been misinterpreted in STM images as adsorbed molecules, such as DNA.[30] In light of the correlation between Γ_{obs} and purposely induced defects (via laser activation or the use of GC), it is very likely that AQDS adsorption occurs on the STM-observable defects on HOPG. Given the strong adsorption of AQDS on Pt, Hg, and pyrolytic graphite reported by others,[18,20] it is not surprising that saturation coverage is achieved on GC and laser-damaged HOPG at bulk concentrations below 10^{-5} M. The 228 pmol/cm^2 [18] saturation coverage for GC is higher than that predicted on the basis of molecular size for flat adsorption (132 pmol/cm^2). Either the AQDS is not lying flat, or the GC surface has a roughness factor of $228/132 \simeq 1.7$. Of course, the roughness will depend on surface preparation, but values for GC ranging from 1.4 to 2.5 have been reported for polished GC following laser activation.[17] While the flat orientation of adsorbed AQDS is not established by the current results, it is the most likely, and the implied roughness factor is within the range expected. In the case of basal plane HOPG, Γ_{AQDS} approaches and exceeds a theoretical monolayer with laser activation.[17,26] As deduced from STM,[3] this indicates both defect formation and roughening by the laser. However, the 10^3–10^5-fold increase in k°_{obs} accompanying laser activation cannot be due soley to roughening, and the major factor in laser activation of HOPG is defect formation.

In order to consider the effect of surface defects more quantitatively, we should first examine the result that Γ_{obs}, C°_{obs} and k°_{obs} for $Fe(CN)_6^{3-/4-}$ all correlate for a series of untreated basal plane surfaces (Table III) and laser-treated basal plane (Table I and ref 6). As noted earlier Γ_{obs}, C°_{obs}, and k°_{obs} all track defect density, and should therefore trace each other. Figure 6 is a plot of C°_{obs} vs Γ_{obs} for both untreated and laser-activated surfaces. Figure 7 shows k°_{obs} vs Γ_{obs}, plotted in log–log format to cover the wide range. Recall that each point on Figures 6 and 7 represents two measurements performed on the *same* surface, largely correcting for unavoidable variation in defect density from surface to surface. The first conclusion from these results is simple but important: the lowest values of C°_{obs}, Γ_{obs}, and k°_{obs} most accurately reflect true basal plane properties. Since even a small

(29) Nicholson, R. S.; Shain, I. *Anal. Chem.* **1964**, *36*, 706.
(30) Clemmer, C. R.; Beebe, T. P. *Science* **1991**, *251*, 640.

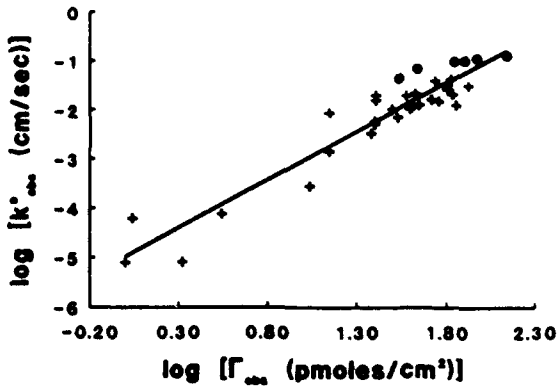

Figure 7. Logarithmic plot of observed adsorption of AQDS, Γ_{obs}, on basal HOPG vs observed heterogeneous electron rate constant, k°_{obs}, of 1 mM $Fe(CN)_6^{4-/3-}$ in 1 M KCl. Pluses indicate cleaved surfaces, points indicate laser treatment. Line is least-squares fit for all points.

defect density can have a large effect on electrochemical observables (particularly k°_{obs}), the true basal plane behavior will be masked by defect behavior unless the defect density is low. In the case of capacitance, C°_{obs} was always below 1.0 $\mu F/cm^2$ when Γ_{obs} was below its detection limit, with the lowest observed value being 0.6 $\mu F/cm^2$. Since the slope of C°_{obs} vs Γ_{obs} is not very steep, the C°_{obs} on a genuinely perfect HOPG surface is not likely to be much lower than 0.6 $\mu F/cm^2$. The best estimate of C°_{obs} for perfect basal plane capacitance is the intercept of the least-squares line in Figure 6, 0.81 $\mu F/cm^2$, with an upper limit of 1.0 $\mu F/cm^2$. This result is lower than that reported by Yeager (3.0 $\mu F/cm^2$),[8-10] due to lower defect density in the present case or to the difference in the method of measurement. The implications of this low capacitance are noted below.

It is not so easy to deduce the true basal plane k° for $Fe(CN)_6^{3-/4-}$, given the much stronger dependence of k°_{obs} on defect density. Variations in Γ_{obs} near the detection limit (< 1.0 pmol/cm²) correspond to large variations in ΔE_p (1020–1500 mV), so it is hard to determine k°_{obs} for a zero-defect surface. Stated differently, even a few ppm of defects (which would be below the detection limit for Γ_{obs}) can significantly increase k°_{obs} so only an upper limit for k°_{obs} on perfect basal plane may be determined. We conclude that perfect basal plane exhibits a ΔE_p of >1500 mV at 1.0 V/s, leading to a k°_{obs} of < 10^{-6} cm/s.

The second observation available from Figures 6 and 7 involves the functional dependence of electrochemical variables on defect density. On the basis of the STM-determined defect density of 0.1–13 μm^{-2}, defects are rarely more than 1 μm apart, and are themselves much less than 1 μm in size.[3,15] At scan rates in the range of 0.1–10 V/s, the defects will behave as a random array of microelectrodes spaced much closer than $(Dt)^{1/2}$. This situation has been considered by Amatore et al.[31] and Armstrong et al.[32,33] for the case of small active sites. In the case of basal plane HOPG, the active sites are not the oxides proposed by Armstrong et al., the unblocked surface assumed by Amatore et al., or the active redox sites proposed by Kuwana et al.[34] for GC, but rather are edge plane defects exhibiting much higher k°_{obs} than the surrounding undamaged basal plane. When the sites are close to each other compared to $(Dt)^{1/2}$, the surface will behave like an ordinary planar microelectrode with a smaller k°_{obs} than that of the active sites. Stated differently, if diffusional cross talk is rapid between active and less active surface regions, the observed k°_{obs} is an average of rate constants for active and less active areas, weighted by surface coverage.[2,31] Even the smallest k° observed here for basal plane HOPG may be due to very small defects spaced closer than $(Dt)^{1/2}$. It is useful to consider a weig average of basal and edge regions for determining electroche observables as a first approximation. Such as assumption lea to eq 2 for capacitance,[6] where f_e is the fractional area of ed

$$C^\circ_{obs} = C^\circ_{basal}(1 - f_e) + C^\circ_{edge} f_e$$

plane present on the surface. For Γ_{obs}, we can assume that Γ basal plane is zero, so

$$\Gamma_{obs} = \Gamma_{sat} f_e$$

Substituting for f_e in eq 2 yields

$$C^\circ_{obs} = C^\circ_{basal}\left(1 - \frac{\Gamma_{obs}}{\Gamma_{sat}}\right) + C^\circ_{edge}\left(\frac{\Gamma_{obs}}{\Gamma_{edge}}\right)$$

or

$$C^\circ_{obs} = C^\circ_{basal} + \frac{\Gamma_{obs}}{\Gamma_{sat}}(C^\circ_{edge} - C^\circ_{basal})$$

Equation 4 predicts linearity for the plot of Figure 6, with intercept equal to C°_{basal}. As noted earlier, the least-squar for all points of Figure 6 yields an intercept of C°_{basal} = $\mu F/cm^2$.

For the case of k°_{obs}, the analogous linear approximation inadequate to explain Figure 7. For laser-activated sur covering a range of Γ_{obs} from 35 to 140 pmol/cm² (Table slope of the log k°_{obs} vs log Γ_{obs} has a slope of 1.2, imply proportionality. However, the slope of the line for all points Figure 7 is 1.9, a value inconsistent with proportionality o and Γ_{obs}. These observations are consistent with a line pendence of C°_{obs}, k°_{obs}, and Γ_{obs} on the fractional coverage edge plane defects on the basal surface for laser-activated surfa but the linear model fails for the near-perfect basal plan

Additional insight into the kinetic behavior of HOPG su is provided by the deviation of voltammogram shape on low-de surfaces from that predicted by conventional Nicholson and Sh theory. As shown in Figure 4, peak widths and relative h differ significantly from conventional theory as ΔE_p increases distortion could originate in several different aspects of the periment. First, it could be caused by some inherent basal pl property which becomes important only at low defect de when edge plane contributions to kinetics are minimize example, Gerisher[35] and Randin and Yeager[7-10] concluded t basal plane HOPG has a low density of states and a low ca citance, with both reaching a minimum at about −0.2 V urated calomel electrode. Either effect could lead to slow k particularly near the potential of zero charge (PZC). Seco the distortion could be caused by a potential-dependent trans coefficient (α) which becomes important as ΔE_p increas For large ΔE_p, the oxidation and reduction are occurring a different potentials, and a nonconstant α is likely. Third, distortion may be caused by some characteristic of the def acting as microelectrodes. For the small and infrequent f present on near-perfect surfaces, the double layer may b planar, and unusual double-layer effects may occur, particul near the PZC.[36]

The distortion occurs for any voltammogram with ΔE_p mV, for which k°_{obs} is < 0.003 cm/s. This k°_{obs} is much than the upper limit for k°_{basal} (10^{-6} cm/s), so a voltammog with ΔE_p = 200–400 mV has negligible contribution from b plane. Thus the distortion is unlikely to be caused by unus plane properties, since distortion occurs when the rate controlled largely by defects. The possibility of a potential pendent α was tested by simulating several voltammograms an α which depended linearly on potential, according to the of Corrigan and Evans.[23] Figure 4A shows a simulated c α_0 = 0.50 and $d\alpha/dE$ = 0.25 V^{-1}, as well as the conventi simulation ($d\alpha/dE$ = 0). For small ΔE_p (<200 mV), inclu

(31) Amatore, J. M.; Saveant, J. M.; Tessier, D. J. *J. Electroanal. Chem.* **1983**, *147*, 39.
(32) Armstrong, F. A.; Bond, A. M.; Hill, A. O.; Psalti, I. S. M.; Zoski, C. G. *J. Phys. Chem.* **1989**, *93*, 6485.
(33) Armstrong, F. A.; Bond, A. M.; Hill, A. O.; Oliver, N.; Psalti, I. S. M. *J. Am. Chem. Soc.* **1989**, *111*, 9185.
(34) Hu, I. F.; Kuwana, T. *Anal. Chem.* **1986**, *58*, 3235.
(35) Gerisher, H. *J. Phys. Chem.* **1985**, *89*, 4249.
(36) Norton, J. D.; White, H. S.; Feldberg, S. W. *J. Phys. Chem.* 1 *94*, 6772.

of $d\alpha/dE$ made little difference to wave shape (Figure 4C), but it did significantly affect curves for $\Delta E_p > 500$ mV. Figure 5 shows experimental and simulation cyclic voltammograms for two scan rates on a low-defect surface, demonstrating a marked effect of nonconstant α on the wave shape. The fits of theory and experiment shown in Figures 4A and 5 and in Table IV are quite good, supporting the conclusion that a potential-dependent α is important when ΔE_p is large. Theory and experiment agree less well for intermediate ΔE_p (Figure 4B), perhaps because the surface is quite defective ($f_s \sim 1$–3%) and irregular. Although these observations do not prove that a potential-dependent α is the sole origin of the distortion from conventional shape, they do indicate that the observations are consistent with a nonconstant α.

Regardless of the details of the shape of the cyclic voltammograms on low-defect surfaces, there is no doubt that the observed kinetics are very slow for $Fe(CN)_6^{3-/4-}$ on the basal plane. We have reported similarly slow kinetics and basal plane for dopamine[4] and solution-phase AQDS.[3] Sufficient data are not yet available to ascertain the generality of slow basal plane kinetics, and until such data are available, it would be risky to speculate an underlying phenomeon causing slow kinetics. The results on AQDS adsorption, capacitance, and $Fe(CN)_6^{3-/4-}$ kinetics reported here establish a means to reduce or eliminate contamination of basal plane behavior by edge plane defects. We are currently studying a wide range of redox systems on low-defect basal plane surfaces, in order to determine the phenomena controlling the electrochemical behavior of the basal plane. The results will be reported separately.

In summary, k°_{obs}, C°_{obs}, and Γ_{obs} for AQDS are controlled largely by defects on basal plane HOPG, and all three observables vary greatly for different surfaces. Although perfect basal plane has a C°_{obs} below 1.0 μF/cm^2, a k°_{obs} for $Fe(CN)_6^{3-/4-}$ below 10^{-6} cm/s, and negligible AQDS adsorption, observed values are usually higher due to adventitious or intentional defects. Since all three phenomena depend on defect density, they correlate with each other provided they are measured on the same plane surface. The voltammetry of $Fe(CN)_6^{3-/4-}$ on partly defective basal plane is consistent with a potential-dependent transfer coefficient, which is a major factor when ΔE_p exceeds about 500 mV at 1 V/s. Finally, the reason for the very slow kinetics of $Fe(CN)_6^{3-/4-}$ on basal plane is not yet clear, but is currently being addressed by studying a variety of redox systems on low-defect basal plane surfaces.

Acknowledgment. This work was supported by the Air Force Office of Scientific Research. We acknowledge Dr. Arthur Moore at Union Carbide for the generous gift of HOPG and Dennis Evans for the simulation software. We also thank Christie Allred for many useful discussions and software for electrochemical experiments.

Reprinted from Analytical Chemistry, 1992, 64.

In Situ Raman Monitoring of Electrochemical Graphite Intercalation and Lattice Damage in Mild Aqueous Acids

Daniel C. Alsmeyer and Richard L. McCreery*

Department of Chemistry, The Ohio State University, 120 West 18th Avenue, Columbus, Ohio 43210

Simultaneous Raman spectroscopy and electrochemical oxidation of highly ordered pyrolytic graphite (HOPG) permitted monitoring of lattice damage and staging. Intercalation of bisulfate in concentrated H_2SO_4 results in well-known Raman spectral changes in the E_{2g} mode at ca. 1600 cm^{-1}. In addition, damage to the sp^2 lattice is revealed by the "D" band at 1360 cm^{-1}, which occurs when graphitic edges are formed. During oxidation of HOPG in 96% H_2SO_4 or 1 M $NaClO_4/CH_3CN$, intercalation was observed but accompanying lattice damage did not occur at the potentials examined. For 1 M H_3PO_4, neither intercalation nor lattice damage was observed at potentials up to 2.0 V vs SSCE. For 1 M H_2SO_4, 1 M $HClO_4$, or 1 M HNO_3, however, intercalation always preceded or accompanied lattice damage. The results are consistent with a mechanism where oxidation results in a graphite intercalation compound (GIC) which oxidizes either water or the graphite itself to produce carbon oxides. The formation of oxides depends on both the thermodynamic stability of the GIC and the kinetics of intercalation, which in turn correlate with the size of the intercalating ion.

INTRODUCTION

The context of this report is established by work in three rather distinct areas. First, the lattice dynamics of graphite and its intercalation compounds have been examined in detail by the solid-state physics community.[1-11] The Raman spectra of highly ordered pyrolytic graphite (HOPG) and related materials are sensitive to intercalation, with changes in the E_{2g} mode at 1582 cm^{-1} being apparent during intercalation of anions, cations, and neutrals. In this context, "staging" refers to the successive insertion of ions or neutrals between graphite layers, such that "stage V" refers to five layers of graphite between each layer of graphite, stage IV to four layers, etc. An E_{2g}' band appears during intercalation at 1610–1640 cm^{-1} depending on intercalant identity and stage, and this phenomenon has been attributed to "boundary layer" graphite planes adjacent to an intercalant layer.[1] The split in the E_{2g} mode upon intercalation arises primarily from changes in symmetry at the boundary layer and secondarily from electronic effects of the intercalant. In some cases, a quantitative measure of the intercalation stage is available from the E_{2g}/E_{2g}' intensity ratio.

A second area of interest is electrochemical intercalation in nonaqueous solutions or strong aqueous acids.[12-20] Stimulated by work on intercalated batteries, graphite has been oxidized and reduced in numerous solvents, notably Li^+/propylene carbonate and >90% H_2SO_4. Two studies are of direct relevance to this report. Maeda et al.[20] monitored Raman spectra of carbon fibers during cyclic voltammetry in 96% H_2SO_4. They found that 0.0–1.4 V potential cycles did not change the "D" (1360-cm^{-1}) and E_{2g} (1582-cm^{-1}) modes of the fibers. However, a potential excursion to +2.3 V increased the "D" intensity, from which they concluded that the graphite lattice was damaged by intercalation. "Lattice damage" is used here to mean breakup of the extended hexagonal sp^2 array of carbon atoms in graphitic planes and does not refer to intercalation per se. The "D" band results from breakdown of the $k = 0$ selection rule when microcrystallite edges are formed in the graphite lattice.[1,2] A more detailed Raman investigation was undertaken by Eklund et al. on HOPG in 96% H_2SO_4.[21] The cell geometry permitted in situ Raman spectra to be obtained either on the immersed HOPG basal plane or on the basal surface just above the H_2SO_4 during constant-current intercalation. The results showed staging with well-defined 1582- and 1620-cm^{-1} Raman modes. Surprisingly, basal surfaces exhibited rapid electrochemical intercalation, implying that intercalating anions enter the basal surface directly, probably through defects such as cracks, grain boundaries, or step edges. The expected route through edges did not appear operative, in fact lateral migration of HSO_4^- appeared quite slow under the conditions employed. Nishitani et al.[22] monitored changes in the E_{2g} modes observed with spatially resolved Raman spectroscopy for the case where only the *a*-face (i.e. edge plane) of the HOPG was in contact with H_2SO_4. The spatial boundary of Raman spectral changes progressed away from the H_2SO_4 surface as intercalation occurred, at a rate which depended on imposed current density. In contrast to Eklund's conclusions, Nishitani's conditions permitted observation of intercalant diffusion along the *a*-axis.

The third background area of relevance is the large literature on electrochemical pretreatment (ECP) of carbon

* To whom correspondence should be addressed.

(1) Dresselhaus, M. S.; Dresselhaus, G. *Adv. Phys.* **1981**, *30*, 139.
(2) Nemanich, R. J.; Lucovsky, G.; Solin, S. A. *Mater. Sci. Eng.* **1977**, *31*, 157.
(3) Solin, S. A. *Graphite Intercalation Compounds I: Structure and Dynamics*; Springer Verlag: Berlin, 1990; pp 157–219.
(4) Nicklow, R.; Wakabayashi, N.; Smith, H. G. *Phys. Rev. B* **1972**, *5*, 4951.
(5) Al-Jishi, R.; Dresselhaus, G. *Phys. Rev. B* **1982**, *26*, 4514.
(6) Elman, B. S.; Dresselhaus, M. S.; Dresselhaus, G.; Maby, E. W.; Mazurek, H. *Phys. Rev. B* **1981**, *24*, 1027.
(7) Lespade, P.; Al-Jishi, R.; Dresselhaus, M. S. *Carbon* **1982**, *20*, 427.
(8) Nemanich, R. J.; Lucovsky, G.; Solin, S. A. *Solid State Commun.* **1977**, *23*, 117.
(9) Vidano, R. P.; Fischbach, D. B.; Willis, L. J.; Loehr, T. M. *Solid State Commun.* **1981**, *39*, 341.
(10) Nakamizo, M.; Tamai, K. *Carbon* **1984**, *22*, 197.
(11) Ekhund, P. C.; Mahan, G. D.; Spolar, J. G.; Zhang, Z. M.; Arakawa, E. T.; Hoffman, D. M. *Phys. Rev. B* **1988**, *37*, 691.
(12) Besenhard, J. O.; Fritz, H. P. *Agnew. Chem., Int. Ed. Engl.* **1983**, *22*, 950.
(13) Kinoshita, K. *Carbon: Electrochemical and Physical Properties*; Wiley: New York, 1988; pp 427–432.
(14) Maeda, Y. *J. Electrochem. Soc.* **1990**, *137*, 3047.
(15) Inagaki, M. *J. Mater. Res.* **1989**, *4*, 1560.
(16) Besenhard, J.; et al. *Synth. Met.* **1983**, *7*, 185.
(17) Fong, R.; VanSacken, U.; Dahn, J. R. *J. Electrochem. Soc.* **1990**, *137*, 2009.
(18) Beck, F.; Krohn, H. *Synth. Met.* **1983**, *7*, 193.
(19) Inagaki, M.; Iwashita, N.; Kouno, E. *Carbon* **1990**, *28*, 49.
(20) Maeda, Y.; Okamoto, Y.; Inogaki, M. *J. Electrochem. Soc.* **1985**, *132*, 2369.
(21) Eklund, P. C.; Olk, C. H.; Holler, F. J.; Spolar, J. G.; Arakawa, E. T. *J. Mater. Res.* **1986**, *1*, 361.
(22) Nishitani, R.; Sasaki, Y.; Nishina, Y. *Synth. Met.* **1989**, *34*, 315.

0003-2700/92/0364-1528$03.00/0

electrodes in milder aqueous media, particularly in the range from pH 0 to 7.[23-34] The bulk of electroanalytical applications of carbon electrodes occur in this pH range, as well as the many examinations of heterogeneous electron transfer and electrochemically initiated homogeneous reactions studied on carbon. As noted by Besenhard in an excellent review,[12] the role of intercalation during ECP of carbon in mildly acidic or neutral solutions is not clear, due to the formation of graphite oxides. The redox potential of graphite intercalation compounds (GIC's) is higher than that for O_2 or CO_2 formation in water, so the GIC is thermodynamically unstable in mild aqueous acids. The result is the formation of the ill-defined electrogenerated graphitic oxide (EGO). Parallel to numerous studies of intercalation, ECP has been used extensively to modify GC and HOPG surfaces, usually for the purpose of electron-transfer activation. Since ECP often leads to large increases in k^0 for many systems,[23,30,35] an understanding of ECP mechanisms may lead to conclusions about what controls k^0 at carbon surfaces. Engstrom et al.[23,24] characterized the GC surface following ECP and concluded that surface contaminants were removed by ECP and that the surface becomes hydrophilic. Kepley and Bard[30] used interferometry and elemental analysis to deduce that the film had an approximately 1.5 ratio of oxygen to carbon and that it formed at a rate of about 45 Å per potential sweep (0–1.80 V) in 0.1 M H_2SO_4. Our group used Raman spectroscopy to conclude that ECP of HOPG in mild acid caused breakup of the graphite lattice, and the edges formed are responsible for the increase in electron-transfer rate accompanying ECP.[35,36]

The work reported here was undertaken to complement the numerous electrochemical studies of ECP in mild acid. By simultaneously monitoring Raman spectra and oxidation current during electrochemical pretreatment, we sought to reveal microstructural changes accompanying the electrochemical effects of ECP. Of particular interest are the effects of anion identity in mild aqueous acids.

EXPERIMENTAL SECTION

A diagram of the experimental apparatus is shown in Figure 1. The electrochemical measurements were all performed with a PAR 173 potentiostat which was interfaced with a PC compatible computer (PC). The custom software allowed extremely slow cyclic voltammograms (ca. 1 mV/min). Slow cyclics were achieved by performing a series of small potential steps, to yield the desired average sweep rate. A standard three-electrode system was employed for the electrochemical measurements. The cell was designed so that the platinum-plate auxiliary and the sodium saturated calomel electrodes (SSCE) were separated from the working electrode by a glass frit. The working electrode was a piece of HOPG with the approximate dimensions of 2 mm × 2 mm × 0.1 mm. The mass of this electrode was obtained prior to any electrochemical modification. This small electrode was held in place by two pieces of platinum plate which were fused in a fashion such that they formed a clamp to hold the electrode. The working electrode was inserted into the glass cell such that the impinging laser beam could enter the cell and excite the basal plane region of the exposed HOPG while the scattered radiation was collected and focused on the spectrograph entrance slit. Both basal and edge surfaces of the HOPG sample were exposed to the solution.

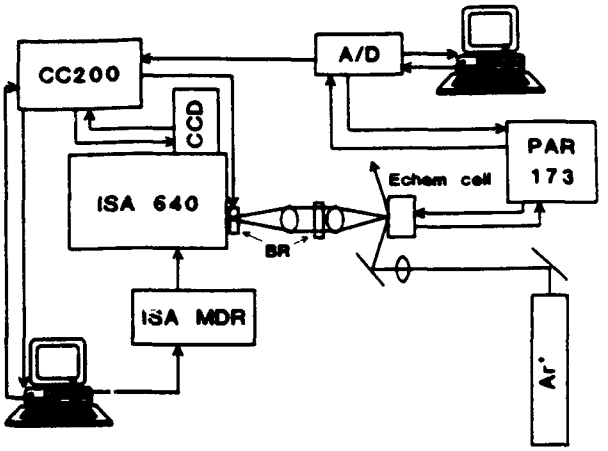

Figure 1. Schematic of experimental apparatus. Abbreviations: CC200, CCD detector; PAR, Princeton Applied Research potentiostat; BR, band reject filter; MDR, motor controller; A/D, computer interface and digitizer.

Raman measurements were performed on an Instruments SA 640 single monochromator equipped with a 300 line/mm grating operating in second order with a Photometrics PM512 charge-coupled device (CCD) detector.[37] The CCD was interfaced to a second PC to control spectral acquisition and store spectra. Dielectric band reject interference filters[37] were placed near the entrance slit and collimating lens to reject the Rayleigh scattered light. An argon ion laser operating at 514.5 nm was used to illuminate the sample with approximately 100 mW of laser power at the laser head. The CCD detector was cooled with liquid nitrogen to −110 °C. The CCD was exposed to the scattered light for integration times varying from 100 to 600 s. The Raman shifts were calibrated using a neon bulb before each set of measurements. The software permitted automatic spectral acquisition at any point in a potential scan or step via a trigger from the electrochemical PC to the CCD computer. Thus the spectral and current vs potential results could be obtained automatically and simultaneously.

RESULTS

Raman spectral changes accompanying intercalation in concentrated H_2SO_4 were observed initially, in order to characterize a well-behaved system and to provide baseline data in the absence of carbon oxide formation. A slow-scan cyclic voltammogram for HOPG in 96% H_2SO_4 is shown in Figure 2, with the potential axis unfolded for clarity. The large oxidation peak at ca. 1.2 V vs SSCE is the stage II to stage I transition, while the current in the 0.6–0.9-V potential range is composed of overlapping peaks for stage V to stage II transitions. The electrochemical results are similar to those reported by Besenhard et al.[12] At positive potentials the HOPG sample expanded and turned blue due to intercalation of HSO_4^- and accompanying H_2SO_4. Since this process has been reported in detail in the literature, only the Raman results will be discussed further here.

Figure 3 shows Raman spectra of the E_{2g} region obtained at various points in the oxidation scan of Figure 2. When the potential remained below 1.5 V, no D band at 1360 cm^{-1} was apparent at any time. Raman shifts are also plotted in Figure 2 for the E_{2g} and E_{2g}' bands. Note that the "boundary layer" mode at ca. 1620 cm^{-1} is clearly visible next to the E_{2g} mode for the potential range from 0.658 to 0.762 V vs SSCE. At

(23) Engstrom, R. C.; Strasser, V. A. *Anal. Chem.* **1984**, *56*, 136.
(24) Engstrom, R. C. *Anal. Chem.* **1982**, *54*, 2310.
(25) Kovach, P. M.; Deakin, M. R.; Wightman, R. M. *J. Phys. Chem.* **1986**, *90*, 4612.
(26) Wang, J.; Hutchins, L. O. *Anal. Chim. Acta* **1985**, *167*, 325.
(27) Cabaniss, G. E.; Diamantis, A. A.; Murphy, W. R., Jr.; Linton, R. W.; Meyer, T. J. *J. Am. Chem. Soc.* **1985**, *107*, 1845.
(28) Palat, L.; Cheng, H. Y. *J. Electroanal. Chem. Interfacial Electrochem.* **1988**, *157*, 393.
(29) Gonon, F. G.; Fombarlet, C. M.; Buda, M. J.; Pujol, J. F. *Anal. Chem.* **1981**, *53*, 1386.
(30) Kepley, L. J.; Bard, A. J. *Anal. Chem.* **1988**, *60*, 1459.
(31) Gewirth, A. A.; Bard, A. J. *J. Phys. Chem.* **1988**, *92*, 5563.
(32) Bowling, R. J.; Packard, R. T.; McCreery, R. L. *Langmuir* **1989**, *5*, 683.
(33) McCreery, R. L. In *Electroanalytical Chemistry*; Bard, A. J., Ed.; Dekker: New York, 1991; Vol. 17, pp 221–374.
(34) Nagaoka, T.; Yoshihino, T. *Anal. Chem.* **1986**, *58*, 1953.
(35) Bowling, R.; Packard, R.; McCreery, R. L. *J. Am. Chem. Soc.* **1989**, *111*, 1217.
(36) Alameyer, Y. W.; McCreery, R. L. *Langmuir* **1991**, *7*, 2270.
(37) Alameyer, Y. W.; McCreery, R. L. *Anal. Chem.* **1991**, *63*, 1289

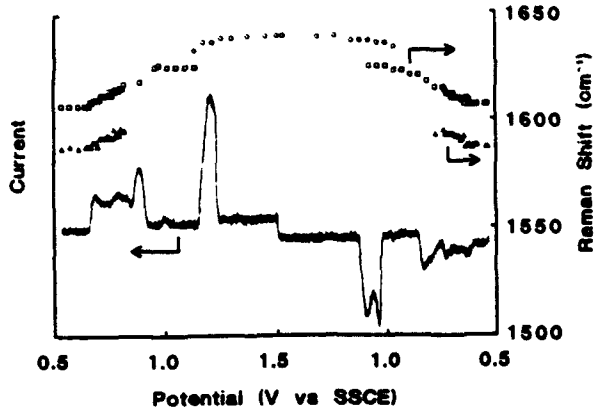

Figure 2. Current and Raman shifts during intercalation of HOPG in 96% H_2SO_4. The scan rate was 1 mV/min. Triangles indicate the E_{2g} band, squares and circles indicate E_{2g}'. Note scan reversal at 1.5 V.

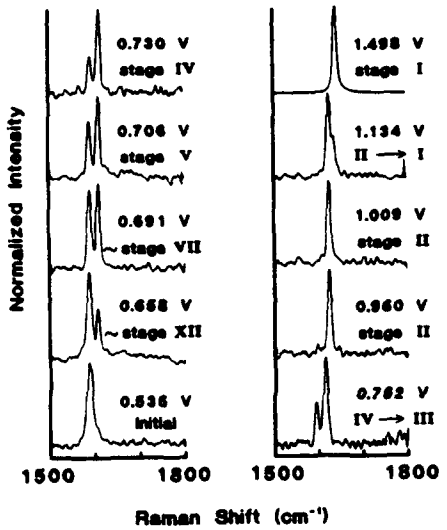

Figure 3. Raman spectra of E_{2g} region acquired during voltammetric scan from Figure 2. Stage numbers were deduced from the E_{2g}/E_{2g}' ratio (Figure 4). Intensities were normalized to maximum values for each spectrum.

0.960 and 1.009 V, only stage II is present (two graphite layers alternating with one intercalant layer), so every graphite layer is a boundary layer and only one peak is observed. A further increase in Raman shift occurs in the transition from stage II to I. Plots of Raman shift vs the inverse of the stage number are linear for both the E_{2g} and E_{2g}' bands, as noted by Dresselhaus and others.[1,3] Figure 4 shows that ratio of the E_{2g} and E_{2g}' bands is linear with stage number, as would be expected if E_{2g}' is derived from boundary layers. Although the slope of this line depends on relative cross sections for E_{2g} and E_{2g}' scattering, smaller values of the ratio indicate higher stage number. The spectra of Figure 3 were normalized to permit easy comparison, but the absolute intensity of the spectra increased during intercalation by a factor of 25 from the initial E_{2g} intensity to the final E_{2g}' intensity. As noted by Maeda et al.[20] and Eklund et al.,[21] oxidation of HOPG or carbon fibers above 1.5 V leads to lattice damage indicated by the "D" band.

While concentrated H_2SO_4 electrolyte leads to well-behaved intercalation, it is not very relevant to electroanalytical and ECP experiments. A series of 1 M aqueous electrolytes was examined with both voltammetry and Raman spectroscopy to consider intercalation under milder conditions. The choice of electrolyte was dictated in part by resistance to oxidation. For example, Cl^- is oxidized at potentials lower than that required for intercalation, so HCl and KCl were not studied.

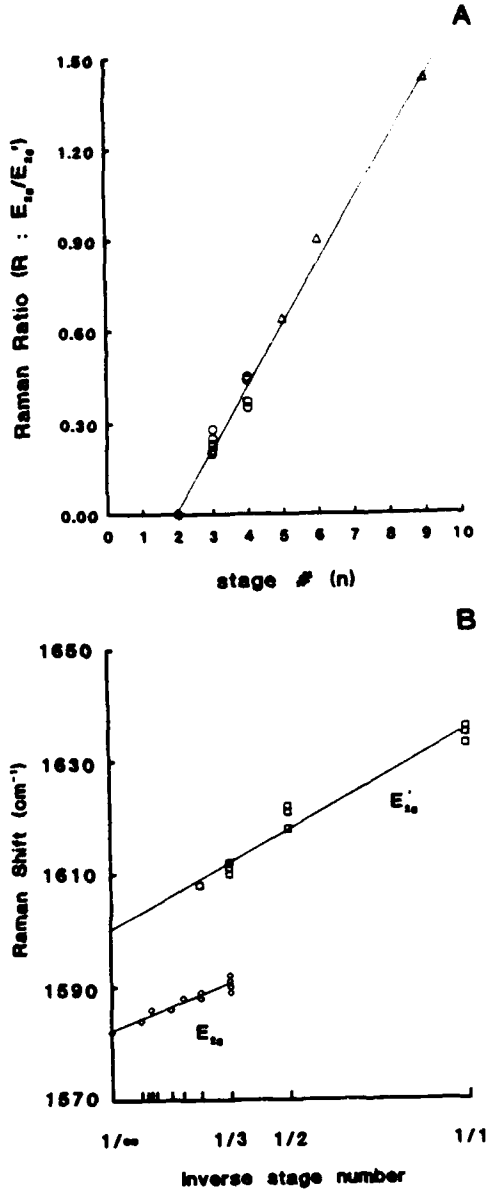

Figure 4. (A) E_{2g}/E_{2g}' integrated Raman intensity ratio vs stage number deduced from voltammetry and charge/mass ratio. (B) Raman frequencies plotted vs inverse stage number for intercalation in 96% H_2SO_4.

From the standpoint of feasibility and previous data from the literature, 1 M solutions of H_2SO_4, $HClO_4$, HNO_3, and H_3PO_4 in water were examined, as was 1 M $NaClO_4$ in acetonitrile.

Figure 5 shows a slow-scan voltammogram of HOPG in 1 M $HClO_4$ with the current integrated to reduce noise and stated as a charge per unit mass of HOPG. Oxidation is evident at ca. +0.8 V vs SSCE, and large currents are present above 1.0 V. Raman spectra obtained at selected potentials during the experiment depicted in Figure 5 are shown in Figure 6. The D band and a distorted E_{2g}' mode are readily apparent at 1.580 V, and some D band intensity is visible at 1.439 V. Figure 6B shows difference spectra of the E_{2g} region at several potentials relative to the spectrum observed at 0.500 V. Changes in the E_{2g} band are apparent at 1.118 V, which increase with potential. Figure 5 includes the E_{2g}'/E_{2g} intensity ratio obtained simultaneously with the voltammetric data. Due to inaccuracies in measuring the E_{2g}'/E_{2g} ratio in Figure 5, the apparent fluctuations in the ratio may not be real. However, the onset and general increase in the ratio

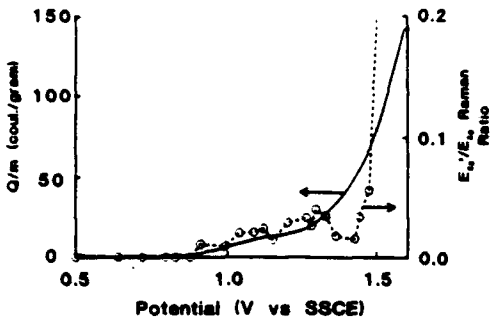

Figure 8. E_{2g}/E_{2g}' Raman intensity ratio (dashed line) and charge/mass ratio (solid line) for intercalation of a 0.1- × 2- × 2-mm HOPG sample in 96% H_2SO_4.

with potential are reproducible. Figures 5 and 6 both indicate that changes in the E_{2g} mode precede observable D band intensity.

Figures 7–9 were taken from potentiostatic pretreatment where the potential of interest was applied for 2 min, with simultaneous acquisition of a Raman spectrum. Spectra for HOPG pretreated at various potentials are shown for three electrolytes in Figure 7. The spectra for 1 M H_2SO_4 and 1 M HNO_3 are qualitatively very similar to those for 1 M $HClO_4$. Note that H_3PO_4 does not intercalate to an observable extent up to 2.0 V, while HNO_3, $HClO_4$, and H_2SO_4 cause obvious intercalation and lattice damage at 1.5–1.7 V. The D/E_{2g} and E_{2g}'/E_{2g} intensity ratios are plotted in Figures 8 and 9 for potentiostatic pretreatment in five electrolytes.

Several useful observations are available from the results shown in Figures 5–9. First, the nature of intercalation in mild electrolytes is strongly dependent on the solvent and salt identities. H_2SO_4, $HClO_4$, and HNO_3 (all 1 M) are qualitatively similar, while $NaClO_4/CH_3CN$ shows intercalation but no lattice damage (indicated by the D band), and H_3PO_4/H_2O shows neither intercalation nor lattice damage. Second, the onset potentials of both intercalation and lattice damage depend strongly on the electrolyte, on the basis of the E_{2g}' and D intensities shown in Figures 8 and 9. Listed in order of decreasing propensity to cause changes in the D and E_{2g} bands, the 1 M electrolytes are $HNO_3 > HClO_4 > H_2SO_4 > NaClO_4/CH_3CN \gg H_3PO_4$. The onset potentials for both the E_{2g}' and D bands are listed in Table I, along with the intensity ratios reached at 2.00 V.

DISCUSSION

Intercalation and related structural changes in HOPG depend on several variables, including site and rate of initial ion insertion between layers, mass transport of intercalants into the bulk lattice, thermodynamic potential of various stages for different intercalants, intraplanar lattice damage, and carbon oxidation to form graphitic oxide, CO_2, etc. Although these factors have been examined in significant detail, the relative importance of each effect in a given experiment depends greatly on conditions. In addition to revealing structural changes during intercalation using Raman spectroscopy, our purpose here is to use conditions similar to those present in the numerous applications of carbon electrodes in analysis and synthesis. The multichannel Raman spectrometer used here to monitor intercalation in situ is particularly valuable, since it provides rapid spectra in real time, simultaneously with intercalation.

Before turning to mild aqueous electrolytes, the results in 96% H_2SO_4 provide useful observations. This medium suppresses oxide formation due to low water activity, so intercalation can proceed to a low stage index without complication from side reactions. Of interest is the immediate (≤2 min) onset of Raman spectral changes to the E_{2g} band even when the laser beam is positioned on the HOPG basal surface far away (1 mm) from edges. If intercalation occurred solely through the cut edge of the sample (the "a" face), there should be a lag before the E_{2g}' band is observed in the center of the sample. As noted by Nishitani et al.,[32] such a delay occurs when only the a-face is immersed in H_2SO_4. In fact, a front corresponding to a stage transition progresses away from the H_2SO_4/a-face junction as intercalant diffuses into the sample. When the entire sample is immersed (as was the case here) intercalation is rapid near or far from the a-face and then propagates into the sample interior. This observation is consistent with intercalant entry through defects and crystallite boundaries on the basal surface. X-ray results indicate a microcrystallite size of ca. 10 μm for HOPG,[33] and numerous step edge defects are observed with STM. Assuming intercalation begins at such defects, the intercalant need only diffuse a few microns to completely intercalate the basal surface. It should be noted that differences in intercalation dynamics may well result from sample-dependent parameters such as microcrystallite size and long-range order.

On the basis of the optical properties of HOPG, the combination of beam penetration and scattered photon escape depth results in a Raman sampling depth of about 130 Å.[37] Intercalation compounds have lower graphite density and different optical properties than the initial HOPG, so one might expect the sampling depth to be greater. On the basis of Figures 3 and 4A, the cross section for boundary layer graphite (E_{2g}') is about 2.5 times that of the inner layer (E_{2g}), at least for HSO_4^- intercalation. For example, the stage IV GIC in Figure 3 exhibits a stronger E_{2g}' peak for an equal number of inner and boundary layers. Since intercalation to stage I yields a 25-fold increase in scattering intensity (for E_{2g}' compared to unintercalated E_{2g}), the Raman sampling depth for the stage I GIC must have increased by a factor of ca. 10 (to about 1500 Å) compared to unmodified HOPG.

The data of Figures 2–4 permit an assessment of stage number from Raman frequencies and intensities, provided the scan rate (1 mV/min in this case) is slow enough to permit intercalation to occur throughout the HOPG sample. Since equilibration can occur, the slow-scan results should reflect the thermodynamic stability of different GIC's, provided intercalation is the only process occurring. Besenhard and Fritz[38] and Rudorff and Hofmann[39] report that the GIC's formed in $HClO_4$ or H_2SO_4 are more stable toward oxide formation than that in HNO_3, which is in turn more stable than that from H_3PO_4. In other words, the reduction potentials for $HClO_4$ and H_2SO_4 GIC's are lower than HNO_3 and H_3PO_4 GIC's, and their thermodynamic propensity to form oxides is lower. Beck et al.[40] reported a quasireversible potential for intercalation of natural graphite flakes which decreased with increasing H_2SO_4 or $HClO_4$ concentration. It is not surprising that intercalation is "easier" for more concentrated intercalants, but the relationship between potential and concentration was not Nernstian. Thus the main thermodynamic conclusion available from slow-scan experiments in concentrated acids is that intercalation occurs at lower potentials for more concentrated acids, and the order of reduction potential is $H_3PO_4 \gg HNO_3 > H_2SO_4 \simeq HClO_4$. Since oxide formation is thermodynamically unfavorable in concentrated acids and since intercalation is permitted to reach equilibrium due to the slow-scan rate, the Raman results reflect the order of reduction potentials of the respective GIC's.

Conclusions about intercalation and lattice damage in mild aqueous acids are best divided into qualitative observations distinguishing different intercalants and more quantitative issues regarding onset potentials and intercalation rates.

(38) Besenhard, J. O.; Fritz, J. P. *Z. Anorg. Allg. Chem.* **1975**, *416*, 106.
(39) Rudorff, W.; Hoffmann, U. *Z. Anorg. Allg. Chem.* **1938**, *238*, 49.
(40) Beck, F.; Junge, H.; Krohn, H. *Electrochim. Acta* **1981**, *26*, 799.

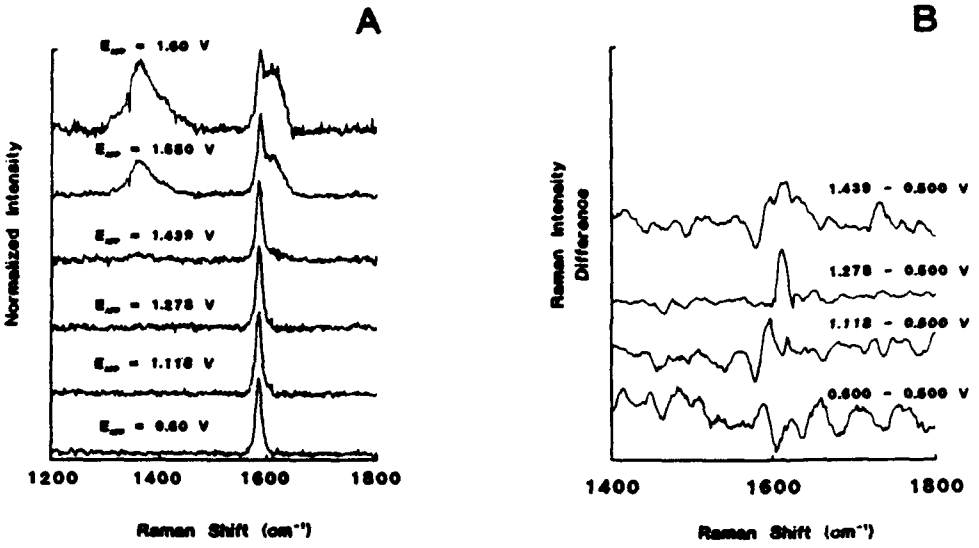

Figure 6. (A) Raman spectra of HOPG obtained during a slow scan from 0.50 V to various potentials in 1 M $HClO_4$. (B) Difference spectra of the E_{2g} region, referenced to 0.500 V. Intensities of both sets of spectra were adjusted for comparison but varied only slightly from run to run.

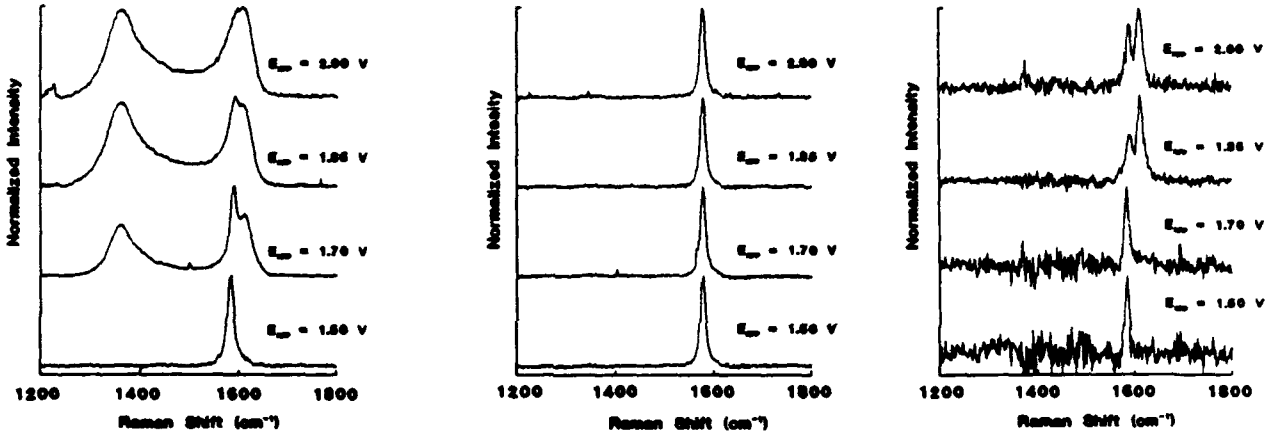

Figure 7. Raman spectra of HOPG after potential steps lasting 2 min from 0.500 V to four potentials in 1 M $HClO_4$, 1 M H_3PO_4, and 1 M $NaClO_4/CH_3CN$. Baseline noise in the CH_3CN case was due to subtraction of solvent bands.

Referring to Figure 7, several qualitative conclusions are available. First, lattice damage as indicated by the D band was always preceded or accompanied by intercalation. In no case did breakup of the sp^2 lattice occur without evidence of accompanying intercalation. Of particular note is 1 M H_3PO_4, when neither intercalation nor lattice damage occurred at potentials up to and including 2.00 V vs SSCE. Second, it was possible to intercalate without lattice damage, in the case of $NaClO_4/CH_3CN$ or 96% H_2SO_4. Thus intercalation per se does not cause lattice damage, but rather an associated or subsequent process. Third, in all cases studied where intercalation occurred in mild aqueous acids (1 M HNO_3, 1 M $HClO_4$, 1 M H_2SO_4), lattice damage resulted. These qualitative conclusions indicate a sequence of events in which intercalation occurs if favorable; then the intercalation compound undergoes chemical reactions leading to lattice damage under certain conditions. In CH_3CN or 96% H_2SO_4, the intercalation compound is stable toward these chemical reactions so damage does not occur, and in 1 M H_3PO_4, intercalation and any subsequent lattice damage were not observed. The evidence indicates that the intercalation compounds formed in mild aqueous acids rapidly form oxides, a process which generates enough strain to result in lattice damage and appearance of the "D" band.

Although based on different evidence obtained in different media, a mechanism based on intercalation followed by lattice damage and oxide formation was concluded by Besenhard et al.[12] and Beck et al.[40] for mild aqueous acids. As the acid strength decreases, the reduction potential for intercalation *increases*, in some cases linearly. Thus weaker acids lead to a higher potential for formation of intercalation compounds. Furthermore, CO, CO_2, O_2, and graphite oxide formation occur at *lower* potentials as the acid concentration decreases. Thus solely on thermodynamic grounds, the potential for intercalation will become more positive than the potential for oxide formation as the acid strength is decreased. The spectral data of Figure 7 indicate that although the intercalation compound is unstable in 1 M HNO_3, $HClO_4$, or H_2SO_4, it does form before or simultaneously with lattice damage. Conversely, without intercalation (as in 1 M H_3PO_4), no lattice damage is observed even at high potentials. This mechanism is also consistent with that proposed earlier, in which oxide formation on carbon edges creates strain which results in lattice damage.[32] Such a process is also consistent with the nucleation and growth mechanism concluded from STM[31] and Raman microprobe[35] observations. The results presented

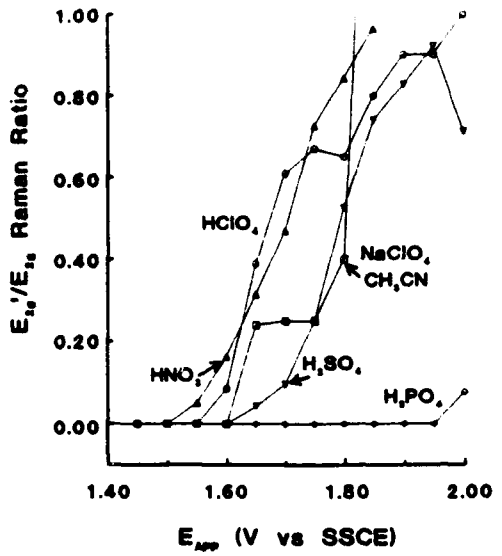

Figure 8. E_{2g}'/E_{2g} integrated intensity ratio for HOPG in five electrolytes: Triangles, HNO_3; circles, $HClO_4$; squares, $NaClO_4/CH_3CN$; inverted triangles, H_2SO_4; diamonds, H_3PO_4. Spectra were acquired during successive potential steps to E_{app}. All electrolyte concentrations were 1 M in water, except for 1 M $NaClO_4$ in CH_3CN.

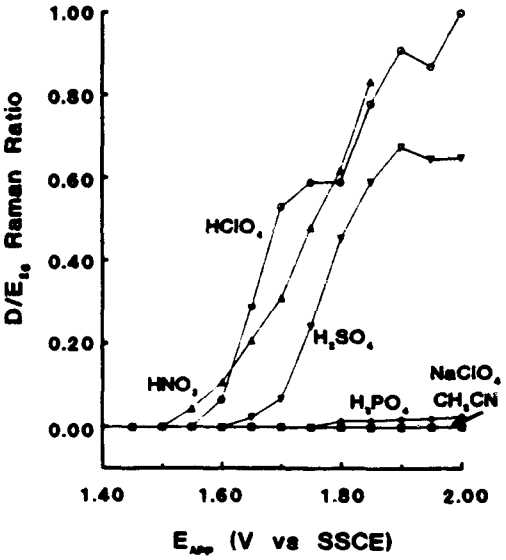

Figure 9. Integrated D/E_{2g} intensity for five electrolytes, otherwise same as Figure 8.

Table I. Raman Peak Intensity Ratios after ECP in 1 M Electrolytes

	D/E_{2g} E_{app} = 2.00 V	E_{2g}'/E_{2g} E_{app} = 2.00 V	D band onset, potential steps[b]	E_{2g}' onset, slow scan[b]
H_2SO_4/H_2O	0.65	0.71	1.65	1.0–1.1
$HClO_4/H_2O$	1.0	1.0	1.60	0.9–1.0
HNO_3/H_2O	0.83 (1.85 V)	0.96 (1.85 V)	1.55	1.1–1.2
H_3PO_4/H_2O	0.025	0.077	>1.80	–[a]
$NaClO_4/CH_3CN$	0.00	1.28	–	–

[a] A dash indicates that no band was observed. [b] Volts vs SSCE.

here add to these previously reported mechanisms the new information that intercalation of HOPG always precedes lattice damage and presumably oxide formation.

The quantitative aspects of intercalation and lattice damage reveal further factors which control the process. On the basis of the onset of the E_{2g}' and D bands noted in Figures 8 and 9 and Table I, 1 M HNO_3 is a more aggressive medium than the other dilute acids studied. On the basis of lattice damage and E_{2g}' appearance, the relative order of electrolytes is HNO_3 > $HClO_4$ > H_2SO_4 ≫ H_3PO_4. Although $HClO_4$ has been reported to be the thermodynamically most favorable intercalant of the group,[39] HNO_3 shows intercalation and lattice damage at lower potentials in mild media. Apparently, a kinetic factor is involved for conditions other than a very slow scan rate. Since carbon oxide formation accompanies intercalation in mild acids, the rate of intercalation relative to oxide formation may be important and a thermodynamic limit may never be reached. $HClO_4$ may be thermodynamically favored to reach a particular stage number at a lower potential than HNO_3, but the more rapid kinetics of NO_3^- intercalation lead to both E_{2g}' intensity and lattice damage at potentials lower than predicted on solely thermodynamic grounds.

Table II. Radii of Selected Anions

anion	ionic radius (pm)	hydrated radius (pm)[a]
ClO_4^-	189	350
SO_4^{2-}	236	400
NO_3^-	230	300
PO_4^{3-}	238	400
HPO_4^{2-}		400
$H_2PO_4^-$		450

[a] Debye Huckel ion size parameter.[41]

The ionic and hydrated radii for the anions studied are listed in Table II. Intercalation has been observed for both solvated and unsolvated anions,[12] and the data presented here do not indicate which occurs in dilute acids. However, for the monoanions concerned, the onset potential for lattice damage is lower for smaller ionic or hydrated radii. Not surprisingly, the smaller ions are more aggressive toward intercalation.

Conclusions about intercalation based on HOPG in mild acid should apply to carbon materials with comparable d_{002} spacing (3.35 Å) such as pyrolytic graphite, spectroscopic graphite rods, and many vapor-deposited carbon films. These materials are less ordered than HOPG, and their higher density of graphitic edges may accelerate oxide formation relative to intercalation, possibly leading to lower sensitivity to anion identity. As d_{002} increases, intercalation behavior may differ. Of particular interest is glassy carbon with a d_{002} of ca. 3.6 Å and much less microcrystalline order than HOPG. GC intercalation, if it occurs at all, has not been studied in detail, and GC is not as amenable to the Raman technique used here because the E_{2g}' and E_{2g} bands are not well resolved. The absence of detectable sulfur in graphite oxide formed during ECP of GC in 0.1 M H_2SO_4[30] implies either that intercalation of HSO_4^- into GC does not occur or that HSO_4^- is lost upon lattice damage and oxide formation.

In summary, the behavior of HOPG upon oxidation in many aqueous acids is strongly dependent on the identity of the anion. If intercalation does not occur (as for 1 M H_3PO_4), no changes in the HOPG were observed. If intercalation does occur, the process might be reversible with no damage to the sp^2 lattice (as with $NaClO_4/CH_3CN$ or 96% H_2SO_4). If intercalation occurs and oxide formation is thermodynamically favorable, lattice damage occurs (e.g. 1 M $HClO_4$, H_2SO_4, or HNO_3). Oxide formation is a function of both thermodynamic and kinetic effects, and the rate of intercalation and subsequent lattice damage appears to be higher for smaller intercalating ions.

ACKNOWLEDGMENT

This work was supported by the Analytical and Surface Chemistry Division of the National Science Foundation.

Received for review January 6, 1992. Accepted April 23, 1992.

(41) Kielland, J. J. Am. Chem. Soc. 1937, 59, 1675.

Reprinted from Analytical Chemistry, 1992, 64.

Effects of Redox System Structure on Electron-Transfer Kinetics at Ordered Graphite and Glassy Carbon Electrodes

Kristin R. Kneten and Richard L. McCreery*

Department of Chemistry, The Ohio State University, 120 West 18th Avenue, Columbus, Ohio 43210

The basal plane of highly ordered pyrolytic graphite (HOPG) serves as an ordered model of more commonly used electrode surfaces such as glassy carbon (GC) and pyrolytic graphite. The defect density on the basal plane HOPG was reduced by careful cleaving and cell design and was verified to be low by requiring that ΔE_p for $Fe(CN)_6^{3-/4-}$ (1 M KCl) be greater than 700 mV for a 0.2 V/s scan rate. Then a variety of redox systems were examined on "validated" HOPG surfaces, and variations in the electron transfer rate constant, k_s^0, were observed. All 13 redox systems exhibited relatively fast kinetics on laser activated GC ($k^0 > 0.03$ cm/s for eight inorganic systems), and in several cases k^0 exceeded the instrumental limit. On HOPG, however, ΔE_p varied greatly for the 13 systems, ranging from 66 to >1200 mV. The reasons for this variation fall into three general classifications. First, reactions involving proton transfer (e.g. catechols) were all slow on HOPG, implying some role of the surface in mediating multistep processes. Second, the observed rate correlated with the exchange rate for homogeneous electron transfer, but the heterogeneous rates on HOPG were 3–5 orders of magnitude slower than that predicted from simple Marcus theory. Third, the physical properties of HOPG, such as density of electronic states and hydrophobicity, may depress k^0 relative to GC and metals.

INTRODUCTION

Due in part to the widespread use of carbon electrodes in electroanalysis and electrosynthesis, a large research effort has been invested in understanding heterogeneous electron transfer at carbon surfaces. Such investigations have dealt with effects of surface structure and pretreatment on electrochemical behavior for a variety of sp^2 carbon materials, including pyrolytic graphite, carbon paste, glassy carbon (GC), carbon films, and highly ordered pyrolytic graphite (HOPG).[1-6] The ultimate goal of electrode kinetic studies of such materials is elucidation of structure/reactivity relationships for carbon surfaces, with a specific goal of controlling electron-transfer rates. Achievement of these goals has been frustrated, however, by the complex nature of the carbon/solution interface caused by variability in surface history, particularly cleanliness, roughness, and the extent of oxide formation. Work in our lab and several others has demonstrated that reproducible kinetics are observable on GC with sufficient attention to surface history.[6-12] In some cases, large changes in rate constants for benchmark redox systems can be effected reliably through laser activation,[8,10] heat treatments,[5,7] ultraclean polishing,[6] and electrochemical pretreatment.[13-16] However, since the structure of the carbon/solution interface after these procedures is ill-defined at the atomic level, it is currently difficult to deduce the structural factors which control electrode kinetics at the molecular level. Without a structurally well defined carbon surface, a rationale for how rates vary for different redox systems will be hard to formulate. Stated differently, structure/reactivity relationships derived from an incompletely characterized carbon surface will be ambiguous.

Ideally, one would like to survey a range of redox systems on an atomically well defined carbon surface. The basal plane of highly ordered pyrolytic graphite (HOPG) has potential for such correlations because of its well-defined structure and relative lack of surface impurities. HOPG was first used as an electrode by Yeager et al.,[17-19] and more recent work has demonstrated a large edge/basal plane rate anisotropy for several redox systems, with large voltammetric peak separations for $Fe(CN)_6^{3-/4-}$ and dopamine at the basal plane and near-reversible voltammetry at the edge plane.[1,20,21] HOPG has also been used as a substrate for the spectroscopy of adsorbates,[22] and its unusual adsorption properties and capacitance have been described.[23] It has not always been possible, however, to study heterogeneous electron-transfer kinetics at basal plane HOPG for a wide range of systems because of several experimental problems. Recently we have shown the dominating role of edge plane defects in various electrochemical processes. HOPG surfaces yield a wide range of results of $Fe(CN)_6^{3-/4-}$ kinetics, 2,6-anthraquinonedisulfonate (AQDS) adsorption, and differential capacitance,

* Author to whom correspondence should be addressed.

(1) McCreery, R. L. In *Electroanalytical Chemistry*, Bard, A., Ed.; Dekker: New York, 1991; Vol. 17.
(2) Kinoshita, K., *Carbon: Electrochemical and Physicochemical Properties*; Wiley: New York, 1988.
(3) Sarangapani, S., Akridge, J. R., Schumm, B., Eds. *Proceedings of the Workshop on the Electrochemistry of Carbon*; The Electrochemical Society: Pennington, NJ, 1984.
(4) Wightman, R. M.; Deakin, M. R.; Kovach, P. M.; Kuhr, P. M.; Stutts, K. J. *J. Electrochem. Soc.* **1984**, *131*, 1578.
(5) Stutts, K. J.; Kovach, P. M.; Kuhr, W. G.; Wightman, R. M. *Anal. Chem.* **1983**, *55*, 1632.
(6) Hu, I. F.; Karweik, D. H.; Kuwana, T. *J. Electroanal. Chem. Interfacial Electrochem.* **1985**, *188*, 59.
(7) Fagan, D. T.; Hu, I. F.; Kuwana, T. *Anal. Chem.* **1985**, *57*, 2759.
(8) Rice, R. J.; Pontikos, N.; McCreery, R. L. *J. Am. Chem. Soc.* **1990**, *112*, 4617.
(9) Deakin, M. R.; Kovach, P. M.; Stutta, K. J.; Wightman, R. M. *Anal. Chem.* **1986**, *58*, 1474.
(10) Poon, M.; McCreery, R. L. *Anal. Chem.* **1986**, *58*, 2745.
(11) Kamau, G. N.; Willis, W. S.; Rusling, J. F. *Anal. Chem.* **1985**, *57*, 545.
(12) Thornton, D. C.; Corby, K. T.; Spendel, V. A.; Jordan, J.; Robbat, A.; Rutstrom, D. J.; Gross, M.; Ritzler, G. *Anal. Chem.* **1985**, *57*, 150.
(13) Engstrom, R. C.; Strasser, V. A. *Anal. Chem.* **1984**, *56*, 136.
(14) Cabaniss, G. E.; Diamantis, A. A.; Murphy, W. R., Jr.; Linton, R. W.; Meyer, T. J. *J. Am. Chem. Soc.* **1985**, *107*, 1845.
(15) Gonon, F. G.; Fombarlet, C. M.; Buda, M. J.; Pujol, J. F. *Anal. Chem.* **1981**, *53*, 1386.
(16) Kepley, L. J.; Bard, A. J. *Anal. Chem.* **1988**, *60*, 1459.
(17) Morcos, I.; Yeager, E. *Electrochim. Acta* **1972**, *15*, 257.
(18) Randin, J. P.; Yeager, E. *J. Electroanal. Chem. Interfacial Electrochem.* **1972**, *36*, 257.
(19) Randin, J. P.; Yeager, E. *J. Electroanal. Chem. Interfacial Electrochem.* **1975**, *58*, 313.
(20) Bowling, R.; Packard, R.; McCreery, R. L. *J. Am. Chem. Soc.* **1989**, *111*, 1217.
(21) Rice, R. J.; McCreery, R. L. *Anal. Chem.* **1989**, *61*, 1638.
(22) Kim, S.; Xu, L. T. B.; Wang, Z.; Scherson, D. A. *Anal. Chem.* **1990**, *62*, 2647.
(23) McDermott, M. T.; Kneten, K.; McCreery, R. L. *J. Phys. Chem.* **1992**, *96*, 3124.

0003-2700/92/0364-2518$03.00/0

depending on surface defect density.[23,24] Capacitance ranging from 0.6 to 6.5 $\mu F/cm^2$, AQDS adsorption from <1.0 to 85 pmol/cm², and heterogeneous electron transfer rate constants for $Fe(CN)_6^{3-/4-}$ from 8×10^{-7} to 0.041 cm/s were obtained depending on the defect density of the surface.[23] It is clear, therefore, that without careful control of surface defects, highly variable rate constants can be obtained on the HOPG basal plane, impeding attempts to understand structure/reactivity relationships.

With an appreciation of the influence of defects on the electrochemical behavior of HOPG, it is possible to prepare low-defect basal surfaces which more accurately reflect the kinetics of the perfect, ordered surface. In the approach used here, we first validated a given HOPG basal surface by noting a very low k^0 for $Fe(CN)_6^{3-/4-}$. Since $Fe(CN)_6^{3-/4-}$ has a high ratio of edge to basal rates, a slow rate indicates minimal defect density. This *same* surface was then used to determine the rates for a variety of redox systems. Since the kinetic results were obtained on validated, low-defect surfaces, the surface-to-surface variability was greatly reduced and the rate comparisons were made on structurally better defined surfaces.

Heterogeneous electron transfer rates for 13 redox systems were determined at validated basal plane HOPG, high-defect density HOPG, and glassy carbon (GC). The results were used to assess the generality of the large edge/basal rate anisotropy and to infer structural variables affecting electrode kinetics at carbon electrodes.

EXPERIMENTAL SECTION

To minimize unintentional defects as well as air and solution exposure time, HOPG experiments were run in an inverted drop "cell" as reported earlier.[23] Ungraded HOPG (gift from Arthur Moore, Union Carbide) was cleaved either with ordinary "scotch" tape or with an Exacto knife blade edge. Best results were obtained when a thick (ca. 5-mm) piece of HOPG was cut perpendicular to the basal plane with a knife blade and the piece delaminated spontaneously. The cleaved piece was placed onto a conductive metal plate with graphite/Nujol paste serving to ensure good electrical contact. A drop of solution was placed onto the reference/auxiliary electrode couple which was then lowered onto a visually defect-free surface giving an effective electrode area of approximately 0.1 cm², as determined by $Fe(CN)_6^{3-/4-}$ chronoamperometry. The acronym HOPG is used henceforth to refer to the basal plane of low-defect HOPG unless noted otherwise.

In order to evaluate the relative defect density of freshly cleaved basal plane surfaces, voltammograms of 1 mM $K_4Fe(CN)_6$ or 1 mM $K_3Fe(CN)_6$ were obtained, in all cases in 1 M KCl with the inverted drop cell. Overall, the peak separation for $Fe(CN)_6^{3-/4-}$ at 0.2 V/s exhibited an average of 459 mV with a standard deviation of 331 mV and a range of 58–1200 mV. The large variability of ΔE_p for $Fe(CN)_6^{3-/4-}$ on HOPG indicates a large variation in adventitious defect density. In order to reduce this kinetic variability, a new surface was first validated with $Fe(CN)_6^{3-/4-}$ by requiring that ΔE_p be greater than 700 mV. After observing a ΔE_p >700 mV, the drop of $Fe(CN)_6^{3-/4-}$ solution was replaced with one of the redox system of interest, taking care to cover the same spot on the surface. It was noted that relatively thick (ca. 5-mm) pieces of HOPG yielded a higher "success rate" presumably due to greater mechanical rigidity. For the slower redox systems (ΔE_p >500 mV for basal plane) it was noted that the order of exposure to the test solution and $Fe(CN)_6^{3-/4-}$ affected ΔE_p, with ΔE_p increasing with air exposure or solution changes. The order of validation and test solutions was routinely reversed to check the effect on ΔE_p for the test systems. In all cases, the voltammetry for $Fe(CN)_6^{3-/4-}$ and the test redox system were completed within 1 min after the HOPG was cleaved.

The following redox systems (all in 1 M KCl unless no otherwise) were used and are numbered here for reference in figures: 1, 0.25 mM potassium hexachloroiridate(IV) (Aldrich Chemical Co.); 2, 1 mM hexammineruthenium(III) chloride (Strem Chemicals); 3, 2 mM tris(1,10-phenanthroline)cobalt chloride (from 2 mM cobalt chloride hexahydrate (reagent gr J. T. Baker Chemical Co.) and 6 mM 1,10-phenanthroline (reagen grade, J. T. Baker Chemical Co.)); 4, 1 mM methyl viologen ($MV^{2+/1+}$) (Sigma); 5, 2 mM tris(1,10-phenanthroline)iron (from 2 mM ferrous ammonium sulfate (reagent grade, J Baker) and 6 mM 1,10-phenanthroline); 6, 1 mM potassiu ferrocyanide (J. T. Baker); 7, 10 mM tris(ethylenediamine)cobalt (III) chloride (Johnson Matthey) + approximately 5 mM exc ethylenediamine (reagent grade, J. T. Baker); 8, 1 mM t (ethylenediamine)ruthenium(II) chloride (Johnson Matthey 0.2 M $HClO_4$. $HClO_4$ was used in the case of $Ru(en)_3^{2+/3+}$ t avoid degradation by air.[25]

Quinone systems included: 9, 1 mM AQDS (Aldrich) in 0.1 H_2SO_4; 10, 1 mM dopamine (Aldrich) in 0.1 M H_2SO_4; 11, 1 m 4-methylcatechol (Aldrich) in 0.1 M H_2SO_4; 12, 1 mM dihydroxyphenylacetic acid (DOPAC, Aldrich) in 0.2 M $HClO_4$, 6-hydroxydopamine (Sigma) in pH 7 phosphate buffer and 1 KCl. All solutions were prepared daily with distilled Nanop water (Barnstead) and degassed with argon.

For inverted drop experiments, either a silver wire quasi-reference electrode (QRE) or a Ag/AgCl (3 M NaCl) electr with a capillary salt bridge was used. The potential of the Q was typically 0 to −5 mV vs SSCE, but in all cases only ΔE_p was determined when the QRE was used, so an absolute potentia was not required. Reference electrodes for GC experiments w either Ag/AgCl or sodium-saturated calomel (SSCE), but all E values are reported relative to the SSCE. Laser irradiation (ca. MW/cm²) of HOPG was conducted either in situ as described previously[20,21] or ex situ with immediate replacement of soluti Ex situ experiments were run by directing the laser beam throu two right-angle prisms onto an inverted drop "cell". Solut was removed prior to and replaced immediately following irradiation. Glassy carbon electrodes (with areas of (2–5) × 1 cm²) were prepared as described previously[8] from a GC-20 pl (Tokai) and embedded in epoxy (Eccobond 55, Emerson & Cuming, Inc.) The GC electrodes were polished conventionally and laser-irradiated (25 MW/cm²) in solution as describ previously.[8]

For scan rates of 0.2–20 V/s, linear sweep voltammetry performed with a computer-triggered function generator (Tektronix) and "Labmaster" A/D converter. For faster scans, data were collected with a digital oscilloscope (Lecroy 9400A), w triggering and data transfer accomplished via locally writ software. A conventional three-electrode potentiostat (Advanced Idea Mechanics, Columbus, OH) was used for all voltammetry, with the RC filter value maintained such that $RCn\nu < 4$ mV

GC voltammetry was performed with scan rates of 0.2–V/s, and rate constants were calculated using the method of Nicholson.[27] In several cases, the GC rate constants were sufficiently large that the ΔE_p approached the reversible li of 57/n mV. For these cases, the rate constant evaluated fr ΔE_p was a lower limit. In no case was ΔE_p for laser-activated GC greater than 150 mV. For validated HOPG, large ΔE_p values bring into question the assumptions of constant transfer co ficient (α) underlying Nicholson's approach, so rate consta were calculated both from ΔE_p and by the approach of Corrig and Evans.[28] Experimental voltammograms were compared with those simulated with potential-dependent α. Unless not otherwise, all HOPG rate constants were determined from t best fit to simulated voltammograms with potential-dependent α. For GC, ΔE_p was sufficiently small that a potential-dependent α was unnecessary for an accurate simulation and rate constants determined from simulations equaled those calculated with t Nicholson approach. The experimentally determined rate c

(24) Robinson, R. S.; Sternitzke, K.; McDermott, M. T.; McCreery, R. L. *J. Electrochem. Soc.* **1991**, *138*, 2454.

(25) Meyer, T.; Taube, H. *Inorg. Chem.* **1968**, *7*, 2369.

(26) Wipf, D. O.; Kristensen, E. W.; Deakin, M. R.; Wightman, R. *Anal. Chem.* **1988**, *60*, 306.

(27) Nicholson, R. S. *Anal. Chem.* **1965**, *37*, 1351.

(28) Corrigan, D. A.; Evans, D. H. *J. Electroanal. Chem. Interfacial Electrochem.* **1980**, *106*, 287.

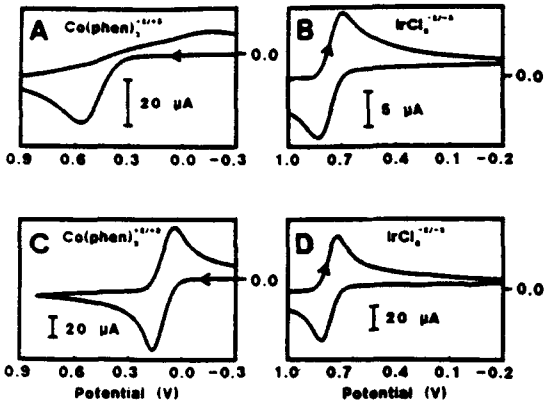

Figure 1. Voltammetry at validated basal plane HOPG for (A) 2 mM $Co(phen)_3^{2+/3+}$, 1 M KCl; (B) 0.25 mM $IrCl_6^{2-/3-}$, 1 M KCl; and at high-defect density HOPG for (C) $Co(phen)_3^{2+/3+}$; (D) $IrCl_6^{2-/3-}$. Scan rate = 0.2 V/s. Potentials are vs Ag QRE.

stants for laser-activated GC are denoted k_{GC}^0, the experimental rate constants for validated basal plane HOPG determined from comparison to simulation are k_b^0, and those for laser activated HOPG are k_{las}^0. The small background currents for HOPG voltammograms were not subtracted before plotting or analysis.

Diffusion coefficients for solutions listed above were determined by chronoamperometry with a GC electrode of known area. A 5-s time scale was used, and background subtraction was utilized. For methyl viologen and $Ru(en)_3^{3+/2+}$, chronoamperometric response was slightly nonideal, apparently due to adsorption, and D_{ox} was assumed to equal 5×10^{-6} cm^2/s. $E_{1/2}$'s for each system were determined as the average of the oxidation and reduction peak potentials for GC voltammograms with scan rates at which the systems were nearly reversible.

RESULTS

Figure 1 shows the importance of defects to the observed voltammetry and illustrates a marked difference in the behavior of two inorganic redox systems. Voltammograms A and B were obtained on HOPG surfaces which met the validation criterion. Voltammogram A is for $Co(phen)_3^{2+/3+}$ on a surface for which ΔE_p of $Fe(CN)_6^{3-/4-}$ was 900 mV, and B is for $IrCl_6^{2-/3-}$ on a surface exhibiting a ΔE_p for $Fe(CN)_6^{3-/4-}$ of 1200 mV. Note the large difference in ΔE_p for the two systems, indicating a much smaller k_b^0 for $Co(phen)_3^{2+/3+}$ than for $IrCl_6^{2-/3-}$. Voltammograms C and D were obtained on surfaces which failed the validation criterion, exhibiting ΔE_p values for $Fe(CN)_6^{3-/4-}$ of 455 and 58 mV, respectively. Note that a decrease in ΔE_p for $Fe(CN)_6^{3-/4-}$ for the surfaces of Figure 1A and 1C from 900 to 445 mV had a large effect on ΔE_p for $Co(phen)_3^{2+/3+}$, implying that $Co(phen)_3^{2+/3+}$ is very sensitive to defects and has a high edge/basal rate ratio. However, an even larger change for the surfaces of Figure 1B and 1D (1200 to 58 mV) had only a slight effect on ΔE_p for $IrCl_6^{2-/3-}$. $IrCl_6^{2-/3-}$ is only slightly faster on a quite defective surface, implying that the basal plane rate is not greatly slower than the edge plane rate. The variation in ΔE_p for $Fe(CN)_6^{3-/4-}$ and various redox systems is shown in Table I for validated surfaces. Significant surface-to-surface variation was observed for $Fe(CN)_6^{3-/4-}$, presumably due to variations in the small residual defect density. This variation confirms the high sensitivity of $Fe(CN)_6^{3-/4-}$ kinetics to defect density. For the systems listed in Table I, the range in ΔE_p among different systems is much greater than the variation for a given system.

Several voltammograms of different redox systems on validated HOPG are exhibited in Figure 2. Note the variety of peak separations and voltammogram shapes. Unusual voltammogram shapes are particularly evident for systems with low k_b^0. We have reported earlier that for $Fe(CN)_6^{3-/4-}$, the voltammogram shape at low-defect HOPG could be fit to simulations that involve a potential-dependent transfer coefficient.[23] We note here that simulations with potential-dependent α do fit the experimental data better for certain systems, but there is still a degree of divergence from theory. For systems with peak separations < 150 mV, simulations with constant α fit well to experimental data. In Figure 3A, experimental data for $Co(en)_3^{2+/3+}$ are compared to a simulation in which α is varied with potential. Note that this best fit to the anodic wave still does not completely match the experimental curve. In Figure 3B, however, $Fe(phen)_3^{2+/3+}$ voltammetry agrees well with the simulation, with a constant α. Results for all systems examined are summarized in Table II. As an additional measure of edge/basal rate anisotropy for HOPG, rate constants for laser-activated HOPG are included in Table II. In all cases, k^0 was larger on laser-damaged HOPG, often by several orders of magnitude.

In order to provide a reference carbon surface for comparison, rate constants for the eight inorganic systems and $MV^{1+/2+}$ were determined on the more commonly studied GC. Polished GC surfaces have been shown to yield very irreproducible rate constants, apparently due to surface impurities.[1,5,6,8] Laser activation of polished GC yields reproducible rate constants for $Fe(CN)_6^{3-/4-}$, comparable to those observed at heat-treated and fractured GC.[1,8,29] Thus laser-activated GC provides a carbon surface with reproducible kinetics with which to compare the behavior on HOPG for the redox systems examined. GC is also a more practical reference surface than edge plane HOPG due to the difficulty of reproducing the fragile edge plane surface.[21] In some cases, adsorption or ohmic potential error prevented the use of sufficiently high scan rates to determine k_{GC}^0 accurately. However, in all cases the ΔE_p observed on GC was lower than that on validated HOPG. As shown in Table II, the difference in rate constants between HOPG and GC was large in some cases, confirming and extending the rate anisotropy observed for $Fe(CN)_6^{3-/4-}$.

DISCUSSION

Considering the results in general terms initially, the most striking observation is the wide range of observed peak separations on validated HOPG, listed in Table II. In many cases, redox systems which exhibit fast electron transfer on GC or damaged HOPG, e.g. dopamine, $Fe(CN)_6^{3-/4-}$, and $Co(phen)_3^{2+/3+}$, are very slow on low-defect HOPG. For all 13 systems examined, the GC rates were faster than validated HOPG rates. On the basis of previous spectroscopic and microstructural information, we have concluded that this difference is due to the greater reactivity of graphitic edge regions compared to ordered basal plane,[1,8,20,21] although this conclusion was initially based on a limited number of redox systems. Since GC surfaces are rich in edge sites, their electrochemical kinetic behavior is similar to edge plane HOPG rather than basal plane.

Given the observation of a large edge/basal or GC/basal rate difference for at least the 13 systems studied, several questions arise. First, are the observations perturbed by some technical problems such as instrumentation limits, residual defects on the validated surface, etc.? Second, are there mechanistic differences among the 13 systems which cause the wide variations in rate? Third, for redox systems with apparently similar charge transfer mechanisms, what controls the rate on HOPG?

One technical limitation is easily recognized from the large k^0 values observed on GC. Fabrication of the GC electrodes

(29) Rice, R.; Allred, C. D.; McCreery, R. L. *J. Electroanal. Chem. Interfacial Electrochem.* **1989**, *263*, 163.

Table I. Peak Separations on Validated HOPG Surfaces

	system	ΔE_p (mV) system[a]	ΔE_p (mV) $Fe(CN)_6^{3-/4-}$	k_N^0 [b] (cm/s) (system)	k_b^0 [c] (cm/s) (system)	α ($d\alpha/dE$)
1	$IrCl_6^{2-/3-}$	137	1200	0.0034	0.0034	0.50
		145	910	0.0029		(0.0)
		96	1160	0.0083		
		126 ± 27		0.0049 ± 0.003		
2	$Ru(NH_3)_6^{2+/3+}$	285	1230	5.6×10^{-4}	9×10^{-4}	0.50
		215	1370	1.0×10^{-3}		(0.0)
		158	1185	2.2×10^{-3}		
		167	1175	2.0×10^{-3}		
		206 ± 58		$1.4 \times 10^{-3} \pm 8 \times 10^{-4}$		
3	$Co(phen)_3^{2+/3+}$	715	900	8.0×10^{-6}	2×10^{-5}	0.50
		675	725	1.3×10^{-5}		(0.25 V^{-1})
		600	940	2.6×10^{-5}		
		695		9.5×10^{-6}		
		671 ± 50		$1.4 \times 10^{-5} \pm 8 \times 10^{-6}$		
4	$MV^{1+/2+}$	76	1235	0.017	0.017	(0.50)
		63	981	>0.075		(0.0)
		65	1080	>0.054		
		68 ± 7		>0.049 ± 0.029		
5	$Fe(phen)_3^{2+/3+}$	63	1300	>0.075	>0.075	0.50
		57	1045			(0.0)
		60	1024			
		66	945	>0.042		
		62 ± 4		>0.059		
7	$Co(en)_3^{2+/3+}$	770	695	5.4×10^{-6}	2×10^{-5}	0.65
		711	1230	9.3×10^{-6}		(0.17 V^{-1})
		790	938	4.2×10^{-6}		
		757 ± 41		$6.3 \times 10^{-6} \pm 2.7 \times 10^{-6}$		
8	$Ru(en)_3^{2+/3+}$	502	1085	7.0×10^{-5}	1.3×10^{-4}	0.62
		373	883	2.3×10^{-4}		(0.0)
		307	1135	4.5×10^{-4}		
		394 ± 99		$2.5 \times 10^{-4} \pm 1.9 \times 10^{-4}$		

[a] All data at 200 mV/s. [b] Determined from ΔE_p by method of Nicholson.[27] [c] Rate constant calculated by comparison to simulations, w. α and $d\alpha/dE$ shown.

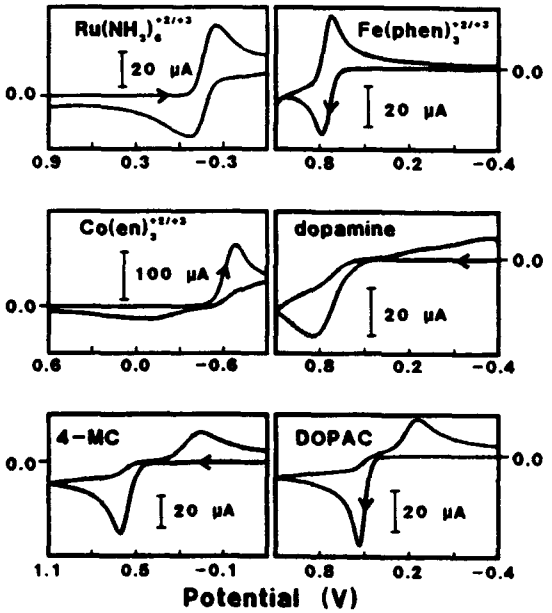

Figure 2. Voltammetry at validated basal plane HOPG: 1 mM $Ru(NH_3)_6^{2+/3+}$, 1 M KCl; 2 mM $Fe(phen)_3^{2+/3+}$, 1 M KCl; 10 mM $Co(en)_3^{2+/3+}$, 1 M KCl; 1 mM dopamine, 0.1 M H_2SO_4; 1 mM 4-methylcatechol (4-MC), 0.1 M H_2SO_4; 1 mM DOPAC, 0.2 M $HClO_4$. Scan rate = 0.2 V/s. Potentials are vs Ag QRE.

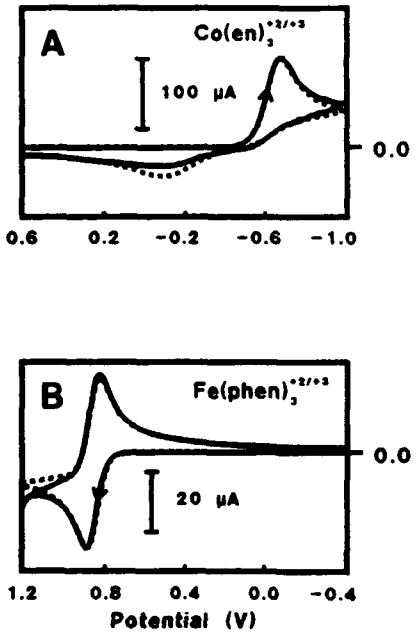

Figure 3. Voltammetry at validated basal plane HOPG. Solid lines: experimental data in both cases. (A) 10 mM $Co(en)_3^{2+/3+}$, 1 M KCl. Dashed line simulated for $k^0 = 2 \times 10^{-5}$ cm/s, $\alpha_0 = 0.65$, $d\alpha/dE = 0.17\ V^{-1}$. (B) 2 mM $Fe(phen)_3^{2+/3+}$, 1 M KCl. Dashed line simulated for $k^0 = 0.11$ cm/s, $\alpha_0 = 0.5$, $d\alpha/dE = 0.0\ V^{-1}$. Scan rate = 0.2 V. Potentials are vs Ag QRE.

from well-characterized GC stock results in electrode surfaces with minimum dimensions of about 0.5 mm × 0.5 mm. Ohmic potential error limits the useful scan rate to about 500 V/s, resulting in an upper limit of observable k^0 on GC of about 0.5 cm/s.[8] In a previous publication, these electrodes were shown to yield reliable k^0 values of 0.5–0.8 cm/s at 100–5 V/s, but larger k^0 values are difficult to measure with

Table II. Composite Redox Potential and Kinetic Data

	system	$E_{1/2}$[a] (V vs SSCE)	ΔE_p[b] (mV)	k_b^0 (cm/s)	k_{bm}^0[c] (cm/s)	k_{GC}^0[d] (cm/s)	k_{GC}^0/k_b^0[e]	k_{exc}[f] (M^{-1} s^{-1})	ref
1	$IrCl_6^{2-/3-}$	0.74	146	0.003	0.05	>0.5	>200	2×10^5	47
2	$Ru(NH_3)_6^{2+/3+}$	−0.19	285	9×10^{-4}	0.05	>0.4	>400	4000	25, 48
3	$Co(phen)_3^{2+/3+}$	0.10	715	2×10^{-5}	0.002	0.06	4000	40	49
4	$MV^{1+/2+}$	−0.67	76	0.017		>0.1	>6	10^7	50
5	$Fe(phen)_3^{2+/3+}$	0.86	66	>0.07		>0.2		3×10^6	51
6	$Fe(CN)_6^{3-/4-}$	0.25	700–1370	10^{-6}[g]	0.05	>0.6	$>6 \times 10^5$	2×10^4	52, 53
7	$Co(en)_3^{2+/3+}$	−0.48	770	2×10^{-5}	0.001	0.03	2000	8×10^{-5}	54
8	$Ru(en)_3^{2+/3+}$	−0.08	502	1×10^{-4}		>0.5	>5000	4000	48
9	AQDS	−0.14	870						
10	dopamine	0.51	1200						
11	4-methylcatechol	0.40	460						
12	DOPAC	0.31	370						
13	6-hydroxydopamine	−0.31	840						

[a] Average of voltammetric peak potentials on laser activated GC. [b] On validated HOPG basal plane surfaces. [c] Laser-activated HOPG, after three 50 MW/cm² pulses ex situ. [d] Laser-activated GC, after three 25 MW/cm² pulses in situ. [e] Ratio of laser-activated GC rate constant to validated HOPG rate constant. [f] Homogeneous self-exchange rate, with literature reference. [g] Value for HOPG surface exhibiting minimum AQDS adsorption, from ref 23.

smaller electrodes.[8] Therefore, GC rate constants reported as 0.2–0.6 cm/s here should be considered lower limits and could in fact be significantly higher. For HOPG examined with the inverted drop, the electrode area is larger, but k^0 is much smaller and high scan rates were not required. Thus the HOPG rate constants are not subject to significant error from solution iR effects. In addition, the relatively high c-axis resistivity of HOPG (0.17 Ω-cm) would yield a typical resistance in the ca. 3-mm-thick pieces of HOPG used here of about 0.3 Ω, not enough to contribute significant ohmic potential error.

A second potential technical problem arises from uncertainty about residual defects on the validated HOPG surface. As noted earlier, the large standard deviation for ΔE_p of $Fe(CN)_6^{3-/4-}$ on unvalidated surfaces indicates that adventitious defects can drastically affect observed kinetics. The requirement that ΔE_p for $Fe(CN)_6^{3-/4-}$ exceed 700 mV significantly reduces this variability (Table I), but it is still possible that residual defects contribute to the apparent k_b^0 on HOPG. Since the rates on GC or edge plane graphite are all faster than those on validated HOPG, residual defects will increase the apparent k_b^0. Strictly speaking, the k_b^0 values measured on validated surfaces are upper limits for the true basal plane k^0 values. However, more can be concluded from the data in Table I. The observed ΔE_p values for the test systems vary much less (and often in different directions) than the $Fe(CN)_6^{3-/4-}$ values, implying no correlation of ΔE_p with defect density on validated surfaces. Furthermore, ΔE_p varies greatly for test systems (e.g. 62 mV for $Fe(phen)_3^{2+/3+}$ vs 670 mV for $Co(phen)_3^{2+/3+}$) on surfaces with similar $Fe(CN)_6^{3-/4-}$ voltammetry. These observations demonstrate that the large differences in observed kinetics among the systems examined on validated surfaces cannot be a consequence solely of residual defects.

A related issue is possible distortions to voltammetry caused by nonplanar diffusion to defects, possibly leading to microelectrode array behavior. As discussed previously,[23] the assumption of planar diffusion will break down if the spacing between defects is comparable to or greater than $(Dt)^{1/2}$, where D is the diffusion coefficient and t is electrolysis time. Such distortions are unlikely to occur for validated HOPG surfaces, however, both because the scan rates used for HOPG are relatively slow (yielding a relatively large $(Dt)^{1/2}$) and because the validation procedure reduces the density of defects to very low levels.

Speaking more quantitatively, the fact that the k_b^0 values are upper limits and the k_{GC}^0 are lower limits indicates that the rate anisotropy between edge and basal plane is at least as large as that reported in Table II. For the purposes of this study, it is sufficient to conclude that all redox systems studied are slower on basal plane HOPG than on GC and that the anisotropy varies greatly from system to system. The precise magnitude of the anisotropy will remain uncertain as long as residual defects are possible.

A final technical issue to be considered here deals with the effect of impurity adsorption on observed kinetics, which is at least one of the important variables for GC.[5-8,29] Although basal HOPG surfaces were examined within 1 min of cleaving, some exposure to air and solution impurities was unavoidable. It was observed that k_b^0 for "fast" systems ($\Delta E_p < 400$ mV) did not vary greatly with time of air or solution exposure, while those with slow kinetics ($\Delta E_p > 400$ mV) exhibited an increasing ΔE_p with time. This observation is consistent with adsorption of impurities to *defects* rather than to basal plane, as is observed with intentional adsorbers such as AQDS.[23] Taken together, these technical concerns reinforce the conclusion that k_{GC}^0 values are lower limits of the true GC rate constants, while k_b^0 values are upper limits for the true basal plane HOPG rate constants. In addition, any errors in k_b^0 caused by residual defects or impurities will be most important for the slowest redox systems.

Let us now turn to the question of the origin of the often large differences between HOPG and GC rates. It is useful to note initially that most of the 13 systems studied exhibit fast electron transfer on laser-activated GC. Past experience with GC in several laboratories indicates that observed kinetics are very sensitive to surface history, with k_{obs}^0 varying by several orders of magnitude for dopamine or $Fe(CN)_6^{3-/4-}$ for nominally similar GC electrodes with varying pretreatment.[1,4-16] For the laser-activated GC surface, however, the rates are consistently fast, often at the instrumental limit for rate constant determination. There may be significant variations in k_{GC}^0 which are masked by the instrumental limit, but clearly the rates are high with only a few exceptions.

In contrast, basal rates for all systems are slower and cover a wider range. The inorganic complexes exhibit a k_b^0 on validated surfaces ranging from $<10^{-6}$ to >0.07 cm/s, while the organic systems have ΔE_p's from 76 to 1200 mV. A possible origin for these variations is differences in mechanism which may involve specific surface chemical interactions. For example, if electron transfer requires a functional group which is present only on edge plane defects, it should be very slow on basal plane. Considering Table II, it is clear that all of the organic systems with multistep electron transfer mechanisms involving protons are slow ($\Delta E_p > 450$ mV) on basal plane. There could be several mechanisms which promote fast electron transfer at defects for reactions involving protons. Cabaniss et al. proposed a proton-assisted electron-transfer

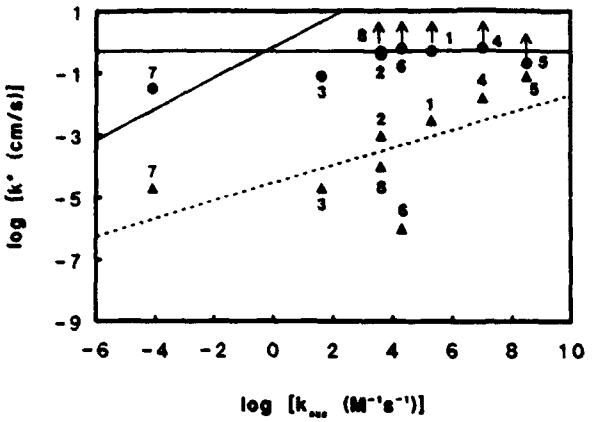

Figure 4. Log–log plot for rate constants versus homogeneous self-exchange rates (k_{exc}) for one-electron systems. Triangles are validated HOPG heterogeneous rate constants. Circles are laser-activated GC rate constants. Solid line is from Marcus theory, eq 1 in text. Dashed line is least squares fit for all points, HOPG data: slope = 0.29, y-intercept = −4.5, correlation coefficient = 0.66 Horizontal line indicates upper limit of measurable rate constants for GC experiments, k^0 = 0.5 cm/s. Data and number assignments from Table II.

route, which would be prevented on perfect basal plane.[14] It could be that proton transfer occurs between a protonated edge plane surface group (or merely adsorbed protons) and the redox system, thus accelerating electron transfer at defects or on GC. There are several other possible mechanisms, but it is clear that all five reactions studied here which involve protons are very slow on basal plane HOPG and fast on defects or GC.

After eliminating the systems with obvious proton involvement, there remain seven inorganic complexes and $MV^{2+/1+}$. These systems all involve one-electron transfers with no major changes in coordination geometry. The reasons for large rate differences between GC and HOPG for these systems should fall into two classes. First, the redox systems may vary in mechanism or homogeneous self-exchange rate (k_{exc}), thus affecting their kinetics with presumably any electrode material. Second, the reason may involve the nature of HOPG itself, particularly some difference in physical properties between basal plane HOPG and GC. Considering the redox systems first, we may suspect $Fe(CN)_6^{3-/4-}$ to be unusual because of the well-known involvement of K^+ in electron transfer.[30,31] It has been concluded that K^+ is involved in the $Fe(CN)_6^{3-/4-}$ transition state and that variations in cation identity and concentration strongly affect the observed rate. It is possible that this K^+ effect requires edge plane sites and cannot operate on basal plane, thus leading to very low basal rates. The large decrease in k_{GC}^0 for $Fe(CN)_6^{3-/4-}$ by intentional anthraquinone adsorption[32] reinforces the importance of surface sites for fast kinetics of $Fe(CN)_6^{3-/4-}$ at carbon.

The relationship between k_{GC}^0, k_b^0, and homogeneous self-exchange rate, k_{exc}, is plotted in Figure 4. Marcus proposed the simplest form of the relationship between k^0 and k_{exc} (eq 1), which is expected to apply in the absence of work terms introduced by the electrode:[33-36]

$$(k_{exc}/Z_{exc})^{1/2} = k^0/Z_{el} \quad (1)$$

where Z_{exc} and Z_{el} are the associated frequency factors (usually taken as 10^{11} M^{-1} s^{-1} and 10^4 cm s^{-1}, respectively). Several investigations support eq 1 for Hg and Pt electrodes for a variety of apparently outer sphere redox systems.[35-38] As pointed out by Weaver, however, eq 1 neglects several potentially important work terms which lead to generally smaller k^0 values than those predicted from eq 1.[39-41] Weaver's treatment predicts a linear dependence of work-corrected log k_{obs}^0 on log k_{exc}, with a slope of 0.5. Since the k_{GC}^0 values are at or near the instrumental limit, no correlation could be observed with k_{exc} for GC electrodes. Ignoring $Fe(CN)_6^{3-/4-}$, the seven apparently uncomplicated systems show a trend with k_{exc} (Figure 4), but the k_b^0 values are 3–5 orders of magnitude lower than that predicted from eq 1. In the absence of some unknown mechanistic complication which requires edge sites, this rate shortfall must be caused either by much larger work terms for HOPG or by some physical property of HOPG, or both.

Basal plane HOPG differs from GC in several ways which could affect electron-transfer kinetics. It is hydrophobic,[42,43] has a relatively high resistance normal to the surface,[1] has a low density of electronic states compared to metals or GC,[44,45] and has unusual double layer effects related to its semimetal character.[17-19,44,45] While the list of "uncomplicated" systems is too short to establish the relative importance of these effects on basal plane kinetics, some observations deserve note. First, hydrophobic effects cannot be the sole cause of slow kinetics since systems of similar charge and structure, and presumably hydrophobicity (e.g., $Fe(phen)_3^{2+/3+}$ and $Co(phen)_3^{2+/3+}$), have very different rates. Furthermore, basal rates are largely independent of redox system charge. Second, the c-axis resistivity of HOPG would yield less than 1 Ω of uncompensated resistance and would be roughly equal for all systems. Third, any unusual double layer or space charge effects for basal plane should vary greatly with the potential relative to the pzc.[17-19,44,45] The pzc for HOPG has been reported as −0.24 V vs SSCE for a variety of aqueous electrolytes,[17-19] and that value was confirmed here for 1 M KCl. As shown in Figure 5, the observed rates show no obvious perturbations when $E_{1/2}$ is near the pzc, with fast and slow rates observed on either side of the pzc. So space charge capacitance (and associated potential drop) and double layer effects are unlikely to be the sole reasons for low k_b^0. Fourth, the low density of states (DOS) near the Fermi level of HOPG could slow down electron transfer relative to GC. According to Gerischer et al.[45] the DOS for HOPG reaches a minimum of 2.2×10^{-3} states $atom^{-1}$ eV^{-1} at the bulk Fermi level of graphite but increases rapidly away from this potential. This minimum is approximately 2 orders of magnitude lower than that of

(30) Peter, L. M.; Durr, W.; Bindra, P.; Gerischer, H. *J. Electroanal. Chem. Interfacial Electrochem.* **1976**, *71*, 31.
(31) Goldstein, E. L.; Van De Mark, M. R. *Electrochim. Acta* **1982**, *27*, 1079.
(32) Pontikos, N. M.; McCreery, R. L., unpublished work.
(33) Marcus, R. A. *J. Phys. Chem.* **1963**, *67*, 853.
(34) Kawiak, J.; Kulesza, P.; Galus, Z. *J. Electroanal. Chem. Interfacial Electrochem.* **1987**, *226*, 305.
(35) Saji, T.; Yamada, T.; Aoyagui, S. *J. Electroanal. Chem. Interfacial Electrchem.* **1975**, *61*, 147.
(36) Saji, T.; Maruyama, T.; Aoyagui, S. *J. Electroanal. Chem. Interfacial Electrchem.* **1978**, *86*, 219.
(37) Sohr, R.; Muller, L. *Electrochim. Acta* **1975**, *20*, 451.
(38) Penner, R.; Heben, M.; Longin, T.; Lewis, N. S. *Science* **1990**, *250*, 1118.
(39) Weaver, M. J., Zuckerman, J. J., Eds. *Inorganic Reactions and Mechanisms*; VCH: New York, 1986; Vol. 15, pp 153–163.
(40) Weaver, M. J. *J. Phys. Chem.* **1980**, *84*, 568.
(41) Weaver, M. J. *J. Phys. Chem.* **1976**, *15*, 1733.
(42) Schrader, M. E. *J. Phys. Chem.* **1975**, *79*, 2508.
(43) Schrader, M. E. *J. Phys. Chem.* **1980**, *84*, 2774.
(44) Gerischer, H. *J. Phys. Chem.* **1985**, *89*, 4249.
(45) Gerischer, H.; McIntyre, R.; Scherson, D.; Storck, W. *J. Phys. Chem.* **1987**, *91*, 1930.

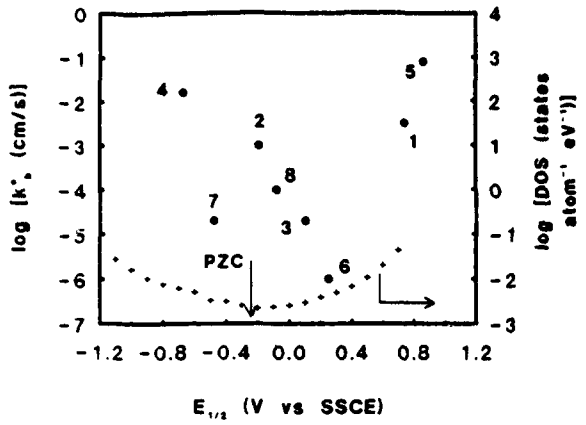

Figure 5. Solids circles are validated basal plane HOPG rate constants (log k_b^0) plotted versus $E_{1/2}$ (defined in text) for systems involving one-electron transfers. Corresponding data and number assignments from Table II. Crosses are the DOS for HOPG, from ref 45.

gold (0.28 states atom^{-1} eV^{-1}).[46] The trend in the DOS calculated by Gerischer et al. from capacitance data for HOPG is shown in Figure 5 for comparison. Note that the variation in k_b^0 with $E_{1/2}$ does not track the DOS in any obvious way. Although the low DOS for HOPG may be a factor in depressing k_b^0 compared to k_{GC}^0, the dependence of k_b^0 on redox system $E_{1/2}$ is not that predicted if the DOS is the only important factor.

CONCLUSIONS

The 13 redox systems exhibit a wide range of electron-transfer rates on the basal plane of HOPG, but all are slower on basal plane graphite than on GC. Although the magnitudes of the differences in rate between GC and HOPG are somewhat uncertain due to residual defects, it is clear that rates on basal plane HOPG are 1–5 orders of magnitude lower than those on GC. The results permit identification of at least three major factors affecting electron transfer at carbon: charge-transfer mechanisms which are promoted by edge plane (e.g. those involving proton transfer), physicochemical properties of basal plane which retard electron transfer (e.g. low density of electronic states), and the homogeneous self-exchange rate of the redox system involved. One or more of these effects can lead to major differences in observed rates for different carbon electrode materials and surface pretreatments. By continuing to examine both ordered graphite and GC surfaces, we intend to characterize these major factors affecting observed rates on carbon electrodes more completely, with the long-range goal of providing a structural basis for electron-transfer reactivity.

ACKNOWLEDGMENT

The authors thank Mark McDermott, Christie Allred McDermott, Robert Jaworski, and Stephen Feldberg for useful discussions and Arthur Moore at Union Carbide for the gift of HOPG. The work was supported by the Air Force Office of Scientific Research.

RECEIVED for review April 6, 1992. Accepted July 20, 1992.

(46) Kokko, K.; Ojala, E.; Mansikka, K. *Phys. Status Solidi B* **1989**, *153*, 235.
(47) Campion, R. J.; Purdie, N.; Sutin, N. *Inorg. Chem.* **1964**, *3*, 1091.
(48) Brown, G.; Sutin, N. *J. Am. Chem. Soc.* **1979**, *101*, 883.
(49) Farina, R.; Wilkins, R. G. *Inorg. Chem.* **1968**, *19*, 514.
(50) Bock, C. R.; Connor, J. A.; Giutierrez, A. R.; Meyer, T. J.; Whitten, D. G.; Sullivan, B. P.; Nagle, J. K. *Chem. Phys. Lett.* **1979**, *61*, 522.
(51) Ruff, I.; Zimonyi, M. *Electrochim. Acta* **1973**, *18*, 515.
(52) Hoddenbaugh, J. M. A.; Macartney, D. H. *Inorg. Chem.* **1990**, *29*, 245.
(53) Kurland, R. J.; Winkler, M. E. *J. Biochem. Biophys. Meth.* **1981**, *4*, 215.
(54) Dwyer, F. P.; Sargeson, A. M. *J. Phys. Chem.* **1961**, *65*, 1892.

Reprinted from Analytical Chemistry, 1993, 65.

Scanning Tunneling Microscopy of Carbon Surfaces: Relationships between Electrode Kinetics, Capacitance, and Morphology for Glassy Carbon Electrodes

Mark T. McDermott, Christie Allred McDermott, and Richard L. McCreery*

Department of Chemistry, The Ohio State University, 120 West 18th Avenue, Columbus, Ohio 43210

Polished, fractured, heat-treated, and laser-activated glassy carbon (GC) surfaces were examined by scanning tunneling microscopy (STM) in ambient air. Polished electrodes, as well as those which were vacuum heat treated (VHT) or laser activated (25 mW/cm²) after being polished, were comparably smooth in 2.5-μm STM scans, exhibiting root-mean-square roughness (RMSR) of ~4 nm. Fractured, unpolished surfaces were significantly rougher (RMSR ~20 nm) and exhibited numerous nodules with diameters in the range of 50–300 nm. Polished surfaces laser activated at high-power density (70 MW/cm²) showed unexpected features along polishing scratches, apparently caused by local melting. The heterogeneous electron-transfer rate constant (k^o, cm/s) and capacitance (C^o, μF/cm²) were also determined for the STM-characterized surfaces. Although rougher surfaces generally exhibited higher C^o, major differences in k^o were observed for surfaces with similar roughness and appearance. The results are consistent with the dominance of surface cleanliness in the mechanism of laser activation. Combined with past results based on adsorption, the morphological data indicate that differences in surface roughness are unimportant for laser activation of $Fe(CN)_6^{4-/3-}$ kinetics. Furthermore, the STM images reveal morphological effects of laser activation and polishing which were not apparent from previous electrochemical results.

INTRODUCTION

Effective applications of solid electrodes in analysis, synthesis, and energy conversion result in part from an understanding of electrode surface properties and their effects on electron transfer. Glassy carbon (GC) is widely used as an electrode for analysis and as a substrate for modified electrodes largely because of its hardness, wide potential range, durability, and cost. However, the surface properties of a typical GC electrode are not thoroughly understood due to the variety of procedures used to prepare these electrodes and the large number of variables at the surface. The many procedures and associated effects on electrode kinetics and capacitance have been reviewed recently.[1] Because these surfaces are not well-defined, the major factors which determine electrochemical behavior have not been completely determined. The relationship between surface structural variables of GC and electrochemical phenomena such as heterogeneous electron-transfer kinetics and differential capacitance is the subject of this report.

Surface properties of carbon electrodes which affect electrochemical reactivity may be classified into four categories: carbon microstructure, surface roughness, physisorbed impurities, and chemisorbed species, particularly oxides. The microstructural properties of various carbon materials are determined by their microcrystallite size, which will in turn determine the relative distribution of basal plane and edge plane regions at the surface. Graphite edge plane has been shown to differ greatly in electrochemical behavior from basal regions on ordered graphite surfaces.[1-10] However, the electrode activity will also be affected by the remaining three variables: roughness may determine the number of active sites, physisorbed impurities may cover or block active sites, and oxides may alter the mechanism of electron transfer altogether. Whether or not these variables are important to the behavior of a given electrode is determined by the electrode material and preparation history.

Our group and others have reported a number of surface preparations for GC electrodes. Pertinent examples of pretreatment methods are polishing,[11-13] laser activation,[14-19] vacuum heat treatment,[13,20-22] and exposure of the fresh bulk carbon by fracturing a GC rod in situ.[17,18,23,24] The purpose of these and other preparation schemes is to modify one or more of the GC surface variables mentioned above in order to affect electron-transfer rates of target redox systems. However, the effect of any particular electrode preparation procedure on the many GC surface factors remains unclear. For example, fracturing a GC electrode in solution should yield a surface relatively free of chemisorbed and physisorbed impurities with a microcrystallite size representative of the bulk carbon material. A polished surface, on the other hand,

* Author to whom correspondence should be addressed.

(1) McCreery, R. L. In *Electroanal. Chemistry*; Bard, A. J., Ed.; Dekker: New York, 1991; Vol. 17, pp 221–374.
(2) Randin, J. P.; Yeager, E. *J. Electrochem. Soc.* **1971**, *118*, 711–714.
(3) Randin, J. P.; Yeager, E. *J. Electroanal. Chem.* **1972**, *36*, 257–276.
(4) Randin, J. P.; Yeager, E. *J. Electroanal. Chem.* **1975**, *58*, 313–322.
(5) Bowling, R.; Packard, R.; McCreery, R. L. *J. Am. Chem. Soc.* **1989**, *111*, 1217–1223.
(6) Bowling, R.; Packard, R. T.; McCreery, R. L. *Langmuir* **1989**, *5*, 683–688.
(7) Rice, R. J.; McCreery, R. L. *Anal. Chem.* **1989**, *61*, 1637–1641.
(8) Robinson, R. S.; Sternitzke, K.; McDermott, M. T.; McCreery, R. L. *J. Electrochem. Soc.* **1991**, *138*, 2412–2418.
(9) McDermott, M. T.; Kneten, K.; McCreery, R. L. *J. Phys. Chem.* **1992**, *96*, 3124–3130.
(10) Kneten, K. R.; McCreery, R. L. *Anal. Chem.* **1992**, *64*, 2518–2524.
(11) Kamau, G. N.; Willis, W. S.; Rusling, J. F. *Anal. Chem.* **1985**, *57*, 545–551.
(12) Hu, I.; Karweik, D. H.; Kuwana, T. *J. Electroanal. Chem.* **1985**, *188*, 59–72.
(13) Wightman, R. M.; Deakin, M. R.; Kovach, P. M.; Kuhr, P. M.; Stutts, K. J. *J. Electrochem. Soc.* **1984**, *131*, 1578–1583.
(14) Poon, M.; McCreery, R. L. *Anal. Chem.* **1986**, *58*, 2745–2750.
(15) Poon, M.; McCreery, R. L. *Anal. Chem.* **1987**, *59*, 1615–1620.
(16) Poon, M.; McCreery, R. L.; Engstrom, R. *Anal. Chem.* **1988**, *60*, 1725–1730.
(17) Rice, R. J.; Pontikos, N.; McCreery, R. L. *J. Am. Chem. Soc.* **1990**, *112*, 4617–4622.
(18) Pontikos, N. M.; McCreery, R. L. *J. Electroanal. Chem.* **1992**, *334*, 229–242.
(19) Strein, T. G.; Ewing, A. G. *Anal. Chem.* **1991**, *63*, 194–198.
(20) Fagan, D. T.; Hu, I.; Kuwana, T. *Anal. Chem.* **1985**, *57*, 2759–2763.
(21) Stutts, K. J.; Kovach, P. M.; Kuhr, W. G.; Wightman, R. M. *Anal. Chem.* **1983**, *55*, 1632–1634.
(22) Hance, G. W.; Kuwana, T. *Anal. Chem.* **1987**, *59*, 131–134.
(23) Rice, R.; Allred, C.; McCreery, R. *J. Electroanal. Chem.* **1989**, *263*, 163–169.
(24) Allred, C. D.; McCreery, R. L. *Anal. Chem.* **1992**, *64*, 444–448.

0003-2700/93/0365-0937$04.00/0

possesses a number of impurities and a microcrystalline structure quite different from that of the bulk carbon.[18,23,24] The fractured surface exhibits large heterogeneous electron-transfer rate constants (k^0) for the ferro-/ferricyanide redox system compared to polished GC surfaces, but it is not clear whether this increase in rate is due to differences in microcrystallite size, microscopic roughness, surface cleanliness, or a combination of these variables.

There have been a number of surface techniques employed to study the surface structure of GC electrodes. Techniques commonly employed are X-ray photoelectron spectroscopy (XPS) and Auger electron spectroscopy (AES),[11,12,20,21,25] Raman spectroscopy,[17,18,23] surface-enhanced Raman spectroscopy (SERS),[26,27] and scanning electron microscopy (SEM).[14,18,25,28] Scanning tunneling microscopy (STM) has been used extensively to characterize highly ordered pyrolytic graphite (HOPG) electrodes at atomic resolution, including examination of the effects of electrochemical and chemical oxidation.[30-32] In several cases, defects on HOPG surfaces have been associated with increased chemical and electrochemical reactivity.[9,31-35] In an SEM study of GC by Bodalbhai and Brajter-Toth,[29] the electrodeposition of copper at active sites was correlated with roughness and electron-transfer kinetics for $Fe(CN)_6^{4-/3-}$. It was concluded that treatments which increase the density of copper nucleation sites also increase the electron-transfer rate. These techniques have been useful for understanding carbon electrode structure/reactivity relationships, but the structural models for GC surfaces remain incomplete at the scale below the SEM resolution limit of ~100 Å. A few reports of atomic scale STM of GC have appeared,[36-38] but in no case was the observed morphology related to electrochemical behavior. Furthermore, the variety of GC preparation procedures and test redox systems has made it difficult to compare the performance of different surfaces under otherwise identical conditions. Accordingly, the current effort involves the use of STM to provide surface morphological information about GC surfaces resulting from several pretreatment procedures and comparison of the electrode kinetics and capacitance of these surfaces. STM is particularly attractive because of high spatial resolution, especially in the vertical direction. In addition, SEM images of polished GC have been shown to be modified by the presence of a carbon microparticle layer.[28]

Electrochemically activated GC surfaces which had previously been polished have been imaged by two groups. Wang et al. compared surface roughness and topography imaged by STM for two different methods of electrochemical pretreatment (ECP)[39] and also used STM to investigate GC surface passivation due to phenol oxidation.[40] Freund et al. compared STM images and atomic force microscopy (AFM) images of polished as well as electrochemically pretreated GC.[41] Both STM studies of electrochemically activated GC concluded that ECP resulted in a rougher surface relative to the initial polished surface. We report here an STM study of a number of other standard pretreatment procedures for GC electrodes. The surface morphology and relative roughness of conventionally polished, laser-irradiated, fractured, and vacuum heat treated GC surfaces are correlated with the electrochemical behavior as determined by the heterogeneous electron-transfer rate constant, k^0, for ferro-/ferricyanide and differential capacitance, C^0, for these surfaces. An essential component of our approach is observation of both STM images and electrochemical behavior on the *same* GC surface in order to reduce common problems with surface reproducibility. By comparing STM morphology and electrochemical activity for polished, laser-activated, fractured, and heat-treated GC, insights into electrode structure/reactivity relationships were obtained.

EXPERIMENTAL SECTION

Reagents. All solutions were prepared with water obtained from a Nanopure II system (Barnstead, Dubuque, IA). Potassium ferrocyanide was used as received from Baker (Phillipsburg, NJ). Potassium chloride was used as received from Jenneile Chemical (Cincinnati, OH). Solutions of 1 mM $K_4Fe(CN)_6$ in 1 M KCl were made fresh daily and purged with purified argon prior to use.

Electrode Preparation. Glassy carbon (GC-20) working electrodes were obtained from Tokai and employed in one of three different mechanical shapes: a 3-mm-diameter GC rod, a GC disk cut from a 2-mm-thick plate and sanded to shape, and GC microelectrodes fabricated as described previously.[18,24] All electrodes (GC disks and microelectrodes) used in the correlation of roughness and morphology with electrochemical behavior (Figures 1–3 and Tables I–III) were manufactured from a single 2-mm-thick plate of Tokai GC-20. The high-resolution STM images of fractured GC in Figure 4 were taken on a 3-mm-diameter Tokai GC-20 rod because of the ease of mounting and lack of sample tilt compared to fractured GC microelectrodes. No differences were observed in the STM images between fractured 3-mm GC rods and fractured GC microelectrodes. The electrochemical cell was made of Teflon and was equipped with a quartz window through which the electrode could be laser irradiated. Disk electrode areas were defined by a viton o-ring and microelectrode areas (ca. 0.5 × 0.5 mm) were defined by the exposed electrode face surrounded by a sheath of epoxy. The three-electrode cell was completed with a Bioanalytical Systems (West Lafayette, IN) Ag/AgCl (3 M NaCl) reference electrode and a platinum wire auxiliary electrode.

Polished electrodes were prepared by polishing with 600-grit silicon carbide paper followed by 1-, 0.3-, and 0.05-μm alumina (Buehler, Lake Bluff, IL) slurries on Microcloth polishing cloth (Buehler). Slurries were prepared from dry alumina and Nanopure water. Polished electrodes were sonicated in Nanopure water for ~5 min before placement in the electrochemical cell. Care was taken to ensure that a drop of water remained on the polished electrode during insertion into the Teflon cell until analyte solution was added. In-situ laser activation of polished electrodes in Nanopure water was performed with a Nd:YAG laser (Model 580-10, Quantel) operating at 1064 nm with 9-ns pulses. In order to partially average spatial and temporal variations of the laser intensity, three successive pulses were applied to the electrode. For this study, power densities of 25 and 70 MW/cm² were utilized. Fracturing procedures were as described previously.[16,17,22,23] Fractured surfaces were created *in situ* by breaking a GC microelectrode flush with the surface of the embedding epoxy (Eccobond 55, Emerson and Cuming, Inc., Woburn, MA). Electrochemical measurements were taken immediately after fracturing. Heat treatment procedures were similar to those of Fagen et al.[39] Rate constant and capacitance data were obtained

(25) Engstrom, R. C.; Strasser, V. A. *Anal. Chem.* **1984**, *56*, 136–141.
(26) Alamoyar, Y. W.; McCreery, R. L. *Anal. Chem.* **1991**, *63*, 1289–1295.
(27) Alamoyar, Y. W.; McCreery, R. L. *Langmuir* **1991**, *7*, 2370–2375.
(28) Kazee, B.; Weisshaar, D. E.; Kuwana, T. *Anal. Chem.* **1985**, *57*, 2739–2740.
(29) Bodalbhai, L.; Brajter-Toth, A. *Anal. Chim. Acta* **1990**, *231*, 191.
(30) Gewirth, A.; Bard, A. J. *J. Phys. Chem.* **1988**, *92*, 5563.
(31) Chang, H.; Bard, A. J. *J. Am. Chem. Soc.* **1990**, *112*, 4598.
(32) Chang, H.; Bard, A. J. *J. Am. Chem. Soc.* **1991**, *113*, 5588.
(33) Bowling, R.; Packard, P.; McCreery, R. L. *J. Am. Chem. Soc.* **1989**, *111*, 1217.
(34) Bowling, R.; McCreery, R. L.; Pharr, C. M.; Engstrom, R. C. *Anal. Chem.* **1989**, *61*, 2763.
(35) Snyder, S. R.; White, H. S.; Lopez, S.; Abruna, H. D. *J. Am. Chem. Soc.* **1990**, *112*, 1322.
(36) Hu, C. Z.; Feng, L.; Andrade, J. D. *Carbon* **1988**, *26*, 543–555.
(37) Elings, V.; Wudl, F. *J. Vac. Sci. Technol. A* **1988**, *6* (2), 412–414.
(38) Brown, N. M. D.; You, H. X. *J. Mater. Chem.* **1991**, *310*, 127–138.
(39) Wang, J.; Martinez, T.; Yaniv, D. R.; McCormick, L. D. *J. Electroanal. Chem.* **1990**, *278*, 379–386.
(40) Wang, J.; Martinez, T.; Yaniv, D. R.; McCormick, L. D. *J. Electroanal. Chem.* **1991**, *313*, 120–140.
(41) Freund, M. S.; Brajter-Toth, A.; Cotton, T. M.; Henderson, E. R. *Anal. Chem.* **1991**, *63*, 1047–1049.

Figure 1. Images, 10 000 nm (full-scale x and y), of GC electrodes after different pretreatment conditions: (A) polished GC, z scale 0–50 nm; (B) polished/laser-activated (25 MW/cm^2) GC, z scale 0–50 nm; (C) polished/laser-activated (70 MW/cm^2) GC, z scale 0–200 nm; (D) fractured GC, z scale 0–250 nm.

on a polished surface first and then this surface was removed from solution and deactivated by exposure to ambient air for ~12 h. After electrochemical kinetics and capacitance were again observed, the same surface was then heat treated and the last set of electrochemical data was obtained. Vacuum heat treatment (VHT) was carried out in an UHV chamber at 10^{-8}–10^{-9} Torr. GC disks were mounted on a sample probe tip, and the temperature was raised by ohmic heating. Heating and temperature sensing occurred on the back side of a GC disk electrode (1.5 mm thick), such that a 700 °C temperature was achieved 1–2 h. Heat-treated electrodes were exposed to ambient air for ~30 s while being inserted into the Teflon cell and bathed in analyte solution.

Highly oriented pyrolytic graphite (HOPG) was obtained from Arthur Moore (Union Carbide, Parma, OH). HOPG electrodes were cleaved with adhesive tape or with a razor blade as described previously.[9,10]

Electrochemical Measurements. Electrode areas were determined by chronoamperometry on a 5-s time scale in 1 mM $Fe(CN)_6^{4-/3-}$ in 1 M KCl. Linear sweep cyclic voltammetry experiments and k° determination were performed as described previously[9,10,18,24] utilizing a function generator (Tektronix Inc., Beaverton, OR) and an Advanced Idea Mechanics (Columbus, OH) potentiostat. Differential capacitance measurements were performed by the method of Gileadi[42,43] and described by us previously[9,17,18,23] using a 100-Hz, 20-mV peak-to-peak triangle wave centered at 0.0 V. All reported C° values are normalized to the projected electrode area, as determined from chronoamperometry. All potentials stated are relative to the Ag/AgCl (3 M NaCl) electrode. Simulated voltammograms were calculated with the finite difference approach, and the computer program was provided by Dennis Evans,[44] with a constant value of the transfer coefficient.

STM Conditions. STM images were obtained with a Nanoscope II (Digital Instruments Inc., Santa Barbara, CA). Most images were obtained with electrochemically etched 0.01-in.-diameter tungsten wire tips, as recommended by the manufacturer. Mechanically cut Pt/Ir (80/20) tips (Digital Instruments) were also used for comparison, but no significant differences between the two types of tips were observable in the STM images at the relatively low resolution utilized for most of this work. All images were taken in ambient air, and no changes were noted in the images for many hours after initial scans.

Low-resolution images (150-nm full scale and greater) were obtained with the 12 × 12 μm scan head in the "height" image mode (constant current) with a bias voltage of 500 mV and a set-point current of 0.5 nA. High-resolution images (25-nm full scale and lower) were taken with a 0.7 × 0.7 μm scan head in the "current" image mode (constant height) with bias voltages of 20–100 mV and set-point current of 2–5 nA.

GC samples were mounted with silver paste to a thin metal plate through which the bias voltage was applied. All polished

(42) Gileadi, E.; Tshernikovski, N. *Electrochim. Acta* **1971**, *16*, 579–584.

(43) Babai, M.; Tshernikovski, N.; Gileadi, E. *J. Electrochem. Soc.* **1972**, *119*, 1018–1021.

(44) Corrigan, D. A.; Evans, D. H. *J. Electroanal. Chem.* **1980**, *106*, 287.

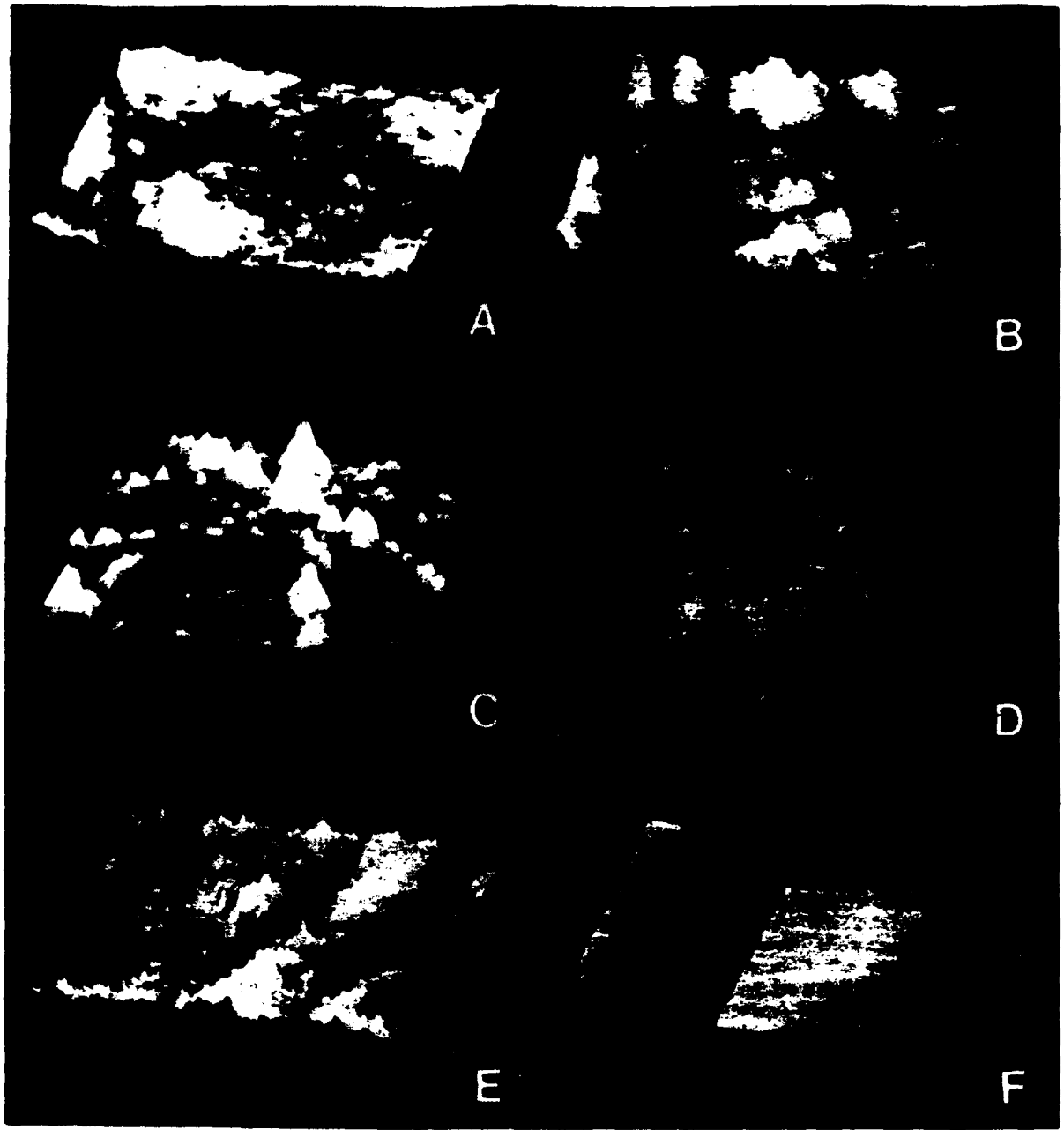

Figure 2. Images, 2500 nm, of electrodes under different pretreatment conditions: (A) polished GC, z scale 0–50 nm; (B) polished/laser-activated (25 MW/cm^2) GC, z scale 0–50 nm; (C) polished/laser-activated (70 MW/cm^2) GC, z scale 0–100 nm; (D) fractured GC, z scale 0–175 nm; (F) polished/vacuum heat treated GC, z scale 0–50 nm; (F) highly ordered pyrolytic graphite, z scale 0–10 nm.

surfaces yielded similar STM images, at the resolution employed, regardless of the electrode configuration (large disk or microelectrode). Images of fractured surfaces were obtained on the piece fractured from the electrode rather than the electrode itself, since the electrode would not fit in the STM sample region. Different surfaces as well as several different areas of each surface were examined to obtain representative images.

RESULTS

Figure 1 shows 10 × 10 μm survey scans of typical GC surfaces that were evaluated electrochemically. Due to image curvature which occurs with large scan areas, the images were software flattened but not smoothed or filtered. STM height scales are shown on the right sides of the plots along with the topographic grey scale; higher points appear as lighter shades. The images shown in Figure 1 are polished, polished/laser-irradiated at 25 MW/cm^2 (denoted P/L 25), polished/laser-irradiated at 70 mW/cm^2 (denoted P/L 70), and fractured surfaces. The polished (Figure 1A) and P/L 25 (Figure 1B) surfaces appear similar in morphology, with polishing scratches visible in both images, and in height, with features not exceeding 50 nm in height. The P/L 70 (Figure 1C) and the fractured (Figure 1D) surfaces cover a greater height range and exhibit distinct morphological features. The P/L 70 surface exhibits isolated protrusions (shown as bright lines) that appear to originate from the polishing scratches that were present on the surface before laser irradiation. The fractured surface displays protrusions or nodules with diameters ranging from 50 to 300 nm. We have previously reported nodules on fractured GC electrodes based on SEM images.[16]

Parts A–D of Figure 2 show the same types of surfaces plotted in a 3-D perspective and on a smaller x, y scale. In

Table I. STM Results for Seven Carbon Electrode Surfaces

surface	samples	images	RMSR (nm)	Z_{max} (nm)
polished	6	13	4.1 ± 1[a]	36 ± 8[a]
P/L 25	4	10	4.4 ± 1	37 ± 10
P/L 70	6	17	11 ± 4	96 ± 33
fractured	5	10	20 ± 5	140 ± 30
P/DEAC	2	4	4.7 ± 1	38 ± 7
P/VHT	3	6	4.5 ± 0.6	37 ± 4
HOPG	1	1	0.24	2.0

[a] Standard deviation of RMSR and Z_{max} for the number of images examined.

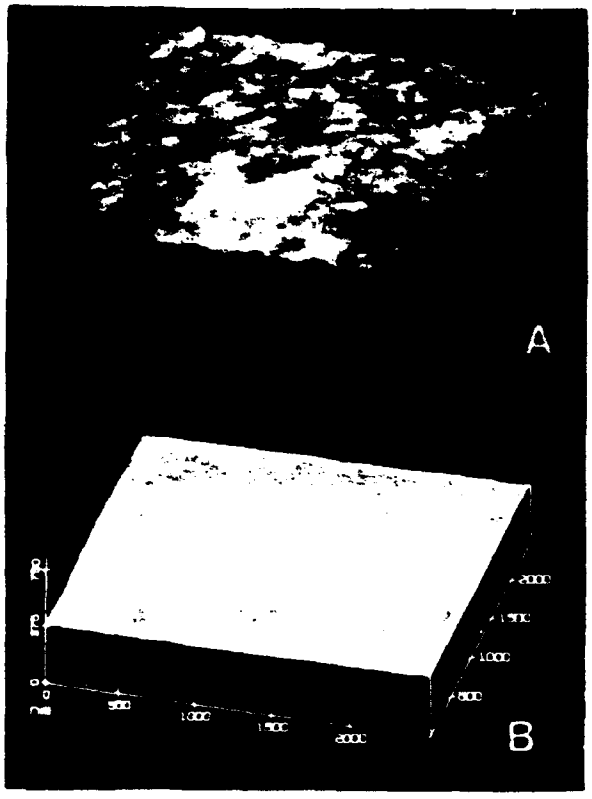

Figure 3. Image, 2500 nm, of (A) fractured GC plotted in a 1:1 aspect ratio compared to a similar image of (B) polished GC. z scale is 0–750 nm.

addition, images of polished/VHT (denoted P/VHT) and highly oriented pyrolytic graphite surfaces are shown in Figure 2E and F. Note the difference in z-axis scale from image to image. With this mode of image display, the differences in the surface morphologies are particularly noticeable. Polished, P/L 25, and P/VHT surfaces (Figure 2A, B, and E) appear similar, with all images employing identical height scales and exhibiting polishing scratches. The distinctive morphologies of the fractured and P/L 70 surfaces (Figure 2C and D) are apparent and will be discussed in detail below. Again, these surfaces exhibit greater height variation than the other surfaces. Figure 2F is a typical HOPG basal plane surface containing a step defect for comparison with the other images.

To provide a quantitative comparison of surface roughness, the root-mean-square roughness (RMSR) function of the Nanoscope II software was employed. RMSR is defined as the standard deviation of the height of the surface calculated from all points obtained during a given scan. For example, the image of HOPG in Figure 2F yields an RMSR of 0.24 nm, while that of fractured GC (Figure 2D) yields 20.4 nm. Although RMSR has not been established as a rigorous quantitative measure of surface roughness, it does provide a comparison for different surfaces. An additional but less statistically useful parameter is Z_{max}, which is the difference between the minimum and maximum surface heights. Z_{max} and RMSR results are listed in Table I. Note that both values also include standard deviations of Z_{max} and RMSR for the number of images indicated.

Figure 3 illustrates how the fractured surface, which exhibits the highest Z_{max} and RMSR, would appear if plotted with a 1:1 aspect ratio between the x, y scale and the z scale. In Figure 2, and in typical STM images, the z scales are expanded in order to enhance surface features. In Figure 3, the distance on the z axis was adjusted to equal those of the x and y axes. A polished surface (from Figure 2A) is plotted similarly for comparison. Without expansion of the z-axis scale, both surfaces appear much smoother.

The unusual morphology of the fractured GC surface is shown at successively higher magnification in Figure 4. Image 4A shows the variation in nodule diameter, while 4B shows an intersection of three nodules with ca. 200-nm diameters. Images C and D show the top of the upper left nodule of Figure 4B, with a full-scale scan range of 25 nm. Note that the apparent roughness persists even on a scale of ca. 1 nm.

Electrochemical Results. Table II shows electron-transfer rate constants and capacitance for the six types of surfaces examined by STM. The relatively large area of several electrode types limited the scan rate to 10 V/s or less, so rate constants above 0.1 cm/s are lower limits of the true values. As noted by several authors,[12,13,17] the variability of k° for $Fe(CN)_6^{4-/3-}$ on polished GC is quite large due to variations in cleanliness but is often in the range of 10^{-3}–10^{-2} cm/s. The k° values obtained here are somewhat higher than typical, but do show a large standard deviation (50%) typical of polished surfaces.

Laser activation at either 25 or 70 MW/cm² or fracturing led to reliably large k° values. Since the ΔE_p's at these surfaces were near the reversible limit of 57 mV, k° determinations based solely on ΔE_p are of limited accuracy. Figure 5 shows a comparison of the experimental voltammogram for $Fe(CN)_6^{4-/3-}$ at a fractured GC surface and a simulated response for $k^\circ = 0.40$ and $\nu = 10$ V/s. A k° of 0.40 was the lowest which yielded a good fit to the experiment, so a k° estimate of >0.4 cm/s is reliable in this case. The aberrant background on the experimental voltammogram is due to the differences in the background current between the $Fe(CN)_6^{4-/3-}$ voltammogram and that obtained in supporting electrolyte, leading to inaccurate background subtraction. The background current on activated GC varies with time, making background subtraction incomplete. A more rigorous investigation of $Fe(CN)_6^{4-/3-}$ kinetics has been performed on these surfaces at scan rates which yielded a more reliable rate constant of 0.5 cm/s.[17] The fractured GC and the P/L 70 surfaces exhibited rate constants at least 6 times greater than that of the initial polished electrode (>0.4 vs 0.060 cm/s). The rate constant value for the P/L 25 electrode is larger than that of the original polished surface by more than a factor of 5 (>0.3 vs 0.060 cm/s). Recall that although the STM data show that the fractured and P/L 70 surfaces possess distinct morphologies with high Z_{max} and RMSR values, the morphology and the Z_{max} and RMSR values of the P/L 25 surface are very similar to those acquired for the polished surface.

Finally, the P/VHT surfaces yielded rate constant values similar to the polished surface. These results are consistent with those of Kuwana et al.[20] The ΔE_p for $Fe(CN)_6^{4-/3-}$ at 10 V/s increased from 98 to 230 mV upon deactivation in ambient air, but after heat treatment, reactivation of the

Figure 4. Fractured GC under higher resolution conditions: (A) 500-nm scan with z scale 0–70 nm; (B) 200-nm scan with z scale 0–40 nm; (C) 25-nm scan with z scale 0–20 nm; (D) 25-nm scan with z scale 0–20 nm. Images C and D were acquired at the upper left corner of sample in image B.

Table II. Electrochemical Results

surface	RMSR (nm)[a]	ΔE_p(mV)[b]	k° of $Fe(CN)_6^{4-/3-}$ (cm/s)	C°[c] (μF/cm^2)	N[d]
polished	4.1	96 ± 29	0.06 ± 0.03	33 ± 6	14
P/L 25	4.4	71 ± 12	>0.3	34 ± 7	4
P/L 70	11.0	62 ± 6	>0.4	120 ± 31	3
fractured	20.0	58 ± 4	>0.4	75 ± 16	4
P/DEAC	4.7	232 ± 42	(8.4 ± 4) × 10^{-3}	15 ± 2	3
P/VHT	4.5	96 ± 13	0.065 ± 0.020	40 ± 5	3
HOPG[e]	0.24	>1200	<1 × 10^{-6}	<1.0	

[a] Values repeated from Table I. [b] ν = 10 V/s. [c] Based on chronoamperometric area. [d] For electrochemical results, not RMSR. [e] Values from ref 8.

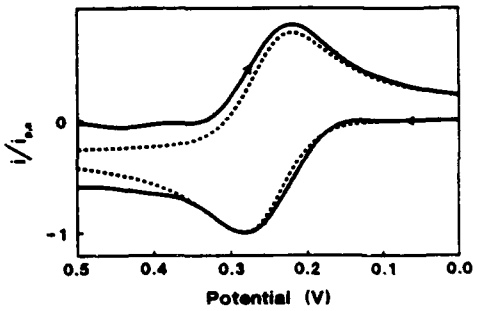

Figure 5. Experimental (solid line) and simulated (dashed line) cyclic voltammograms of 1 mM $Fe(CN)_6^{4-/3-}$ on fractured GC in 1 M KCl at ν = 10 V/s. Simulation assumed α = 0.5, k° = 0.4 cm/s, and D_{red} = 6.32 × 10^{-6} cm^2/s.

electrode occurred to a level equal to or greater than that of the initial polished surface.

Differential capacitance (C°) values are also shown in Table II. The fractured and P/L 70 surfaces exhibit higher C° values than the other surfaces as well as the largest variation in capacitances. C° values for polished, P/L 25, and VHT surfaces are similar. Note that deactivation decreased C° by a factor of 2 while decreasing k° of $Fe(CN)_6^{4-/3-}$ by a factor of 7 from the original polished surface. The significant influence of adsorbed airborne impurities on the activity of GC is illustrated in these decreases in k° of $Fe(CN)_6^{4-/3-}$ and C° from the polished to the P/DEAC surface. We have observed that exposure of a polished GC surface to air for even a few seconds leads to lower rate constants for $Fe(CN)_6^{4-/3-}$. As noted in the Experimental Section, great care was taken to ensure that a drop of water remained on the electrode surface during handling after polishing and sonication. Also note that the marked decrease in electrochemical activity through exposure to ambient conditions followed by reactivation via VHT was not accompanied by significant morphological changes.

DISCUSSION

The STM results discussed above are relevant to two issues regarding GC surface structure: morphological characteristics of GC electrodes under different pretreatment conditions and the quantitation of microscopic roughness and electrochemical activity. Previous insight on the morphology of GC electrodes prepared according to the methods reported here has originated from scanning electron microscopy.[18,28,29] Although SEM provides the necessary magnification for elementary image analysis, the resolution (particularly in the vertical direction) is poor compared to STM. Electrode roughness has been investigated previously by indirect means such as

Table III. Effect of Laser Power on Surface Protrusions for P/L Surfaces

power density (MW/cm^2)	no./ image[a]	% coverage[b]	av ht (nm)[c]
25	0		
30	0.5	1.3	20
40	2	4.5	20
50	5.6	10	26
70	12	42	57

[a] Average number of protrusions per 10 × 10 μm scan image based on four images. [b] Percentage of the total area in a 10 × 10 μm scan covered by protrusions. [c] Average height of protrusions for a given power density.

adsorption and differential capacitance measurements.[17,18,20,29,45] One would expect that k° and capacitance should scale with microscopic area of the electrode, all else being equal, and that activation may be caused in part by increases in surface roughness.

At first glance, there does appear to be a correlation between the STM determined RMSR, k°, and C°. The surfaces with the largest k° and C° (fractured and P/L 70) also exhibit the highest RMSR. Further consideration, however, reveals that the correlation is inconsistent. Polished, P/L 25, P/VHT, and P/DEAC surfaces have RMSR values which vary by less than 15%, while their k°'s vary by at least a factor of 50. Laser activation at 25 MW/cm^2 leads to an increase in k° of more than a factor of 5, yet the RMSR increase is only ~7%. These results are consistent with those presented previously based on SEM and phenanthrenequinone (PQ) adsorption.[17,18] They also confirm the conclusions from other laboratories that changes in microscopic roughness are not sufficient to explain the effects of activation procedures on kinetics and adsorption.[29,45] Large increases in k° occurred upon laser activation with only minor changes in morphology and microscopic area as determined from phenanthrenequinone adsorption.[17] In the case of the fractured surface, the higher RMSR is due to nodules and obviously implies higher roughness. On the basis of PQ adsorption, the fractured surface has about twice the microscopic area of the polished or P/L 25 surfaces.[18] Thus variations in roughness could reasonably account for a factor of ~2 in k°, but the major source(s) for k° variation must lie elsewhere.

We have previously attributed k° increases caused by laser activation to the removal of adsorbed impurities.[17] This conclusion is reinforced by the VHT experiments of Fagan et al.[20] and Stutts et al.,[21] repeated here with the addition of STM characterization. Deactivation and subsequent VHT led to minimal changes in RMSR from the polished surface yet yielded large variation in k°. As expected for impurity adsorption, the capacitance decreases for the P/DEAC surface. The low C° values reported by Fagan et al. were not observed here, probably due to the very different frequency domains used in the capacitance measurements. Taken together with results from other laboratories, the STM and electrochemical results strongly support the conclusion that the major factor controlling k° for $Fe(CN)_6^{4-/3-}$ on GC is surface cleanliness, with surface roughness playing a minor role. Stated semiquantitatively, roughness accounts for a factor of ~2 in observed k° on GC, while surface cleanliness can affect k° for $Fe(CN)_6^{4-/3-}$ by factors as large as several hundred.

The second major issue addressed by the STM examination deals with the morphological effects of various pretreatments, particularly laser activation. The unique features of the fractured surface are obvious from SEM or STM. The increased roughness leads to increases in capacitance and k° for fractured surfaces compared to P/L 25 surfaces, but these effects are not large (a factor of ~2). The major consequence of in-situ fracturing with regard to k° enhancement is the avoidance of impurity adsorption. At least at the resolution employed here, the morphological differences between fractured and polished surfaces do not appear to have major consequences for observed kinetics. The effect of polishing is to flatten the tops of nodules, yielding the surfaces of Figures 1A and 2A, accompanied by the undesired consequence of impurity adsorption.

While laser activation at 25 MW/cm^2 had no observable morphological effects at the resolution employed, higher power densities led to qualitatively distinct features. The protrusions apparent in Figure 2C formed along polishing scratches (apparent in Figure 1C). Atomic force microscope images of these features were very similar in appearance, indicating that they are not an artifact due to multiple tunneling points as the STM tip negotiates the scratches. The density and height of the protrusions increase with power density (Table III). At 30 MW/cm^2 and lower, they are very infrequent or not present, while at 70 MW/cm^2, they cover more than 40% of the surface. We have reported previously that significant excursions in C° and PQ adsorption occur at powers above 30 MW/cm^2 [18] and that a surface temperature simulation predicts that local melting should occur with a threshold between 30 and 40 MW/cm^2 for GC.[46] It is likely that the protrusions are caused by local melting, perhaps followed by expansion of heated, entrapped gases. The localization of protrusions on polishing scratches may result from the lower reflectivity inside the scratches, resulting in more efficient coupling of the laser light into the GC. In addition, the thermal conductivity near scratches could be different, leading to localized temperature variations.

The high-resolution images of the top of a nodule on the fractured surface (Figure 4C and D) are not of sufficient resolution to image individual atoms. The apparent roughness, which is on a much smaller scale than that shown in Figures 1 and 2, could be due to genuine morphological features or to variations in electronic interactions between the tip and the surface during scanning. Although these features are reproducible, it is not yet clear what they represent. A few reports here appeared on high-resolution STM of disordered carbon materials.[36-38] Atomic resolution was achieved, although the polishing procedures employed leaves some doubt about the condition of the surface. Unusual arrangements of carbon atoms were observed, perhaps because of deviations of the electronic structure of disordered carbons from that of HOPG. The high-resolution images on the fractured surface obtained here are of value because the fractured surface is unmodified by polishing and should be more representative of bulk structure. Attempts to obtain atomic scale images of the fractured surface are currently being made.

SUMMARY

The foremost conclusion drawn from the correlation of electrochemical properties with STM images is that some phenomenon other than surface roughening is responsible for increases in electrode activity toward $Fe(CN)_6^{4-/3-}$ upon laser or VHT activation. This statement is especially apparent with comparison of the polished and P/L 25 surfaces. Results show that laser activation at 25 MW/cm^2 causes no changes in capacitance and roughness, but causes a drastic increase in activity as evidenced by the heterogeneous rate constant for $Fe(CN)_6^{4-/3-}$. These results are consistent with a mech-

(45) Bodalbhai, L.; Brajter-Toth, A. *Anal. Chem.* **1988**, *60*, 2557.

(46) Rice, R. J.; McCreery, R. L. *J. Electroanal. Chem.* **1991**, *310*, 127-138.

anism in which electrode activity is determined by exposure of active sites and activation occurs through a cleaning process. STM images of polished, P/L 25, P/VHT, and P/DEAC electrodes show them to be similar in morphology, indicating that any changes induced by laser activation at low power densities and vacuum heat treatment at temperatures of ~700 °C are minimal. Fractured and P/L 70 surfaces exhibit distinct morphologies with a large amount of roughness and some variability in electrochemical behavior. Morphological characteristics of the P/L 70 surface are attributed to possible melting of the GC substrate at high laser power densities, beginning at 30–40 MW/cm^2. Investigation of these surfaces with AFM and with STM at higher resolution is currently underway.

ACKNOWLEDGMENT

The authors thank Robert S. Robinson for assistance with STM techniques and initial STM examinations of GC surfaces and Roy Tucker for assistance with UHV heat treatment. The work was supported by the Air Force Office of Scientific Research, an ACS Analytical Division Fellowship sponsored by Eli Lilly and Co. to C.A.M., and an Amoco Foundation Doctoral Fellowship to M.T.M.

RECEIVED for review July 27, 1992. Accepted December 30, 1992.

Reprinted from JOURNAL OF THE ELECTROCHEMICAL SOCIETY
Vol. 140, No. 5, May 1993
Printed in U.S.A.

Laser-Induced Transient Currents on Glassy Carbon Electrodes

Double Layer and Ion Adsorption Effects

Robert K. Jaworski* and Richard L. McCreery*

Department of Chemistry, The Ohio State University, Columbus, Ohio 43210

ABSTRACT

Intense laser pulses delivered to a glassy carbon (GC) surface *in situ* result in a transient current which depends both on electrode potential and the electrolyte solution. The transient decayed with a time constant of several hundred microseconds, much longer than the laser optical or thermal transient. The linear dependence of the transient charges on potential implies that the mechanism involves perturbation and restoration of the double layer and adsorbed ions. The charge contained in the current transient was a small (<10%) fraction of the total double layer charge indicating incomplete disruption of the double layer. In addition, the magnitude of the response is higher for surfaces with higher oxide coverage. The observations are consistent with adsorption of electrolyte cations with the strength of interaction decreasing in the order $H^+ > Li^+ > Na^+ > K^+ > Et_4N^+$. The cation interaction increases with increasing surface oxidation, probably because of interactions with surface functional groups.

Understanding the structure of the electrode/solution interface is of paramount importance in investigations of electrode kinetics at carbon electrodes. It is well-known that the rich surface chemistry of carbon materials contributes to the complexity and irreproducibility of kinetic measurements. Several electrode pretreatment procedures have been proposed to alleviate this problem and obtain more controllable surface structures and faster electrode kinetics, particularly for glassy carbon (GC). These include polishing,[1,2] electrochemical activation,[3-9] vacuum heating,[10-13] fracturing,[2,14-17] and laser activation.[16-24] Of relevance to the current report is the observation that intense laser pulses (*ca.* 25 MW/cm^2, 9 ns, 1064 nm) delivered to glassy carbon *in situ* results in a *ca.* 100-fold increase in the electron transfer rate for the $Fe(CN)_6^{-3/-4}$ couple.[17,19] Roughness changes and gross microstructural changes have been ruled out as mechanisms for the observed activation, and the rate enhancement was attributed to effective surface cleaning for the case of GC.[16,17] A unique feature of pulsed laser activation compared to conventional pretreatments is the ability to monitor an active surface very quickly after its creation, with microsecond time resolution if desired. The current effort was undertaken to investigate transient electrochemical phenomena initiated by laser activation, not only to learn about carbon surface properties, but also to investigate electrochemical events occurring very quickly after exposure of a reactive carbon surface to electrolyte solution. The overall objective of the work is an understanding of the factors affecting electrode kinetics on carbon electrodes and particularly the mechanism of laser activation.

* Electrochemical Society Active Member.

Much lower energy pulses which cause only a slight transient increase of the electrode surface temperature were employed in studies of the electrical double layer on mercury electrodes[25-28] and more recently to probe the electrode kinetics of fast reactions.[29,30] It was shown that pulsed irradiation of the electrode in supporting electrolyte solution produced current transients when the electrode was held at constant potential.[25] Analysis of the total charge of the current transients at various potentials gives the charge *vs.* potential curve. This technique did not become widely accepted for routine analysis of double layer properties on mercury, mainly because the existing classical techniques[31] were simpler, cheaper, and offered superb accuracy. Open-circuit potential measurements after laser pulses, however, were successfully employed to study thermal properties of the double layer.[25-28] It should be emphasized that the laser pulses used for activation of carbon electrodes have much higher power density and should be much more disruptive to the interfacial region.

A significant difference between mercury and solid electrodes (including carbon) lies in the fact that the surface of a solid electrode is not easily renewable. This problem significantly complicates double layer studies on carbon electrodes using classical methods.[32-36] Differential capacity and surface tension on carbon materials were studied by Soffer and co-workers[37-44] using differential cyclic voltammetry and spatial measurements of the electrodes.

In this paper we present a different approach for studying double layer properties on carbon electrodes. It is based on the application of laser pulses to probe the properties of the carbon electrode/solution interface and takes advantage of *in situ* surface cleaning by the laser pulse. The temperature transients generated by laser pulses with power

densities of 10 and 20 MW cm^{-2} are too low to cause major structural changes on GC and highly oriented pyrolytic graphite (HOPG) electrodes, but high enough to cause transient disturbance of the interfacial region and induce current transients. Short laser pulses also renew the surface by impurity desorption, thus activating the surface toward electron transfer. Therefore, the laser pulse provides not only a way of probing the properties of the interface but also *in situ* renewal of the electrode surface. Of particular note is the time resolution of the method compared to other pretreatment procedures. Since the laser pulse and resulting temperature transient occur on a nanosecond and microsecond time scale, respectively, the electrode may be monitored within microseconds after perturbation by the laser. A variety of electrochemical effects, including double layer relaxation, adsorption, and electron transfer may thus be examined within microseconds of the laser perturbation. In the case of laser activation of kinetics, the time resolution is many orders of magnitude faster than heat-treatments, polishing, or chemical pretreatments. In this study, we examined laser-induced perturbation of the double layer, with particular attention to the effects of electrolyte composition.

Experimental

The experimental apparatus is shown in Fig. 1. The Nd:YAG beam (Quantel 580-10) operating at 1064 nm (9 ns pulse length) was used to illuminate the electrode surface. Before entering the electrochemical cell through a quartz window, the laser beam passed near a photodiode (Scientech) which generated a trigger for the LeCroy 9400 digital oscilloscope. A conventional three-electrode potentiostat with a 0.1 μs time constant was used to monitor laser-induced current transients. The time constant of the cell was measured with a 5 mV square wave potential applied to a polished electrode in 0.1*M* KCl, and equaled 120 μs. In all cases, the charge resulting from a laser pulse, Q, was determined by numerically integrating the current *vs.* time transient. The Nd:YAG beam was aligned with a 632.8 nm HeNe pilot beam to allow positioning of the Nd:YAG beam on the electrode. The beam passed through approximately 5 mm of solution before striking the electrode, and totally illuminated the GC surface exposed to electrolyte. The measurements with GC were performed by applying a given electrode potential for 1 s before irradiating the electrode surface with the laser pulse. The measurements were performed in series of ten laser pulses separated by 1 min intervals. The working electrode was at open circuit between the measurements. Each series was carried out with a freshly polished and, where noted, further pretreated electrode (see below).

Commercial GC-20 electrodes (Bioanalytical Systems), GC-20 disks (Tokai), and HOPG (a gift from Arthur Moore of Union Carbide) were used. Standard procedure for the GC electrode surface preparation consisted of polishing with silicon carbide paper (600 grit) and then with 1.0, 0.3,

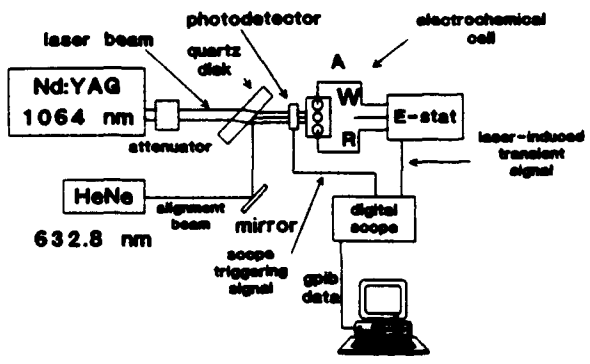

Fig. 1. Experimental apparatus for recording laser-induced current transients. A, W, and R stand for auxiliary, working, and reference electrodes, respectively.

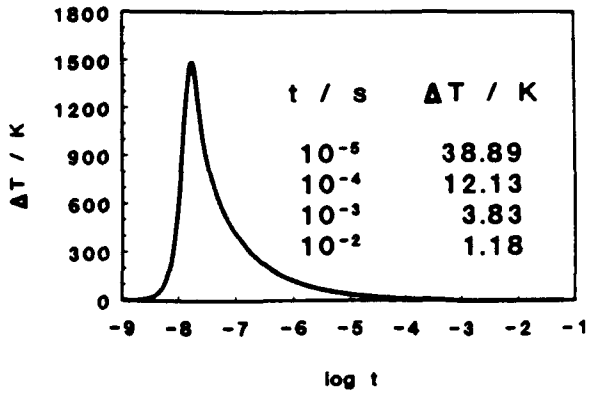

Fig. 2. The simulated temperature profile of a GC electrode surface in water during and after a 9 ns laser pulse with power density of 10 MW cm^{-2}. The temperature values after selected times are indicated, and the peak laser intensity occurs at log (t) = −8.3.

and 0.05 μm alumina. Electrodes were sonicated for 5 min between the polishing steps. Where noted, electrodes were further pretreated by anodic oxidation in 0.1*M* $NaNO_3$ at 1.8 V for 3 min, oxidation in a saturated solution of $(NH_3)_2Ce(NO_3)_6$ for 5 min, or ultrahigh vacuum heating at 600°C and 2 × 10^{-9} Torr for 2 h. Basal plane HOPG electrodes were prepared by cleaving superficial layers with adhesive tape. All working electrodes used in this work had surface areas equal to 0.071 cm^2. Platinum wire served as the auxiliary electrode. All potentials were measured and reported *vs.* Ag/AgCl reference electrode (BAS). Cathodic currents and charges are reported as positive values in tables and figures.

All chemicals were of reagent grade and were used without further purification. Solutions and rinses employed house distilled water, further purified using a Barnstead "NanoPure" System.

Results

The major effect of a short, intense, 1064 nm laser pulse on the electrode surface is a transient temperature excursion. With the significant assumption of no phase changes in electrode or solution, the surface temperature may be simulated, as noted previously by us and others.[15-30] The transient in Fig. 2 should be considered the maximum excursion of surface temperature for a 10 MW/cm^2, 9 ns, 1064 nm laser pulse on GC, and it provides an estimate of the duration of the transient. Even when solvent vaporization is ignored, ΔT decreases to 100 K in about 1 μs, and to 12 K in 100 μs.

The current transient resulting from a 10 mW/cm^2 laser pulse delivered to a GC electrode at a fixed potential of −0.2 V *vs.* Ag/AgCl is shown in Fig. 3A (points). The current represents a response to the laser perturbation in the absence of any intentional electroactive species and is presumably due to restoration of the surface and double layer after thermal disturbance. The integrated charge under the current transient is 0.59 μC/cm^2 in this case. For comparison, a GC electrode with a typical capacitance of 30 μF/cm^2 [16,17] held at a potential 280 mV away from the PZC has a double layer charge of 8.4 μC/cm^2. Thus the laser perturbation is small relative to the total charge present. Although the current transient follows a roughly exponential decay, a plot of log i *vs.* t is nonlinear. Figure 3b shows three exponential decays which are summed to yield the smooth curve of Fig. 3A. The three time constants indicated in Fig. 3B vary only slightly with potential and remain approximately an order of magnitude apart.

Figure 4 indicates the reproducibility of the integrated charge following the laser pulse (Q) for different surfaces. Figure 4A is a Q *vs.* laser pulse number for three physically different freshly polished electrodes, and Fig. 4B is a similar plot for a single electrode polished a total of four times.

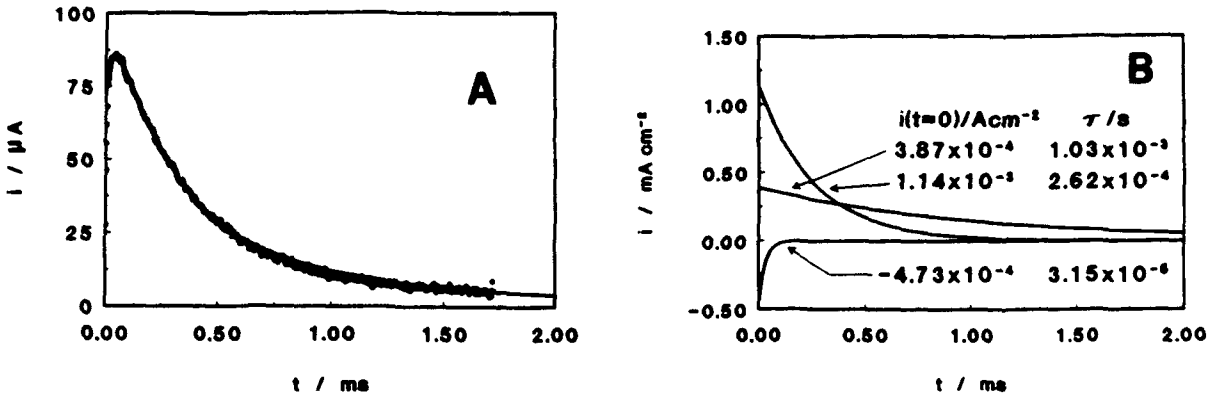

Fig. 3. Laser-induced current transient recorded at GC electrode in 0.1*M* KCl solution at −0.2 V. Laser power density was 10 MW cm^{-2}. Plot A shows the experimental transient (points) and the sum of the three component exponentials (smooth curve). Plot B shows the three exponential components and associated parameters.

In both cases, several laser pulses (3 to 5) were required to reach a constant value of Q for subsequent pulses, probably due to removal of surface debris or oxides by the laser. After this induction period, fairly constant Q values were observed for pulses 6-10. The relative standard deviation for the 6th to the 10th pulse on the same electrode polished four times was 13% (N = 18), while that for four different electrodes polished once each was 20% (N = 19). In subsequent measurements and plots, the Q of pulses 6 to 10 was averaged for a given surface unless noted otherwise.

As shown in Fig. 5, the laser-induced current transient is strongly dependent on the applied potential. For E_{app} = 0.1 V, the transient is quite small, while Q was positive or negative at potentials away from 0.1 V. As shown in Fig. 6, Q *vs.* E_{app} is linear, with an x-intercept of 0.18 V in this case. The slope of this plot is 2.8 μF/cm^2, much less than the differential capacitance of *ca.* 30 μF/cm^2. Note also from Fig. 6 that a higher laser power density changes both the slope and x-intercept of the Q *vs.* E_{app} plot. Figure 6 was based on the average of 6th to 10th laser pulses after polishing, where Q was weakly dependent on pulse number.

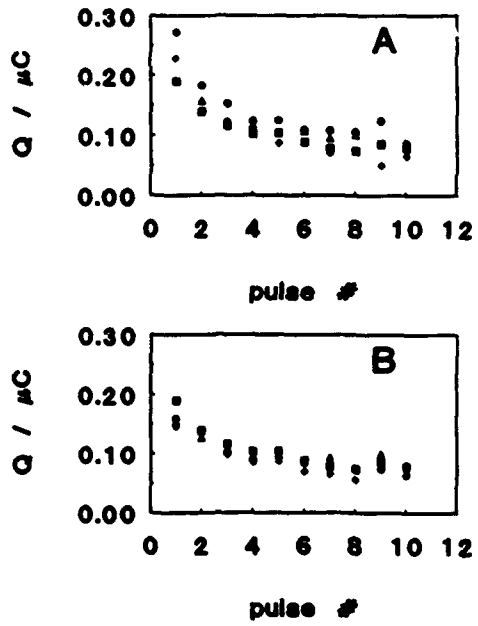

Fig. 4. The effect of the polishing procedure on the reproducibility of Q on GC in 0.1*M* HCl at −0.1 V with laser power density of 20 MW cm^{-2}. (A) Physically different electrodes polished before pulse no. 1. (B) A single GC electrode, repolished before each pulse series.

When the first pulse after polishing was used to construct Q *vs.* E, the plot was linear but with a higher slope. The x-intercept did not depend on laser pulse number, showing no trend with repeated pulses, and a mean and standard deviation of 0.19 ± 0.02 V (N = 10). The potential of zero response (PZR, where Q total = 0), is listed in Table I for several electrolytes.

The effect of electrolyte concentration on the transient response was examined briefly for KCl electrolytes, but the available range of concentrations was limited. For a range of concentrations from 1.0 to 0.01*M* KCl, the observed time constant increased greatly with decreasing concentration, as expected due to increasing solution resistance, and therefore RC. For example, the time constant increased by a factor of eight when the KCl concentration was decreased from 0.10 to 0.01*M*. Concentrations other than 0.1*M* were not studied in detail due to the poor signal to noise ratio for lower concentrations and potentiostat saturation for high concentrations.

Finally, several modifications to the carbon electrode surface were considered to explore their effects on the laser-induced current transient. Figure 7 shows transients for E_{app} = −0.1 V for polished GC (b); heat-treated GC (c, heated for 2 h at 600°C, at 2 × 10^{-6} Torr); HOPG freshly cleaved (d), and anodized GC (a, 1.8 V, 3 min, in 0.1*M* $NaNO_3$). Note that Q for HOPG is much smaller than for polished GC, and heat-treatment reduces Q for GC significantly. Anodized GC has a much larger Q than any other surface considered. The charge, PZR, and $\Delta Q/\Delta E$ for these surfaces are listed in Table II.

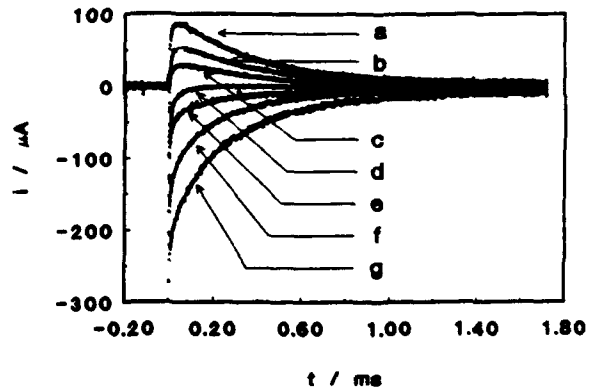

Fig. 5. The effect of the electrode potential on the laser-induced current transients on GC electrode in 0.1*M* KCl at power density of 10 MW cm^{-2}. The electrode potential was: a, −0.2 V; b, −0.1; c, 0.0; d, 0.1; e, 0.2; f, 0.3; and g, 0.4 V. Electrode was repolished before each transient.

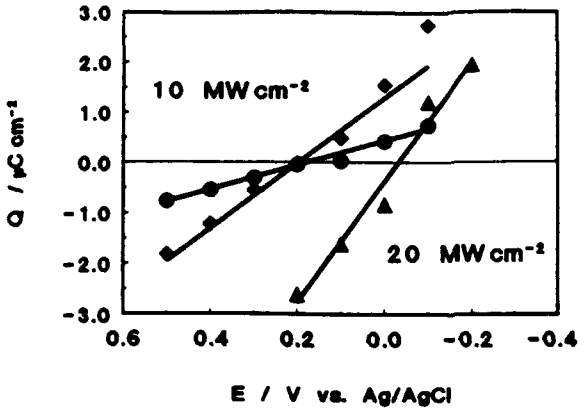

Fig. 6. The effect of the laser power density on Q in 0.1M HCl. Circles: 10 MW/cm², average 6th to 10th laser pulse after polishing; diamonds, 10 MW/cm², first pulse after polishing; triangles, 20 MW/cm², 6th to 10th pulse after polishing.

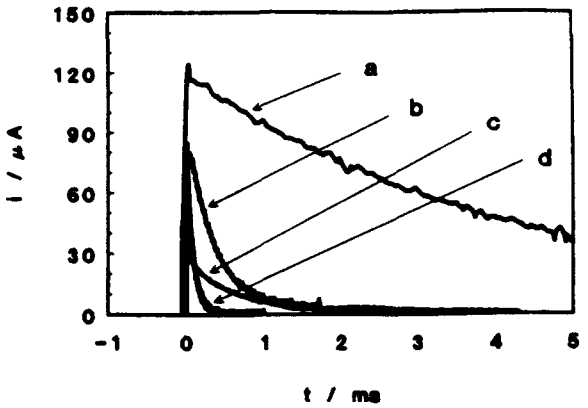

Fig. 7. The effect of electrode surface preparation on the current transient in 0.1M $NaNO_3$ at −0.1 V. Laser power density 10 MW cm⁻². Surfaces: a, GC after electro-oxidation in 0.1M $NaNO_3$ at 1.8 V for 3 min; b, polished GC; c, polished GC heated for 2 h at 600°C and 2×10^{-6} Torr; d, HOPG. The transient at HOPG was recorded in 0.1M NaCl solution.

Discussion

The first question which arises about the laser-induced current transient at a given potential is its origin. Superficially, the transient behaves as expected for reestablishment of the double layer after thermal perturbation by the laser pulse. The charge involved is only about 7% of that stored in the double layer, implying that the double layer structure is only partially disrupted. The time required for recharging is roughly a millisecond or so, much longer than the microsecond scale of the surface temperature transient, implying that most of the double layer restoration occurs at the ambient solution temperature.

Upon closer inspection, the transient is not simply an exponential decay expected for double layer charging, but rather consists of at least three exponentials with different time constants. The shortest (<40 μs time constant) involves very little charge (<10% of total), is weakly potential dependent, and may reflect a thermal or even electronic effect. It will not be considered further, except to say that it accounts for the initial rise during the first 50 μs of the observed transients. The remainder of the current decay is empirically accounted for by two exponentials with roughly equal contributions to the total charge, but time constants which differ by about a factor of ten. The time constants do not depend on the applied potential, but the charge attributable to each exponential does, approximately linearly. The faster of the two has a time constant of about 300 μs, close to the cell time constant observed for a small potential step (120 μs). It would be premature to associate these exponential decays with particular or even distinct chemical phenomena, but it appears unlikely that the observed decay is related to a Faradaic process. One would expect a redox process (surface or otherwise) to be strongly potential dependent, and not to show a linear progression through $Q = 0$ as the potential is varied around the PZR (Fig. 6). The potential dependence will be discussed in more detail below, but suffice it to say for now that Q *vs.* E_{app} has the behavior expected for a capacitor, without involving any Faradaic processes. Whatever the origin of the nonidealities in the exponential decay of the transient, the results are consistent with an origin based on thermally induced disruption of the double layer. There is no evidence for Faradaic processes, but the transient may involve both classical double layer effects and adsorption.

Surface reproducibility is a well-known problem with solid electrodes and was tested here by repetitive trials on several electrodes. Figure 4 demonstrates that the variation in Q is smaller for repetitive polishing than for physically different GC pieces. Previous experiments demonstrated that laser pulses of 25 MW/cm² and less have minimal effects on microscopic area.[16] The variability observed here for repetitive experiments is much smaller than the effects of potential, electrolyte, and carbon type on the current transients.

The potential dependence of the current transient shown in Fig. 5 and 6 demonstrates a linear dependence of Q on E. Both the overall Q and the charge attributed to both "slow" exponential decays show the same linear potential dependence. It is useful to define a potential of zero response (PZR) as the applied potential where Q is zero. Figure 6 shows that the PZR is about 0.18 V for 10 MW/cm² in 0.1M HCl. The PZR depends weakly on pulse number, with no trend observed in PZR for ten successive pulses. The PZR does vary with power density, as does the slope of Q *vs.* E. Like the total charge, the slope of the Q *vs.* E_{app} plot decreases

Table I. The effect of supporting electrolyte ions on the laser-induced current transients recorded with polished GC electrode at 10 MW cm⁻².

Solution[a]	Q at −0.1 V (C cm⁻²)	Q at 0.3 V (C cm⁻²)	PZR (V)	ΔQ/ΔE (F cm⁻²)
HCl	7.6×10^{-7}	-3.2×10^{-7}	0.18	2.8×10^{-6}
LiCl	4.5×10^{-7}	-3.5×10^{-7}	0.12	2.0×10^{-6}
NaCl	4.6×10^{-7}	-4.5×10^{-7}	0.10	2.3×10^{-6}
KCl	3.5×10^{-7}	-4.4×10^{-7}	0.08	2.0×10^{-6}
$(Et)_4NBr$	2.4×10^{-7}	-3.9×10^{-7}	0.05	2.2×10^{-6}
NaF	1.3×10^{-7}	-2.1×10^{-6}	−0.08	5.5×10^{-6}
$NaClO_4$	2.7×10^{-7}	-9.6×10^{-7}	−0.01	3.1×10^{-6}
$NaNO_3$	4.5×10^{-7}	-5.8×10^{-7}	0.08	2.6×10^{-6}
NaCl	4.6×10^{-7}	-4.5×10^{-7}	0.10	2.3×10^{-6}
NaBr	4.9×10^{-7}	-6.3×10^{-7}	0.08	2.8×10^{-6}
NaI	5.6×10^{-7}	-4.2×10^{-6}	0.13	2.5×10^{-6}

[a] 0.1M concentrations.

Table II. The effect of electrode surface preparation on the observed current transients on GC and HOPG in 0.1M $NaNO_3$ at 10 MW cm⁻².

Surface[a]	Q at −0.1 V (C cm⁻²)	Q at 0.3 V (C cm⁻²)	PZR (V)	ΔQ/ΔE (F cm⁻²)
GC oxidized[b]	7.5×10^{-6}	-1.2×10^{-6}	0.24	2.2×10^{-5}
GC oxidized[c]	3.8×10^{-6}	-2.3×10^{-6}	0.15	1.4×10^{-5}
GC polished	4.5×10^{-7}	-5.8×10^{-7}	0.08	2.6×10^{-6}
GC vacuum heated	2.5×10^{-7}	-3.2×10^{-7}	0.08	1.4×10^{-6}
HOPG[d]	9.7×10^{-8}	-1.2×10^{-7}	0.09	5.3×10^{-7}

[a] See text for the details of surface preparation.
[b] Anodic oxidation for 3 min at 1.8 V.
[c] Oxidation in saturated solution of $(NH_4)_2Ce(NO_3)_3$ for 5 min.
[d] In 0.1M KCl.

with pulse number, reaching a steady value after *ca.* five pulses.

Although the PZR does not necessarily equal the PZC, it is analogous in several ways. At potentials positive of the PZR, the transient resulting from the laser pulse is in the anodic direction, indicating electron flow away from the interface, and a buildup of excess anionic charge in the double layer. Similarly, a positive charge excess occurs when the potential is negative of the PZR. The linear change of Q with E_{app} is expected for an ideal capacitor, but the slope is less than the full double-layer capacitance because the double layer is not completely destroyed by the pulse. If such experiments were possible, complete destruction of the layer should yield a Q *vs.* E_{app} slope equal to that observed if an electrode were suddenly exposed to the solution and the double layer is formed.

In order to evaluate the ability of the current technique to study the properties of the electrode/solution interface, a series of experiments with various supporting electrolytes was performed. The results (Table I) are divided into two groups. The first one contains solutions of alkali metal chlorides, tetraethylammonium bromide, and hydrochloric acid to test the effect of cations on the transients and PZR. Sodium halides, nitrate, and perchlorate solutions constitute the second group, selected to test the effect of anions on the PZR. It is reasonable to assume after Barker and Cloke[25] that the PZR is related to the potential of zero charge (PZC), and that the direction of PZR shifts is the same as that of PZC. Therefore, the shifts of the PZR value can be used as a test of adsorption of ions on the electrode surface. It is well known (see, for example Ref. 31), that adsorption of cations will shift the PZC in a positive direction and adsorption of anions will shift it in negative direction. The variation in the PZR with cation (Table II) is consistent with adsorption of cations on the GC surface, with the strength of the interaction decreasing in the order $H^+ > Li^+ > Na^+ > K^+ > Et_4N^+$. In studies of ion uptake on electrochemically pretreated GC, Nagaoka *et al.*[51-55] reported a similar sequence $Li^+ > Na^+ \approx K^+ > Ba^{+2}$. At this point we cannot completely explain the nature of interactions leading to apparent adsorption of cations on the carbon electrode surface. However, it is not unreasonable to assume that the functional groups present on the surface of GC[56] are at least partially responsible for the observed behavior. Carboxylate or semiquinoid groups on carbon are either anionic or can exchange cations, and the strength of the surface interaction should vary with the cation size and charge density. Oxides are also known to affect the polarizability of the carbon surface, thus enhancing interactions with polar or ionic species. Such a mechanism could also enhance ion adsorption for cations with high charge density such as H^+ and Li^+.

Variation of the electrolyte anion does not produce a trend similar to the cations. Except for fluoride, the sodium halides show no trend in the PZR with anion size. The PZR for NaF is substantially more negative, implying a stronger anion interaction for F^- than for Cl^-, Br^-, or I^-. This observation is opposite to that observed for Pt, where larger halides chemisorb more strongly. In addition, fluoride would not be expected to interact more strongly with carbon via dispersion interactions, since it is less polarizable than iodide. However, these observations are consistent with ion adsorption mediated by surface oxides. The results in Table I imply that the cation is the major determinant of the PZR, probably due to cation interactions with anionic surface groups. Variation of the anion has a small effect for the sodium salts due to the relatively stronger interaction of Na^+ with the surface. In the case of fluoride, a bridging mechanism may be possible

$$>C = O^{\delta-} \cdots M^+ \cdots A^-$$

In such a case the stability of the structure is expected to be greater for F^- than for large anions, due to the stronger interaction of the F^- anion with metal ions compared to Cl^-, Br^-, or I^-.

To test the hypothesis that surface functional groups play a part in adsorption of ions on GC electrodes, the surface concentration of those groups was intentionally modified by either oxidation or vacuum heat-treatment of the electrode. Oxidation of a GC surface will increase the amount of surface functional groups,[9,57-63] while vacuum heat-treatment reduces the surface O/C ratio.[10-13] In addition to the specially treated GC electrodes, highly oriented pyrolytic graphite was employed as an electrode material. HOPG is known to have very low surface oxide concentration with the surface functional groups (if any) located on defects in the lattice structure. It should be emphasized that there are significant differences in structural and electronic properties between GC and HOPG which have to be taken into account when comparing these two materials.[56] However, these materials can be used to qualitatively correlate the charges observed in laser-induced current transients with a surface concentration of functional groups. The results for HOPG and GC after various pretreatments are shown in Table II. The Q for HOPG was much smaller than for GC, as would be expected for its smaller capacitance. More importantly, the substantial decrease in Q for vacuum heat-treated GC compared to polished GC supports the hypothesis that surface oxides play a role. Since heat-treatment does not affect surface morphology or roughness,[64] its main observable effect is reduction of surface oxygen. The much larger Q observed for anodized GC also indicates the strong dependence of surface charge on surface oxides.

Summary

The current *vs.* time and charge *vs.* potential responses to an *in situ* laser pulse on glassy carbon result in the following conclusions: first, the laser-induced temperature transient causes disruption of the double layer and adsorbed species, but the perturbation is small compared to the total double layer charge. Second, the potential dependence of the transient is consistent with double layer effects, but not a Faradaic process. Third, the potential dependence shows a trend with cation size, implying adsorption of cations in the order $H^+ > Li^+ > Na^+ > K^+ > Et_4N^+$, similar to that observed by Nagaoka *et al.* for anodized GC.[52-55] Finally, the response increases greatly with surface oxidation, implying increased cation adsorption to oxygen containing functional groups. The importance of both cation adsorption and surface oxides to activation mechanisms is currently under study.

Acknowledgment

This work was supported by the U.S. Air Force Office of Scientific Research.

Manuscript received Dec. 4, 1992.

The Ohio State University assisted in meeting the publication costs of this article.

REFERENCES

1. G. N. Kamau, W. S. Willis, and J. F. Rusling, *Anal. Chem.*, **57**, 545 (1985).
2. I. F. Hu, D. Karweik, and T. Kuwana, *J. Electroanal. Chem.*, **188**, 59 (1985).
3. R. C. Engstrom, *Anal. Chem.*, **54**, 2310 (1982).
4. T. Nagaoka and T. Yoshino, *ibid.*, **58**, 1037 (1986).
5. L. J. Kepley and A. J. Bard, *ibid.*, **60**, 1459 (1988).
6. G. M. Swain and T. Kuwana, *ibid.*, **63**, 517 (1991).
7. M. S. Freund, A. Brajter-Toth, T. M. Cotton, and E. R. Henderson, *ibid.*, **63**, 1047 (1991).
8. J. Wang, T. Martinez, D. R. Yaniv, and L. D. McCormick, *J. Electroanal. Chem.*, **278**, 379 (1990).
9. R. C. Engstrom and V. A. Strasser, *Anal. Chem.*, **56**, 136 (1984).
10. D. T. Fagan, I. F. Hu, and T. Kuwana, *ibid.*, **57**, 2759 (1985).
11. G. W. Hance and T. Kuwana, *ibid.*, **59**, 131 (1987).
12. K. J. Stutts, P. M. Kovach, W. G. Kuhr, and R. M. Wightman, *ibid.*, **55**, 1632 (1983).
13. M. R. Deakin, K. J. Stutts, and R. M. Wightman, *J. Electroanal. Chem.*, **182**, 113 (1985).
14. C. D. Allred and R. L. McCreery, *Anal. Chem.*, **64**, 444 (1992).

Electron Transfer Kinetics of Aquated $Fe^{+3/+2}$, $Eu^{+3/+2}$, and $V^{+3/+2}$ at Carbon Electrodes

Inner Sphere Catalysis by Surface Oxides

Christie Allred McDermott, Kristin R. Kneten,* and Richard L. McCreery**

Department of Chemistry, The Ohio State University, Columbus, Ohio 43210

ABSTRACT

The electron-transfer kinetics for three aquated metal ions with low self-exchange rates were examined on well-characterized carbon surfaces. All three ions exhibited slow kinetics on clean fractured glassy carbon (GC) and on the basal plane of highly ordered pyrolytic graphite (HOPG). The reactions appeared to be outer sphere and had rates approximately consistent with those predicted from the self-exchange rates. Electrochemical oxidation of either GC or HOPG greatly increased the electron-transfer rate constant to values significantly greater than predicted for outer-sphere reactions. The increase was greatest for $Eu_{aq}^{+3/+2}$ and was eliminated if the surface was silanized. Surface oxides provide sites for inner-sphere catalysis of the aquated ions at carbon, perhaps involving a surface oxide structure similar to the common ligand acetoacetonate.

Due principally to their widespread use in electrosynthesis and electroanalysis, carbon electrodes have been examined extensively, with particular attention to factors affecting electrode kinetics and background currents.[1-3] Most previous studies have been dominated by characteristics of the carbon surface and by pretreatments which alter the structure and reactivity of the carbon electrode. Since carbon has several forms and a rich surface chemistry, the task of relating surface structure and reactivity has been formidable. The results of these efforts have been discussed extensively, with particular attention to issues of surface microstructure, cleanliness, roughness, and oxidation.[1,4-11] In general, previous efforts have dealt with relatively few redox systems, particularly $Fe(CN)_6^{-4/-3}$, ascorbic acid, $Ru(NH_3)_6^{+2/+3}$, and several quinones. Of relevance to the current report are the observation that GC exhibits much higher heterogeneous-electron-transfer rate constants (k°) than the basal plane of HOPG,[9,12,13] and that thermal[6,14] or laser[12,13] activation or ultraclean polishing[5,8] greatly increases k° on GC. In addition, the observed kinetics for $Fe(CN)_6^{-3/-4}$ and similar benchmark systems do not correlate with surface oxidation provided the GC surface is initially clean.[1,15] A variety of arguments support the conclusion that activation of HOPG toward $Fe(CN)_6^{-3/-4}$ is not related to oxides *per se*, but rather to lattice damage accompanying their formation.

When the discussion is broadened to a wider variety of redox systems, the picture becomes somewhat more complex and less thoroughly understood. Seven inorganic redox systems normally regarded as outer-sphere systems exhibited k° values 1 to 5 orders of magnitude lower on HOPG than on activated GC,[16] as expected from the $Fe(CN)_6^{-3/-4}$ results noted earlier. In addition, several quinone systems were very slow on HOPG, perhaps because of the lack of sites for proton transfer.[11] Several workers have noted that the observed k° for $Fe^{+3/+2}$ increases when a polished GC surface is oxidized,[10,17,18] sometimes by factors of more than 100. Kovach *et al.* have reported large effects of electrochemical pretreatment (ECP) on the behavior of several metal complexes as well as dopamine and ascorbate, due largely to discrimination of the oxidized surface for cations over anions.[19] Armstrong *et al.* have described the importance of oxide sites to cytochrome charge transfer on carbon, with binding of the cytochrome to a surface oxide greatly accelerating electron transfer.[20,21] Cabaniss *et al.*,[11] Kepley and Bard,[22] and Nagaoka *et al.*[23,24] also have attributed kinetic activation of electrochemically pretreated GC to surface oxides. These results imply that different redox systems are affected differently by carbon surface variables, with some dependent on surface oxides and others not.

The issue of relating carbon surface structure to electron-transfer reactivity is important to the broader area of electrode kinetics. A large research effort has been invested in understanding the relationship between k° and homogeneous-electron-transfer rates, particularly in the context of Marcus theory.[25-34] To simplify the problem as much as possible, attempted correlations of k° and homogeneous rates used well-defined electrodes, particularly mercury. For outer-sphere redox systems after suitable work-term and double-layer corrections, k° tracks the square root of the homogeneous-self-exchange rate constant (k_{exc}) as predicted by Marcush theory.[31,34] The existence of an inner-sphere reaction pathway (such as a halide-bridging ligand on a platinum electrode) can greatly increase k° over that predicted from k_{exc}.[35-37] While significant progress has been made toward understanding and predicting k° on well-defined metal electrodes, such progress for carbon electrodes has been frustrated by their complex surface. The long-term goal of our work in this area is to understand both electrode-surface and redox-system variables which control k° on carbon.

Although polished GC is the most widely studied GC surface, its oxide coverage is variable, typically 7 to 15 atom percent (a/o),[1] and the involvement of oxide catalyzed routes in electron transfer is difficult to assess. Our approach here is to start with better defined carbon surfaces with very low oxide coverage. Basal plane HOPG is one example of a well-defined carbon surface with near zero surface oxides, provided it is prepared properly. We have reported also that the freshly exposed surface of GC is quite reactive for several redox systems.[12] Although it is rougher than polished GC,[38,39] it is initially free of oxides or polishing debris, and should closely approximate a pristine GC surface. The current report concerns the behavior of aquated $Fe^{+3/+2}$, $Eu^{+3/+2}$, and $V^{+3/+2}$ on HOPG and fractured GC before and after electrochemical oxidation of the carbon surface. In addition to the fact that HOPG and fractured GC provide less complex and better defined carbon surfaces than more conventional electrodes, the aquated redox systems exhibit unusual kinetic behavior which permits useful conclusions about electron-transfer mechanisms at carbon electrodes. The primary advantage of the current approach is the low initial surface oxide concentration on HOPG and fractured GC.

Experimental

Electrode preparation.—Glassy carbon (GC-20) electrodes were prepared from GC-20 plate as described previously.[12,39] Polished GC electrodes were prepared by initial sanding of the epoxy (Eccobond) mounted GC with SiC

* Electrochemical Society Student Member.
** Electrochemical Society Active Member.

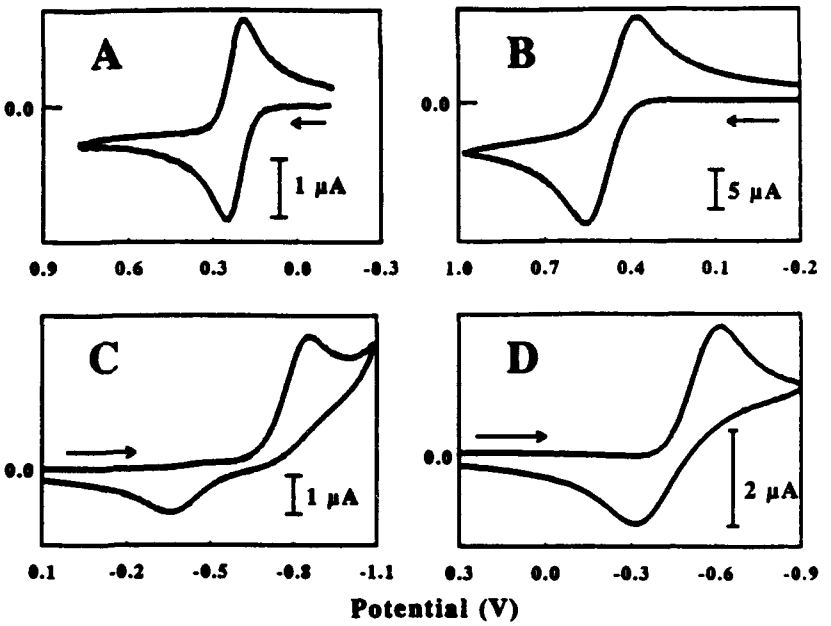

Fig. 1. Voltammetry at fractured GC; (A) 1 mM $Fe(CN)_6^{3-/4-}$ in 1M KCl, ΔE_p = 58 mV; (B) 5 mM $Fe^{2+/3+}$ in 0.2M $HClO_4$, ΔE_p = 181 mV; (C) 5 mM $Eu^{3+/2+}$ in 0.2M $HClO_4$, ΔE_p = 503 mV; and (D) 3 mM $V^{3+/2+}$ in 0.2M $HClO_4$, ΔE_p = 304 mV; ν = 0.2 V/s, voltammograms were all background-subtracted. Arrows indicate initial scan direction.

grinding paper, then polishing with successive 1, 0.3, and 0.05 μm alumina slurries on Microcloth polishing cloth (Buehler). Polished electrodes were sonicated in NANOpure water (Barnstead) for approximately 5 min before placement in the electrochemical cell. During transfer, exposure of the electrode surface to air was reduced by keeping the surface wet. Fractured surfaces were created by first filing away the embedding epoxy and exposing a short length of GC post. The fractured surface was created in situ by breaking this postflush with the epoxy surface.[40] The exposed GC surface remaining embedded in the epoxy served as the electrode surface. For both polished and fractured electrodes the exposed GC surface area was 0.003 to 0.008 cm^2. Voltammetry was performed immediately (within 5 s) of fracturing.

Laser activation of HOPG and polished GC electrodes was performed with a Nd:YAG laser (Quantel) operating at 1064 nm with 9 ns pulses.[12,13] To average spatial variations of the laser, three successive pulses were applied to the electrode. Power densities were 25 MW/cm^2 for GC surfaces and 50 MW/cm^2 for HOPG surfaces. For both HOPG and GC, laser activation was performed in 1M H_2SO_4. Electrochemical pretreatment procedures were all performed by cycling from 0 to 2.2 V *vs.* Ag/AgCl at 0.2 V/s. For HOPG electrodes, this procedure was performed in 0.1M H_2SO_4 for 20 cycles. For GC electrodes, this procedure was performed in 1M H_2SO_4 for 1 to 13 cycles, as discussed later. Generally, 1 to 5 cycles were necessary to observe full activation on GC.

HOPG was obtained from Arthur Moore at Union Carbide and was cleaved with adhesive tape before use. Since laser activation and ECP required an electrochemical cell, the inverted drop cell and validation procedure reported previously[16,41] were not employed. The term validation is used here to refer to HOPG basal plane surfaces which were verified to have high ΔE_p for $Fe(CN)_6^{-2/-4}$ (ΔE_p > 700 mV) as an indication of low defect density.[16]

The procedure for surface modification with organosilanes was similar to literature techniques.[20,21,42] A fractured GC surface was electrochemically pretreated with one cycle under the conditions stated above. The electrode was rinsed and a Kimwipe used to wick off residual water before placing the electrode in neat chlorotrimethylsilane for 5 h. The chlorotrimethylsilane liquid was kept under argon before and during the derivatization procedure. Upon removal from the chlorotrimethylsilane, the electrode was washed once or twice with methanol for 30 min. Voltammetry was performed after the first and second methanol washes. The electrode then was placed in saturated KOH/methanol solution for 1 h to remove the silane, after which final voltammetric measurements were performed. To ensure that the changes in the observed voltammetry were due to derivatization of surface oxides, a control experiment was performed in which tetramethylsilane was used instead of chlorotrimethylsilane but otherwise identical conditions were employed. The tetramethylsilane is not labile toward substitution, and surface oxides are unaffected.

Electrochemical measurements.—Cyclic voltammetry was performed at 0.2 V/s as described previously,[38] with an analog triangular waveform and a laboratory computer. For GC and HOPG experiments, the electrochemical cell was constructed of Teflon and was equipped with a quartz window through which the electrode could be laser irradiated. The three-electrode cell was completed with a Bioanalytical Systems Ag/AgCl (3M NaCl) reference electrode and a platinum wire auxiliary electrode. Electrode areas for HOPG were defined by an o-ring and were approximately 0.02 cm^2.

Rate constants for GC were calculated by the method of Nicholson,[43] assuming α = 0.5; k° values for HOPG were obtained through comparison of experimental voltammetry to simulations involving a potential-dependent α.[44] The rate constants were calculated with literature values for diffusion coefficients: Fe^{2+}_{aq}, $D_R = 9 \times 10^{-6}$ cm^2/s (0.1M $HClO_4$);[45,46] Eu^{+3}_{aq}, $D_o = 7.9 \times 10^{-6}$ cm^2/s (pH 0.3, 1M $NaClO_4$/$HClO_4$);[47] V^{+3}_{aq}, $D_o = 5.2 \times 10^{-6}$ cm^2/s (1M $HClO_4$).[48] In all cases, it was assumed that $D_R = D_o$ for the rate-constant calculations.

Reagents.—Fe^{2+}_{aq} and Eu^{+2}_{aq} solutions were prepared at 5 mM concentrations for GC experiments and at 10 mM concentrations for HOPG experiments from $Fe(NH_4)_2(SO_4)_2 \cdot 6H_2O$ (J.T. Baker, Inc.) and $Eu(NO_3)_3 \cdot (H_2O)_5$ (Aldrich). V^{2+}_{aq} solutions were prepared at 3 to 5 mM concentrations for GC and HOPG experiments from VCl_3 (Aldrich). Supporting electrolyte solutions were prepared with 70% $HClO_4$ (GFS Chemicals) at a concentration of 0.2M unless specified otherwise. $HClO_4$ was used as the supporting electrolyte due to its weak interaction with aquated metal ions.[37,49,50] Electrochemical pretreatment and laser activation procedures were performed in H_2SO_4 (Mallinckrodt). All solutions were prepared with NANOpure water and were degassed with argon or nitrogen prior to use. $ClSiMe_3$ and $SiMe_4$ were obtained from Aldrich, and $ClSiMe_3$ was distilled before use.

Table I. ΔE_p (mV) values at GC and HOPG electrodes under different pretreatment conditions.[a]

	Polished GC	Polished GC/ laser activated (3 × at 25 MW/cm²)[b]	Fractured GC	Frac/ECP[c] GC	HOPG	HOPG/ECP[d]
$Fe^{+3/+2}_{aq}$	258 ± 39[e] [5][f]	263 [2]	186 ± 19 [9]	93 ± 11 [6]	1062 ± 225 [9]	162 ± 22 [4]
$Eu^{+3/+2}_{aq}$	428 ± 27 [7]	>531 [3]	509 ± 42 [8]	70 ± 4 [4]	936 ± 168 [5]	193 ± 18 [3]
$V^{+3/+2}_{aq}$	441 ± 72 [6]		314 ± 13 [4]	95 ± 9 [4]	>835 [4]	372 ± 6 [3]

[a] ν = 0.2 V/s.
[b] Laser activation performed in 1.0*M* H_2SO_4.
[c] ECP procedure for GC consisted of cycling from 0 to 2.2 V at 0.2 V/s for 3 to 5 cycles.
[d] ECP procedure same as GC, but 20 cycles.
[e] Standard deviation.
[f] Number of trials.

Results

The first issue to consider is the kinetic behavior of $Fe^{+3/+2}_{aq}$, $Eu^{+3/+2}_{aq}$, and $V^{+3/+2}_{aq}$ on carbon surfaces which are as well characterized as currently possible. When considering the voltammograms of Fig. 1 to 3, a visual indication of increased electron-transfer rate is a decrease in ΔE_p, which is then reflected in the k° results. Figure 1 shows voltammograms for the aquated systems and $Fe(CN)_6^{-3/-4}$ on a GC surface immediately after exposure to the solution by fracturing. It is clear that the aquated ions are kinetically slower than $Fe(CN)_6^{-3/-4}$ on fractured GC. As indicated in Table I, laser activation of a polished GC surface has little effect on $Fe^{+3/+2}_{aq}$ and $Eu^{+3/+2}_{aq}$ kinetics, in contrast to the large increase in rate observed for $Fe(CN)_6^{-3/-4}$.[1,13] Figure 2 shows voltammograms obtained on HOPG, with all four redox systems exhibiting much larger ΔE_p values than on GC. Although the use of a conventional cell prevented validation of the HOPG surfaces,[16] the ΔE_p values listed in Table I were reproducibly high, exceeding 800 mV for the aquated ions. Thus the behavior of $Fe^{+3/+2}_{aq}$, $Eu^{+2/+3}_{aq}$, and $V^{+3/+2}_{aq}$ on either fractured GC or basal plane HOPG is consistent with slow electron-transfer kinetics.

Figure 3A and B shows the dramatic effect of one ECP cycle on the voltammetry of $Fe^{+3/+2}$ and $Eu^{+3/+2}$ on GC. After even this minimal treatment, ΔE_p for $Eu^{+3/+2}$ decreased from 440 mV for the fractured surface to 76 mV (Table I). $Fe^{+3/+2}$ and $V^{+3/+2}$ also exhibited major decreases in ΔE_p on ECP. Figure 4 shows the effects of successive ECP cycles on ΔE_p, with the greatest changes occurring in the first few cycles. A qualitatively similar effect was observed for HOPG, although a larger number of ECP cycles was required (20 *vs.* 1 to 3). The voltammetry for $Fe^{+3/+2}$ and $Eu^{+3/+2}$ on HOPG before and after ECP is shown in Fig. 3C and D, and the results are listed in Table I.

To test whether the kinetic effects of ECP are mediated by surface oxides, the surface was silanized with $ClSiMe_3$. The unreactive $SiMe_4$ acted as a control. The effects of silanization on $Eu^{+3/+2}$ voltammetry are shown in Table II, with entries A to E representing successive treatments, starting with fractured GC. $ClSiMe_3$ completely negates the effects of ECP-induced activation on $Eu^{+3/+2}$ kinetics (entry C), while hydrolysis of the silanized surface with base restores most of the reactivity of the ECP surface (entry E). The $SiMe_4$ reagent increases ΔE_p somewhat, but its effects are much smaller and probably due to adsorption of organic impurities. Table II demonstrates that the ECP-induced activation of $Eu^{+2/+3}$ charge transfer on GC is eliminated by silanization.

The possibility of Cl^- catalysis[25-27] on GC was tested by adding small amounts of Cl^- to the electrolyte. For Au and Pt electrodes, Cl^- chemisorption greatly accelerates $Fe^{+2/+3}$ electron transfer even at low ($10^{-5}M$) Cl^- concentrations. Neither 10^{-4} nor 0.2*M* Cl^- had any observable effect on $Fe^{+2/+3}$ voltammetry at fractured GC. High (1*M*) Cl^- did increase k° for $Eu^{+3/+2}$ on fractured GC, probably via formation of a chloro complex of $Eu^{+3/+2}$ rather than a bridging

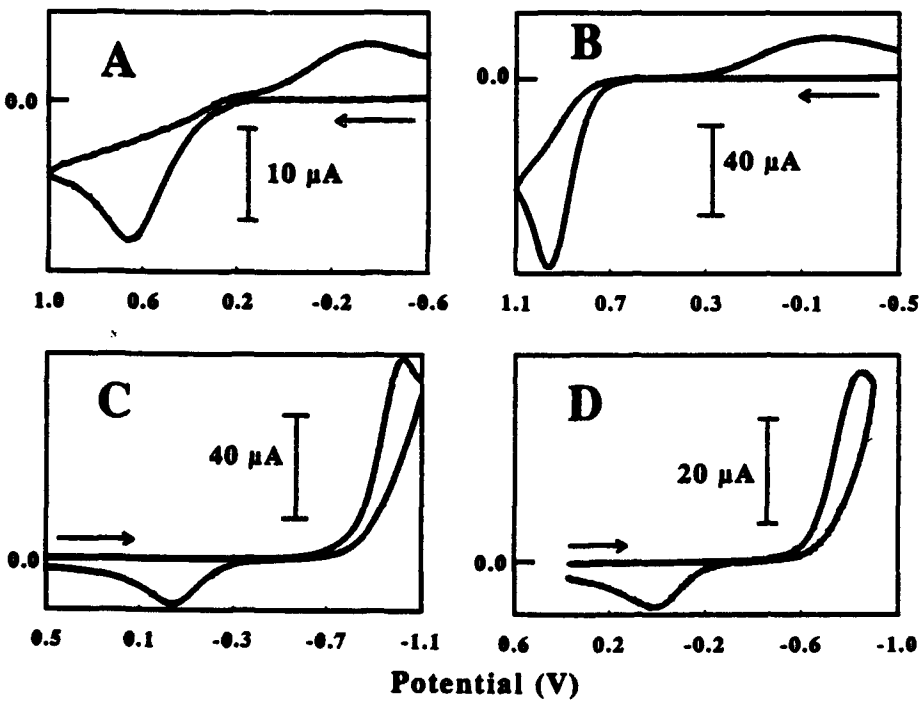

Fig. 2. Voltammetry at HOPG; (A) 1 mM $Fe(CN)_6^{3-/4-}$ in 1*M* KCl, ΔE_p = 1007 mV; (B) 10 mM $Fe^{2+/3+}$ in 0.2*M* $HClO_4$, ΔE_p = 1164 mV; (C) 10 mM $Eu^{3+/2+}$ in 0.2*M* $HClO_4$, ΔE_p = 980 mV; (D) 5 mM V^{+3} in 0.2*M* $HClO_4$, ΔE_p = 860 mV; ν = 0.2 V/s, voltammograms were not background-subtracted; $Fe(CN)_6^{3-/4-}$ voltammetry was obtained using an inverted drop cell as described in Ref. 16. All others were obtained in a cell as described in the Experimental section.

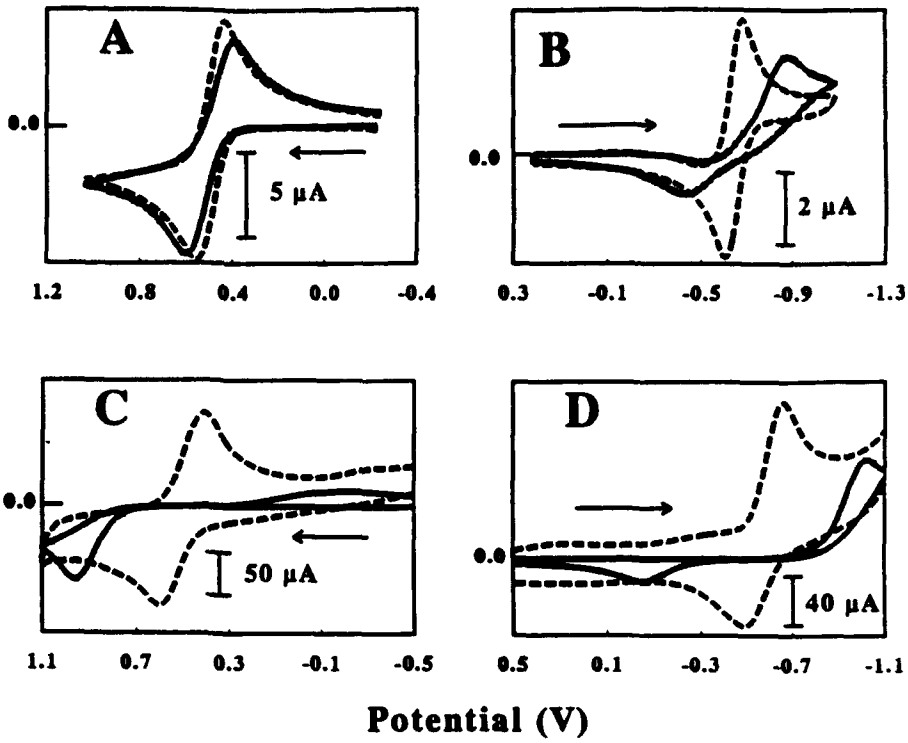

Fig. 3. Voltammetry of Fe^{+2} and Eu^{+3} at HOPG and fractured GC electrodes (solid curves) and the same surfaces after ECP (dashed curves); (A) 5 mM Fe^{+2} on fractured GC and fractured/ECP GC; (B) 5 mM Eu^{+3} on fractured GC and fractured/ECP GC; (C) 10 mM Fe^{+2} on HOPG and HOPG/ECP; and (D) 10 mM Eu^{+3} on HOPG and HOPG/ECP; ν = 0.2 V/s, voltammograms on GC were background subtracted, ECP procedure on GC was 1 cycle from 0 to 2.2 V in 1M H_2SO_4, ECP procedure on HOPG was 20 cycles from 0 to 2.2 V in 0.1M H_2SO_4.

mechanism. Finally, the possibility that freshly fractured GC was oxidized by dissolved oxygen was tested by repeating the kinetic measurement in 1M $HClO_4$ saturated with air. No change in the behavior of $Fe^{+2/+3}$ was observed, neither initially nor after 1 h in air-saturated electrolyte.

Discussion

Past efforts to characterize carbon electrode surfaces have led to the proposal that fractured GC is the GC surface least modified by impurities, oxides, and intentional surface chemical changes.[12,38-40] Accordingly, the fractured GC surface should represent the closest approximation currently available to a pristine GC surface. Similarly, low-defect HOPG basal plane is an ordered surface of known structure which has been characterized electrochemically. These two electrode materials provide good reference surfaces for evaluating the kinetics of various redox systems on carbon electrodes. We reported previously the heterogeneous rate constants for several redox systems on HOPG and laser-activated GC.[16] Although the rate constants on HOPG were significantly lower than those on GC, they did correlate with homogeneous-self-exchange rate constants (k_{exc}). Unfortunately, the k° values on laser-activated or fractured GC are near or above the upper instrumental limit for the systems studied previously, so reliable correlations of k° and k_{exc} were not possible for GC.

First for the unoxidized carbon surfaces, it is possible to relate k° to k_{exc} for $Fe_{aq}^{+3/+2}$, $Eu_{aq}^{+3/+2}$, and $V_{aq}^{+3/+2}$, in part because their k° values are well within the measurable range. The first four columns of Table III compare kinetic data and predictions for five redox systems on fractured GC and basal-plane HOPG. The theoretical k° values, (k_{th}°) were calculated from the simplest Marcus equation

$$\left(\frac{k_{exc}}{Z_{exc}}\right)^{1/2} = \frac{k^\circ}{Z_{el}} \qquad [1]$$

where $Z_{exc} = 10^{11}\ M^{-1}\ s^{-1}$ and $Z_{el} = 10^4\ cm\ s^{-1}$. Several important work-term and double-layer corrections have been developed for this expression by Weaver *et al.*, but both the simple and corrected expression predict that k° tracks $k_{exc}^{1/2}$.[31-34] Since these corrections are not yet possible for carbon electrodes due to their unknown double-layer properties, we shall use Eq. 1 as a first approximation for predictions of k_{th}° from k_{exc}.

Several observations are available from Table III. First, the five redox systems cover a wide range of predicted k_{th}°, with the aquated ions easily within the measurable range of rate constants. Second, the k° on fractured GC (k_{frac}°) is within a factor of 16 of that predicted from Eq. 1. Third,

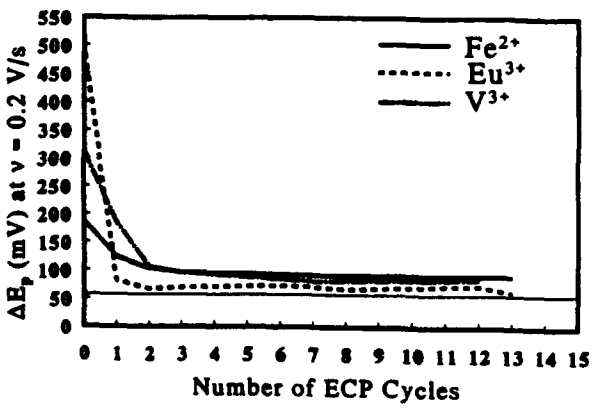

Fig. 4. Decrease in peak separation with number of ECP cycles for Fe_{aq}^{2+}, Eu_{aq}^{3+}, and V_{aq}^{3+} on fractured GC. ECP procedures employed 0 to 2.2 V cycles in 1M H_2SO_4. Line indicates reversible limit.

Table II. Effects of silanization on $Eu_{aq}^{+3/+2}$ voltammetry.

	ΔE_p (mV)[a] Reagents	
	$ClSiMe_3$	$SiMe_4$
A. Fractured GC	490	492
B. Fractured after ECP	70	68
C. B. + silane + MeOH wash	442	149
D. C. + second MeOH wash	470	202
E. D. + KOH/MeOH wash	123	110

[a] ΔE_p values were acquired at 0.2 V/s and are averages of two trials for both reagents.

Table III. Kinetic results for fractured GC and HOPG.

System	k_{exc} ($M^{-1}s^{-1}$)	k°_{th} [b] (cm/s)	k°_{frac} [c] (cm/s)	k°_{HOPG} [d] (cm/s)	$k^\circ_{ECP/GC}$ (cm/s)
$Fe_{aq}^{+3/+2}$ [a]	1×10^{-3}	1×10^{-3}	$(2.3 \pm 0.5) \times 10^{-3}$ [8]	1.4×10^{-5} [3]	$(1.2 \pm 0.3) \times 10^{-2}$ [5]
$Eu_{aq}^{+3/+2}$ [a]	2×10^{-4}	4×10^{-4}	$(8 \pm 4) \times 10^{-5}$ [8]	2.5×10^{-6} [2]	$(4.0 \pm 0.1) \times 10^{-2}$ [4]
$V_{aq}^{+3/+2}$ [a]	0.05	7×10^{-3}	$(4.5 \pm 0.5) \times 10^{-4}$ [4]	$<3 \times 10^{-6}$ [1]	$(8.7 \pm 0.3) \times 10^{-1}$ [4]
$Fe(CN)_6^{-3/-4}$ [e]	2×10^4	4.2	≥ 0.5	$<10^{-6}$	
$Ru(NH_3)_6^{+3/+2}$ [e]	4×10^3	1.9	0.3	9×10^{-4}	

[a] k_{exc} data from Ref. 34.
[b] Calculated from Eq. 1.
[c] Rate constants indicate mean and standard deviation, number in brackets is number of trials.
[d] HOPG rate constants obtained from comparison to simulations for HOPG C-V's; surfaces were not validated.
[e] Data from Ref. 16.

k°_{frac} is lower than k°_{th} for all cases except $Fe^{+3/+2}$, consistent with Hupp and Weaver's observations of the effects of work terms on k° for mercury electrodes.[34] Fourth, k° on HOPG is much lower than both k° on fractured GC and k°_{th} as observed previously for numerous outer-sphere systems.[16] The most likely cause of this difference is the low density of electronic states in HOPG. As noted in the Experimental section, the HOPG surfaces were not validated due to the use of a cell rather than inverted drop (resulting in strain-induced defects), so the k°_{HOPG} values represent upper limits of the true basal-plane values. Fifth, a least squares line for a plot of log k°_{frac} *vs.* log k_{exc} for the systems in Table III has a slope of 0.42 ± 0.08, intercept of -2.2 ± 0.6, and a correlation coefficient of 0.95. Although the fit is not as good as that for a more sophisticated treatment of the aquated redox systems on a mercury electrode,[34] the slope and intercept are near the values of 0.50 and -1.5 predicted from Eq. 1. Since the double-layer and work-term corrections for carbon electrodes are not available, the observed heterogeneous rate constants observed on fractured GC are approximately consistent with Eq. 1. Finally, the rates on fractured GC were slightly higher than those on laser-activated GC for the aquated ions (see Table I), but this difference is insignificant compared to the difference between GC and HOPG.

The overall conclusion for fractured GC and HOPG before ECP is that $Fe^{+3/+2}$, $Eu^{+3/+2}$, and $V^{+3/+2}$ behave approximately the same as outer-sphere systems such as $Ru(NH_3)_6^{+3/+2}$, $IrCl_6^{-2/-3}$, etc. In particular, the observed k° for fractured GC (when it can be measured) is within an order of magnitude of that predicted from Eq. 1, and the deviation from k°_{th} is generally on the low side. As was the case for previous outer-sphere systems, aquated ions exhibit substantially slower kinetics on HOPG, probably because of the unusual electronic properties of HOPG. Figure 5 shows the aquated ion results from fractured GC and HOPG plotted together with previous data for other redox systems. Although the scatter is significant, the aquated ions follow the same trends as the faster outer-sphere systems.

Although the kinetics observed on fractured GC and HOPG for the aquated ions are reasonably consistent with that expected for outer-sphere electron transfer, the behavior following electrochemical surface oxidation is different. As shown in Fig. 3 and Table III (fifth column), ECP significantly increases k°, by factors of 5.2 (for $Fe^{+3/+2}$), 19 ($V^{+3/+2}$), and 500 ($Eu^{+3/+2}$). For $Eu^{+3/+2}$, the ECP-induced rate increase is eliminated reversibly by silanization, indicating that the rate enhancement is mediated by surface oxides. The intent of using HOPG basal plane and fractured GC was to compare ECP surfaces with reference surfaces as low as possible in surface oxides. Low defect HOPG is certainly low in oxides, and fractured GC also has zero oxide coverage, at least at the instant of fracture. Schrader[31,32] used x-ray photoemission spectroscopy (XPS) to demonstrate that argon-ion-damaged HOPG does not react with H_2O to form surface oxides in UHV conditions. That saturation of the solution with air before fracturing has no effect on the $Fe^{+3/+2}$ rate implies that oxidation by air does not lead to a catalytically active surface. It is difficult to rule out low levels of oxides on fractured GC, but it is clear that ECP causes a major rate increase, and that fractured GC is a useful reference surface exhibiting primarily outer-sphere electron transfer. Thus the kinetic behavior exhibited in Fig. 1 and 2 and the third and fourth columns of Table III is that for surfaces with minimal (if any) oxide related catalysis.

The possible origins of the ECP-induced rate may involve several phenomena, including indirect effects such as double-layer corrections, changes in hydrophobicity or adsorption, or more direct effects such as inner-sphere catalysis. While ECP-induced oxide formation may alter double-layer structure substantially, such effects seem unlikely in the aquated ions studied here. A double-layer correction should depend strongly on the position of $E_{1/2}$ relative to the pzc (-0.2 *vs.* Ag/AgCl for HOPG,[53,54] *ca.* +0.1 V for GC).[55] Yet all three systems show rate increases even though they have $E_{1/2}$ values ranging from ca. +0.5 to -0.7 V *vs.* Ag/AgCl. Wightman *et al.* showed that Frumkin effects are observed for GC at elevated pH where surface carboxylates are deprotonated, but disappeared below pH 3.[56] All the current results were obtained in 0.2*M* acid, where carboxylates should be uncharged. Adsorption to the oxidized surface was tested by comparing experimental and simulated voltammograms and by semi-integration.[57] No evidence of adsorption was observed on the surfaces formed by 3 to 5 ECP cycles, although some was apparent for heav-

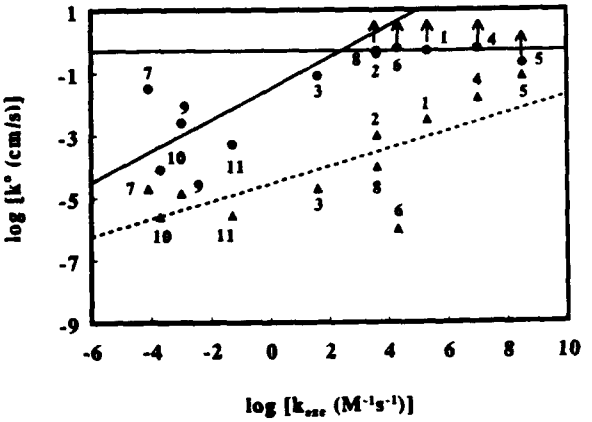

Fig. 5. Log-log plot for heterogeneous rate constants (k°) vs. homogeneous self-exchange rates (k_{exc}) for redox systems in Table III and from Ref. 16, Table II. Triangles are for HOPG basal plane, circles are for GC. Solid line is from Marcus theory, Eq. 1 in text. Dashed line is least squares fit for all points, HOPG data: slope = 0.28, y-intercept = −4.5, correlation coefficient = 0.75. Horizontal line indicates upper limit of measurable rate constants for GC experiments, $k^\circ = 0.5$ cm/s. Number assignments for redox systems are: (1) $IrCl_6^{-2/-3}$; (2) $Ru(NH_3)_6^{+3/+2}$; (3) $Co(phen)_3^{+3/+2}$; (4) $MV^{+2/+1}$; (5) $Fe(phen)_3^{+3/+2}$; (6) $Fe(CN)_6^{-3/-4}$; (7) $Co(en)_3^{+3/+2}$; (8) $Ru(en)_3^{+3/+2}$; (9) $Fe_{aq}^{+3/+2}$; (10) $Eu_{aq}^{+3/+2}$; and (11) $V_{aq}^{+3/+2}$.

ily oxidized surfaces. The oxidized surface is probably less hydrophobic than fractured GC and certainly less than HOPG, but hydrophobic effects did not appear important for the series of outer-sphere systems studied previously. Redox systems of different electrostatic charge, and presumably different sensitivity to hydrophobic effects, did not vary greatly in rate on HOPG.[16]

The key observation leading to the origin of the ECP-induced rate increase is that ECP yields k° values above those predicted by Eq. 1 for outer-sphere electron transfer. Furthermore, inner-sphere catalysis via bridging groups has been reported for $Fe^{+2/+3}$ on Pt and Au in Cl^- media,[35-37] and for $Fe^{+2/+3}$ in cytochromes on polished graphite.[21] In the latter case, catalysis was blocked by silanization or cationic species such as Mg^{+2}. The observations lead to a proposal that surface oxides on carbon provide an inner-sphere route for electron transfer to $Fe_{aq}^{+3/+2}$, $Eu_{aq}^{+3/+2}$, and $V_{aq}^{+3/+2}$ which increases the rate constant substantially over the outer-sphere value. Oxide catalysis at GC is analogous to Cl^- catalysis of $Fe^{+3/+2}$ at Au and Pt, and likely involves a qualitatively similar bridging mechanism. ECP also reduced the rate differences among the three aquated ions observed on the fractured GC surface, with the k°_{fmc} values differing by a factor of 28 and $k^\circ_{GC/ECP}$ by a factor of 5. For a bridging mechanism to be significant for $Fe_{aq}^{+2/+3}$, $Eu_{aq}^{+2/+3}$, and $V_{aq}^{+2/+3}$, the aquated ions must be substitution labile. The water-exchange rate constants for several relevant ions are as follows, all expressed as common logorithms: Fe^{+2}, 6.64; Fe^{+3}, 2.20; V^{+2}, 1.9; V^{+3}, 2.7;[38] and Ru^{+2}, −1.84; Ru^{+3}, −5.3.[38] $Eu^{+2/+3}$ water exchange is too fast to measure, but similar lanthanides have water-exchange rate constants in the range of 10^7 to 10^9 M^{-1} s^{-1}.[40] Thus $Fe_{aq}^{+2/+3}$, $Eu_{aq}^{+2/+3}$, and $V_{aq}^{+2/+3}$ exhibit fast ligand exchange rates compared to the substitution inert $Ru^{+2/+3}$ systems.

The inhibition of oxide catalysis by silanization implies the involvement of -OH, -COOH, or similar hydroxyl-containing functional groups in the inner-sphere route. Although hydroxyl-containing functional groups in the inner-sphere route. Although hydroxyl and carboxylate functional groups have long been known to occur on oxidized carbon surfaces, a structure proposed by Kozlowski and Sherwood[41] may be particularly relevant here. XPS spectra of carbon fibers after ECP supports the formation of structure 1. This structure may exist primarily as structure 2, which is itself similar to the common inorganic ligand acetoacetonate (acac). Presumably the formation of structure 2 would be prevented by silanization.

Structures

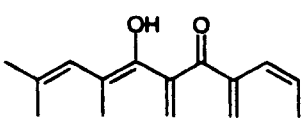

(1)

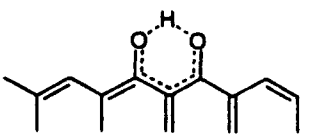

(2)

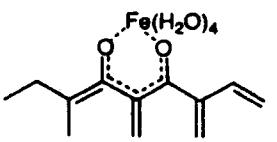

(3)

The aquated ions studied here are fairly weak and substitution labile, while the corresponding acac complexes are quite strong (*e.g.*, K_{form} for $[Fe(III)acac(H_2O)_4]^{+2}$ is 10^{10}).[42] It is reasonable to propose that inner-sphere catalysis of $Fe_{aq}^{+2/+3}$, $Eu_{aq}^{+2/+3}$, and $V_{aq}^{+2/+3}$ involves an intermediate such as structure 3. The relatively strong interaction of the metal ion with the surface acac group may provide the driving force for inner-sphere catalysis, and possibly for displacement of the proton in structure 2.

In summary, the $Fe_{aq}^{+3/+2}$, $Eu_{aq}^{+2/+2}$, and $V_{aq}^{+3/+2}$ redox systems are slow on either fractured GC or HOPG, as is consistent with their low self-exchange rates. On fractured GC with presumably low oxide coverage, the observed rate constants are approximately those predicted from simple Marcus theory. Even minor electrochemical oxidation of the GC (or HOPG) surface leads to large increases in observed rate constants, consistent with an oxide mediated inner-sphere catalytic route. A surface oxide structure observed on oxidized carbon fibers is a possible site for transient metal-ion binding and catalysis, although alternative mechanisms based on double-layer or hydrophobic effects cannot be ruled out completely.

Acknowledgment

This work was supported by a grant from the Air Force Office of Scientific Research and an ACS Analytical Division Fellowship sponsored by Eli Lilly for CAM. The authors thank John Pudelski for assistance with the silanization procedure.

Manuscript submitted Feb. 11, 1993; revised manuscript received June 4, 1993.

The Ohio State University assisted in meeting the publication costs of this article.

REFERENCES

1. R. L. McCreery, in *Electroanalytical Chemistry*, Vol. 17, A. J. Bard, Editor, Dekker, New York (1991).
2. K. Kinoshita, *Carbon: Electrochemical and Physicochemical Properties*, Wiley, New York (1988).
3. S. Sarangapani, J. R. Akridge, and B. Schumm, Editors, *Proceedings of the Workshop on the Electrochemistry of Carbon*, The Electrochemical Society, Pennington, NJ (1984).
4. R. M. Wightman, M. R. Deakin, P. M. Kovach, P. M. Kuhr, and K. J. Stutts, *This Journal*, **131**, 1578 (1984).
5. I. F. Hu, D. H. Karweik, and T. Kuwana, *J. Electroanal. Chem.*, **188**, 59 (1985).
6. D. T. Fagan, I. F. Hu, and T. Kuwana, *Anal. Chem.*, **57**, 2759 (1985).
7. M. R. Deakin, P. M. Kovach, K. J. Stutts, and R. M. Wightman, *ibid.*, **58**, 1474 (1986).
8. G. N. Kamau, W. S. Willis, and J. F. Rusling, *ibid.*, **57**, 545 (1985).
9. D. C. Thornton, K. T. Corby, V. A. Spendel, J. Jordar., A. Robbat, D. J. Rutstrom, M. Gross, and G. Ritzler, *ibid.*, **57**, 150 (1985).
10. R. C. Engstrom and V. A. Strasser, *ibid.*, **56**, 136 (1984).
11. G. E. Cabaniss, A. A. Diamantis, W. R. Murphy, Jr., R. W. Linton, and T. J. Meyer, *J. Am. Chem. Soc.*, **107**, 1845 (1985).
12. R. J. Rice, N. Pontikos, and R. L. McCreery, *ibid.*, **112**, 4617 (1990).
13. M. Poon and R. L. McCreey, *Anal. Chem.*, **58**, 2745 (1986).
14. K. J. Stutts, P. M. Kovach, W. G. Kuhr, and R. M. Wightman, *ibid.*, **55**, 1632 (1983).
15. R. Bowling, R. T. Packard, and R. L. McCreery, *Langmuir*, **5**, 683 (1989).
16. K. R. Kneten and R. L. McCreery, *Anal. Chem.*, **64**, 2518 (1992).
17. R. J. Taylor and A. A. Humffray, *J. Electroanal. Chem.*, **42**, 347 (1973).
18. C. Barbero, J. J. Silber, and L. Sereno, *ibid.*, **248**, 321 (1988).
19. P. M. Kovach, M. R. Deakin, and R. M. Wightman, *J. Phys. Chem.*, **90**, 4612 (1986).
20. F. A. Armstrong and K. J. Brown, *J. Electroanal. Chem.*, **219**, 319 (1987).
21. F. A. Armstrong, A. M. Bond, H. A. O. Hill, B. N. Oliver, and I. S. M. Psalti, *J. Am. Chem. Soc.*, **111**, 9185 (1989).
22. L. J. Kepley and A. J. Bard, *Anal. Chem.*, **60**, 1459 (1988).
23. T. Nagaoka and T. Yoshino, *ibid.*, **58**, 1037 (1986).
24. T. Nagaoka, T. Fukunaga, T. Yoshino, I. Watanabe, T. Nakayama, and S. Okazaki, *ibid.*, **60**, 2766 (1988).
25. R. A. Marcus, *J. Phys. Chem.*, **67**, 853 (1963).

26. J. Kawiak, P. Kulesza, and Z. Galus, *J. Electroanal. Chem.*, **226**, 305 (1987).
27. T. Saji, T. Yamada, and S. Aoyagui, *ibid.*, **61**, 147 (1975).
28. T. Saji, T. Maruyama, and S. Aoyagui, *ibid.*, **86**, 219 (1978).
29. R. Sohr and L. Muller, *Electrochim. Acta*, **20**, 451 (1975).
30. R. Penner, M. Heben, T. Longin, and N. S. Lewis, *Science*, **250**, 1118 (1990).
31. M. J. Weaver and J. J. Zuckerman, Editors, *Inorganic Reactions and Methods*, VCH, **15**, 153-163 (1986).
32. M. J. Weaver, *J. Phys. Chem.*, **84**, 568 (1980).
33. M. J. Weaver, *ibid.*, **15**, 1733 (1976).
34. J. T. Hupp and M. J. Weaver, *Inorg. Chem.*, **22**, 2557 (1983).
35. N. C. Hung and Z. Nagy, *This Journal*, **134**, 2215 (1987).
36. J. Weber, Z. Samec, and V. Marecek, *ibid.*, **89**, 271 (1978).
37. D. C. Johnson and E. W. Resnick, *Anal. Chem.*, **49**, 1918 (1977).
38. N. M. Pontikos and R. L. McCreery, *J. Electroanal. Chem.*, **324**, 229 (1992).
39. M. T. McDermott, C. A. McDermott, and R. L. McCreery, *Anal. Chem.*, **65**, 937 (1993).
40. C. D. Allred and R. L. McCreery, *ibid.*, **64**, 444 (1992).
41. M. T. McDermott, K. Kneten, and R. L. McCreery, *J. Phys. Chem.*, **96**, 3124 (1992).
42. C. M. Elliott and R. W. Murray, *Anal. Chem.*, **48**, 1247 (1976).
43. R. S. Nicholson, *ibid.*, **37**, 1351 (1965).
44. D. A. Corrigan and D. H. Evans, *J. Electroanal. Chem.*, **106**, 287 (1980).
45. R. J. Bowling, Ph.D. Thesis, The Ohio State University, Columbus, OH (1989).
46. M. Stulikova and F. Vydra, *J. Electroanal. Chem. Interfacial Electrochem.*, **38**, 349 (1972).
47. T. Matusinovic and D. E. Smith, *Inorg. Chem.*, **20**, 3121 (1981).
48. J. Lipkowski, A. Czerwinski, E. Ciesznyska, Z. Galus, and J. Sobkoswski, *J. Electroanal. Chem.*, **119**, 261 (1981).
49. M. R. Rosenthal, *J. Chem. Educ.*, **50**, 331 (1973).
50. L. Johansson, *Coord. Chem. Rev.*, **12**, 241 (1974).
51. M. E. Schrader, *J. Phys. Chem.*, **79**, 2508 (1975).
52. M. E. Schrader, *ibid.*, **84**, 2774 (1980).
53. H. J. Gerischer, *ibid.*, **89**, 4249 (1985).
54. H. Gerischer, R. McIntyre, D. Scherson, and W. Storck, *ibid.*, **91**, 1930 (1987).
55. R. K. Jaworski and R. L. McCreery, *This Journal*, **140**, 1360 (1993).
56. M. R. Deakin, K. J. Stutts, and R. M. Wightman, *J. Electroanal. Chem.*, **182**, 113 (1985).
57. R. Bowling and R. L. McCreery, *Anal. Chem.*, **60**, 605 (1988).
58. M. L. Tobe, in *Comprensive Coordinate Chemistry*, Vol. 1, p. 284, G. Wilkinson, Editor, Pergamon Press, New York (1987).
59. P. Bernhard, L. Helm, I. Rapaport, A. Ludi, and A. E. Merbach, *J. Chem. Soc. Chem. Commun.* p. 302 (1984).
60. C. Cossy, L. Helm, and A. E. Merbach, *Inorg. Chem.*, **27**, 1973 (1988).
61. C. Kozlowski and P. M. A. Sherwood, *J. Chem. Soc., Faraday Trans.*, **81**, 2745 (1985).
62. A. E. Martell and R. M. Smith, *Critical Stability Constants*, Vol. 3, pp. 244-247, Plenum Press, New York (1977).

Reprinted from JOURNAL OF THE ELECTROCHEMICAL SOCIETY
Vol. 140, No. 9, September 1993
Printed in U.S.A.